

DISSERTATION

CONTRIBUTIONS OF GAS-PHASE PLASMA CHEMISTRY TO SURFACE  
MODIFICATIONS AND GAS-SURFACE INTERACTIONS: INVESTIGATIONS OF  
FLUOROCARBON RF PLASMAS

Submitted by

Michael F. Cuddy II

Department of Chemistry

In partial fulfillment of the requirements

For the Degree of Doctor of Philosophy

Colorado State University

Fort Collins, Colorado

Summer 2012

Doctoral Committee:

Advisor: Ellen R. Fisher

Amber Krummel  
Nancy E. Levinger  
Dawn Rickey  
Azer P. Yalin

## ABSTRACT

### CONTRIBUTIONS OF GAS-PHASE PLASMA CHEMISTRY TO SURFACE MODIFICATIONS AND GAS-SURFACE INTERACTIONS: INVESTIGATIONS OF FLUOROCARBON RF PLASMAS

The fundamental aspects of inductively coupled fluorocarbon (FC) plasma chemistry were examined, with special emphasis on the contributions of gas-phase species to surface modifications. Characterization of the gas-phase constituents of single-source  $\text{CF}_4$ -,  $\text{C}_2\text{F}_6$ -,  $\text{C}_3\text{F}_8$ -, and  $\text{C}_3\text{F}_6$ -based plasmas was performed using spectroscopic and mass spectrometric techniques. The effects of varying plasma parameters, including applied rf power ( $P$ ) and system pressure ( $p$ ) were examined. Optical emission spectroscopy (OES) and laser-induced fluorescence (LIF) spectroscopy were employed to monitor the behavior of excited and ground  $\text{CF}_x$  ( $x = 1,2$ ) radicals, respectively. Mass spectrometric techniques, including ion energy analyses, elucidated behaviors of nascent ions in the FC plasmas. These gas-phase data were correlated with the net effect of substrate processing for Si and  $\text{ZrO}_2$  surfaces. Surface-specific analyses were performed for post-processed substrates via x-ray photoelectron spectroscopy (XPS) and contact angle goniometry. Generally, precursors with lower F/C ratios tended to deposit robust FC films of high surface energy. Precursors of higher F/C ratio, such as  $\text{CF}_4$ , were associated with etching or removal of material from surfaces. Nonetheless, a net balance between deposition of FC moieties and etching of material exists for each plasma system.

The imaging of radicals interacting with surfaces (IRIS) technique provided insight into the phenomena occurring at the interface of the plasma gas-phase and substrate of interest. IRIS results demonstrate that  $CF_x$  radicals scatter copiously, with surface scatter coefficients,  $S$ , generally greater than unity under most experimental conditions. Such considerable  $S$  values imply *surface-mediated production* of the  $CF_x$  radicals at FC-passivated sites. It is inferred that the primary route to surface production of  $CF_x$  arises from energetic ion bombardment and ablation of surface FC films. Other factors which may influence the observed  $CF_x$  scatter coefficient include the surface with which the radical interacts, the vibrational temperature ( $\Theta_v$ ) of the radical in its gas-phase, and radical interactions in the gas phase. The analyses of  $\Theta_v$  in particular were extended to diatomic radicals from other plasma sources, including nitric oxide and fluorosilane systems, to gauge the contributions of vibrational energy to surface reactivity. In general, a monotonic increase in  $S$  is observed for CF, NO, and SiF radicals with increasing  $\Theta_v$ .

Preliminary results for mixed plasma precursor systems (i.e. FC/H<sub>2</sub>, FC/O<sub>2</sub>) indicate that the choice of feed gas additives has a profound effect on surface modification. Hydrogen additions tend to promote FC film deposition through scavenging of fluorine atoms, whereas oxygen consumes polymerizing species, thus favoring etching regimes. Time-resolved optical emission spectroscopy (TR-OES) studies of gas-phase species elucidate the mechanisms by which these processes occur. Ultimately, the work presented herein expands the fundamental chemical and physical understanding of fluorocarbon plasma systems.

## ACKNOWLEDGMENTS

I am eternally grateful to all those who have guided, mentored, and supported me in pursuit of this educational milestone. There are countless individuals to whom I owe thanks. To my advisor, Prof. Ellen R. Fisher, whose guidance through the morass of scientific muddle helped hone my competence. Early in my graduate career, I was humbled by all that which I did *not* know; your counsel propelled me to approach those obstacles as a scientist. To my fellow graduate students in the Fisher group, whose solidarity and encouragement made the experience not only bearable, but enjoyable. To my advisors in Chemistry at Eastern Illinois University, Dr. Barbara Lawrence and Drs. Richard and Ellen Keiter, who inspired an impetuous, young undergraduate researcher to pursue a PhD. To my family, especially my mother, Lora, my father, Michael, and my brothers, Jesse and Connor, who fostered my interests in science and mathematics from the start. To my wife, Kristin, whose tolerance for my idiosyncrasies defies my understanding. To the SMART Fellowship, that funded nearly my entire graduate career. To those I've forgotten, to those come and gone, to those friends and acquaintances, to those teachers and colleagues, to those who have influenced, motivated, inspired and educated, I am dearly indebted. Thank you, this dissertation is dedicated to you.

TABLE OF CONTENTS

**ABSTRACT** ..... ii

**ACKNOWLEDGMENTS** ..... iv

**TABLE OF CONTENTS** ..... v

**LIST OF TABLES** ..... ix

**LIST OF FIGURES** ..... x

**CHAPTER 1. Introduction** ..... 1

    1.1. Plasma Chemistry and Physics ..... 2

    1.2. Motivations for Fluorocarbon Investigations ..... 6

    1.3. Overview of Research ..... 10

    1.4. References ..... 15

**CHAPTER 2. Experimental Methods** ..... 18

    2.1. General Information ..... 19

    2.2. Gas-phase Plasma Diagnostics ..... 20

    2.3. Gas-Surface Interactions ..... 28

    2.4. Surface Analyses ..... 29

    2.5. References ..... 32

**CHAPTER 3. Investigation of the Roles of Gas-Phase CF<sub>2</sub> Molecules and F Atoms  
During Fluorocarbon Plasma Processing of Si and ZrO<sub>2</sub> Substrates** ..... 34

    3.1. Introduction ..... 35

    3.2. Results ..... 37

3.3. Discussion .....	49
3.4. Summary .....	60
3.5. Supplemental Information .....	61
3.6. References.....	63
<b>CHAPTER 4. Contributions of CF and CF<sub>2</sub> Species to Fluorocarbon Film Composition and Properties for C<sub>x</sub>F<sub>y</sub> Plasma-Enhanced Chemical Vapor Deposition .....</b>	<b>66</b>
4.1. Introduction.....	67
4.2. Results.....	69
4.3. Discussion.....	78
4.4. Summary .....	88
4.5. Supplemental Information .....	90
4.6. References.....	91
<b>CHAPTER 5. Energy Partitioning in Diatomic Radicals and Its Influence on Surface Scatter Coefficients for NO, SiF and CF in Inductively Coupled Plasmas .....</b>	<b>94</b>
5.1. Introduction.....	95
5.2. Results.....	97
5.3. Discussion.....	109
5.4. Summary .....	121
5.5. References.....	122
<b>CHAPTER 6. Ion Contributions to Gas-Surface Interactions in Inductively Coupled Fluorocarbon Plasmas.....</b>	<b>125</b>
6.1. Introduction.....	126
6.2. Results.....	130

6.3. Discussion .....	142
6.4. Summary .....	151
6.5. Supplemental Information .....	153
6.6. References.....	161
<b>CHAPTER 7. Effect of Mixed Fluorocarbon Precursor Plasmas on Carbon- and Fluorine-Containing Species .....</b>	<b>166</b>
7.1. Introduction.....	167
7.2. Results and Discussion .....	170
7.3. Summary .....	182
7.4. References.....	184
<b>CHAPTER 8. Research Summary and Perspectives .....</b>	<b>187</b>
8.1. Research Summary .....	188
8.2. Future Directions .....	190
8.3. References.....	195
<b>APPENDIX A. Calculations of Characteristic Plasma Temperatures .....</b>	<b>196</b>
A.1. Electron Temperatures .....	196
A.2. Vibrational Temperatures .....	200
A.3. References.....	203
<b>APPENDIX B. Preliminary Results for Characteristic CF<sub>2</sub> Temperatures .....</b>	<b>204</b>
B.1. Vibrational Temperatures.....	204
B.2. Translational Temperatures.....	207
B.3. References .....	211

<b>APPENDIX C. Independent Research Proposal</b> .....	212
C.1. Abstract .....	213
C.2. Background and Significance.....	214
C.3. Research Design and Methods .....	217
C.3.1. Experimental Approaches .....	217
C.3.1.a. Analysis of Binding Strengths of ECs.....	217
C.3.1.b. Two-dimensional Fluorescence Imaging of SWNT/EC So- lutions, Complexes.....	221
C.3.2. Potential Limitations .....	223
C.4. Summary and Outlook .....	225
C.5. References .....	226
<b>LIST OF ABBREVIATIONS</b> .....	229

## LIST OF TABLES

<b>1.1.</b> Threshold energies for selected plasma processes .....	8
<b>2.1.</b> Transitions used for actinometry .....	22
<b>2.2.</b> CF, CF <sub>2</sub> , and NO OES, LIF, and IRIS parameters .....	25
<b>2.3.</b> Liquid-vapor surface tensions for H <sub>2</sub> O/CH <sub>3</sub> OH .....	31
<b>3.1.</b> CF <sub>2</sub> <sup>+</sup> mean ion energies.....	41
<b>3.2.</b> <i>S</i> (CF <sub>2</sub> ) vs. <i>P</i> for various plasma/substrate combinations .....	46
<b>4.1.</b> Properties of plasma-deposited FC films.....	76
<b>5.1.</b> <i>S</i> (SiF) and $\Theta_T$ , $\Theta_V$ , and $\Theta_R$ for SiF .....	100
<b>5.2.</b> <i>S</i> (NO)/Si and <i>S</i> (NO)/Pt and $\Theta_V$ and $\Theta_R$ for NO .....	101
<b>5.3.</b> <i>S</i> (CF) and $\Theta_V$ and $\Theta_R$ for CF .....	102
<b>5.4.</b> <i>T<sub>e</sub></i> values for CF <sub>4</sub> , C <sub>2</sub> F <sub>6</sub> , NO, and SiF <sub>4</sub> plasmas .....	113
<b>6.1.</b> $\Delta S$ (CF <sub><i>x</i></sub> ) for different FC plasmas.....	138
<b>A.1.</b> Ar emission parameters for <i>T<sub>e</sub></i> calculations .....	197
<b>A.2.</b> Vibrational modes and energies for CF <sub>2</sub> .....	201
<b>B.1.</b> $\Theta_T$ (CF <sub>2</sub> ) for C <sub>2</sub> F <sub>6</sub> and C <sub>3</sub> F <sub>6</sub> plasmas .....	210
<b>C.1.</b> Model EC/substrate test materials.....	219

## LIST OF FIGURES

<b>1.1.</b> Plasma sheath potential.....	5
<b>2.1.</b> LIF apparatus schematic .....	23
<b>2.2.</b> IRIS apparatus schematic.....	27
<b>3.1.</b> OES and actinometry data for CF <sub>4</sub> and C <sub>2</sub> F <sub>6</sub> plasmas .....	38
<b>3.2.</b> Actinometric OES data for CF <sub>2</sub> <sup>*</sup> and F <sup>*</sup> in FC/substrate systems.....	40
<b>3.3.</b> CF <sub>2</sub> LIF excitation spectrum and ground state densities .....	43
<b>3.4.</b> LIF images and IRIS cross-sections for CF <sub>2</sub> in CF <sub>4</sub> plasma.....	44
<b>3.5.</b> C <sub>1s</sub> and F <sub>1s</sub> XPS spectra of CF <sub>4</sub> -deposited films .....	47
<b>3.6.</b> C <sub>1s</sub> and F <sub>1s</sub> XPS spectra of C <sub>2</sub> F <sub>6</sub> -deposited films.....	48
<b>3.7.</b> CF <sub>4</sub> and C <sub>2</sub> F <sub>6</sub> plasma-surface interaction schematic.....	52
<b>3.8.</b> S(CF <sub>2</sub> ) values as a function of mean CF <sub>2</sub> <sup>+</sup> ion energies.....	56
<b>3.9.</b> C <sub>1s</sub> XPS spectra for C <sub>2</sub> F <sub>6</sub> films as a function of substrate position .....	62
<b>4.1.</b> Time-resolved OES analyses of CF <sup>*</sup> and CF <sub>2</sub> <sup>*</sup> .....	70
<b>4.2.</b> LIF images and IRIS cross-sections for CF and CF <sub>2</sub> in C <sub>3</sub> F <sub>6</sub> plasmas .....	72
<b>4.3.</b> S(CF) and S(CF <sub>2</sub> ) as a function of FC precursor choice .....	73
<b>4.4.</b> C <sub>1s</sub> XPS spectra for FC films from CF <sub>4</sub> , C <sub>2</sub> F <sub>6</sub> , C <sub>3</sub> F <sub>8</sub> , and C <sub>3</sub> F <sub>6</sub> plasmas.....	75
<b>4.5.</b> Zisman plots for bare Si and CF <sub>4</sub> -deposited film.....	77
<b>4.6.</b> Δγ <sub>c</sub> vs. film F/C ratio and S(CF <sub>x</sub> ) vs. Δγ <sub>c</sub> .....	85
<b>4.7.</b> SEM and AFM micrographs for FC films .....	87

<b>4.8.</b> CF LIF excitation spectrum .....	90
<b>5.1.</b> Experimental and simulated NO emission spectra for $\Theta_V$ determination.....	99
<b>5.2.</b> $\Theta_V$ vs. $P$ for NO $^2\Pi$ and $^2\Sigma^+$ states .....	103
<b>5.3.</b> IRIS images and cross-sections for NO .....	104
<b>5.4.</b> SiF characteristic temperatures and $S(\text{SiF})$ vs. $P$ .....	106
<b>5.5.</b> Internal temperatures and scatter coefficients for NO .....	107
<b>5.6.</b> $S(\text{CF})$ vs. $\Theta_V(\text{CF})$ for several precursor systems .....	108
<b>6.1.</b> Mass spectra of nascent ions in FC plasmas .....	131
<b>6.2.</b> Ion energy distributions for $\text{CF}_3^+$ in FC plasmas .....	132
<b>6.3.</b> Ion energy distributions for ions in $\text{C}_2\text{F}_6$ plasmas .....	134
<b>6.4.</b> Total mean ion energies for FC plasmas.....	135
<b>6.5.</b> IRIS images and cross sections for $\text{CF}_2$ in HFPO.....	137
<b>6.6.</b> Oligomer abundance in FC plasmas as functions of $P$ .....	140
<b>6.7.</b> Deposition rates of FC plasmas as functions of $P$ .....	141
<b>6.8.</b> $\Delta S(\text{CF}_x)$ vs. $\langle E_i \rangle_{\text{total}}$ .....	148
<b>6.9.</b> IEDs for FC plasma ions as a function of $p$ .....	154
<b>6.10.</b> $\langle E_i \rangle$ and $\Delta S(\text{CF}_2)$ vs. $p$ in $\text{CF}_4$ plasmas.....	155
<b>6.11.</b> Oligomer abundance and deposition rates in $\text{CF}_4$ and $\text{C}_3\text{F}_6$ plasmas.....	157
<b>6.12.</b> High-resolution $\text{C}_{1s}$ XPS spectra of HFPO films.....	160
<b>7.1.</b> OES spectra and actinometric analyses of $\text{CH}_2\text{F}_2/\text{C}_3\text{F}_8$ plasmas .....	172

<b>7.2.</b> $I_{CF_2}/I_{Ar}$ vs. feed $CF_4/C_2F_6$ ratio.....	174
<b>7.3.</b> TR-OES analyses of major species and $k_{decay}(CF_2)$ vs. $P$ for $C_2F_6/H_2$ plasmas.....	176
<b>7.4.</b> High-resolution XPS spectra of $C_2F_6$ -, $C_2F_6/H_2$ -, and $C_2F_6/O_2$ -deposited films.....	179
<b>7.5.</b> AOES and TR-OES analyses of $C_2F_6/O_2$ plasmas.....	181
<b>8.1.</b> SFGVS chamber schematic .....	192
<b>8.2.</b> Time-dependent $CF_2$ emission signal .....	193
<b>A.1.</b> Electron temperatures for $C_2F_6$ plasmas .....	199
<b>A.2.</b> Simulated and experimental $CF_2$ emission spectra.....	202
<b>B.1.</b> $\Theta_V(CF_2)$ for $CF_4$ and $C_2F_6$ plasmas .....	205
<b>B.2.</b> LIF results for determination of $\Theta_T(CF_2)$ .....	208
<b>C.1.</b> Carbon nanotube chirality.....	215
<b>C.2.</b> Two-dimensional fluorescence spectrum of SWNTs .....	216
<b>C.3.</b> Binding energy as a function of SWNT/molecule proximity .....	220

## **CHAPTER 1**

### **INTRODUCTION**

Herein is an introductory chapter detailing pertinent and fundamental aspects of plasma discharges, with special emphasis on inductively-coupled fluorocarbon plasmas. It addresses the inherent complexity of plasmas and introduces the techniques discussed in subsequent sections to facilitate a thorough investigation of such systems. This chapter concludes with an overview of the research described in forthcoming chapters.

## 1.1. Plasma Chemistry and Physics

The near ubiquitous plasma, a collective term for a partially ionized discharge comprising energetic radicals, reactive neutral and excited state species, ions, and electrons, is speculated to account for more than 99% of the composition of the known universe. For example, naturally-occurring plasmas exist in the coronae of stars and in arcs of lightning. In addition, plasma discharges may also be reproduced under controlled laboratory conditions. Plasmas can generally be classed under two main categories: thermal and non-thermal systems. The former is characterized by the thermal equilibration of ion and electron temperatures ( $T_i$  and  $T_e$ , respectively) within the plasma discharge, whereas non-thermal plasmas typically consist of fast-moving electrons with  $T_e$  far exceeding  $T_i$ , often by up to two orders of magnitude.

The non-thermal radio frequency (rf) discharge is of particular interest to technological applications because it is relatively simple to control the parameters associated with the system and hence controllably promote desirable chemical reactions. An example of a fundamental variable parameter is the power,  $P$ , supplied to the plasma. The average power,  $P_v$ , transferred to a unit volume of plasma gas through rf coupling at frequency  $\omega$  is given by equation 1.1<sup>1</sup> where  $n_e$  represents the electron density,  $\nu$  the elastic collision frequency between electrons and other species, and  $E_0$  the amplitude of the applied electric field.

$$P_v = \frac{n_e e^2 E_0^2}{2m_e} \left( \frac{m}{\nu^2 + \omega^2} \right) \quad (1.1)$$

The movement of electrons to mitigate the effects of an external electric field stimulates Brownian motion in the system,<sup>2</sup> ultimately yielding even more electron-based collisions with other gas species. In such a way, a cascade of electron-mediated interac-

tions produces the characteristic plasma discharge. Electrons can eventually achieve enough energy through inelastic collisions to ionize essentially any molecule present in the gas-phase, even at relatively low applied field strengths ( $\leq 10$  V/cm). In addition, electrons can also generate excited species or cause dissociation of a parent molecule. The ramifications of such processes are summarized in the reactions outlined in 1.2-1.4 for elastic electron collisions with partner  $AB$ .



It should be noted that radical  $A$  or  $B$  formed via 1.4 can also be electronically excited.

This electron-induced dissociative excitation is arbitrarily illustrated for  $A$  in reaction 1.5.



An equilibration of electrons and positive ions (generated via reaction 1.2) render the bulk of the plasma gas quasi-neutral, confined by a sheath of positive space-charge. In this quasi-neutral environment, several characteristic and distinct temperatures may be observed, including  $T_e$ ,  $T_i$ , and translational and internal temperatures for molecules, such as vibrational ( $\Theta_v$ ) and rotational ( $\Theta_R$ ) temperatures. Knowledge of characteristic temperature values can be used to elucidate the chemical processes leading to plasma behavior and assist in unraveling the complex properties of the plasma system.

Even as  $T_i$  values approach  $T_e$ , the thermal velocity of electrons  $[(T_e/m)^{1/2}]$  is at least 100 times the velocity of ions  $[(T_i/M_i)^{1/2}]$ . Thus, very shortly after plasma ignition, electrons rapidly move toward surfaces (i.e. reactor walls), in response to the effect of the externally applied electric field. Thin layers of positive ions subsequently amass around

the walls forming the plasma sheath. Equilibrium is quickly established to maintain ion flux into and out of the sheath. The potential within the sheath ( $\Phi$ ) falls off precipitously nearer to the walls, Fig. 1.1, as compared to the plasma potential,  $V_p$ . The boundary at the sheath edge separating it from the plasma bulk (dotted lines in Fig. 1.1) is the presheath. Positive ions that traverse the presheath are accelerated due to their proximity to the sheath, presumably achieving the Bohm velocity,  $v_s$ , equation (1.6),<sup>3</sup> where  $M_i$  is the mass of ion  $i$ .

$$v_s = \sqrt{\left(\frac{k_b T_e}{M_i}\right)} \quad (1.6)$$

Ions penetrating the sheath can attain energy through acceleration to the Bohm velocity, as well as through collisions within the sheath. Thus, a broad range of ion energies can be observed for species exiting the confined plasma. It should be noted that sheaths form over *all* surfaces exposed to the plasma, and not exclusively reactor walls. Thus, sheath effects and, as follows, ion effects, are crucial phenomena to consider in understanding the processes contributing to surface modification of a material.

We have incorporated several spectroscopy-based diagnostic techniques to discern gas-phase behavior of plasma species, including identification of the major species produced via reactions 1.2-1.5. In addition, we have examined the energy distributions of nascent ions formed in the plasma through mass spectrometric techniques. In all, a significant body of knowledge regarding the characterization of gas-phase plasma species as a function of various associated parameters has been realized. Nevertheless, a comprehensive understanding of the plasma system as used for materials-based applications necessarily must include processes that occur at surfaces, specifically, the plasma-surface interface.

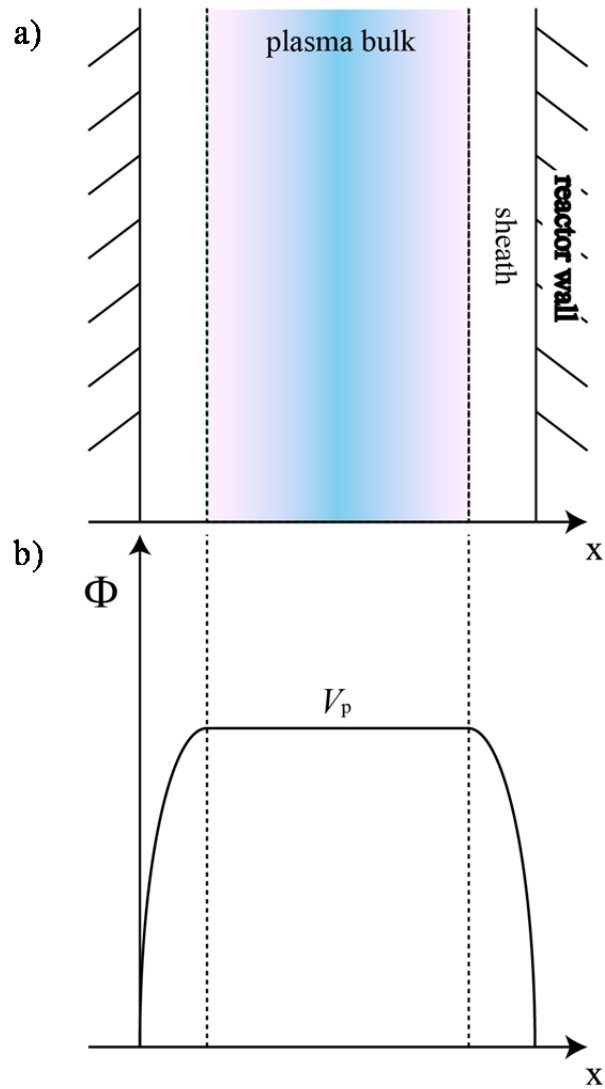


**Figure 1.1.** a) Cross-section of an arbitrary position along a plasma reactor illustrating the bulk plasma confined by a sheath which is a region of positive space-charge. b) Generalized depiction of the sheath potential,  $\Phi$ , as a function of the distance  $x$  along the cross-section shown in a). The plasma potential is unchanging in the bulk and denoted  $V_p$ .

One central application of plasma processing is the modification of surfaces for industrially or scientifically relevant purposes. Here, the term “modification” can apply to processes including substrate etch, film deposition, or creation of reactive sites at an existing surface and/or implantation of functional groups. Although plasmas are widely employed to such ends,<sup>4-12</sup> the fundamental plasma-surface interactions that lead to etching and/or deposition are often poorly understood. Additionally, to more efficiently tailor surface processing techniques, a thorough knowledge of these processes is crucial. In particular, our efforts have been aimed toward explicating fluorocarbon (FC) plasma species behavior for surface analyses, as FC systems are widely employed in the fabrication of such market-driven technology as integrated circuits and semiconductor devices.

To that end, this dissertation focuses primarily on understanding the contributions of gas-phase plasma species produced from inductively coupled rf plasmas to surface modification processes, especially as related to the deposition of fluorocarbon films from FC plasma systems. A more detailed description of the fluorocarbon systems follows in section 1.2.

## **1.2. Motivations for Fluorocarbon Investigations**

Inductively coupled FC plasmas are widely employed in industrial processes for their unique utility. For example, in a depositing regime, FC systems can be desirable because of the low dielectric constant of the deposited material, making the deposited films ideal for interlayers in semiconductor devices.<sup>13,14</sup> The same FC systems can also be used in an etching scheme, depending upon the parameters associated with the plasma, such as feed gas type, ion flux, and applied rf power.<sup>15-17</sup>

FC film growth is thought to be controlled by  $C_xF_{y(g)}$  species and becomes more efficient as the  $y/x$  ratio is decreased.<sup>18,19</sup> The manipulation of substrate temperature and bias, and position within the plasma reactor also influence the physical and chemical modification of a surface exposed to the FC plasma.<sup>20-22</sup> Additives to FC plasmas can be employed as well, that may increase the deposition or etching efficiency of the particular plasma system. For example,  $H_2$  additions to the plasma feed have been shown to promote deposition,<sup>23</sup> whereas  $O_2$  additives generally favor etching regimes.<sup>24</sup>

A wide range of decomposition products, including neutrals, ions, and excited species may be produced from a single FC precursor, according to reactions (1.2)-(1.5). The threshold energy required for production of plasma breakdown products is shown for selected processes in Table 1.1. Generally,  $CF_3$  neutrals and ions are more facily produced than corresponding  $CF_2$  species from the  $CF_4$  source gas. The ostensible implications for the  $CF_4$  plasma system are that the total concentrations (including excited state, ground state, neutral, and charged species) rank as  $CF_3 > CF_2 > CF$ . However, this is not always the case, due to the inherent complexity of the plasma as a whole. Gas-phase recombination reactions, surface interactions, charge-transfer reactions, and other source/sink processes influence the overall concentrations of plasma species and modulate the ranking.<sup>25</sup> Consequently, the roles and fates of  $CF_x$  species are of paramount interest in understanding the overall FC plasma system.

In both etching and depositing regimes, the role of  $CF_x$  molecules in the gas-phase

**Table 1.1.** Threshold energies for selected plasma processes.

<b>Reaction</b>	<b>Threshold Energy (eV)</b>	<b>Reference</b>
(1.7) $\text{CF}_4 + e^- \rightarrow \text{CF}_3 + \text{F} + e^-$	12.5	26
(1.8) $\text{CF}_4 + e^- \rightarrow \text{CF}_2 + 2\text{F} + e^-$	15.0	26
(1.9) $\text{CF}_4 + e^- \rightarrow \text{CF} + 3\text{F} + e^-$	20.0	26
(1.10) $\text{CF}_4 + e^- \rightarrow \text{CF}_3^+ + \text{F} + 2e^-$	15.9	26
(1.11) $\text{CF}_4 + e^- \rightarrow \text{CF}_2^+ + 2\text{F} + 2e^-$	22.0	26
(1.12) $\text{CF}_4 + e^- \rightarrow \text{CF}^+ + 3\text{F} + 2e^-$	27.0	26
(1.13) $\text{CF}_3 + e^- \rightarrow \text{CF}_2 + \text{F} + e^-$	3.7	26
(1.14) $\text{CF}_2 + e^- \rightarrow \text{CF} + \text{F} + e^-$	5.4	26
(1.15) $\text{CF}_2 + e^- \rightarrow \text{CF}_2^* + e^-$	4.5	27
(1.16) $\text{CF} + e^- \rightarrow \text{CF}^* + e^-$	6.1	27
(1.17) $\text{F} + e^- \rightarrow \text{F}^* + e^-$	14.8	27
(1.18) $\text{Ar} + e^- \rightarrow \text{Ar}^* + e^-$	13.5	27

and at the gas-surface interface is a significant contributing factor in the net effect of substrate exposure to the FC plasma.<sup>18</sup> For example, under conditions of low ion bombardment and VUV/UV radiation, films rich in CF<sub>2</sub> content may be deposited.<sup>19,21</sup> Indeed, CF<sub>2</sub> is considered vital for FC film deposition; Millard and Kay first reported strong correlations between gas-phase (CF<sub>2</sub>)<sub>n</sub> concentration and the rate of FC film formation.<sup>28</sup> CF<sub>2</sub> has also been observed as an etch product as ion energies in the plasma increase.<sup>29</sup> Surface production of CF<sub>2</sub> radicals during FC plasma processing of Si has been studied previously in the Fisher group and is found to be strongly correlated with mean ion energies.<sup>18</sup> These studies focused solely on large monomer precursors, namely C<sub>3</sub>F<sub>8</sub> and C<sub>4</sub>F<sub>8</sub>. Interestingly, a direct relationship exists between CF<sub>2</sub> scattering as the ion energy increases in these systems. The results of these experiments agree, in principle, with the findings of Booth, *et al.*, that suggest CF<sub>2</sub> might be produced predominantly by reactions of CF<sub>2</sub><sup>+</sup> ions rather than via direct dissociation from a precursor.<sup>30</sup>

Despite the seemingly extensive quantity of literature devoted to understanding the roles of CF<sub>x</sub> species in FC plasma processing, there remains a lack of fundamental understanding of the reactions and mechanisms that occur to drive FC film deposition. For example, several hypotheses of the role of CF<sub>2</sub> suggest that the radical simply sticks to the surface, thereby generating a PTFE-like film comprising (CF<sub>2</sub>)<sub>n</sub> moieties.<sup>25,28</sup> Direct evidence to the contrary has been provided by the Fisher group in the form of high-resolution XPS analyses of deposited FC films, that demonstrate a veritable wealth of cross-linking and CF<sub>x(s)</sub> (x=1-3) moieties.<sup>18,31-33</sup> Thus, a significant body of work in this dissertation is devoted to explicating the roles and behaviors of CF<sub>x</sub> radicals in FC plasmas.

The approach to investigating FC systems in this dissertation is threefold: (1) gas-phase diagnostics of the FC plasma, (2) surface analyses of deposited FC films, and (3) examination of the gas-surface interface. Optical emission spectroscopy (OES) and laser-induced fluorescence spectroscopy (LIF) were employed to monitor relative excited and ground state concentrations, respectively, for gas-phase species as a function of changing plasma parameters, such as  $P$ , pressure ( $p$ ), feed gas choice, substrate inclusion, etc. The OES technique was extended to accommodate investigations of  $\Theta_V$  and time-resolved kinetics analyses to probe species production and destruction events within the plasma. FC deposits on Si and ZrO<sub>2</sub> substrates were analyzed using surface-sensitive techniques including x-ray photoelectron spectroscopy (XPS) and contact angle (CA) goniometry. An empirical method based upon the Zisman analysis to estimate relative surface energies of deposited films was developed using results from CA measurements. Finally, the gas-surface interface was probed using the imaging of radicals interacting with surfaces (IRIS) experiment, a unique LIF-based approach. Some of these techniques were also extended to the investigation of NO in nitric oxide plasmas, and to SiF in SiF<sub>4</sub> plasmas to provide complementary data.

### **1.3. Overview of Research**

As aforementioned, the research efforts recounted in this dissertation revolve heavily around expounding the fundamental processes that drive FC plasma processing of substrates. An enriched understanding of these systems may elucidate the mechanisms contributing to film growth and might pave the way for improved plasma applications. The experimental methods used to prepare and analyze FC systems, including gas-phase

diagnostics, surface analyses of deposited material, and gas-surface interface analyses, are discussed in detail in Chapter 2.

Chapter 3 reports on the molecular-level chemistry involved in the processing of silicon and zirconia substrates by inductively coupled fluorocarbon plasmas produced from  $\text{CF}_4$  and  $\text{C}_2\text{F}_6$  precursors. The roles of gas-phase excited, neutral, and ionic species, especially  $\text{CF}_2$  and  $\text{F}$ , were examined as they contribute to FC film formation and substrate etching. The surface reactivity of  $\text{CF}_2$  radicals in  $\text{C}_2\text{F}_6$  plasmas has a dependence on substrate material and plasma system, as measured by the IRIS technique. Relative concentrations of excited state species also depend upon substrate type. Moreover, differences in the nature and concentrations of gas-phase species in  $\text{CF}_4$  and  $\text{C}_2\text{F}_6$  plasmas contribute to markedly different surface compositions for FC films deposited on substrates as revealed from XPS analysis. These data have led to the development of a scheme that illustrates the mechanisms of film formation and destruction in these FC/substrate systems with respect to  $\text{CF}_2$  and  $\text{F}$  gas-phase species and also  $\text{Si}$  and  $\text{ZrO}_2$  substrates.

Chapter 4 extends the topics posed in the preceding chapter to encompass the analysis of four separate  $\text{C}_x\text{F}_y$  systems. Surface reactivities are reported for  $\text{CF}$  and  $\text{CF}_2$  radicals, and the behaviors of these species are related to both the choice of precursor gas and the net effect of plasma deposition. Inductively-coupled  $\text{C}_x\text{F}_y$  ( $y/x = 2.0-4.0$ ) plasma systems were investigated to determine relationships between precursor chemistry,  $\text{CF}_n$  radical-surface reactivities, and surface properties of deposited films. The contributions of  $\text{CF}_n$  ( $n = 1, 2$ ) radicals to film properties were probed via gas-phase diagnostics and the IRIS technique. Time-resolved radical emission data elucidate  $\text{CF}_{(g)}$  and  $\text{CF}_{2(g)}$  production kinetics from the  $\text{C}_x\text{F}_y$  source gases and demonstrate that  $\text{CF}_4$  plasmas inherently lag

in efficacy of film formation when compared to  $C_2F_6$ ,  $C_3F_8$ , and  $C_3F_6$  systems. IRIS data show that as the precursor  $y/x$  ratio decreases, the propensity for  $CF_n$  scatter concomitantly declines. Analyses of the composition and characteristics of FC films deposited on Si wafers demonstrate that surface energies of the films decrease markedly with increasing film fluorine content. In turn, increased surface energies correspond with significant decreases in the observed scatter coefficients for both CF and  $CF_2$ . These data improve our molecular-level understanding of  $CF_n$  contributions to fluorocarbon film deposition which promises advancements in the ability to tailor FC films to specific applications.

The effect of the internal energies, including  $\Theta_V$  and  $\Theta_R$ , along with translational temperatures,  $\Theta_T$ , on plasma species behavior at a gas-surface interface is examined in Chapter 5. This chapter broadens the scope of the dissertation as it focuses not only on fluorocarbon species, but also on nitric oxide radicals formed in NO plasmas and SiF radicals in tetrafluorosilane systems.  $\Theta_V$  values were significantly greater than either  $\Theta_R$  or  $\Theta_T$ , indicating that vibrational modes are preferentially excited over other degrees of freedom. In all cases, rotational temperatures for the radicals equilibrate to the plasma gas temperature and remain independent of changing plasma parameters. Translational temperatures for SiF increase concomitantly with increasing vibrational temperatures, suggesting that the V-T energy exchange mechanism is the preferred pathway for vibrational relaxation in these molecules. In general, it is determined that the distribution of vibrational energies for a given radical at a given set of conditions significantly influences its propensity for surface scatter during plasma processing.

Chapter 6 focuses on the role of ions in fluorocarbon plasma systems. Increases in mean ion energies for nascent gas-phase FC plasma species correspond with increases

in observed scatter coefficients for both CF and CF<sub>2</sub> radicals. In ion-limited IRIS experiments, scatter coefficients for CF<sub>x</sub> species decrease considerably with respect to the ion-rich case under all conditions, suggesting that ion-mediated processes are crucial for determining CF<sub>x</sub> behavior at the gas-surface interface. Mass spectrometric techniques were also used to determine the relative gas-phase proportions of oligomeric film precursors. The amount of oligomeric species relative to CF<sub>3</sub> in all systems influences film deposition significantly, substantiating the concept that oligomers are directly responsible for FC film growth. Speculations on the role of low-energy ions in the plasma systems are presented for their expected contributions to FC film propagation.

The comparatively simple single-source plasma is replaced by mixed precursor systems under the scope of Chapter 7. Here, gas-phase diagnostic and preliminary gas-surface interaction data are presented for species in CH<sub>2</sub>F<sub>2</sub>/C<sub>3</sub>F<sub>8</sub>, C<sub>2</sub>F<sub>6</sub>/H<sub>2</sub>, and C<sub>2</sub>F<sub>6</sub>/O<sub>2</sub> plasmas. Overall contributions to FC film deposition and relevant gas-phase recombination reactions and mechanisms are discussed. The effect of H<sub>2</sub> addition to the plasma feed results in increased efficacy of FC film deposition with a corresponding decrease in the observed scatter coefficients for CF<sub>2</sub> species. On the other hand, O<sub>2</sub> additives to the FC feed promote removal of passivating film layers at surfaces, effectively inhibiting film formation. Time-resolved OES data elucidate the fates of gas-phase CF<sub>x</sub> species amidst the introduction of discrete plasma additives. Ultimately, the aim of this chapter aspires to extend the understanding of one-source FC plasmas to a more industrially relevant sector.

Finally, a brief summary of the research contained in this dissertation and suggestions for future avenues of investigations are presented in Chapter 8. Collectively, the

work presented herein represents a comprehensive examination of inductively coupled FC plasmas as a whole, with special emphasis on elucidating the phenomena occurring at the plasma-surface interface. Aspects of this work are globally pertinent for plasma applications, and thus aim to further the fundamental understanding of the plasma system required for improved or novel uses.

#### 1.4. References

1. Grill, A., *Cold Plasma in Materials Fabrication*. IEEE Press: Piscataway, NJ, 1994.
2. Iverson, G. J.; Williams, R. M., Brownian motion of electrons in time-dependent magnetic fields. *J. Phys. A: Math., Nucl., Gen.* **1973**, 6, (1), 106.
3. Panagopoulos, T.; Economou, D. J., Plasma sheath model and ion energy distribution for all radio frequencies. *J. Appl. Phys.* **1999**, 85, (7), 3435-3443.
4. Abe, H.; Yoneda, M.; Fujlwar, N., Developments of plasma etching technology for fabricating semiconductor devices. *Jpn. J. Appl. Phys.* **2008**, 47, (3), 1435-1455.
5. Lee, Y. H.; Sung, Y. J.; Yeom, G. Y.; Lee, J. W.; Kim, T. I., Magnetized inductively coupled plasma etching of GaN in Cl<sub>2</sub>/BCl<sub>3</sub> plasmas. *J. Vac. Sci. Technol. A* **2000**, 18, (4), 1390-1394.
6. Shin, M. H.; Na, S. W.; Lee, N. E.; Oh, T. K.; Kim, J.; Lee, T.; Ahn, J., Dry etching of TaN/HfO<sub>2</sub> gate stack structure by Cl<sub>2</sub>/SF<sub>6</sub>/Ar inductively coupled plasma. *Jpn. J. Appl. Phys.* **2005**, 44, (7B), 5811-5818.
7. Barreca, D.; Gasparotto, A.; Maccato, C.; Tondello, E.; Rossetto, G., A Soft Plasma Enhanced-Chemical Vapor Deposition process for the tailored synthesis of SiO<sub>2</sub> films. *Thin Solid Films* **2008**, 516, (21), 7393-7399.
8. Martinu, L.; Poitras, D., Plasma deposition of optical films and coatings: A review. *J. Vac. Sci. Technol. A* **2000**, 18, (6), 2619-2645.
9. Choy, K. L., Chemical vapour deposition of coatings. *Prog. Mater. Sci.* **2003**, 48, (2), 57-170.
10. Inagaki, N.; Narushim, K.; Tuchida, N.; Miyazak, K., Surface characterization of plasma-modified poly(ethylene terephthalate) film surfaces. *J. Polym. Sci. B: Pol. Phys.* **2004**, 42, (20), 3727-3740.
11. Griesser, H. J.; Gengenbach, T. R.; Dai, L. M.; Li, S.; Chatelier, R. C., Plasma surface modifications for structural and biomedical adhesion applications. In *First International Congress on Adhesion Science and Technology - Invited Papers*, Brill Academy Publishing: Leiden, Netherlands, 1998; pp 307-328.
12. Liston, E. M.; Martinu, L.; Wertheimer, M. R., Plasma Surface Modification of Polymers for Improved Adhesion - a Critical-Review. *J. Adhes. Sci. Technol.* **1993**, 7, (10), 1091-1127.
13. Jin, Y.; Ajmera, P. K.; Lee, G. S.; Singh, V., Ultralow-k silicon containing fluorocarbon films prepared by plasma-enhanced chemical vapor deposition. *J. Electron. Mater.* **2005**, 34, (9), 1193-1205.
14. Itoh, A.; Inokuchi, A.; Yasuda, S.; Teramoto, A.; Goto, T.; Hirayama, M.; Ohmi, T., Low Dielectric Constant Nonporous Fluorocarbon Films for Interlayer Dielectrics. *Jpn. J. Appl. Phys.* **2008**, 47, (4), 2515-2520.
15. SchaePKens, M.; Standaert, T.; Rueger, N. R.; Sebel, P. G. M.; Oehrlein, G. S.; Cook, J. M., Study of the SiO<sub>2</sub>-to-Si<sub>3</sub>N<sub>4</sub> etch selectivity mechanism in inductively coupled fluorocarbon plasmas and a comparison with the SiO<sub>2</sub>-to-Si mechanism. *J. Vac. Sci. Technol. A* **1999**, 17, (1), 26-37.
16. Rueger, N. R.; Beulens, J. J.; SchaePKens, M.; Doemling, M. F.; Mirza, J. M.; Standaert, T.; Oehrlein, G. S., Role of steady state fluorocarbon films in the etch-

- ing of silicon dioxide using  $\text{CHF}_3$  in an inductively coupled plasma reactor. *J. Vac. Sci. Technol. A* **1997**, 15, (4), 1881-1889.
17. Li, X.; Hua, X. F.; Ling, L.; Oehrlein, G. S.; Barela, M.; Anderson, H. M., Fluorocarbon-based plasma etching of  $\text{SiO}_2$ : Comparison of  $\text{C}_4\text{F}_6/\text{Ar}$  and  $\text{C}_4\text{F}_8/\text{Ar}$  discharges. *J. Vac. Sci. Technol. A* **2002**, 20, (6), 2052-2061.
  18. Martin, I. T.; Malkov, G. S.; Butoi, C. I.; Fisher, E. R., Comparison of pulsed and downstream deposition of fluorocarbon materials from  $\text{C}_3\text{F}_8$  and  $\text{c-C}_4\text{F}_8$  plasmas. *J. Vac. Sci. Technol. A* **2004**, 22, (2), 227-235.
  19. Tajima, S.; Komvopoulos, K., Physicochemical Properties and Morphology of Fluorocarbon Films Synthesized on Crosslinked Polyethylene by Capacitively Coupled Octafluorocyclobutane Plasma. *J. Phys. Chem. C* **2007**, 111, (11), 4358-4367.
  20. Cicala, G.; Milella, A.; Palumbo, F.; Rossini, P.; Favia, P.; d'Agostino, R., Nanostructure and Composition Control of Fluorocarbon Films from Modulated Tetrafluoroethylene Plasmas. *Macromolecules* **2002**, 35, (24), 8920-8922.
  21. Favia, P.; Perez-Luna, V.; Boland, T.; Castner, D.; Ratner, B., Surface chemical composition and fibrinogen adsorption-retention of fluoropolymer films deposited from an RF glow discharge. *Plasmas Polym.* **1996**, 1, (4), 299-326.
  22. Agarwal, A.; Kushner, M. J., Effect of nonsinusoidal bias waveforms on ion energy distributions and fluorocarbon plasma etch selectivity. *J. Vac. Sci. Technol. A* **2005**, 23, (5), 1440-1449.
  23. Endo, K.; Shinoda, K.; Tatsumi, T., Plasma deposition of low-dielectric-constant fluorinated amorphous carbon. *J. Appl. Phys.* **1999**, 86, (5), 2739-2745.
  24. Coburn, J. W.; Kay, E., Abstract: Some chemical aspects of the fluorocarbon plasma etching of silicon and its compounds. *J. Vac. Sci. Technol.* **1979**, 16, (2), 407-407.
  25. d'Agostino, R., *Plasma Deposition, Treatment, and Etching of Polymers*. Academic Press, Inc.: San Diego, 1990.
  26. Nakano, T.; Sugai, H., Partial Cross Sections for Electron Impact Dissociation of  $\text{CF}_4$  into Neutral Radicals. *Jpn. J. Appl. Phys.* **1992**, 31, 2919-2924.
  27. Kiss, L. D. B.; Nicolai, J. P.; Conner, W. T.; Sawin, H. H.,  $\text{CF}$  and  $\text{CF}_2$  actinometry in a  $\text{CF}_4/\text{Ar}$  plasma. *J. Appl. Phys.* **1992**, 71, (7), 3186-3192.
  28. Millard, M. M.; Kay, E., Difluorocarbene Emission Spectra from Fluorocarbon Plasmas and Its Relationship to Fluorocarbon Polymer Formation. *J. Electrochem. Soc.* **1982**, 129, (1), 160-165.
  29. Zhang, D.; Kushner, M. J., Mechanisms for  $\text{CF}_2$  radical generation and loss on surfaces in fluorocarbon plasmas. *J. Vac. Sci. Technol. A* **2000**, 18, (6), 2661-2668.
  30. Booth, J. P.; Cunge, G.; Chabert, P.; Sadeghi, N.,  $\text{CF}_x$  radical production and loss in a  $\text{CF}_4$  reactive ion etching plasma: Fluorine rich conditions. *J. Appl. Phys.* **1999**, 85, (6), 3097-3107.
  31. Mackie, N. M.; Dalleska, N. F.; Castner, D. G.; Fisher, E. R., Comparison of Pulsed and Continuous-Wave Deposition of Thin Films from Saturated Fluorocarbon/ $\text{H}_2$  Inductively Coupled rf Plasmas. *Chem. Mater.* **1997**, 9, (1), 349-362.

32. Martin, I. T.; Fisher, E. R., Ion effects on  $\text{CF}_2$  surface interactions during  $\text{C}_3\text{F}_8$  and  $\text{C}_4\text{F}_8$  plasma processing of Si. *J. Vac. Sci. Technol. A* **2004**, 22, (5), 2168-2176.
33. Liu, D.; Fisher, E. R., Surface interactions of  $\text{C}_3$  radicals during the deposition of fluorocarbon and hydrocarbon films. *J. Vac. Sci. Technol. A* **2007**, 25, (6), 1519-1523.

## **CHAPTER 2**

### **EXPERIMENTAL METHODS**

This chapter contains a detailed description of the materials, methods, experimental apparatus, instruments and techniques used to perform the research discussed in the bulk of this dissertation. Section 2.1 provides an overview of the plasma systems used herein. Sections 2.2-2.4 discuss gas-phase diagnostic techniques, the IRIS experiment, and surface analyses, respectively.

## 2.1. General Information

**Reactor Design.** Each of the plasmas discussed in this dissertation were ignited in a glass tubular reactor, described at length previously,<sup>1-3</sup> by supplying 13.56 MHz rf power ( $P$ ) through an eight-turn Ni-plated copper coil from a RFPP 5S power supply. The reactor itself consists of two 50 mm i.d. Pyrex glass tubes mated with an o-ring to allow for access to the reactor interior. Feed gases were supplied to an evacuated reactor through an inlet stem on one side, situated upstream from the coil region, and were removed after traveling the length (~35-40 cm) of the reactor through use of mechanical rotary pumps operating at pumping speeds of 2-4 l/s. The pressure in the reactor was monitored by an MKS Baratron capacitance manometer, and gas flow was metered using MKS mass flow controllers. Ceramic sleeves (45 mm i.d.) inserted into the reactor prevented etching and subsequent redeposition of undesirable Na byproducts from the walls of the glass reactors by particularly harsh plasma systems.

For most FC studies, individual plasmas consisting of CF<sub>4</sub>, C<sub>2</sub>F<sub>6</sub>, C<sub>3</sub>F<sub>8</sub>, C<sub>3</sub>F<sub>6</sub> (all Airgas, >95%) or hexafluoropropylene oxide, HFPO, (Aldrich, 98%) were employed. For some studies discussed herein, mixtures of a particular fluorocarbon gas with additives such as H<sub>2</sub> (Airgas, 99%) or O<sub>2</sub> (Airgas, 99.5%) were investigated. For actinometric optical emission spectroscopy, small amounts (5-10% of the total gas flow) of Ar, (Airgas, 99.9%) were added to the plasma feed. In the cases of mixed feed gas systems, all gases were mixed prior to entering the plasma reactor. Total pressures were varied from 50-200 mTorr above base pressure at constant  $P$  for some studies; in others,  $P$  was varied from 25-200 W at constant feed pressure. Studies of nitric oxide (Matheson, 99% and Airgas, 99%) were carried out at 50 mTorr and  $P = 25-300$  W.

**Substrates.** The substrates used for investigations of plasma-surface interactions included Si (100) with native oxide layer, ZrO<sub>2</sub>, and Pt. Substrates were placed in the standard plasma reactors described above in one of the following positions: (1) in the coil region, (2) 9 cm downstream (d.s.) from the terminus of the coil, or (3) 14 cm d.s. Deposition duration for FC precursors on individual substrates varied from 5-30 min. Substrates were also employed in the IRIS experiment, in which case, they are approximately 14 cm from the exit orifice of the plasma molecular beam. Though plasma reactors were generally cleaned using a high-powered O<sub>2</sub> plasma prior to introduction of a substrate to remove contaminants from reactor walls, the substrates were employed without pretreatment.

## 2.2. Gas-phase Plasma Diagnostics

**Optical Emission Spectroscopy (OES).** OE spectra were collected by fitting the reactor with a replaceable fused quartz window at the downstream end, allowing for coaxial collection of plasma emission for maximum signal intensities. Spectra were imaged onto the 10 μm entrance slit of an Avantes multichannel spectrometer comprising four fiber optic gratings and four 3648 pixel charge-coupled array detectors with a combined wavelength range 187 to 1016 nm with ~0.1 nm resolution. Spectra were generally collected by averaging ten accumulations at integration times of 10-100 ms.

In certain time-resolved OES (TR-OES) studies, wherein rapid data collection was desirable, an Avantes AvaSpec-2048-USB2 spectrometer, blazed in the UV with a 200-450 nm wavelength range and 0.1 nm FWHM resolution was employed. A 600 μm diameter fiber optic cable imaged spectra onto a 10 μm entrance slit. A nominal temporal

resolution of 5  $\mu\text{s}$  was realized using this instrument with rapid integration times of  $\sim 3 \mu\text{s}$  under all plasma operating conditions.

Excited electronic state densities for emitting species of interest in the FC plasmas were estimated by employing an Ar actinometer. Some principle species analyzed included  $\text{F}^*$  (703.7 nm),<sup>5</sup>  $\text{CF}^*$  (202.4 nm),<sup>6</sup>  $\text{CF}_2^*$  (251.9 nm),<sup>5</sup> and  $\text{Ar}^*$  (750.3 nm).<sup>7</sup> A concise list of the species analyzed via actinometry and discussed in this dissertation is provided in Table 2.1. This table also lists associated actinometric wavelengths and corresponding transitions. Internal temperatures of vibration ( $\Theta_v$ ) for  $\text{CF}_x^*$  ( $x = 1$  or  $2$ ) were calculated by fitting emission spectra over an appropriate wavelength range (see Table 2.2) with simulated data obtained from either of the fitting routines LIFbase<sup>8</sup> or pGopher<sup>9</sup> (see Appendix A). Argon emission lines in OE spectra were used to determine the electron temperature ( $T_e$ ) of select plasma systems (see Appendix for more information on characteristic temperature calculations).

**Laser-Induced Fluorescence (LIF) Spectroscopy.** LIF spectra were acquired using a system depicted in Figure 2.1. Plasmas are generated in a reactor mated to the LIF chamber that is similar in design to that described above. The plasma expands through a series of collimating slits into a differentially pumped interaction region. This effusive molecular beam consists of virtually all species present in the plasma. Pressure in this region is maintained at  $\sim 10^{-5}$  Torr during all LIF experiments.

Tunable laser light generated from an excimer-pumped (Lambda Physik LPX210i, XeCl, 180 mJ/pulse, 25 Hz) dye laser is directed through the centers of two

**Table 2.1.** Transitions and corresponding wavelengths used for actinometric analyses of selected species.

<b>Emitting Species</b>	<b>Transition</b>	<b>Wavelength (nm)</b>	<b>Reference</b>
Ar	$4p^1 \rightarrow 4s^1$	750.4	7
C <sub>3</sub>	$A^1\Pi_u \rightarrow X^1\Sigma_g^+$	405.1	5
CH	$A^2\Delta \rightarrow X^2\Pi$	431.4	5
CHF	$A^1a \rightarrow X^1A$	578.5	8
CF	$B^2\Delta \rightarrow X^2\Pi$	202.4	6
CF <sub>2</sub>	$A^1B_1 \rightarrow X^1A_1$	251.9	5
CO	$B^1\Sigma^+ \rightarrow A^1\Pi$	483.4	5
H <sub>α</sub>	$^2P^0 \rightarrow ^2D$	656.3	5
F	$2p^4 3p^1 \rightarrow 2p^4 3s^1$	703.7	5
O	$^3S^0 \rightarrow ^3P$	777.2	5

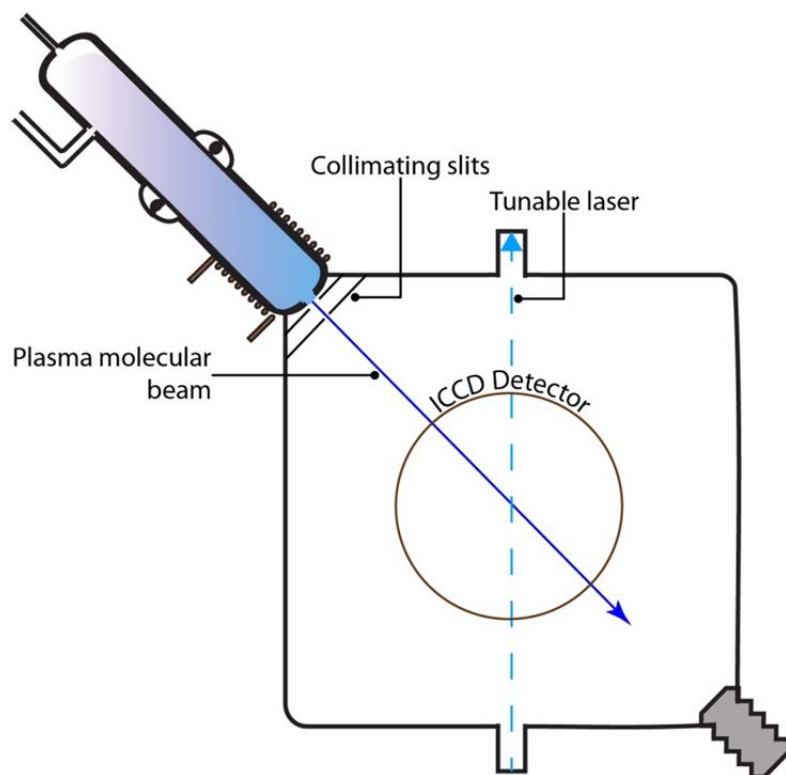


**Figure 2.1.** Top-down schematic view of the LIF system.

quartz windows, such that it is focused at the position of the plasma molecular beam, intersecting it at a  $45^\circ$  angle. For LIF studies requiring UV radiation, the output of the laser was frequency doubled using BBO I crystals. Transitions and related parameters associated with radicals of interest are presented in Table 2.2. All LIF data were collected in optically saturated regimes, so minute fluctuations in laser power were ignored. Total fluorescence was imaged through two focusing lenses (300 mm and 75 mm focal lengths, respectively) onto a 512 x 512 pixel array of an intensified charge-coupled device (ICCD) located directly above the region of intersection and perpendicular to the laser and plasma molecular beam. Pixels were binned 4 x 4 to generate a spatially resolved LIF spot in a  $\sim 2500 \text{ mm}^2$  area. Ground state species densities were determined by accumulating 15 images at the on-resonance wavelength of a species of interest and image-subtracting the same number of accumulations collected at an off-resonance wavelength (see Table 2.2). The resulting image was pixel averaged over a 20 x 128 region around the center of highest fluorescence intensity, corresponding to the relative density of the species of interest at a given set of plasma parameters. In a similar method, excitation spectra were collected by iteratively stepping the laser frequency by no more than 0.01 nm and collecting successive LIF images. Individual images were pixel averaged for a 20 x 128 region and the intensities were plotted as a function of the corresponding laser wavelength to generate the excitation spectrum. Rotationally resolved LIF excitation spectra for CF were fit with the simulation software LIFbase<sup>8</sup> to calculate rotational temperatures ( $\Theta_R$ ) for the radical.

**Table 2.2.** Parameters associated with CF<sub>x</sub> and NO OES, LIF, and IRIS measurements. Fluorescence lifetimes obtained from references 10-12.

Radical	OES Transition, Range (nm)	LIF Transition, Range (nm)	Fluorescent lifetime (ns)	$\lambda$ (nm)		Laser dye	Slit sizes (mm)	<u>ICCD parameters</u>	
				On- resonance	Off- resonance			Gate width (ns)	Gate delay ( $\mu$ s)
CF	B <sup>2</sup> $\Delta$ →X <sup>2</sup> $\Pi$ , 200.0-210.0	A <sup>2</sup> $\Sigma^+$ ←X <sup>2</sup> $\Pi$ , 223.5-224.5	26	223.838	laser off	Coumarin 450	0.9-1.2	60	1.55
CF <sub>2</sub>	A <sup>1</sup> B <sub>1</sub> →X <sup>1</sup> A <sub>1</sub> , 250.0-340.0 a <sup>3</sup> B <sub>1</sub> →X <sup>1</sup> A <sub>1</sub> , >340	A <sup>1</sup> B <sub>1</sub> ←X <sup>1</sup> A <sub>1</sub> [(0,11,0)←(0,0,0)], 233.0-235.0	61	234.278	235.000	Coumarin 460	1.0-1.4	100	1.55
NO	A <sup>2</sup> $\Sigma^+$ →X <sup>2</sup> $\Pi$ , 210.0-275.0	A <sup>2</sup> $\Sigma^+$ ←X <sup>2</sup> $\Pi$ , 226.1-227.0	54	226.199	226.500	Coumarin 460	0.9-1.1	100	1.60

**Mass Spectrometry (MS).** Mass spectra were acquired for plasmas produced in an independent though similar glass tubular reactor using a Hiden PSM003 quadrupole mass spectrometer.<sup>13</sup> The instrument comprises an ion extractor, electron impact ionization source, Bessel box energy filter, a triple filter quadrupole, and a secondary electron multiplier detector. Nascent ions produced in the plasma were sampled by keeping the ionizing source off for the duration of the experiment. Ions entered the sampling probe through a 600  $\mu\text{m}$  orifice located 5 cm from the exit orifice on the plasma reactor. A 60 l/s turbomolecular pump backed by a 400 l/min mechanical pump was used to maintain a base pressure of approximately  $9 \times 10^{-7}$  Torr in the probe region and  $<10^{-5}$  Torr in the main chamber. At these pressures, the distance that plasma species travel from the exit orifice of the plasma reactor to the sample orifice of the probe is significantly less than the mean free path of the species, ensuring that no undesirable collisions occur during transit.

Both residual gas analysis, RGA (ionization source active), and positive ion, +ion (ionization source deactivated), modes were used to sample species in FC plasmas. Mass spectra were obtained over a 0.40-300.00 amu range with 0.1 amu mass resolution. Ion energy distributions were scanned in +ion mode for selected nascent ions over a range of 0 to 200 eV with 0.05 eV resolution. Average ion energies,  $\langle E_i \rangle$ , were calculated according to equation 2.1,<sup>14</sup> where  $f(E_i)$  represents the distribution function at energy  $E_i$ .

$$\langle E_i \rangle = \frac{\int_0^{200} f(E_i) E_i dE_i}{\int_0^{200} f(E_i) dE_i} \quad (2.1)$$

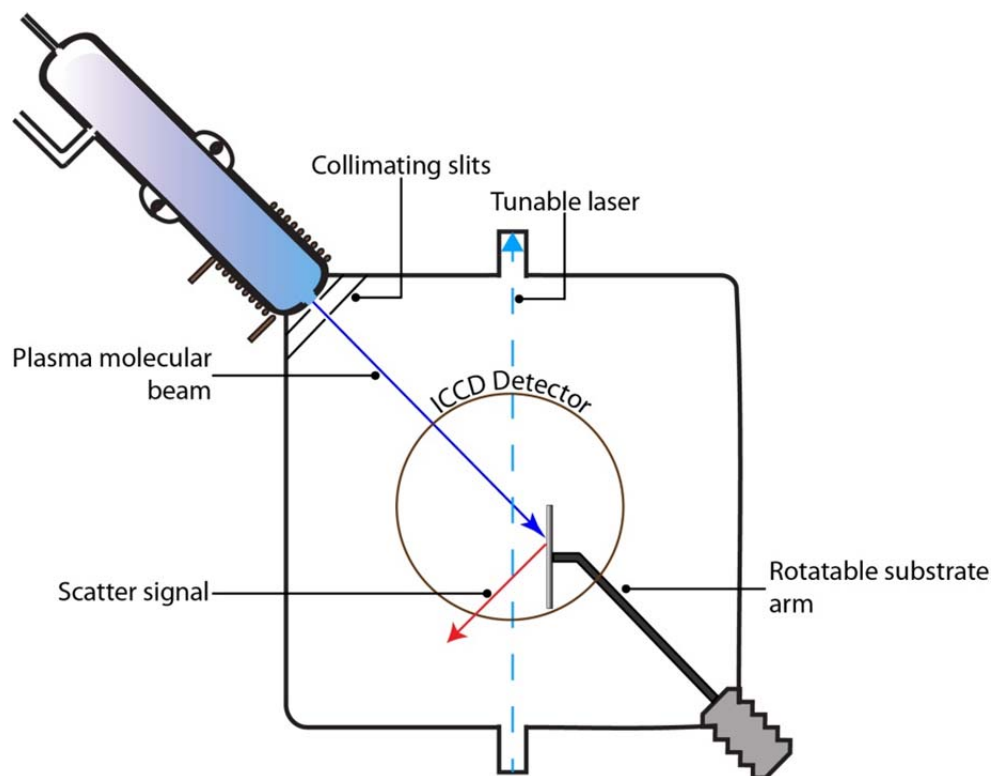


**Figure 2.2.** Top-down schematic view of the LIF chamber, modified for the IRIS experiment.

### 2.3. Gas-Surface Interactions

The IRIS experiment, described in detail previously,<sup>15</sup> was used to investigate the phenomena that occur at the interface of plasma vapor and surface. Briefly, this approach employs LIF techniques similar to those described above to investigate steady-state surface reactivities of plasma radical species. Here, a substrate can be rotated into the path of the molecular beam, Figure 2.2, and LIF images are obtained for a species of interest with and without the substrate present. The laser is tuned to an appropriate “on-resonance” wavelength to induce fluorescence from a particular species (Table 2.2) and the corresponding “off-resonance” frequency is used as a background. Both on- and off-resonance images are acquired for the cases of substrate in and substrate out. The difference in LIF intensities between these two cases is directly proportional to the density of scattered species from the surface. Resultant “beam-only” and “scatter” images are cross-sectioned along the laser propagation axis using a 20 pixel average around the center of most intense fluorescence. These cross-sections are compared to a geometrical model<sup>16</sup> and used to calculate scatter coefficients ( $S$ ) for the radicals of interest. The scatter coefficient is essentially a measure of the propensity for a particular type of species to react at the surface, where surface reactivity,  $R$ , is defined as  $1 - S$ . It should be noted that  $S$  values may surpass unity, in which case  $R$  is negative (a physically unrealistic situation). Ion effects in the IRIS experiment were, in certain cases, mitigated by biasing the substrate with +200 V dc bias to repel positively charged species or by placing a grounded mesh at the collimating slits to neutralize ions in the plasma molecular beam.

## 2.4. Surface Analyses

**X-ray Photoelectron Spectroscopy (XPS).** XPS data for post-processed substrates were collected using a Physical Electronics PHI-5800 ESCA/AES instrument. In general, FC films were examined. Survey spectra were collected to identify the significant species present at the surface. High resolution spectra, mainly for C<sub>1s</sub> and F<sub>1s</sub>, were collected using a monochromatic Al K $\alpha$  source with a pass energy of 23.5 eV. Fluorocarbon peaks were generally shifted to the F-C binding environment at 689.0 eV. Spectral signals were deconstructed in the open-source fitting routine, XPSpeak v4.1. All fits were made by constraining the FWHM to  $\leq 2.0$  eV and using a 100% Gaussian function. For XPS analyses of IRIS-subjected wafers, spectra were acquired within a day of performing depositions in the IRIS experiment. Typical plasma exposure times for substrates in the IRIS chamber were 60 to 90 min.

**Variable Angle Spectroscopic Ellipsometry (VASE).** The thicknesses ( $d_{FC}$ ) of deposited FC films were measured using a Woollam M-2000 Model DI ellipsometer. Depositions were performed from FC plasma sources for durations ( $t_{dep}$ ) of 5-30 min. VASE spectra were acquired over a 200-1100 nm range at incident angles of 55°, 65°, and 75°. Spectra were deconvoluted using manufacturer-supplied WVASE modeling software to extract information regarding film thickness. A Cauchy dispersion model was used to determine  $d_{FC}$ . Thickness values were plotted as a function of corresponding  $t_{dep}$  and fitted with a linear regression to calculate deposition rates.

**Surface Energy Calculations.** The surface energy of deposited FC films was determined using an empirical method based upon analyses of static contact angles (CA). The CA of sessile water/methanol droplets of discrete compositions, Table 2.3, were ac-

quired by capturing an image within 2 s of dispensing a 2  $\mu$ L droplet on the FC film. CA values were measured in triplicate for each film investigated and analyzed using the circle-fitting profile. The Zisman method<sup>17</sup> was used to relate the CA values to the critical surface tensions of FC films to estimate surface energies. For comparisons to bare wafers, complementary experiments were performed prior to FC film deposition on the (100) face of Si containing a native oxide layer.

**Morphology Analyses.** SEM micrographs were collected using a JEOL JSM-6500F field emission microscope, operating with an accelerating voltage of 15 kV and a working distance of 10 nm. Individual samples were sputter coated with 5 nm Au prior to SEM analysis. Atomic force microscopy was employed to characterize surface topography. A Nanosurf Easyscan 2 AFM was operated in contact mode and utilized Si-tipped probes. Surface root-mean-square (rms) roughness values were derived directly from AFM images.

**Table 2.3.** Literature liquid-vapor surface tensions in atmosphere at 25 °C.<sup>a</sup>

<b>Constituents</b>	<b><math>\gamma_{lv}</math> (dyn/cm)</b>
100% H <sub>2</sub> O	72.01
10/90 CH <sub>3</sub> OH/H <sub>2</sub> O (w/w)	56.18
20/80 CH <sub>3</sub> OH/H <sub>2</sub> O (w/w)	47.21
50/50 CH <sub>3</sub> OH/H <sub>2</sub> O (w/w)	32.86
100% CH <sub>3</sub> OH	22.51

<sup>a</sup>Maximum errors < 0.4%. Values taken from Reference 17.

## 2.5. References

1. Bogart, K. H. A.; Dalleska, N. F.; Bogart, G. R.; Ellen, R. F., Plasma enhanced chemical vapor deposition of SiO<sub>2</sub> using novel alkoxy silane precursors. *J. Vac. Sci. Technol. A* **1995**, 13, (2), 476-480.
2. Mackie, N. M.; Dalleska, N. F.; Castner, D. G.; Fisher, E. R., Comparison of Pulsed and Continuous-Wave Deposition of Thin Films from Saturated Fluorocarbon/H<sub>2</sub> Inductively Coupled rf Plasmas. *Chem. Mater.* **1997**, 9, (1), 349-362.
3. Martin, I. T.; Malkov, G. S.; Butoi, C. I.; Fisher, E. R., Comparison of pulsed and downstream deposition of fluorocarbon materials from C<sub>3</sub>F<sub>8</sub> and c-C<sub>4</sub>F<sub>8</sub> plasmas. *J. Vac. Sci. Technol. A* **2004**, 22, (2), 227-235.
4. Ashfold, M. N. R.; Castano, F.; Hancock, G.; Ketley, G. W., Laser-induced fluorescence of the CHF radical. *Chem. Phys. Lett.* **1980**, 73, (3), 421-424.
5. Stillahn, J.; Trevino, K.; Fisher, E. R., Plasma diagnostics for unraveling process chemistry. *Annu. Rev. Anal. Chem.* **2008**, 1, 261-91. .
6. Booth, J. P.; Cunge, G.; Chabert, P.; Sadeghi, N., CF<sub>x</sub> radical production and loss in a CF<sub>4</sub> reactive ion etching plasma: Fluorine rich conditions. *J. Appl. Phys.* **1999**, 85, (6), 3097-3107.
7. Francis, A.; Czarnetzki, U.; Dobeles, H. F.; Sadeghi, N., Quenching of the 750.4 nm argon actinometry line by H<sub>2</sub> and several hydrocarbon molecules. *Appl. Phys. Lett.* **1997**, 71, (26), 3796-3798.
8. Luque, J.; Crosley, D. R. *LIFBASE: Database and Spectral Simulation Program*, 1.5; SRI International Report MP 99-009: 1999.
9. Western, C. M. *PGOPHER, a Program for Simulating Rotational Structure*, University of Bristol, <http://pgopher.chm.bris.ac.uk>.
10. Nizamov, B.; Dagdighian, P. J., Collisional Quenching and Vibrational Energy Transfer in the A<sup>2</sup>Σ<sup>+</sup> Electronic State of the CF Radical. *J. Phys. Chem. A* **2000**, 105, (1), 29-33.
11. King, D. S.; Schenck, P. K.; Stephenson, J. C., Spectroscopy and photophysics of the CF<sub>2</sub> A<sup>1</sup>B<sub>1</sub>-X<sup>1</sup>A<sub>1</sub> system. *J. Mol. Spectrosc.* **1979**, 78, (1), 1-15.
12. Zhang, D.; Kushner, M. J., Mechanisms for CF<sub>2</sub> radical generation and loss on surfaces in fluorocarbon plasmas. *J. Vac. Sci. Technol. A* **2000**, 18, (6), 2661-2668.
13. Zhou, J.; Martin, I. T.; Ayers, R.; Adams, E.; Liu, D.; Fisher, E. R., Investigation of inductively coupled Ar and CH<sub>4</sub> /Ar plasmas and the effect of ion energy on DLC film properties. *Plasma Sources Sci. Technol.* **2006**, 15, (4), 714.
14. Edelberg, E. A.; Perry, A.; Benjamin, N.; Aydil, E. S., Energy distribution of ions bombarding biased electrodes in high density plasma reactors. *J. Vac. Sci. Technol. A* **1999**, 17, (2), 506-516.
15. McCurdy, P. R.; Bogart, K. H. A.; Dalleska, N. F.; Fisher, E. R., A Modified Molecular Beam Instrument for the Imaging of Radicals Interacting with Surfaces During Plasma Processing. *Rev. Sci. Instrum.* **1997**, 68, 1684-1693.
16. Bogart, K. H. A.; Cushing, J. P.; Fisher, E. R., Effects of Plasma Processing Parameters on the Surface Reactivity of OH in Tetraethoxysilane/O<sub>2</sub> Plasmas during Deposition of SiO<sub>2</sub>. *J. Phys. Chem. B* **1997**, 101, (48), 10016-10023.

17. Vazquez, G.; Alvarez, E.; Navaza, J. M., Surface Tension of Alcohol Water + Water from 20 to 50 .degree.C. *J. Chem. Eng. Data* **1995**, 40, (3), 611-614.

## CHAPTER 3

### INVESTIGATION OF THE ROLES OF GAS-PHASE $\text{CF}_2$ MOLECULES AND F ATOMS DURING FLUOROCARBON PLASMA PROCESSING OF Si AND $\text{ZrO}_2$ SUBSTRATES

This chapter contains data and discussion from a full paper published in the *Journal of Applied Physics*, written by Michael F. Cuddy and Ellen R. Fisher. The work presented here examines plasma gas-phase phenomena and gas-surface interactions in  $\text{CF}_4$  and  $\text{C}_2\text{F}_6$  plasmas, with a focus on the roles of  $\text{CF}_2$  and F neutrals and the  $\text{CF}_2^+$  ion.

### 3.1. Introduction

The study of small monomer FC (e.g.:  $\text{CF}_4$ ,  $\text{C}_2\text{F}_6$ ) plasmas has generated a veritable wealth of data for and understanding of plasma-based processing of materials.<sup>1-4</sup> We revisit them here to ascertain the relevance of FC plasma processing to novel material applications and to further explore the detailed chemical reactions associated with plasma species such as  $\text{CF}_2$  and F. One aspect of FC plasmas that has garnered interest in the processing of materials for implementation in the microelectronics industry, particularly with respect to ultralarge-scale integrated circuits (ULSIs), is the competition between etching and film deposition. Previous work focused on Si and  $\text{SiO}_2$  substrate processing, as these materials are ubiquitous in semiconductor manufacturing.<sup>5,6</sup> Recent trends have, however, turned toward downscaling and the use of higher dielectric constant ( $k$ ) materials such as  $\text{ZrO}_2$ .<sup>7-9</sup> Although selective etching of  $\text{ZrO}_2$  for dielectric applications has been accomplished using chlorine-based plasmas,<sup>10</sup> little is known about FC plasma etching of, or film deposition on  $\text{ZrO}_2$  substrates. Notably, FC plasma chemistry is very complex and substrate-dependent processes have not been elucidated in great detail in the literature. As the implementation of new materials in semiconductor devices continues to advance, it is critical to develop a deeper understanding of the fundamental mechanisms that drive the processing in such systems.

Plasmas produced from FC feed gases are well known to exhibit dichotomy as both an etching tool and as precursors to film deposition.<sup>11-13</sup> Traditionally,  $\text{CF}_4$  is recognized as an etchant,<sup>1</sup> whereas  $\text{C}_2\text{F}_6$  is more likely to behave as a slowly depositing system. Notably, the propensity for deposition increases with decreasing F/C ratio of the feed gas or with the addition of a reducing gas to the feed such as  $\text{H}_2$ .<sup>3,12</sup> Hydrogen ef-

fectively consumes etchant radicals in the plasma such as atomic fluorine through gas phase reactions.  $\text{CF}_x$  units produced by electron impact dissociation of the precursor contribute to FC film formation.<sup>14</sup> Interestingly, the  $\text{CF}_2$  molecule in particular has shown a propensity for both substrate etching and incorporation into films.<sup>15</sup> Moreover, we have previously shown that  $\text{CF}_2$  appears to be produced not only by direct dissociation of the parent gas, but also at surfaces passivated with fluorocarbon films.<sup>3, 16, 17</sup>

An overarching goal of our research is to understand the entirety of the plasma chemistry, requiring knowledge of the gas-phase, surface, and gas-surface interactions that occur within our systems. To this end, we have utilized gas-phase diagnostics, surface analyses, and our unique imaging of radicals interacting with surfaces (IRIS) technique to fully describe the plasma chemistry. In short, the IRIS technique allows for spatially resolved two-dimensional (2D) laser induced fluorescence (LIF) imaging of a species of interest. Images collected for the species after surface impingement of a plasma molecular beam contain information regarding species scattered from a substrate. Through IRIS we have previously demonstrated substrate dependence of species scatter for silicon and silica using  $\text{C}_2\text{F}_6$  plasmas,<sup>3</sup> but have not explored the effect of a  $\text{CF}_4$  feed gas, or the dependence upon substrates such as  $\text{ZrO}_2$ . Such studies should help to elucidate the mechanisms of plasma-surface interactions. In this Chapter, we focus on the role of  $\text{CF}_2$  during plasma processing of Si and  $\text{ZrO}_2$  substrates and correlate our findings with the relative concentrations of fluorine present in our plasma systems.

We also turn attention to the roles of ions in FC plasmas, as many studies have shown that energetic ions may play a crucial role in substrate processing. For example, in their seminal work, Coburn and Winters postulated that ions must factor into Si etch-

ing, demonstrating that the presence of  $\text{CF}_3^+$  ions in a  $\text{CF}_4$  plasma enhanced the overall etch rate of the system.<sup>18</sup> In addition, Oehrlein and Williams showed that ion bombardment in reactive ion etching FC plasmas curtails the growth of FC films.<sup>19</sup> Previous work in our group has also demonstrated that ions contribute to both film formation and surface production of a range of species, including  $\text{CF}_2$ ,  $\text{SiF}_2$ , and  $\text{SiCl}_2$ .<sup>3, 16</sup> Thus, a more robust understanding of the mechanisms of plasma processing of both Si and  $\text{ZrO}_2$  substrates necessarily includes a discussion on the role of ions as well as an examination of the surface properties of the processed materials.

### 3.2. Results

OES spectra were acquired for  $\text{CF}_4$  and  $\text{C}_2\text{F}_6$  plasmas, Figures 3.1(a) and 3.1(b), that show that  $\text{CF}_2^*$  emission from the  $\text{A}^1\text{B}_1\text{—X}^1\text{A}_1$  transition dominates the region from 230 to 340 nm in both systems.  $\text{CF}_2^*$  emission from a forbidden  $^3\text{B}_1\text{—}^1\text{A}_1$  transition at wavelengths  $>340$  nm also contributes substantially to the observed spectra.<sup>13, 20</sup> The emission line at 251.9 nm was used for actinometric analysis.<sup>21</sup> Although multiple transitions are observed for  $\text{F}^*$  at wavelengths  $>600$  nm, we focus on the  $3s\ ^2\text{P}_2\text{—}3p\ ^2\text{P}_2$  line at 703.7 nm.<sup>21, 22</sup> Argon was added to these systems as an actinometer, and emission from  $\text{Ar}^*$  at 750.3 nm was used to scale the signal intensity of emission from emitting species of interest. Figures 3.1(c) and 3.1(d) show actinometric  $\text{CF}_2^*$  and  $\text{F}^*$  data as a function of  $P$ . In the  $\text{CF}_4$  plasma, Fig. 3.1(c), relative  $\text{CF}_2^*$  concentrations decrease dramatically with increasing  $P$ , whereas  $[\text{F}^*]$  increases monotonically over the same applied rf power range. In contrast,  $\text{CF}_2^*$  production in  $\text{C}_2\text{F}_6$  plasmas, Fig. 3.1(d), markedly dominates production

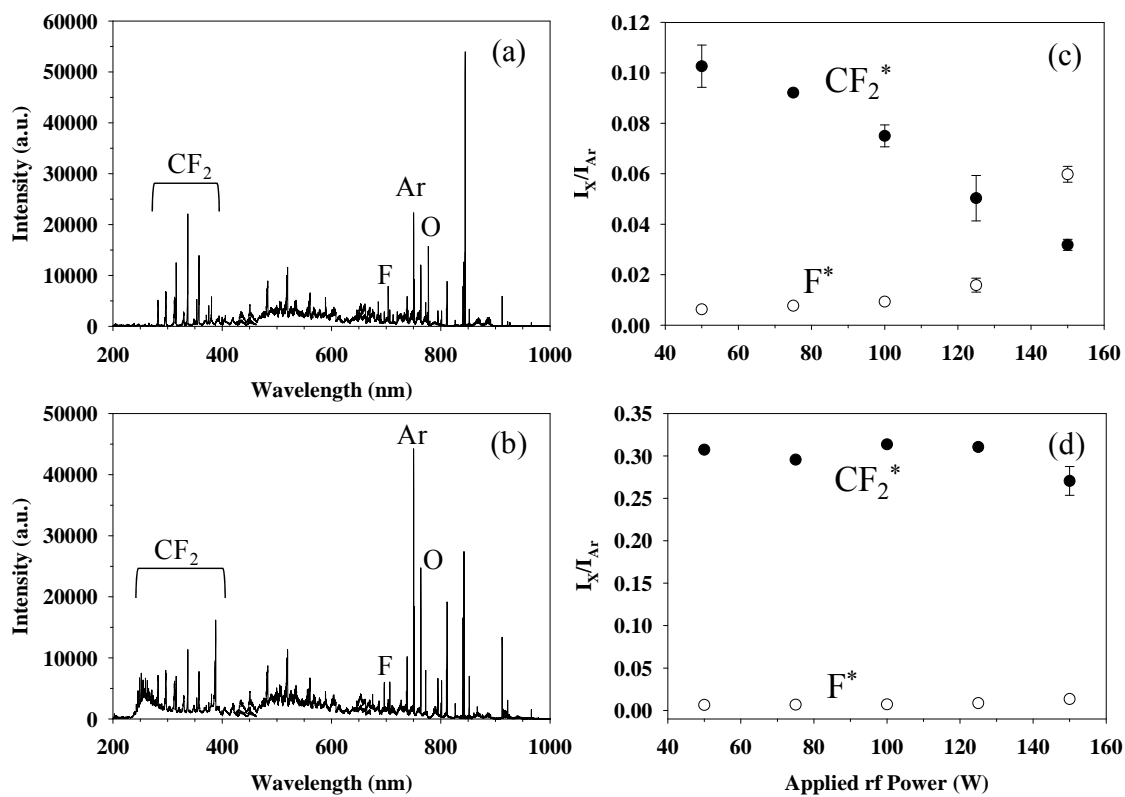


**Figure 3.1.** Raw OES spectra of (a) CF<sub>4</sub> and (b) C<sub>2</sub>F<sub>6</sub> plasmas ( $P = 100$  W). Actinometry data for CF<sub>2</sub><sup>\*</sup> and F<sup>\*</sup> species as a function of  $P$  for (c) CF<sub>4</sub> and (d) C<sub>2</sub>F<sub>6</sub> systems without substrates.

of  $\text{CF}_2^*$  in  $\text{CF}_4$  plasmas, whereas  $\text{F}^*$  concentrations appear to remain essentially unchanged as  $P$  increases. It should be noted that this method of actinometry is a more precise indicator of  $[\text{F}^*]$  than  $[\text{CF}_2^*]$ , due to the proximity of respective threshold energies for excitation to  $\text{Ar}^*$  (see Table 1.1). Regardless, the method is appropriate for examining *trends* with respect to these species.

Additional actinometry data are provided in Figure 3.2, where the relative emission intensities of both  $\text{CF}_2^*$  and  $\text{F}^*$  have been plotted as a function of  $P$  for all combinations of  $\text{CF}_4$  and  $\text{C}_2\text{F}_6$  plasmas with Si and  $\text{ZrO}_2$  substrates. Interestingly, the introduction of a substrate to  $\text{CF}_4$  plasmas, Figs. 3.2(a) and 3.2(c), has a significant impact on excited species concentrations. Excited atomic fluorine concentrations for the  $\text{CF}_4/\text{Si}$  system, Fig. 3.1(a), increase significantly at  $P > 75$  W, and both  $[\text{F}^*]$  and  $[\text{CF}_2^*]$  exhibit plateaus at  $P > 100$  W. In the  $\text{CF}_4/\text{ZrO}_2$  system, Fig. 3.2(c),  $\text{F}^*$  concentrations are essentially constant. This trend is reflected in the  $\text{C}_2\text{F}_6/\text{substrate}$  systems, Figs. 3.2(b) and 3.2(d). Nonetheless,  $\text{CF}_2^*$  concentrations in  $\text{C}_2\text{F}_6/\text{substrate}$  systems exceed those of the corresponding  $\text{CF}_4$  plasmas for all values of  $P$ , with a noticeably steep climb in  $[\text{CF}_2^*]$  concentrations with respect to  $P$  in the  $\text{C}_2\text{F}_6/\text{ZrO}_2$  system, Fig. 3.2(d).

OES data provide insight on relative concentrations of excited species in plasmas; to garner a more robust understanding of the plasma, however, the types of ions and ion energy distributions (IEDs) are also of interest. Mass spectra were acquired for nascent ions produced in  $\text{CF}_4$  and  $\text{C}_2\text{F}_6$  plasmas at applied rf powers ranging from 50 to 150 W. By focusing on the signal at 50 amu ( $\text{CF}_2^+$ ), we obtained IEDs as a function of  $P$ . Mean ion energies,  $\langle E_i \rangle$ , were then calculated by averaging these distributions, Table 3.1.<sup>23,24</sup>

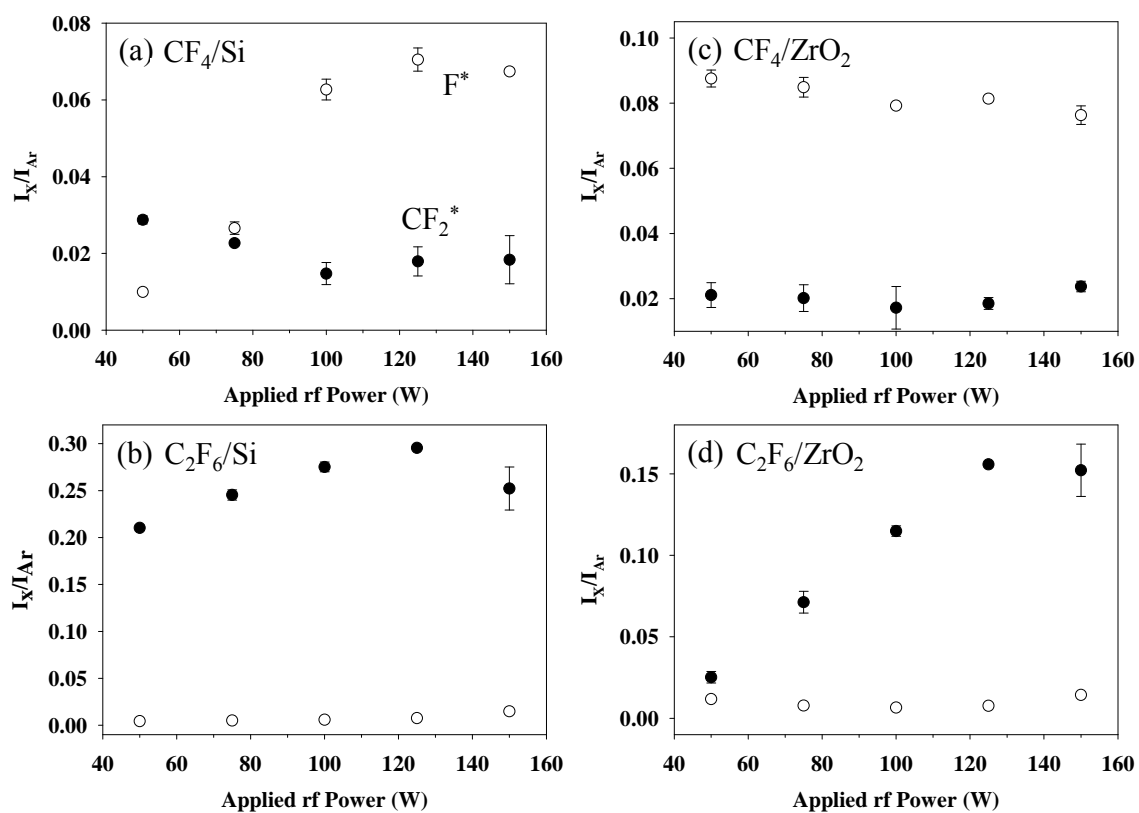


**Figure 3.2.** Actinometric OES data for  $CF_2^*$  and  $F^*$  in (a)  $CF_4/Si$  (b)  $C_2F_6/Si$  (c)  $CF_4/ZrO_2$  and (d)  $C_2F_6/ZrO_2$  systems. In all cases, substrates were placed 14 cm downstream from the reactor coil.

**Table 3.1.** Mean ion energies (in eV) for  $\text{CF}_2^+$  in FC plasmas. Values in parentheses represent one standard deviation from the mean of three trials.

Applied rf power (W)	$\text{CF}_4$ Plasma	$\text{C}_2\text{F}_6$ Plasma
50	83.1 (0.1)	41.1 (5.1)
75	80.0 (0.2)	49.0 (5.8)
100	80.0 (0.5)	55.8 (7.6)
125	80.2 (2.2)	75.2 (19)
150	59.7 (1.3)	65.1 (9.1)

In general,  $\langle E_i \rangle$  values were larger for  $\text{CF}_2^+$  ions produced from  $\text{CF}_4$  plasmas than from  $\text{C}_2\text{F}_6$  systems. There was, however, little variation in  $\langle E_i \rangle$  values for  $\text{CF}_2^+$  in  $\text{CF}_4$  plasmas, whereas  $\langle E_i \rangle$  in the  $\text{C}_2\text{F}_6$  systems gradually increased with increasing  $P$ .

LIF spectroscopy was also employed to characterize gas-phase species, specifically the  $\text{CF}_2$  radical. A typical portion of an excitation spectrum, Figure 3.3(a), clearly displays a broad, intense peak at 234.28 nm. This band corresponds to the (0,11,0)—(0,0,0) vibronic band of the  $A^1B_1—X^1A_1$  transition for  $\text{CF}_2$ , with peak identity confirmed upon comparison to the literature.<sup>25</sup>  $\text{CF}_2$  species densities were obtained by accumulating fifteen LIF images at 234.280 nm (on-resonance) and subtracting the same number of accumulations at 235.000 nm (off-resonance). This was repeated for each set of plasma parameters for both  $\text{CF}_4$  and  $\text{C}_2\text{F}_6$  systems, with the results plotted in Figure 3.3(b). The  $\text{CF}_2$  ground state species density, Fig. 3.3(b), is significantly higher in  $\text{C}_2\text{F}_6$  plasmas than in  $\text{CF}_4$  systems, especially with higher  $P$ .

IRIS data were generated by acquiring LIF images for  $\text{CF}_2$  during plasma processing of a substrate by rotating a Si or  $\text{ZrO}_2$  wafer into the path of the molecular beam. For each IRIS experiment, an LIF image taken of  $\text{CF}_2$  in the molecular beam (no substrate), Figure 3.4(a) (center image), was averaged over a 20 pixel range across the center of highest intensity and cross-sectioned to generate a one dimensional (1D) trace for  $\text{CF}_2$  in the incident beam only, Fig. 3.4(b). With a substrate rotated into the path of the plasma, this process was repeated to produce an image that contained both scatter and incident beam data, Fig. 3.4(a) (leftmost image). The pixelated intensities from these images were subtracted to produce an image of the scattered  $\text{CF}_2$  signal, Figure 3.4(a)

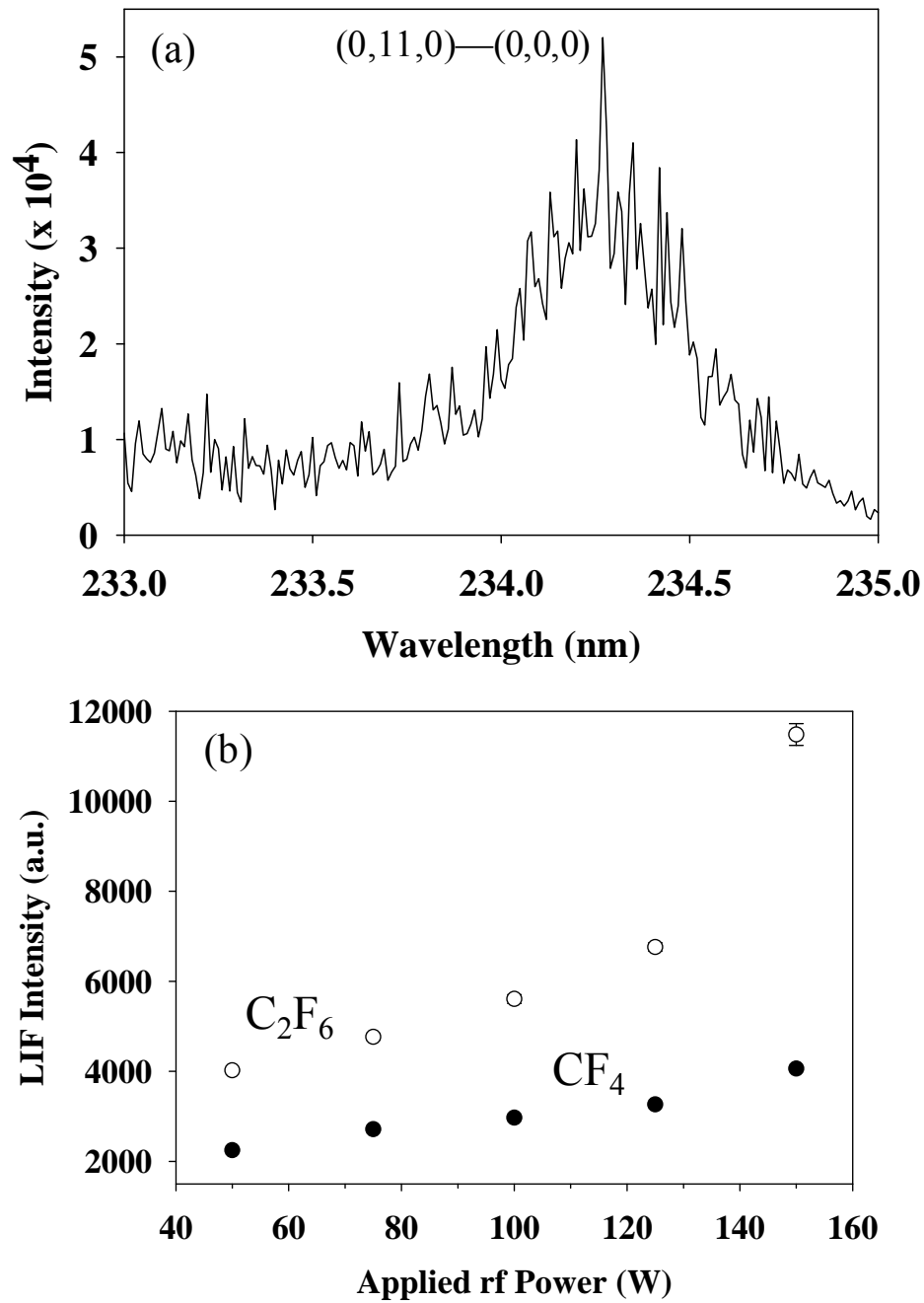


**Figure 3.3.** (a) Fluorescence excitation spectrum showing the (0,11,0)—(0,0,0) vibronic band of the  $A^1B_1-X^1A_1$  transition at 234.280 nm for  $CF_2$  formed in a  $C_2F_6$  plasma with  $P = 100$  W. (b) LIF intensities as a function of  $P$  for  $CF_2$  formed in  $CF_4$  (closed circles) and  $C_2F_6$  (open circles) plasma molecular beams.

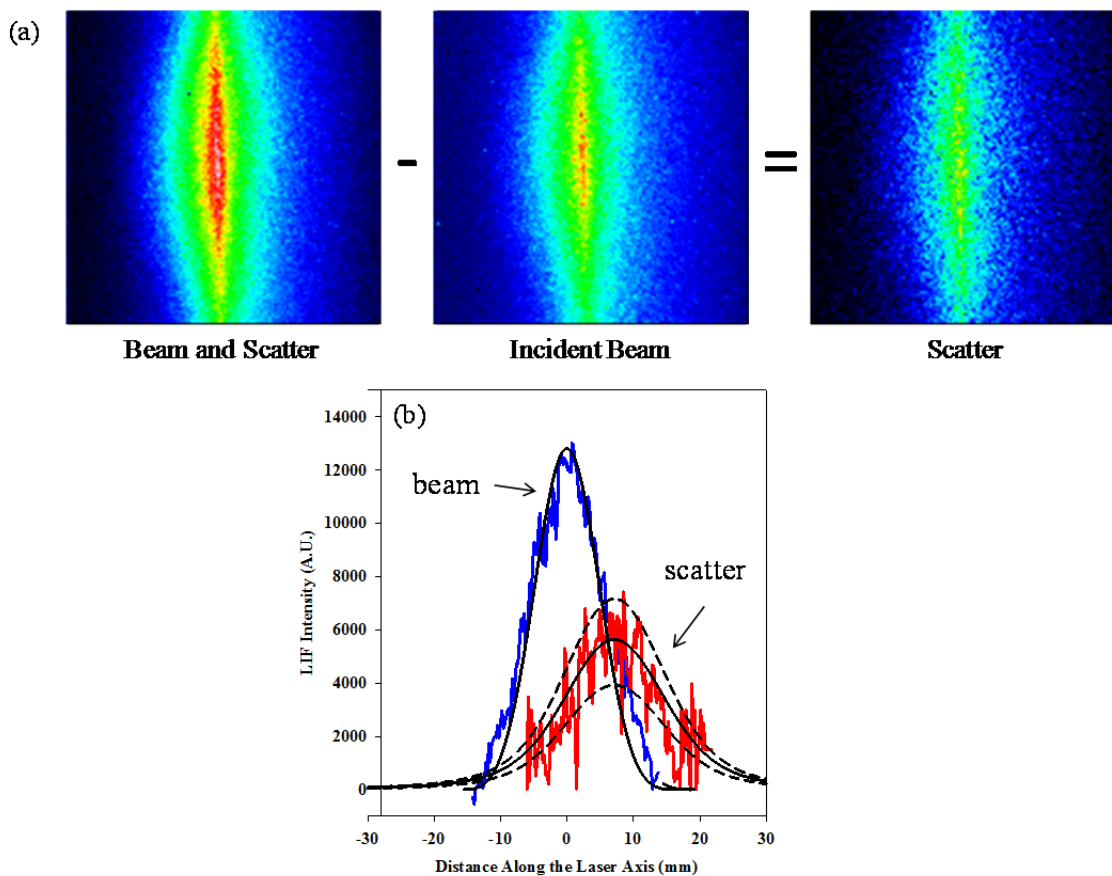


**Figure 3.4.** (a) LIF images collected during IRIS experiments for  $\text{CF}_2$  formed in a  $\text{CF}_4$  plasma molecular beam (incident beam) and with a  $\text{ZrO}_2$  substrate rotated into the same molecular beam, showing both  $\text{CF}_2$  in the incident beam and  $\text{CF}_2$  scattered from the substrate (beam and scatter). The image on the right (scatter) arises from image subtraction yielding a spot representing  $\text{CF}_2$  scattering from the  $\text{ZrO}_2$  system ( $P = 100$  W). (b) The images in (a) are converted to cross sections along the laser beam for  $\text{CF}_2$  LIF signals in the incident beam (blue) and scattered from the surface (red) along with simulated data (black lines) for this system. The best fit to this data set yields  $S(\text{CF}_2) = 1.41$ .

(right image). This signal was cross-sectioned to produce a 1D depiction of the scatter from the surface, Fig. 3.4(b). Figure 3.4(b) also shows simulated cross sectional data generated based upon the geometry of the experiment.<sup>26</sup> By fitting the simulated lines to the experimental data, a value was obtained for the scatter coefficient of  $\text{CF}_2$ ,  $S(\text{CF}_2)$ . Similar images and cross sectional data were collected under different experimental conditions and the resulting  $S(\text{CF}_2)$  values are listed in Table 3.2. In general,  $S(\text{CF}_2)$  values were greater than unity, Table 3.2, with the exception of the  $\text{C}_2\text{F}_6/\text{ZrO}_2$  systems. These values are similar to previous IRIS results for  $S(\text{CF}_2)$  measured using other FC precursors.<sup>3</sup> Also of note, scatter coefficients tended to be higher for  $\text{CF}_4$  systems than for  $\text{C}_2\text{F}_6$  systems. An additional observation from the Table 3.2 data is that the type of substrate processed influenced the value of  $S(\text{CF}_2)$ , with Si tending to yield higher scatter coefficients than  $\text{ZrO}_2$ . Measurements of scatter coefficients were repeated at  $P = 100$  W for plasmas with feeds composed of 1:1 mixtures of  $\text{CF}_4$  or  $\text{C}_2\text{F}_6$  with  $\text{H}_2$  gas. The addition of  $\text{H}_2$  significantly decreased the values for  $S(\text{CF}_2)$  in each system, Table 3.2.

Surface analysis of the substrates used in IRIS experiments was performed using XPS. Representative high-resolution  $\text{C}_{1s}$  and  $\text{F}_{1s}$  XPS spectra are shown in Figures 3.5 and 3.6 for the  $\text{CF}_4/\text{Si}$  and  $\text{C}_2\text{F}_6/\text{Si}$  systems, respectively. In addition, a high-resolution  $\text{F}_{1s}$  spectrum is shown for a  $\text{ZrO}_2$  wafer processed with  $\text{CF}_4$ , Fig. 3.5(c). As evidenced by the obvious differences between the two figures, the deposited FC films are inherently distinct especially with respect to the carbon and fluorine binding environments on Si in each system. Most notably, the  $\text{C}_{1s}$  XPS spectrum for an Si wafer processed in a  $\text{CF}_4$  plasma, Fig. 3.5(a), shows little FC character, whereas a similar wafer processed in a

**Table 3.2.** Surface scatter coefficients [ $S(\text{CF}_2)$ ] for different plasma/surface combinations. Values in parentheses are error estimates based on the error in the simulated fits to the data and includes several replicates of the data. Error estimates for data collected at 75 and 125 W are based solely on the error in the simulated fits to one data set.

$P$ (W)	$\text{CF}_4/\text{Si}$	$\text{CF}_4/\text{ZrO}_2$	$\text{C}_2\text{F}_6/\text{Si}$	$\text{C}_2\text{F}_6/\text{ZrO}_2$	$\text{CF}_4/\text{H}_2/\text{Si}$	$\text{C}_2\text{F}_6/\text{H}_2/\text{Si}$
50	1.52 (0.10)	1.38 (0.10)	1.28 (0.02)	0.83 (0.03)	--	--
75	1.42 (0.14)	--	1.30 (0.08)	--	--	--
100	1.45 (0.15)	1.40 (0.10)	1.33 (0.02)	0.99 (0.02)	1.21 (0.06)	1.11 (0.05)
125	1.75 (0.01)	--	1.41 (0.09)	--	--	--
150	1.87 (0.19)	1.37 (0.14)	1.65 (0.08)	0.95 (0.05)	--	--

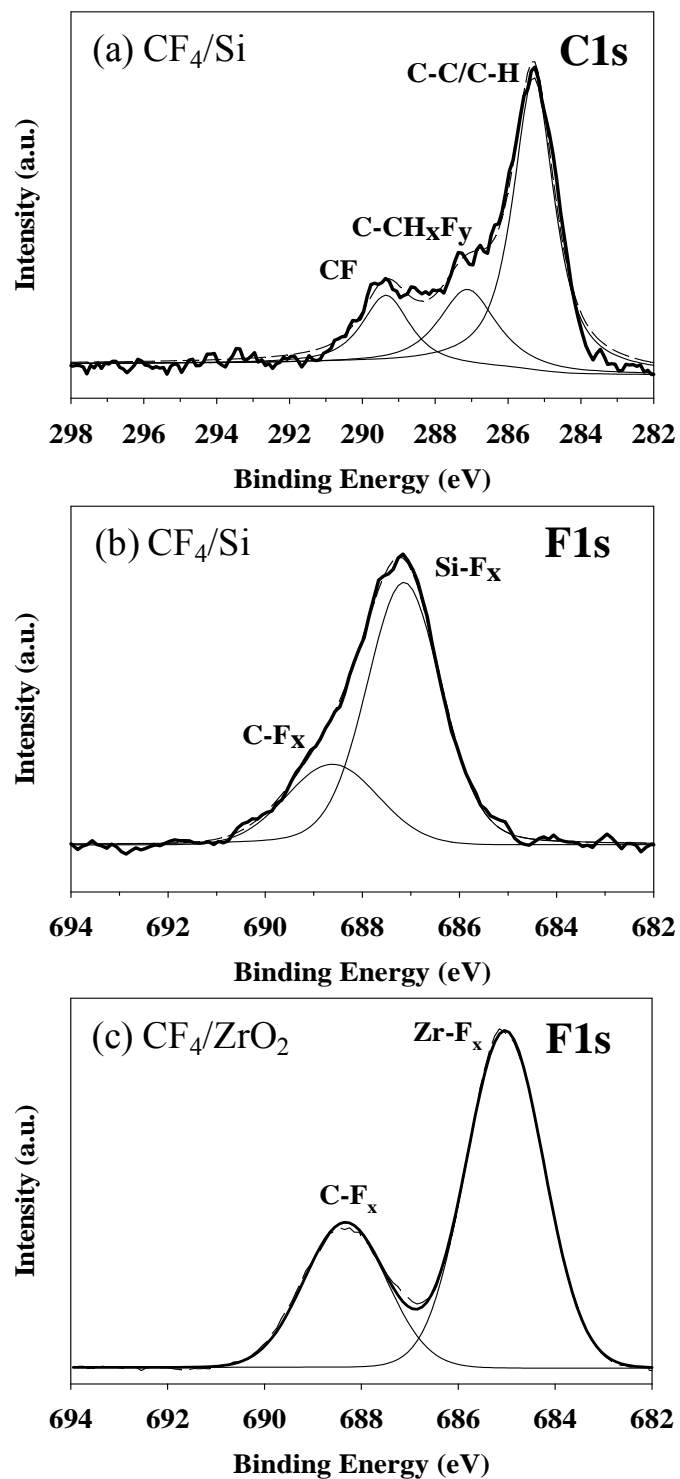


**Figure 3.5.** (a) High-resolution  $\text{C}_{1s}$  XPS spectrum of a Si wafer processed in an IRIS experiment with a 50 W  $\text{CF}_4$  plasma molecular beam. (b) High-resolution  $\text{F}_{1s}$  XPS spectrum of the same wafer. (c) High-resolution  $\text{F}_{1s}$  spectrum of a  $\text{ZrO}_2$  wafer processed in an IRIS experiment under similar conditions.

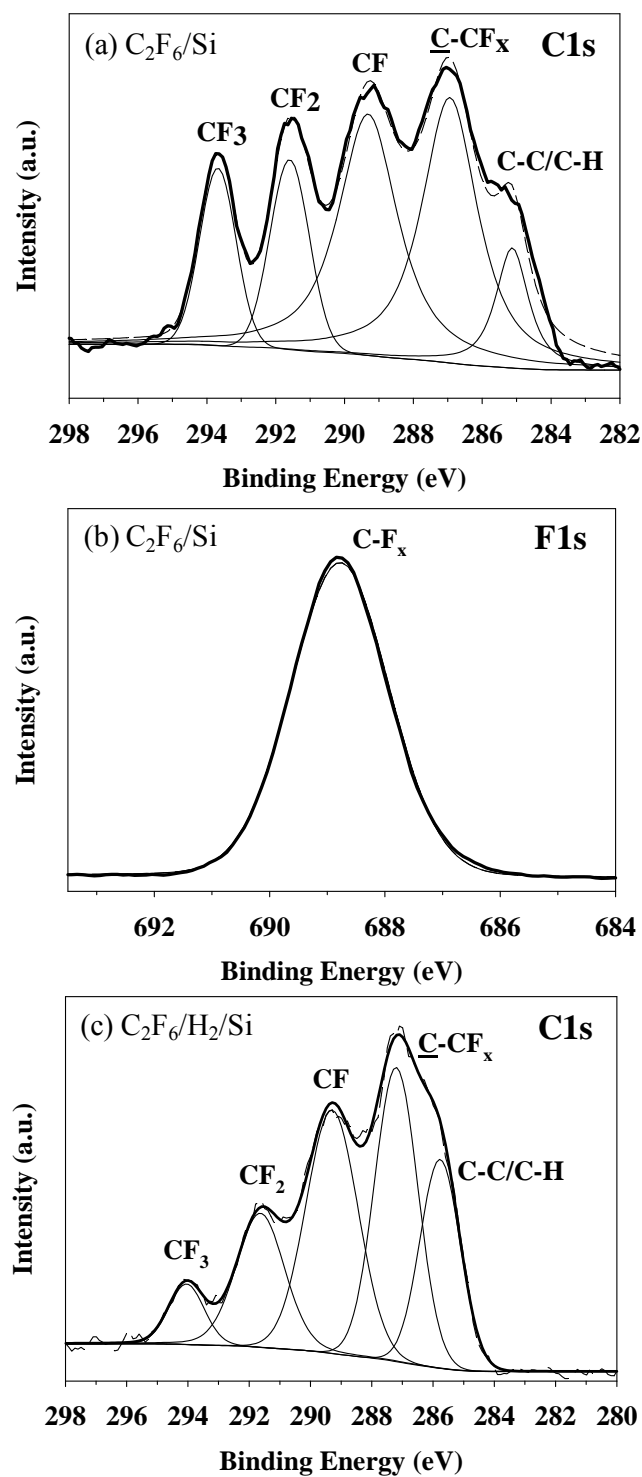


**Figure 3.6.** High-resolution XPS  $C_{1s}$  (a) and  $F_{1s}$  (b) spectra of a Si substrate processed in the IRIS system using a  $C_2F_6$  plasma molecular beam with  $P = 150$  W. A high-resolution  $C_{1s}$  spectrum is shown in (c) for a Si substrate processed under similar conditions using a  $C_2F_6/H_2$  plasma.

$C_2F_6$  plasma, Fig. 3.6(a), consists of multiple FC polymer moieties, including  $CF_2$  and  $CF_3$  linkages that are completely absent in the  $CF_4/Si$  system. Fluorine binding environments on Si were also affected by the type of plasma used for processing, Figs. 3.5(b) and 3.6(b), such that fluorine incorporation occurred in the underlying substrate in the case of  $CF_4$  processing (68% of F is present as Si- $F_x$ ), whereas all surface fluorine in the case of  $C_2F_6$  processing was present in a C- $F_x$  type environment. Notably, the  $F_{1s}$  spectrum for the  $CF_4/ZrO_2$  system also shows significant incorporation of F into the  $ZrO_2$  substrate, with nearly 65% of the signal arising from Zr- $F_x$  species, Fig. 3.5(c). For comparison, we also analyzed films deposited from FC/ $H_2$  plasmas. The  $C_{1s}$  spectrum for a film deposited on a Si substrate using a 50:50  $C_2F_6/H_2$  plasma is shown in Fig. 3.6(c). As expected, the contribution from the C-C/C-H binding environment is greater than that seen in Fig. 3.6(a), but there are still significant contributions from  $CF_x$  moieties. Similar  $C_{1s}$  spectra were collected for films deposited in  $CF_4/H_2/Si$  systems.

### 3.3. Discussion

As noted in the Introduction, little work exists that focuses specifically on FC/ $ZrO_2$  processing; as such, it remains unclear what the true potential may yield for optical or microelectronic applications in FC plasma processing of zirconia substrates. To understand the mechanisms of FC plasma-surface processing for any plasma/substrate system, it is necessary to recognize the role of gas-phase species and to identify the mechanisms behind gas-surface interactions. Actinometry provides a useful gauge of the excited gaseous species present within a plasma system. In a  $CF_4$  plasma, relative  $CF_2^*$  concentrations decrease with increasing  $P$ , Fig. 3.1(c). In turn, atomic fluorine increases,

suggesting subsequent electron impact decomposition of plasma species after precursor fragmentation, process (3.1),



Although such results have been demonstrated previously,<sup>2</sup> it is important to note that a wide variety of species can exist in these systems, contributing to the overall complexity of plasma-surface interactions. In contrast, both  $\text{CF}_2^*$  and  $\text{F}^*$  concentrations remain relatively stable with respect to changes in applied rf power in  $\text{C}_2\text{F}_6$  plasmas, Fig. 3.1(d).

Because of the chemical structure of the precursor, the effect of the type seen in reaction (3.1) does not figure prominently until  $P > 175$  W, as there are likely to be fragmentations of the form  $\text{C}_2\text{F}_y \rightarrow 2\text{CF}_x$  in  $\text{C}_2\text{F}_6$  systems. In other words,  $\text{CF}_2$  depletion via pathway (3.1) is not significant because much more  $\text{CF}_2$  is formed directly from the  $\text{C}_2\text{F}_6$  precursor than is formed from  $\text{CF}_4$  under similar conditions.

Interestingly, the relative concentrations of these species are affected by the introduction of a substrate, Si or  $\text{ZrO}_2$ , and appear to be substrate-dependent, Fig. 3.2. The trends seen in Fig. 3.2(a) may be a result of the formation of strong Si-F bonds in a comparatively small concentration of F at low rf powers. Volatile  $\text{SiF}_2$  and  $\text{SiF}_4$  species, along with volatile FC moieties, can readily desorb from the surface,<sup>27</sup> exposing new reactive sites for further fluorine incorporation. As fluorine concentrations reach sufficient levels at high  $P$ , fluorine saturates exposed reactive sites at the Si surface and generates a significant excess of  $\text{F}^*$ , leading to the trends observed with increased  $P$ . With  $\text{ZrO}_2$  processing, such a marked increase in  $[\text{F}^*]$  is not observed with increased  $P$ , Fig. 3.2(c).

Although the enthalpy of formation of  $\text{ZrF}_4$  ( $-1.9 \times 10^3 \text{ kJ}\cdot\text{mol}^{-1}$ ) is not drastically different from that of  $\text{SiF}_4$  ( $-1.6 \times 10^3 \text{ kJ}\cdot\text{mol}^{-1}$ ),<sup>28,29</sup> the formation of nonvolatile surface prod-

ucts in a FC passivation layer hinders desorption of  $ZrF_4$ . Indeed, Kim and co-workers<sup>30</sup> suggested that formation of such products served as the limiting step to etching of  $ZrO_2$  in high density  $CF_4$  plasmas. The ramifications of these processes are discussed below.

The introduction of a substrate to a  $C_2F_6$  plasma system does not have as profound an effect on relative species concentrations as is seen in the  $CF_4$  systems. Figures 3.2(b) and 3.2(d) are similar in appearance to the actinometry data for the  $C_2F_6$  plasma alone, Fig. 3.1(d). This suggests that other fundamental differences in the gas-phase of the two plasmas may contribute to plasma surface interactions. Consequently, we further studied gas-phase FC systems through use of LIF spectroscopy to provide insight into the behavior of ground state  $CF_2$  molecules. Figure 3.3 illustrates more gas-phase  $CF_2$  is produced in  $C_2F_6$  plasmas than in  $CF_4$  plasmas. This is consistent with actinometric data for excited state  $CF_2^*$ , and may help to explain the differences in substrate processing between the two systems. Evidence in the literature suggests the incorporation of  $CF_2$  and  $C_xF_y$  species produced in the gas phase from  $CF_2$  contribute to film formation and growth.<sup>31</sup> To elucidate mechanisms of plasma-surface interactions, an understanding of what occurs at the surface is critical. Thus, the results of IRIS experiments can be scrutinized for trends in plasma processing of Si and  $ZrO_2$ , Table 3.2.

Figure 3.7 illustrates a generalized view of the roles of different FC plasma species in the  $CF_4/Si$ ,  $C_2F_6/Si$ , and  $FC/ZrO_2$  systems, showing schematically how film formation and etching processes are reflected in the measured  $S(CF_2)$  values. In  $CF_4/Si$  plasma systems, a thin (~5 nm) FC passivation layer is deposited, but is simultaneously etched through the interaction of plasma species with the film. In  $CF_4$  systems, the

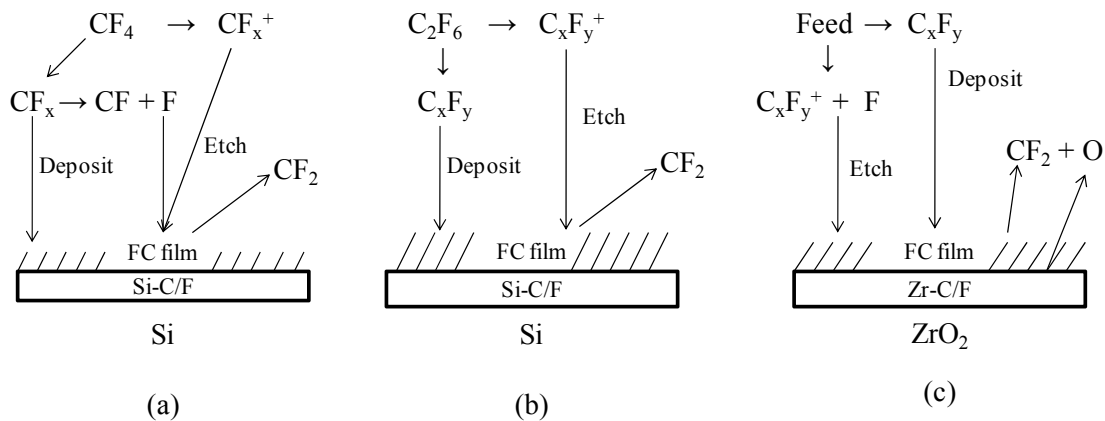


**Figure 3.7.** Depiction of the processes by which major gas phase species in  $\text{CF}_4$  and  $\text{C}_2\text{F}_6$  fluorocarbon plasmas contribute to FC film deposition and etching of Si and  $\text{ZrO}_2$ .

abundant F atoms can react with the deposited layer to form  $CF_x$  ( $x = 1, 2, 3$ ), which subsequently desorb from the surface. When  $CF_2$  units are formed the LIF signal from scattered  $CF_2$  increases, reaction (3.2), where  $A(s)$  represents an activated site on the surface.

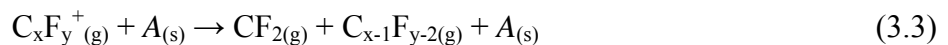


Given that  $S(CF_2)$  values are the ratio of incident to scattered  $CF_2$  molecules, the measured  $S(CF_2)$  value increases under these circumstances. This mechanism, Figure 3.7(a), is supported by the lack of FC character on the substrate and fluorine incorporation into the underlying Si, Fig. 3.5.

In contrast to the  $CF_4/Si$  system, the  $C_2F_6/Si$  plasma system contains much lower fluorine concentrations with respect to  $CF_2$ , Figs. 3.2(b) and 3.2(d). A lack of fluorine flux to the surface may decrease surface production of  $CF_2$ , as the reaction (3.2) contributions to the scatter signal lose significance, Fig. 3.7(b). The contributions of F atoms to the measured  $S(CF_2)$  values can be further probed by examining the effects of adding  $H_2$  to the plasmas. Hydrogen atoms are known scavengers of gas-phase fluorine atoms, serving to deplete the amount of  $F_{(g)}$  available in the system.<sup>12</sup>  $S(CF_2)$  values measured in both  $CF_4/H_2/Si$  and  $C_2F_6/H_2/Si$  systems are significantly lower than those measured without  $H_2$  addition, Table 3.2. This effect implies that depletion in relative fluorine concentration has a profound influence on the observed surface scatter coefficient of  $CF_2$ . Thus, we deduce that the presence or scarcity of atomic fluorine plays a significant role in  $CF_2$  scatter from FC films at a Si surface. Consequently, the smaller  $S(CF_2)$  values in  $C_2F_6/Si$  systems relative to  $CF_4/Si$  likely result from a lower relative fluorine concentration in the  $C_2F_6$  plasma. An additional consequence of decreased F atom production in  $C_2F_6$  plasmas also allows for thicker films to be deposited (~10-20 nm). Moreover, the films de-

posited from C<sub>2</sub>F<sub>6</sub> plasmas all had the amorphous FC character exemplified in Figure 3.6(a), with C-C/C-H, C-CF<sub>x</sub>, CF, CF<sub>2</sub>, and CF<sub>3</sub> features. Films deposited from C<sub>2</sub>F<sub>6</sub>/H<sub>2</sub> systems were also relatively thick and amorphous with a high degree of cross-linking, Fig. 3.6(c). Chapter 7 further examines the effect of plasma additives, including H<sub>2</sub>, with special emphasis on gas-phase reactions and their contributions to substrate processing.

In addition to F atom contributions to CF<sub>2</sub> surface production, highly energetic ions can also ablate the surface FC film to generate CF<sub>2</sub>, as depicted in Figure 3.7. Both theoretical and experimental work supports this hypothesis. For example, Zhang and Kushner<sup>32</sup> calculated that increasing ion energies yielded increased surface production of CF<sub>2</sub> in FC plasmas. Oehrlein and co-workers<sup>33</sup> have also shown that high energy ions serve to fragment and defluorinate the deposited FC film in high density, high power C<sub>4</sub>F<sub>8</sub> plasmas. Interestingly, simulated ion penetration depths for FC ions suggest a limit of ~2 nm for 50 eV ions and that for FC film thicknesses >2 nm, F atom diffusion to the interface controls substrate etching.<sup>33, 34</sup> Previous IRIS studies in our lab have demonstrated that removing ions from the incident molecular beam lowers *S*(CF<sub>2</sub>) in a range of FC plasmas. Furthermore, we have shown that the scatter coefficient and mean ion energy,  $\langle E_i \rangle$  for the CF<sub>2</sub><sup>+</sup> ion are directly correlated in plasmas formed from large FC precursors.<sup>24</sup> These calculations and observations suggest that ions, rather than atomic F, may contribute most significantly to the surface production of CF<sub>2</sub> at FC films deposited from C<sub>2</sub>F<sub>6</sub> plasmas. Ion-induced production of CF<sub>2(g)</sub> can proceed either via surface dissociation and neutralization of large ions with subsequent desorption of CF<sub>2</sub>, or by sputtering of FC films to produce CF<sub>2</sub>, reactions (3.3) and (3.4),<sup>32</sup>





where the energetic ion leaves a surface vacancy in the case of reaction (3.4). We have extended the connection between  $\langle E_i \rangle$  and  $S(\text{CF}_2)$  to  $\text{CF}_4$  and  $\text{C}_2\text{F}_6$  systems, Fig. 3.8, that shows a clear trend between these two values. Figure 3.8 also contains data from the  $\text{C}_3\text{F}_8$  and  $\text{C}_4\text{F}_8$  systems for comparison, and includes a linear correlation drawn across all four plasma systems. As can be seen from Fig. 3.8 and the data in Table 3.1,  $\langle E_i \rangle$  values in  $\text{CF}_4$  plasmas have little variation, implying that the role of ion bombardment is constant for all processing conditions. This also suggests that reactions (3.3) and (3.4) are not strong contributors to surface production of  $\text{CF}_2$  in  $\text{CF}_4/\text{Si}$  systems, further corroborating the hypothesis that high fluorine concentrations cause the increase in  $S(\text{CF}_2)$  with increasing  $P$  in these systems. The lack of variation in  $\langle E_i \rangle$  values for  $\text{CF}_2^+$  in  $\text{CF}_4$  plasmas may result from collisionless ion movement through the plasma sheath. In contrast, ion energies for  $\text{CF}_2^+$  increase steadily with increasing  $P$  in  $\text{C}_2\text{F}_6$  plasmas, Table 3.1, whereas the F atom concentrations are reasonably constant with  $P$ , Fig. 3.2(b). Thus, energetic ions, rather than fluorine, are likely the primary source of increased  $\text{CF}_2$  scatter in the  $\text{C}_2\text{F}_6/\text{Si}$  systems. A more detailed discussion of ion contributions to FC plasma processing is presented in Chapter 6.

Given that we have observed some dependence of  $S(\text{CF}_2)$  values on the underlying substrate,<sup>3</sup> it is useful to consider the FC/ $\text{ZrO}_2$  systems with respect to mechanisms for surface production of  $\text{CF}_2$ . With the  $\text{CF}_4$  plasma, the  $S(\text{CF}_2)$  values for the  $\text{ZrO}_2$  substrates are slightly lower than with Si substrates, but are within the combined experimental error, Table 3.2. In contrast, with  $\text{C}_2\text{F}_6$  plasmas, the  $S(\text{CF}_2)$  values are uniformly

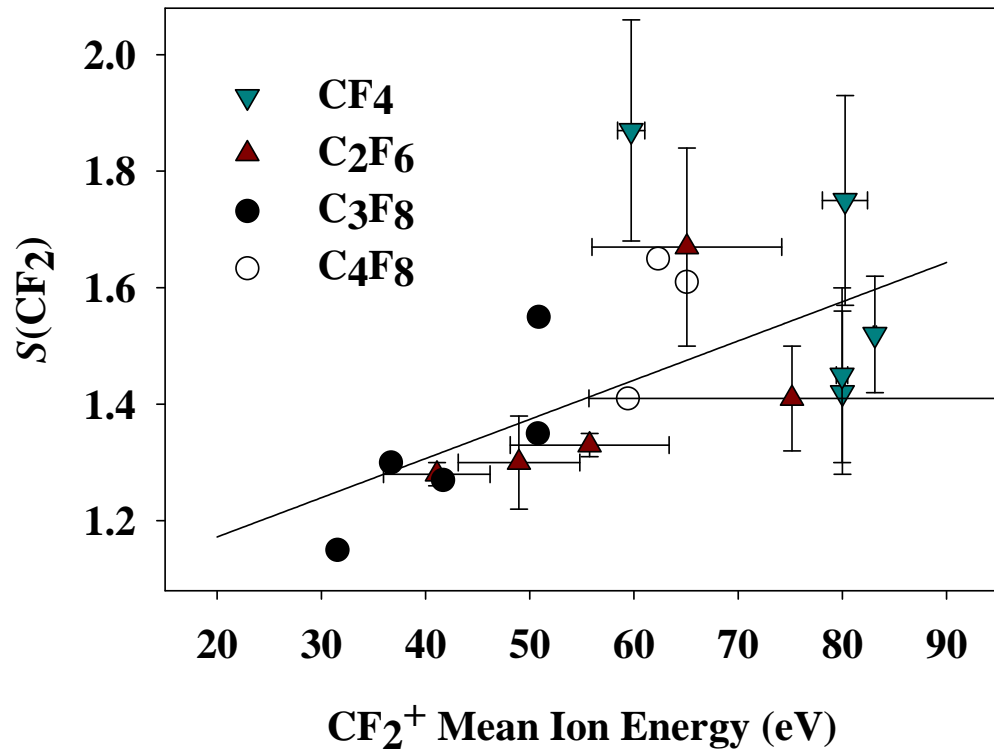


**Figure 3.8.** Comparison of  $S(\text{CF}_2)$  and corresponding  $\text{CF}_2^+$  mean ion energies in  $\text{CF}_4$  and  $\text{C}_2\text{F}_6$  along with corresponding data from  $\text{C}_3\text{F}_8$  and  $\text{C}_4\text{F}_8$  plasmas published previously (Ref. 24). The line is a linear regression fit to all of the data ( $R^2 = 0.45$ ).

lower than those measured on Si substrates. The decrease in surface production of  $\text{CF}_2$  with  $\text{ZrO}_2$  likely arises from a shift in the equilibrium of the deposition-etch competition. Specifically,  $\text{CF}_4$  is considered an etching system, whereas  $\text{C}_2\text{F}_6$  appears to be a slowly depositing system with some competitive etching occurring. Thus, the overall process mechanisms for  $\text{CF}_4$  plasmas are governed by fluorine flux to the surface, regardless of the substrate. As such, the competition lies in favor of etching over film deposition. Consequently,  $S(\text{CF}_2)$  values for the  $\text{CF}_4/\text{ZrO}_2$  system are not appreciably different from results obtained for the  $\text{CF}_4/\text{Si}$  system, Table 3.2.

In  $\text{C}_2\text{F}_6$  plasmas, the process mechanisms appear to be much more complex. Films deposited on  $\text{ZrO}_2$  substrates in  $\text{C}_2\text{F}_6$  plasmas are approximately the same thickness as those deposited on Si substrates. Although this might suggest that the etch-deposition equilibrium has not shifted, we postulate that the substrate dependence observed in our  $S(\text{CF}_2)$  values likely arise from the ability to form volatile products which can then desorb from the surface. As noted above, the dominant etching species in  $\text{C}_2\text{F}_6$  plasmas are ions rather than fluorine atoms. Through zero dimensional kinetic models and comparison to experimental results, Kim et al. have suggested that  $\text{ZrO}_2$  etching is controlled via neutral species rather than ions.<sup>30, 35</sup> They conclude that species such as fluorine atoms are more effective at forming volatile products than high energy ions. Similarly, Oehrlein and co-workers<sup>33</sup> have demonstrated that an overall fluorine deficiency in a plasma etching system will limit the ability of etch products to desorb. We have shown that there is a deficiency of fluorine in  $\text{C}_2\text{F}_6$  plasmas relative to other species, suggesting a limit on desorbing etch products. Another factor influencing the ability of a particular surface to produce  $\text{CF}_2$  is the metal-C bond strength. The heat of formation of Zr-C bonds in a ZrC

lattice is 2.1 eV/pair, whereas that for Si-C bonds in a SiC lattice is only 0.6 eV/pair.<sup>36</sup> Thus, the lower  $S(\text{CF}_2)$  values measured in the  $\text{C}_2\text{F}_6/\text{ZrO}_2$  system may also be the result of much stronger ZrC bonds being formed between the  $\text{ZrO}_2$  substrate and the FC passivation layer.

As an additional note, molecular dynamics simulations of FC etching of  $\text{SiO}_2$  substrates demonstrated that a loss of oxygen preferential to Si occurred during removal of the first few surface layers.<sup>37</sup> Analogously, oxygen is likely depleted by removal of the  $\text{ZrO}_2$  surface layer as well. In these systems, it is possible that  $\text{CF}_2$  and O combine prior to desorbing from the surface as  $\text{CF}_2\text{O}$ , thereby reducing the amount of scattered  $\text{CF}_2$ . This is supported by the observation that our actinometry data reveal there is ~50% more atomic oxygen present during plasma processing of  $\text{ZrO}_2$  substrates relative to processing Si substrates. Although ions and fluorine likely contribute to  $\text{CF}_2$  surface production from  $\text{ZrO}_2$  surfaces in both plasma systems, Figure 3.7(c), as noted above, the formation of volatile products is hindered with  $\text{ZrO}_2$  substrates.

Regardless of substrate type,  $S(\text{CF}_2)$  values for  $\text{CF}_4$  systems are generally greater than those for counterpart  $\text{C}_2\text{F}_6$  systems. In considering the mechanism for  $\text{CF}_2$  surface production, we must therefore also understand the reactions that affect the observed scatter in our IRIS experiments. As discussed previously,<sup>3, 15, 24</sup> several possible reactions can contribute to surface production of  $\text{CF}_2$ . Three of these that are likely to be important in the  $\text{CF}_4$  and  $\text{C}_2\text{F}_6$  systems are shown in reactions (3.5)-(3.7):



Reaction (3.5) represents a simple adsorption-desorption reaction for  $\text{CF}_2$ , which accounts for the majority of the observed  $\text{CF}_2$  scatter in all FC systems. Given the high concentrations of  $\text{CF}_3$  and F atoms in  $\text{CF}_4$  plasmas, reactions (3.6) and (3.7) likely give rise to the large (i.e.  $>1$ )  $S(\text{CF}_2)$  values. In comparison, for the  $\text{C}_2\text{F}_6$  plasmas, reaction (3.6) is not likely to be as influential. Because reactions (3.5)-(3.7) all affect the observed  $S(\text{CF}_2)$  value for a given system, an examination of those processes that can alter their contributions is prudent. At high  $\text{F}_{(\text{g})}$  concentrations, some recombination of  $\text{CF}_x$  species and F likely occurs outside the coil region of the plasma, at the reactor wall:<sup>2</sup>



Incorporation of F atoms into a substrate/film depletes both  $\text{CF}_{x(\text{g})}$  and  $\text{F}_{(\text{g})}$  relative to what would be available if only gas-phase reactions were considered. Reaction (3.8) also diminishes the relative importance of reaction (3.6) to the surface production of  $\text{CF}_2$ .

Likewise, formation of oligomeric units,<sup>31</sup> reaction (3.9),



where x and y are not necessarily equal, can have a profound impact on the significance of reactions (3.5) and (3.7). Reaction (3.9) is more likely to occur in  $\text{C}_2\text{F}_6$  plasmas.

Thus, the observed differences in  $S(\text{CF}_2)$  values between the  $\text{CF}_4$  and  $\text{C}_2\text{F}_6$  plasmas can be largely attributed to two primary factors: the excess of F atoms with respect to  $\text{CF}_x$  species in  $\text{CF}_4$  plasmas and the formation of oligomeric units along with increased film formation in  $\text{C}_2\text{F}_6$  plasmas. Additional IRIS studies discussed in later chapters of this dissertation seek to explore the surface interactions of CF as well as the energetics of the gas-phase species in  $\text{CF}_4$  and  $\text{C}_2\text{F}_6$  plasmas. Clearly, these studies will further illuminate the relative importance of processes (3.5)-(3.9).

### 3.4. Summary

Despite the enormous utility of FC plasmas, much work remains to be done to fully understand the complex chemistry occurring in these systems. This is especially true for new plasma/substrate systems. Here, we have demonstrated that the roles of  $\text{CF}_2$  and F species as well as those of energetic ions are of significant importance to substrate processing during FC plasma treatment of Si and  $\text{ZrO}_2$  substrates. By combining analysis of gas-phase species, surface analysis and gas-surface interface data from the IRIS technique, an overarching scheme that summarizes the individual contributions to a particular surface was formulated. For  $\text{CF}_4$  plasma/substrate systems, fluorine atoms strongly influence the observed trends in  $S(\text{CF}_2)$ , whereas highly energetic ions are the determining factor in  $\text{C}_2\text{F}_6$  plasmas. Overall, the combination of gas-phase, surface and gas-surface interface data presented here provides significant insight into the seemingly subtle differences in FC plasma processing using different plasma/substrate combinations.

### 3.5. Supplemental Information

FC film deposition is dependent not only on the parameters associated with the plasma (i.e. feed gas choice,  $P$ , pressure, etc.) but also upon the position of the substrate within the plasma reactor and its proximity to the coil region. Within the coil region of the reactor exists a harsh environment, rife with highly energetic species, including ions and electrons. Here, film deposition is limited to creation of thin FC passivation layers. As gas-phase species traverse the length of the reactor (due to mechanical pumping), collisional effects and gas-phase interactions lead to the formation of oligomeric deposition precursors (see discussion, Chapter 6) that enhance the efficacy of film deposition. Thus, substrates exposed to the plasma at a location far downstream from the coil region of the reactor tend to exhibit more highly-ordered (less crosslinked) films, that demonstrate a propensity toward PTFE-like  $-(CF_2)_n-$  moieties. This effect is shown for films deposited simultaneously from a  $C_2F_6$  plasma on substrates located (a) in the coil region, (b) 14 cm d.s. from the coil, and (c) 25 cm d.s. from the coil in high-resolution  $C_{1s}$  XPS spectra, Fig. 3.9. The films exhibit strikingly different trends with respect to binding environments. Ultimately, for the FC film deposited in the coil region, Fig. 3.9(a), the F/C ratio is  $0.7 \pm 0.1$  with  $87\% \pm 2\%$  crosslinking. At 14 cm d.s., the F/C ratio is  $1.0 \pm 0.1$ , with  $69\% \pm 3\%$  crosslinking. Finally, for a film deposited 25 cm d.s., the F/C ratio =  $1.7 \pm 0.1$  and the film is  $41\% \pm 1\%$  crosslinked.

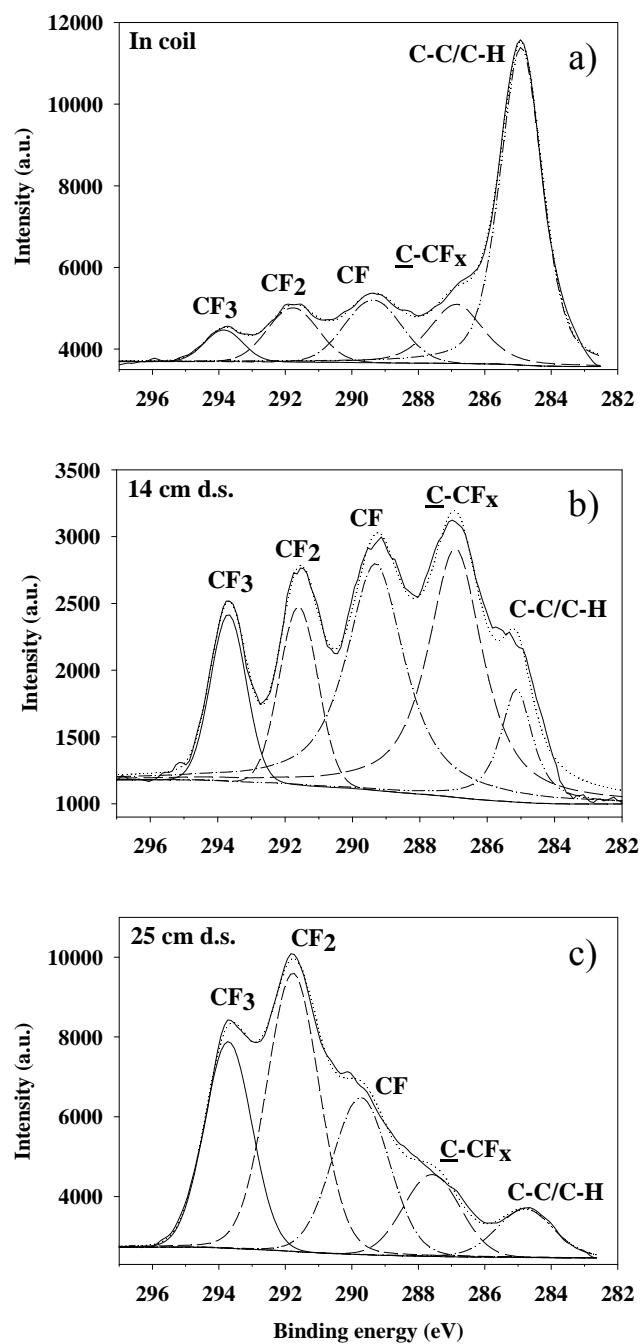


**Figure 3.9.** High-resolution  $C_{1s}$  XPS spectra for FC films deposited from  $C_2F_6$  with  $P = 150$  W on Si substrates positioned a) in the coil region of the plasma reactor, b) 14 cm d.s., and c) 25 cm d.s. All depositions were performed simultaneously, such that all three Si wafers were exposed to the plasma.

### 3.6. References

1. Oehrlein, G. S.; Zhang, Y.; Vender, D.; Haverlag, M., Fluorocarbon high-density plasmas. I. Fluorocarbon film deposition and etching using  $\text{CF}_4$  and  $\text{CHF}_3$ . *J. Vac. Sci. Technol. A* **1994**, 12, (2), 323.
2. Booth, J. P.; Cunge, G.; Chabert, P.; Sadeghi, N.,  $\text{CF}_x$  radical production and loss in a  $\text{CF}_4$  reactive ion etching plasma: Fluorine rich conditions. *J. Appl. Phys.* **1999**, 85, 3097.
3. Butoi, C. I.; Mackie, N. M.; Williams, K. L.; Capps, N. E.; Fisher, E. R., Ion and substrate effects on surface reactions of  $\text{CF}_2$  using  $\text{C}_2\text{F}_6$ ,  $\text{C}_2\text{F}_6/\text{H}_2$ , and hexafluoropropylene oxide plasmas. *J. Vac. Sci. Technol. A* **2000**, 18, (6), 2685-2698.
4. d'Agostino, R.; Capezzuto, P.; Bruno, G.; Cramarossa, F., Mechanism of etching, polymerization and deposition in rf discharges. *Pure & Appl. Chem.* **1985**, 57, (9), 1287-1298.
5. Rueger, N. R.; Beulens, J. J.; Schaepekens, M.; Doemling, M. F.; Mirza, J. M.; Standaert, T. E. F. M.; Oehrlein, G. S., Role of steady state fluorocarbon films in the etching of silicon dioxide using  $\text{CHF}_3$  in an inductively coupled plasma reactor. *J. Vac. Sci. Technol. A* **1997**, 15, (4), 1881.
6. Samukawa, S., Highly selective and highly anisotropic  $\text{SiO}_2$  etching in pulse-time modulated electron cyclotron resonance plasma. *Jpn. J. Appl. Phys.* **1994**, 33, 2133-2138.
7. Woo, J.; Kim, S.; Koo, J.; Kim, G.; Kim, D.; Yu, C.; Kang, J.; Kim, C., A study on dry etching for profile and selectivity of  $\text{ZrO}_2$  thin films over Si by using high density plasma. *Thin Solid Films* **2009**, 517, 4246-4250.
8. Chang, J. P.; Lin, Y.; Chu, K., Rapid thermal chemical vapor deposition of zirconium oxide for metal-oxide-semiconductor field effect transistor application. *J. Vac. Sci. Technol. B* **2001**, 19, (5), 1782-1787.
9. Copel, M.; Gribelyuk, M.; Gusev, E., Structure and stability of ultrathin  $\text{ZrO}_2$  layers on Si(001). *Appl. Phys. Lett.* **2000**, 76, (4), 436.
10. Sha, L.; Cho, B.; Chang, J. P., Ion-enhanced chemical etching of  $\text{ZrO}_2$  in a chlorine discharge. *J. Vac. Sci. Technol. A* **2002**, 20, (5), 1525-1531.
11. Visser, S. A.; Hewitt, C. E.; Fornalik, J.; Braunstein, G.; Srividya, C.; Babu, S. V., Surface and bulk compositional characterization of plasma-polymerized fluorocarbons prepared from hexafluoroethane and acetylene or butadiene reactant gases. *J. Appl. Polym. Sci.* **1997**, 66, 409-421.
12. d'Agostino, R.; Cramarossa, F.; Fracassi, F.; Illuzzi, F., *Plasma Polymerization of Fluorocarbons*. Academic Press, Inc. : San Diego, CA, 1990.
13. Cicala, G.; Milella, A.; Palumbo, F.; Rossini, P.; Favia, P.; d'Agostino, R., Nanostructure and composition control of fluorocarbon films from modulated tetrafluoroethylene plasmas. *Macromolecules* **2002**, 35, 8920-8922.
14. Haverlag, M.; Stoffels, E.; Stoffels, W. W.; Kroesen, G. M. W.; de Hoog, F. J., Measurements of radical densities in rf plasmas using infrared absorption spectroscopy. *J. Vac. Sci. Technol. A* **1994**, 12, 3102.
15. Martin, I. T.; Fisher, E. R., Ion effects on  $\text{CF}_2$  surface interactions during  $\text{C}_3\text{F}_8$  and  $\text{C}_4\text{F}_8$  plasma processing of Si. *J. Vac. Sci. Technol. A* **2004**, 22, (5), 2168-2176.

16. Liu, D.; Martin, I. T.; Fisher, E. R., CF<sub>2</sub> surface reactivity during hot filament and PECVD of FC films. *Chem. Phys. Lett.* **2006**, 430, (1-3), 113-116.
17. Liu, D.; Cuddy, M. F.; Fisher, E. R., Comparison of CH, C, CHF, and CF surface reactivities during plasma-enhanced chemical vapor deposition of fluorocarbon films. *ACS Appl. Mater. Interfaces* **2009**, 1, (4), 934-943.
18. Coburn, J. W.; Winters, H. F., The Role of Energetic Ion-Bombardment in Silicon-Fluorine Chemistry. *Nuclear Instrum. Meth. Phys. Res. B* **1987**, 27, (1), 243-248.
19. Oehrlein, G. S.; Williams, H. L., Silicon Etching Mechanisms in a CF/H<sub>2</sub> Glow-Discharge. *J. Appl. Phys.* **1987**, 62, (2), 662-672.
20. Trung, Q.; Durocher, G.; Sauvageau, P.; Sandorfy, C., The emission of the CF<sub>2</sub> radical in a microwave discharge. *Chem. Phys. Lett.* **1977**, 47, (3), 404-407.
21. Stillahn, J.; Trevino, K.; Fisher, E. R., Plasma diagnostics for unraveling process chemistry. *Annu. Rev. Anal. Chem.* **2008**, 1, 261-91. .
22. Harshbarger, W. R.; Porter, R. A.; Miller, T. A.; Norton, P., A study of the optical emission from an rf plasma during semiconductor etching. *Appl. Spectrosc.* **1977**, 31, (3), 201-207.
23. Edelberg, E. A.; Perry, A.; Benjamin, N.; Aydil, E. S., Energy distribution of ions bombarding biased electrodes in high density plasma reactors. *J. Vac. Sci. Technol. A* **1999**, 17, (2), 506-516.
24. Martin, I. T.; Zhou, J.; Fisher, E. R., Correlating ion energies and CF<sub>2</sub> surface production during fluorocarbon plasma processing of Si. *J. Appl. Phys.* **2006**, 100, 013301.
25. King, D. S.; Schenck, P. K.; Stephenson, J. C., Spectroscopy and photophysics of the CF<sub>2</sub> A<sup>1</sup>B<sub>1</sub>--X<sup>1</sup>A<sub>1</sub> system. *J. Mol. Spectrosc.* **1979**, 78, 1-15.
26. McCurdy, P. R.; Bogart, K. H. A.; Dalleska, N. F.; Fisher, E. R., A modified molecular beam instrument for the imaging of radicals interacting with surfaces during plasma processing. *Rev. Sci. Instrum.* **1997**, 68, (4), 1684-1693.
27. Belen, R. J.; Gomez, S.; Kiehlbauch, M.; Aydil, E. S., Feature scale model of Si etching in SF<sub>6</sub>/O<sub>2</sub>/HBr plasma and comparison with experiments. *J. Vac. Sci. Technol. A* **2006**, 24, (2), 350.
28. Allulli, S.; Massucci, M. A.; Tomassini, N., The standard enthalpy of formation of Zr(HPO). *J. Chem. Thermodynamics* **1979**, 11, 613-618.
29. Johnson, G. K., The standard molar enthalpy of formation of SiF<sub>4</sub> at 298.15 K by fluorine bomb calorimetry. *J. Chem. Thermodynamics* **1986**, 18, 801-802.
30. Woo, J.; Kim, G.; Kim, D.; Um, D.; Kim, C., Etch characteristics of ZrO<sub>2</sub> thin films in high density plasma. *Jpn. J. Appl. Phys.* **2009**, 48, (8), 08HD03.
31. Cunge, G.; Booth, J. P., CF<sub>2</sub> production and loss mechanisms in fluorocarbon discharges: fluorine-poor conditions and polymerization. *J. Appl. Phys.* **1999**, 85, (8), 3952.
32. Zhang, D.; Kushner, M. J., Mechanisms for CF<sub>2</sub> radical generation and loss on surfaces in FC plasmas. *J. Vac. Sci. Technol. A* **2000**, 18, 2661.
33. Standaert, T. E. F. M.; Hedlund, C.; Joseph, E. A.; Oehrlein, G. S.; Dalton, T. J., Role of fluorocarbon film formation in the etching of Si, SiO<sub>2</sub>, Si<sub>3</sub>N<sub>4</sub>, and a-SiC:H. *J. Vac. Sci. Technol. A* **2004**, 22, (1), 53-60.

34. Standaert, T. E. F. M.; Matsuo, P. J.; Allen, S. D.; Oehrlein, G. S.; Dalton, T. J., Patterning of fluorine-, hydrogen-, and carbon-containing SiO<sub>2</sub>-like low dielectric constant materials in high-density fluorocarbon plasmas: Comparison with SiO<sub>2</sub>. *J. Vac. Sci. Technol. A* **1999**, 17, (3), 741-748.
35. Woo, J.-C.; Kim, G.-H.; Kim, D.-P.; Um, D.-S.; Kim, C.-I., Improving the Etch Selectivity of ZrO<sub>2</sub> Thin Films over Si by Using High Density Plasma. *Ferroelectrics* **2009**, 384, 47-55.
36. Ju, L.; Dongyi, L.; Sidney, Y.; Reza, N.; Lynne, E., Force-based many-body interatomic potential for ZrC. *J. Appl. Phys.* **2003**, 93, (11), 9072-9085.
37. Rauf, S.; Sparks, T.; Ventzek, P. L. G.; Smirnov, V. V.; Stengach, A. V.; Gaynulin, K. G.; Pavlovsky, V. A., A molecular dynamics investigation of fluorocarbon based layer-by-layer etching of silicon and SiO<sub>2</sub>. *J. Appl. Phys.* **2007**, 101, 033308.

## CHAPTER 4

### CONTRIBUTIONS OF CF AND CF<sub>2</sub> SPECIES TO FLUOROCARBON FILM COMPOSITION AND PROPERTIES FOR C<sub>x</sub>F<sub>y</sub> PLASMA-ENHANCED CHEM- ICAL VAPOR DEPOSITION

This chapter relates the contents of a full paper published in the journal *ACS Applied Materials and Interfaces* by Michael F. Cuddy and Ellen R. Fisher. It explores FC film deposition from a range of plasma precursors and details surface analyses of deposited films. The contributions of CF<sub>n</sub> ( $n = 1, 2$ ) radicals to film properties were probed via gas-phase diagnostics and the IRIS technique. Surface energies of deposited films were calculated and assessed with respect to film fluorine content, and in turn to the plasma gas-surface interactions.

## 4.1. Introduction

FC plasmas are widely used to deposit high quality fluorocarbon films for a range of applications including superhydrophobicity, protective coatings, and biocompatible materials. Specific applications include preparation of ultralow- $k$  materials,<sup>1,2</sup> development of superhydrophobic surfaces<sup>3</sup> and implementation in medical devices such as stents to improve biocompatibility without initiating coagulation.<sup>4-8</sup> Moreover, FC polymers are increasingly utilized in micromachining to alleviate detrimental adhesion in microstructures.<sup>9,10</sup> The utility of fluorocarbons employed in plasma-enhanced chemical vapor deposition (PECVD) is influenced by associated parameters, including applied power ( $P$ ) and system pressure ( $p$ ).<sup>11</sup> Another driving force that dictates the efficacy and nature of FC film deposition is the choice of plasma precursor. Generally, for  $C_xF_y$  systems with low  $y/x$  ratios film deposition is most efficacious.<sup>12</sup> Although much evidence exists that lower  $y/x$  ratio precursors deposit FC films more readily than do high ratio feeds, the precise route toward film deposition (i.e. the phenomena that occur at the gas-surface interface) is poorly understood. The approach we employ attempts to correlate plasma gas-phase diagnostics with plasma-surface interface data to elucidate those processes responsible for FC film characteristics in  $CF_4$ ,  $C_2F_6$ ,  $C_3F_8$ , and  $C_3F_6$  systems ( $y/x$  ranging from 2.0 to 4.0).

Gas-phase neutral species, especially of the form  $CF_n$ , have long been identified with critical functions contributing to FC film deposition.<sup>13,14</sup> Previous work in our group has implicated  $CF_2$  radicals in particular for their role in film formation, as these species are readily produced at the surface of depositing FC films.<sup>15-17</sup> Here, we employed time-resolved optical emission spectroscopy (TR-OES) to investigate the initial

production of  $CF_n$  species through direct decomposition of the  $C_xF_y$  precursor. An understanding of the production of film-initiating and film-propagating species in the gas-phase is of critical importance to determining the efficacy of FC film deposition. In addition, through IRIS experiments, we have garnered new insight into the behavior of these radical species near Si surfaces during substrate processing. The IRIS technique provides a spatially-resolved, two-dimensional, *in-situ* representation of radical-substrate interactions during plasma processing. Via IRIS, we have studied the near-surface phenomena associated with  $CF_n$  radicals produced from a range of  $C_xF_y$  precursors. Coupled with gas-phase diagnostics and surface analyses, we have generated a correlation between choice of precursor, the role of gas-phase species and the net effect of FC film deposition.

A principal application of this understanding lies in tailoring the surface properties of plasma-deposited films. Important materials properties issues with respect to the specific applications include (1) surface composition; (2) surface energy; and (3) mechanical properties (e.g. crosslinking, brittleness, adhesion). Here, we employed XPS analyses of deposited FC films to provide compositional data. Although  $C_xF_y$  systems commonly deposit highly crosslinked films, we have achieved high  $-CF_2-$  content films with low crosslinking and brittleness from hexafluoropropylene oxide (HFPO) and  $C_3F_8$  by careful adjustment of plasma parameters.<sup>15</sup> In addition to chemical composition, the surface energy of a deposited film is an important metric for determining the wettability and adhesive properties of the material.<sup>18, 19</sup> To this extent, we used a somewhat indirect route to estimate surface energies, the Zisman method,<sup>20</sup> that involves a straightforward empirical analysis of liquid contact angles to calculate the critical surface tension of a material. This value is in turn analogous to the surface energy of the material. The rela-

tionships determined here between film composition and physical properties with IRIS data and gas-phase diagnostics provide the basis for film deposition mechanisms in  $C_xF_y$  plasmas.

## 4.2. Results

Representative raw OES spectra are depicted in Fig. 4.1(a) for emission collected from a  $C_3F_8$  plasma with  $P = 150$  W, at  $t = 0, 0.01,$  and  $0.20$  s after plasma ignition. The plots show a conspicuous increase in emission intensity from  $CF_2$   $A^1B_1 \rightarrow X^1A_1$  in the range of 250-400 nm, corresponding to the time dependence of the species production. Less prominently, CF emission lines from the  $B^2\Delta \rightarrow X^2\Pi$  transition around 200 nm also increase in intensity as  $t$  increases to 0.20 s. The absolute intensities of the emission peaks were plotted as a function of  $t$  for both CF and  $CF_2$ , with Fig. 4.1(b) showing a typical plot for  $CF_2$ . Clearly, the relative concentrations of both CF and  $CF_2$  follow a first-order rate dependence, and as such, these plots were fit with a regression in the form of a three-parameter exponential decay proportional to  $e^{-kt}$ , where  $k$  represents the production rate constant for a given species. Calculated values of  $k$  for CF and  $CF_2$  production are illustrated in Figs. 4.1(c) and 4.1(d), respectively, as a function of  $P$  in all the  $C_xF_y$  systems studied. One important observation in both plots is that  $k(CF_n)$  (where  $n = 1$  or  $2$ ) values are very similar for  $CF_n$  production from a broad range of precursors, specifically for  $C_2F_6, C_3F_8,$  and  $C_3F_6$  plasmas. However,  $CF_n$  production from  $CF_4$  plasmas deviates from this trend. In particular,  $k(CF)$  values for  $CF_4$  plasmas are similar to those for all other plasma systems at  $P = 50$  W, but increase over these systems by a factor of four as  $P$  approaches 200 W. In contrast,  $k(CF_2)$  values are consistently an order of magnitude

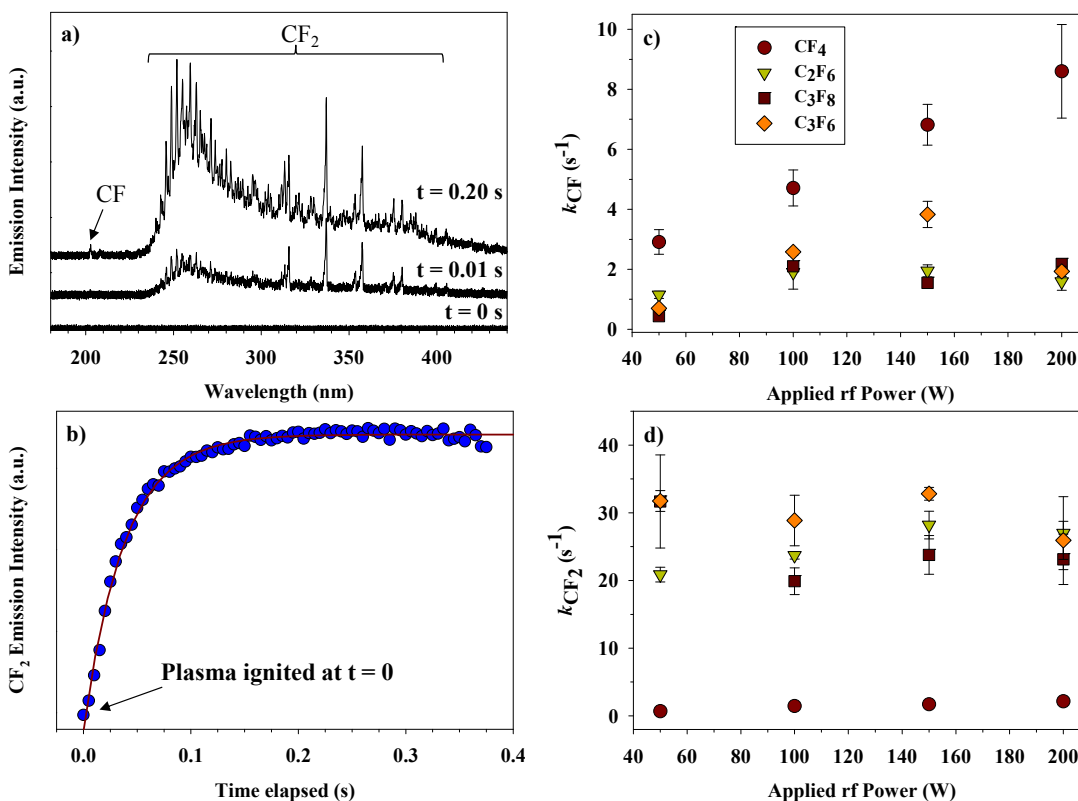


**Figure 4.1.** a) Raw OES spectra collected at  $t = 0$ ,  $0.01$ , and  $0.20$  s after  $C_3F_8$  ( $P = 150$  W) plasma ignition. b)  $CF_2$  emission intensity ( $\lambda = 251.9$  nm) as a function of time from plasma ignition in a  $P = 150$  W  $C_3F_8$  plasma. The exponential fit to these data yields a formation rate constant,  $k(CF_2) = 26.3$   $s^{-1}$ , with  $R^2 > 0.99$ . Rate constants for formation of  $CF$  and  $CF_2$  in  $C_xF_y$  plasmas obtained from time-resolved analyses of the  $\lambda = 202.4$  and  $251.9$  nm OES lines are plotted as functions of  $P$  in c) and d), respectively.

less for  $\text{CF}_4$  plasmas as compared to those values for all other  $\text{C}_x\text{F}_y$  systems at all  $P$ . Another notable trend in these data is that there is no strong dependence of  $k$  on  $P$ , with the sole exception of CF production from  $\text{CF}_4$  plasmas, where, again,  $k(\text{CF})$  essentially directly correlates with increasing applied rf power.

LIF images taken during IRIS experiments are shown in Figs. 4.2(a) and 4.2(b) for CF and  $\text{CF}_2$ , respectively. In each of these schemes, the middle panels depict  $\text{CF}_n$  fluorescence from the molecular beam-only trial, whereas the left-most panels show signal from  $\text{CF}_n$  species both in the plasma beam and scattered from a Si substrate. Image subtraction yields the right image panels that thus depict only scatter of  $\text{CF}_n$ . Cross-sections for the beam-only and scatter images are plotted as a function of distance along the laser axis in the graphs at the far right, and are used to calculate scatter coefficients. For these specific data sets,  $S(\text{CF}) = 0.72$  and  $S(\text{CF}_2) = 0.63$  for radicals in a  $\text{C}_3\text{F}_6$  plasma at  $P = 150$  W. Mean  $S$  values from several different sets of images are plotted as functions of the feed gas  $y/x$  ratio for CF and  $\text{CF}_2$  in Figs. 4.3(a) and 4.3(b), respectively. These figures clearly demonstrate that  $P$  does not have as dramatic an effect on scatter values as does the choice of precursor used for the plasma. For example,  $S(\text{CF}_n)$  values at a given  $y/x$  ratio generally differ by only 0.2-0.4 as a function of  $P$ . As the  $y/x$  ratio increases, a more marked disparity in scatter values appears, accentuated most dramatically by the difference in  $S(\text{CF}_2)$  at  $P = 150$  W for  $y/x = 4.0$ , where  $\Delta S(\text{CF}_2) = 1.2$ , Fig. 4.3(b). Interestingly, both  $S(\text{CF})$  and  $S(\text{CF}_2)$  increase with increasing  $y/x$  ratio of the  $\text{C}_x\text{F}_y$  precursor feed. As the scatter coefficient is essentially a metric of the probability for species scatter, an increase in  $S(\text{CF}_n)$  denotes a decreased propensity for reactivity at a surface.

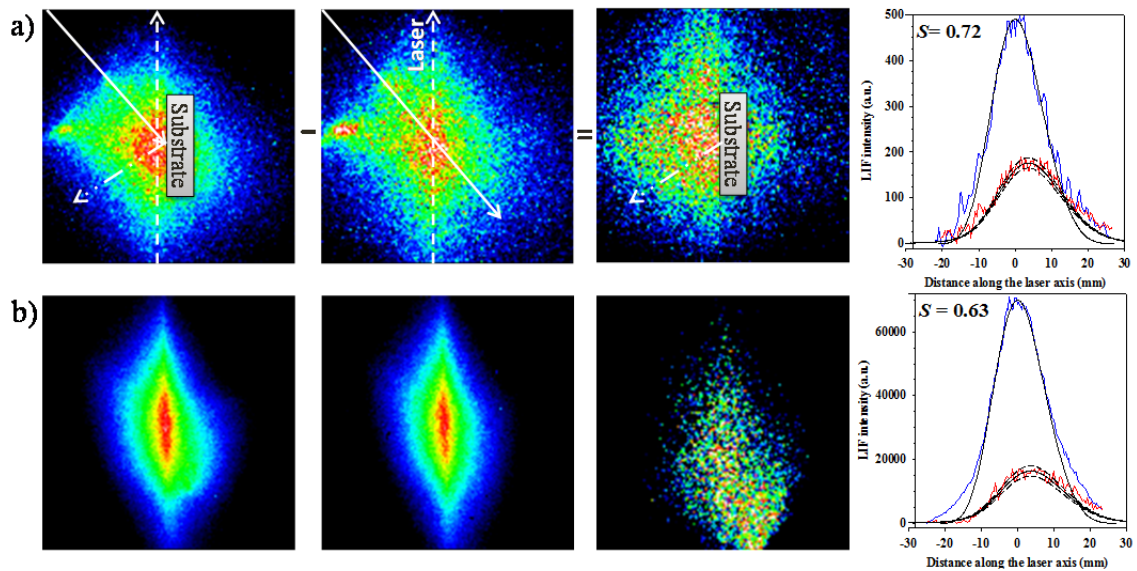


**Figure 4.2.** IRIS images for Si substrate interactions of a) CF, and b) CF<sub>2</sub>, in C<sub>3</sub>F<sub>6</sub> plasma molecular beams at  $P = 150$  W. The left-most images in each set of images were acquired with a substrate rotated into the path of the plasma molecular beam (solid arrow), and thus contain signal from molecules both in the incident beam and scattered (dashed/dotted arrow). The middle panels depict signal arising solely from the plasma molecular beam. The right-most panels are obtained through image subtraction of the previous two images, resulting in signal that corresponds to scattered molecules alone. Cross-sections along the axis of laser propagation are compared to geometric simulations to obtain a scatter coefficient,  $S$ , where  $S(\text{CF}) = 0.72$  and  $S(\text{CF}_2) = 0.63$  for a) and b), respectively.

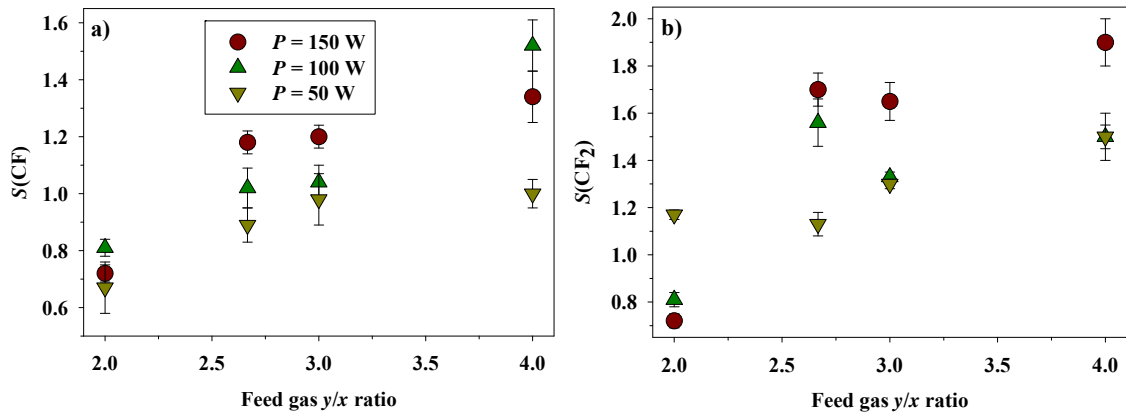


**Figure 4.3.** Scatter coefficients for a) CF and b) CF<sub>2</sub> as a function of C<sub>x</sub>F<sub>y</sub> feed gas y/x ratio at P = 50, 100, and 150 W.

Of particular note is that the  $S$  values ultimately surpass unity, indicating a surface-mediated production mechanism for  $CF_n$  species whereby radicals are generated at a FC-passivated surface. Thus, radical-surface reactions appear to be an important and integral aspect of fluorocarbon plasma processing.

High-resolution  $C_{1s}$  XPS spectra are shown in Fig. 4.4 for films deposited from  $C_xF_y$  precursors during IRIS experiments. Generally, with the exception of films deposited from  $CF_4$  plasmas, the FC films appear to be amorphous,  $CF_2$ -rich, and robust, with several  $\underline{C}-F_x$  binding environments present. Generally, with decreasing  $y/x$  ratio, the FC plasmas appear to tend toward polymerizing systems that favor deposition. This agrees well with the deposition rates calculated for each of these systems, Table 4.1, as the duration of substrate exposure to a plasma source in a typical IRIS experiment is  $\sim 60$  min. Table 4.1 also lists the film F/C ratio, calculated from XPS data, and the percent crosslinking (defined here as the  $\%C-C/C-H + \% \underline{C}-CF_x + \%CF$  in the high resolution XPS spectra),<sup>21</sup> that demonstrate that FC film crosslinking decreases significantly as the  $y/x$  ratio of the precursor decreases. Specifically, with decreasing  $y/x$  ratios, the F/C values for the film approach 2.0, the value expected for a film composed exclusively of  $CF_2$ , and the crosslinking decreases, indicating a depletion of amorphous moieties in the film.

Contact angle values ( $\theta$ ) were used to construct Zisman plots for both deposited fluorocarbon films and bare Si substrates. Here,  $\cos(\theta)$  values were plotted as a function of the surface tension of the liquid droplet used to make the CA measurement, Table 2.3. Figure 4.5 demonstrates Zisman plots for both a Si wafer analyzed prior to plasma processing, and after exposure to  $CF_4$  plasma. These plots are fitted with a linear regression

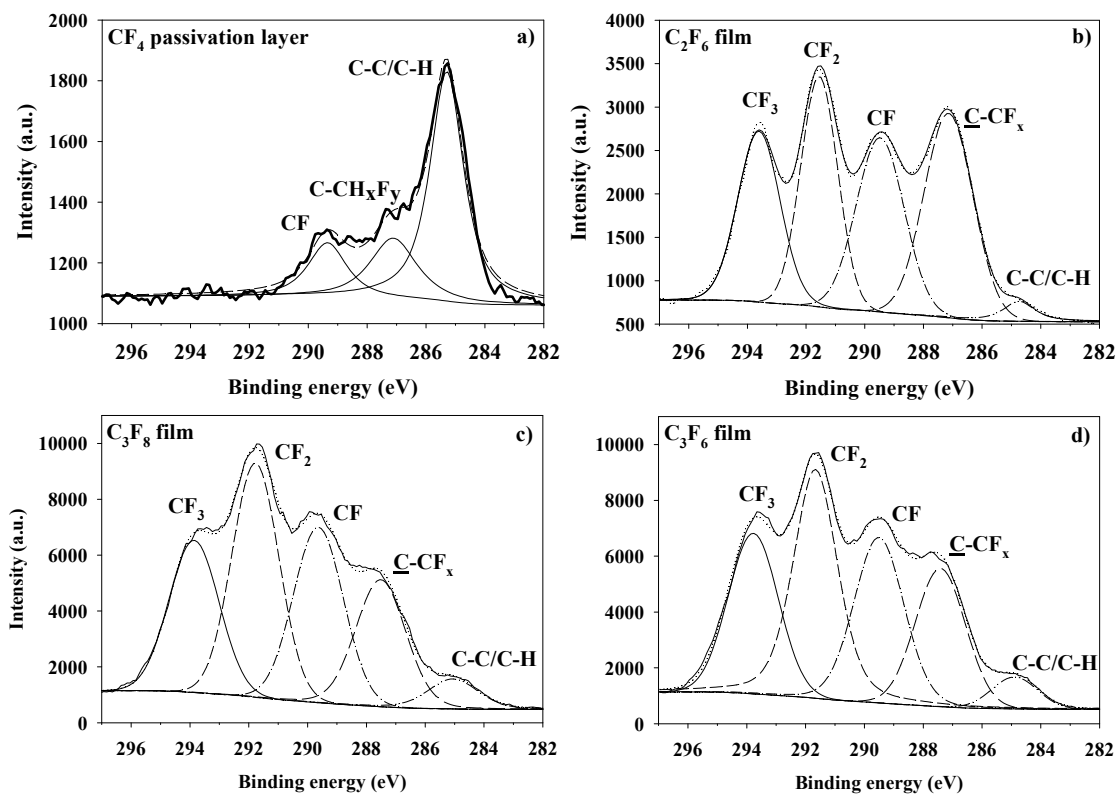


**Figure 4.4.** High-resolution  $C_{1s}$  XPS spectra for fluorocarbon films deposited from a)  $CF_4$ , b)  $C_2F_6$ , c)  $C_3F_8$ , and d)  $C_3F_6$  plasmas. Specific binding environments are labeled accordingly.

**Table 4.1.** Properties of plasma-deposited fluorocarbon films.<sup>a</sup>

<b>PECVD Source</b>	<b>Film F/C ratio</b>	<b>Film % cross-linking</b>	<b><math>\Delta\gamma_c</math> (dyn/cm)</b>	<b>Deposition Rate (nm/min)</b>
CF <sub>4</sub>	0.10(0.02)	N/A <sup>b</sup>	6.1(0.9)	0.12(0.02)
C <sub>2</sub> F <sub>6</sub>	1.0(0.1)	69(3)	23.5(0.5)	1.82(0.02)
C <sub>3</sub> F <sub>8</sub>	1.3(0.1)	49(2)	32.7(0.5)	3.4(0.4)
C <sub>3</sub> F <sub>6</sub>	1.59(0.08)	43(4)	35.2(0.7)	4.2(0.5)

<sup>a</sup>Values in parentheses represent one standard deviation for the measurement. <sup>b</sup>Percent cross-linking values were not determined for CF<sub>4</sub>-deposited films due to the lack of CF<sub>x</sub> binding environments in the high-resolution C<sub>1s</sub> XPS spectra.

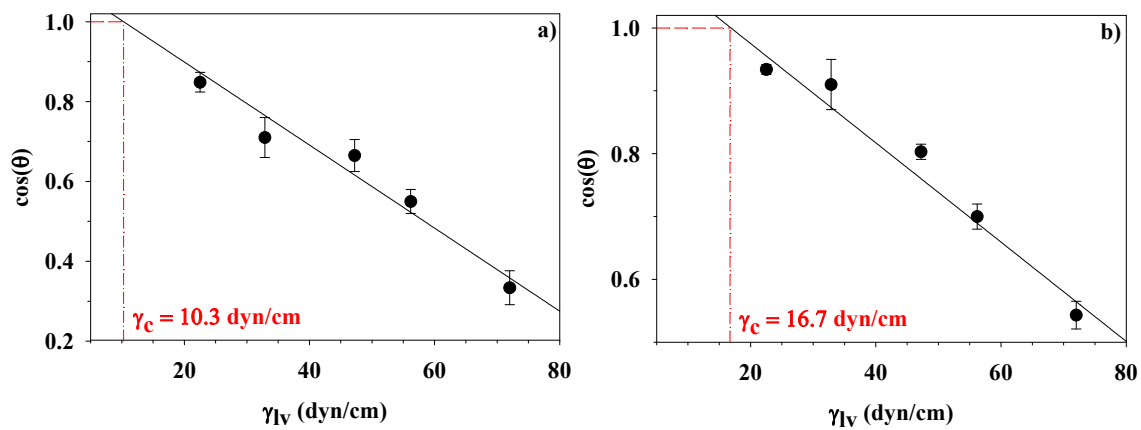


**Figure 4.5.** Zisman plots for a) a bare Si wafer, with critical surface tension of 10.3 dyn  $\text{cm}^{-1}$  and b) a  $\text{CF}_4$  film deposited on Si, with  $\gamma_c = 16.7$  dyn  $\text{cm}^{-1}$ . Best-fit linear regression lines are extrapolated to  $\cos(\theta) = 1$ , where the value  $\gamma_c$  is obtained.

that is extrapolated to  $\cos(\theta) = 1$ , where a hypothetical liquid droplet of the corresponding surface tension would be instantaneously and completely wetting. This value, denoted  $\gamma_c$ , is the critical surface tension,<sup>20</sup> and is analogous to the surface energy ( $\gamma_{sv}$ ) of the substrate or film via the Young equation (4.1), where  $\gamma_{sl}$  represents the interfacial tension at the liquid-surface boundary.

$$\gamma_{sv} = \gamma_{lv}\cos(\theta) + \gamma_{sl} \quad (4.1)$$

To account for underlying substrate effects in the comparisons of surface energies, we report the value  $\Delta\gamma_c$ , which is the difference between the measured  $\gamma_c$  for a deposited FC film and the substrate (e.g. Si wafer) upon which it was deposited. Thus, the  $\Delta\gamma_c$  value measured for the  $\text{CF}_4$ -deposited film illustrated in Fig. 4.5 is 6.4 dyn/cm. Representative  $\Delta\gamma_c$  values are compiled in Table 4.1 for all the  $\text{C}_x\text{F}_y$ -deposited films. Notably, these values generally increase with decreasing  $y/x$  ratios of the feed gas, and, more importantly, with increased fluorine content in the deposited films.

### 4.3. Discussion

Although plasmas are widely employed for substrate processing, including etching and film deposition, the fundamental interfacial interactions that lead to surface modification are often poorly understood. Efforts to more efficiently tailor surface processing techniques require a thorough knowledge of these processes. To this end, FC systems have received much attention, with aims devoted to explicating FC plasma gas-phase species behavior and correlating this behavior with surface phenomena. The scope of investigations into these systems has expanded as FC plasmas have become more widely employed in the fabrication of such market-driven technology as integrated circuits and

semiconductor devices. Here, the roles of  $CF_n$  radical species have been investigated to determine a correlation between gas-phase phenomena and film deposition from  $C_xF_y$  plasma systems.

Optical emission spectroscopy provides an expedient and practical method of gauging the behavior of gas-phase plasma species. We have examined the formation of  $CF^*$  and  $CF_2^*$  in the gas-phase through TR-OES. Production of these species from a given precursor follows first-order processes, whereby rate constants for production are calculated using exponential fits to the TR-OES data. These rate constants reflect the production of  $CF_n^*$  species in the plasma gas-phase but do not distinguish specific mechanisms of formation. Indeed, the complex processes that lead to generation of  $CF_n^*$ , including direct decomposition of the precursor and gas-phase recombination reactions, are inherently incorporated in these  $k$  values. In addition, over a longer duration ( $t \gg 0.3$  s), the apparent steady-state concentration of  $CF_n^*$  species tends to decrease as consumption of the gas-phase species commences via intricate gas-phase reactions or increased dissociation of the fragment in a reactant-starved scenario. Thus, due to the complexity of the system as a whole, we focus here on the initial production of  $CF_n^*$  upon plasma ignition.

The values of these rate constants are largely independent of changing  $P$ , and as such the effect of  $P$  on the efficacy of plasma production of  $CF_n$  can be ignored. The only exception to this is for  $k(CF)$  measured in  $CF_4$  plasmas. In the  $CF_4$  system, the linear correlation between the production rate constants and  $P$  indicates that the power applied to the system is the main driving force for CF production from the precursor. Conversely,  $k(CF_2)$  in  $CF_4$  systems is completely independent of  $P$ , so that the production rate of  $CF_2$  is effectively constant. The value of  $k(CF)$  increases by nearly an order of magnitude

over  $k(\text{CF}_2)$ , Figs. 4.1(c-d), demonstrating that the  $\text{CF}_4$  system favors production of CF species over  $\text{CF}_2$  as  $P$  increases. This appears to be unique to  $\text{CF}_4$  plasmas in comparison to the other  $\text{C}_x\text{F}_y$  systems studied here.

$\text{CF}_2$  gas-phase production also appears to be dependent upon feed gas choice. The  $k(\text{CF}_2)$  values measured in  $\text{CF}_4$  plasmas are essentially an order of magnitude lower than those measured in any of the other  $\text{C}_x\text{F}_y$  systems, Fig. 4.1(d). This indicates that upon ignition of the plasma, a dearth of  $\text{CF}_2$  units exist in  $\text{CF}_4$  as compared to the other plasma systems. Moreover, as  $k(\text{CF}_2)$  values are effectively constant for plasmas with precursor  $y/x$  ratios  $< 4.0$ , we assume there is little variation in initial  $\text{CF}_2$  concentration (i.e.,  $t = 0-0.5$  s after plasma ignition) in these plasma systems. These observations are important in that they suggest a “trickle-down” effect of a lack of  $\text{CF}_2$  in the case of the  $\text{CF}_4$  system. Specifically, gas-phase reactions, such as that depicted in (4.2),



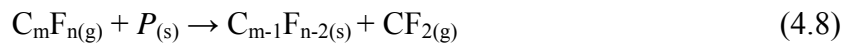
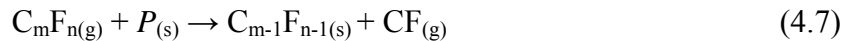
and suggested by Zhang and Kushner,<sup>22</sup> generate oligomeric gas-phase species that are not necessarily formed from direct decomposition of the plasma precursor. The rate constants for such generic reactions at 50 mTorr are generally  $\sim 10^{-13}$  molec<sup>-1</sup>cm<sup>3</sup>s<sup>-1</sup> and are expected to proceed with a third body interaction.<sup>22, 23</sup> Indeed, Gabriel and coworkers speculated that  $\text{C}_2\text{F}_4$  formation was the major loss mechanism of  $\text{CF}_2$  in  $\text{CF}_4$ -based pulsed discharges.<sup>24</sup> These oligomeric units, in conjunction with  $\text{CF}_{2(\text{g})}$  species, are thought to contribute to surface passivation and ultimately film growth at reactor walls and on substrates, reactions (4.3)-(4.6).





Interaction with an activated surface site ( $\text{A}_{(\text{s})}$ ) can proceed to passivate the site ( $\text{P}_{(\text{s})}$ ) and film growth can progress through continued interactions of gas-phase species with  $\text{P}_{(\text{s})}$ , especially propagating FC films through reactions at reactive sites of passivating oligomeric units.<sup>25</sup> Ultimately, the languid production of  $\text{CF}_2$  in  $\text{CF}_4$  plasma systems may conceivably result in a significant discrepancy in FC film deposition efficacy compared to  $\text{C}_2\text{F}_6$ ,  $\text{C}_3\text{F}_8$ , and  $\text{C}_3\text{F}_6$  systems. Indeed, we observe a steep decline in deposition rate as the precursor  $y/x$  ratio approaches 4.0, Table 4.1. FC deposition schemes arising from film growth based upon oligomeric units [i.e. reactions (4.3) and (4.4)] could be of paramount importance in  $\text{C}_3\text{F}_6$  systems. Here, the  $\pi$ -bond can be easily broken under relatively mild plasma conditions to produce a highly reactive and moderately large deposition precursor (i.e.  $\text{C}_3\text{F}_6$  radical).<sup>26</sup> Thus,  $\text{C}_3\text{F}_6$  plasmas ought to facilitate efficient FC film initiation and propagation. Accordingly, this system demonstrates the highest deposition rate of any of the feed gases discussed here, as illustrated in Table 4.1.

In addition to film formation, gas-surface interactions can also promote generation of  $\text{CF}_n$  species at a fluorocarbon-passivated surface site, reactions (4.7) and (4.8). These processes illustrate the gas-phase production of CF or  $\text{CF}_2$  via reactions involving a gas-phase oligomer.  $\text{CF}_n$  species can also interact with a surface without reacting, as in (4.9), effectively adsorbing and then desorbing intact from the surface.



We have monitored the gas-surface interactions that occur in our  $C_xF_y$  systems using the IRIS technique. It is apparent from these data that the choice of precursor strongly influences the propensity for  $CF_n$  surface scatter, as both  $S(CF)$  and  $S(CF_2)$  increase with increased feed gas  $y/x$  ratio, Fig. 4.3. In particular,  $S$  values far surpass unity as the precursor  $y/x$  ratio approaches 4.0, indicating a significant increase in the amount of  $CF_{n(g)}$  produced *at surfaces* during deposition of FC films.

The dependence of  $S$  on precursor choice can be rationalized in a number of ways. Specifically, in the highly depositing systems (those with low  $y/x$  ratios;  $C_3F_6$  and  $C_3F_8$ ), a wealth of reactive species, including oligomers with unpaired electrons, exist in the gas-phase. These include a plethora of species such as  $C_2F_4$ ,  $C_2F_5$ ,  $C_3F_5$ , and  $C_3F_3$ , as verified in our systems by mass spectrometric analyses. Under conditions in which such gas-phase species proliferate, as in the case of low  $y/x$  ratio precursors, recombination with surface-produced  $CF_n$  and subsequent redeposition of the product is plausible. Such a scenario effectively reduces the observed scatter coefficient for  $CF_n$  species by consuming  $CF_n$  produced via reactions (4.7)-(4.9). Refer to Chapter 6 for a more detailed discussion of the contributions of oligomeric species to FC film deposition.

In these scenarios, one must consider the effect of ions as well. Average ion energy  $\langle E_i \rangle$  values in our systems increase significantly with increasing  $y/x$  ratio of the precursor, so that the total average ion energies in the  $CF_4$  plasma system are approximately twice those of the  $C_3F_6$  system. We have previously demonstrated that ion bombardment can be a major contributing factor in surface production of  $CF_2$ , and that  $\langle E_i \rangle$  and  $S$  values correlate linearly.<sup>17,27</sup> Thus, ions may be partially responsible for the rise seen in  $S$  as the plasma precursor  $y/x$  ratio increases. A third contributing factor to consider is the rel-

ative distribution of electronically excited  $CF_n$  states in the plasma gas-phase. Because our IRIS experiments probe only ground state CF or  $CF_2$  radicals, excited species are disregarded. Especially with CF surface interactions, however, the electronic excited states appear to have a strong influence on the observed  $S(CF)$  value. Using OES, we generally observe increasing relative concentrations of excited  $CF(^2\Delta)$  with increasing precursor  $y/x$  ratios, concomitant with significantly increased vibrational temperatures (see Chapter 5). We speculate that the  $CF(^2\Delta)$  quenches upon interaction with the surface. Unfortunately, this excited state is inaccessible using our current IRIS apparatus due to wavelength limitations. The relatively high vibrational energy associated with the molecule assists it in overcoming a barrier of desorption to re-enter the gas-phase as a ground state  $CF(^2\Pi)$  radical, detectable in our LIF scheme. This particular scenario is exacerbated as the plasma precursor  $y/x$  ratio increases, making it a potential contribution to the increase in observed  $S(CF)$ .

The net effect of gas-surface interactions can be gauged by analyzing the deposited FC film. It is clear from high-resolution  $C_{1s}$  XPS analyses of substrates processed in IRIS experiments that  $CF_4$  plasmas generally do not deposit a robust FC film as compared to the other  $C_xF_y$  systems. Note that the difference in substrate processing times among different  $C_xF_y$  precursors in IRIS experiments was negligible, such that the duration of plasma exposure corresponding to each spectrum in Fig. 4.4 was essentially identical. Thus, the disparity in  $CF_4$  film deposition is thought to result from a combination of the comparative *lack* of formation of film-forming or film-propagating units in the gas-phase of the  $CF_4$  system and the effect of ion bombardment on passivating FC films. These data complement the idea that  $CF_4$  plasmas are generally considered highly profi-

cient etching systems. As the  $y/x$  ratio of the plasma system decreases from 4.0, the FC films tend to become less crosslinked and the films' fluorine content increases, indicating a higher degree of incorporation of  $CF_2$  species (Table 4.1). These increases in film fluorine content are concomitant with increases in film surface energy,  $\Delta\gamma_c$ . Notably, this correlation is linear, Fig. 4.6(a), where  $\Delta\gamma_c$  values are plotted as a function of the corresponding film F/C ratio. These data were collected for films deposited in independent plasma reactors, not in the IRIS apparatus, at a range of plasma conditions, and include data for each of the  $C_xF_y$  precursors. Although this relationship would seem to imply that the surface energy is dependent upon the potential of interaction and that increasing fluorine content increases the film potential, this is not the case. Indeed, Zisman was among the first to report there is effectively no difference in potential of interaction of  $C-F_x$  and  $C-H_x$  species in contact angle experiments.<sup>28</sup> Thus, the relationship between fluorine content and surface energy is related to the packing efficiency of propagating units in the FC film.<sup>28,29</sup> Specifically, the contact angle of a liquid droplet is dependent upon the molar volume of C-X (where X = C, H, or F) with which it comes in contact. Zisman suggests that surfaces rich in  $-CF_n-$  linkages are likely to give rise to high surface energies.<sup>28</sup> As such, the move toward higher  $\Delta\gamma_c$  and increased fluorine content in the film could indicate a greater extent of surface coverage of  $CF_n$  moieties.

Though the  $\Delta\gamma_c$  values reported here tend to be higher than those values reported in the literature for FC films,<sup>30,31</sup> we expect the general trends observed here to be valid. One possible contributing factor to the apparently high surface energy values may lie in the method used for investigation. The variability in contact angles with decreasing

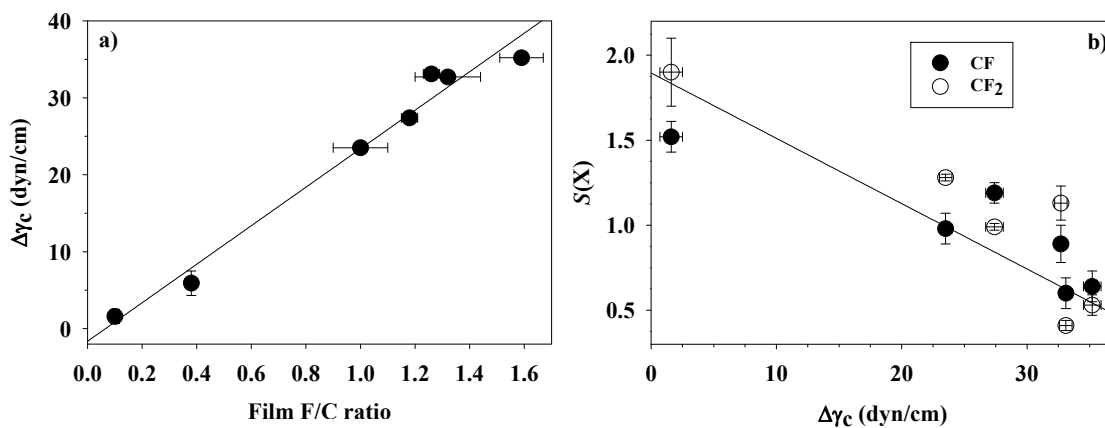


**Figure 4.6.** a)  $\Delta\gamma_c$  values plotted as a function of film fluorine to carbon ratios (obtained from XPS analyses) fitted with a linear regression where  $R^2 = 0.98$ . b) Scatter coefficients,  $S(\text{CF})$  and  $S(\text{CF}_2)$ , plotted as a function of  $\Delta\gamma_c$ , with a linear fit with  $R^2 = 0.80$ .

surface tension of the contact droplet (i.e. higher relative concentration of methanol:water) becomes much more significant as the droplet more completely wets the FC film and results are generally skewed toward higher CA values. As such, the extrapolated fit to CA data yield results of a higher surface energy. Despite these discrepancies, the shift toward higher surface energy with increased CF<sub>2</sub> content in the FC film is reasonable.

Generally, FC films deposited on Si wafers tend to be smooth and relatively defect-free, as confirmed by SEM and AFM analyses, Fig. 4.7(a-b). It is of interest, however, to gauge whether the phenomena associated with  $\Delta\gamma_c$  are dependent upon surface roughness. To this end, C<sub>3</sub>F<sub>6</sub> films were deposited on supported Fe<sub>2</sub>O<sub>3</sub> nanoparticle surfaces.<sup>32</sup> Values for rms roughness were calculated for 2500  $\mu\text{m}^2$  areas on both FC-coated and uncoated Fe<sub>2</sub>O<sub>3</sub> substrates. The deposition of a FC film on Fe<sub>2</sub>O<sub>3</sub> nanoparticles (rms roughness =  $0.84 \pm 0.05 \mu\text{m}$ , Fig. 4(c)) resulted in a slight decrease in surface roughness over uncoated particles (rms roughness =  $1.05 \pm 0.09 \mu\text{m}$ ). These roughness factors are nevertheless significantly higher than the rms roughness of a FC film on a flat Si substrate,  $\sim 0.01 \mu\text{m}$ , Fig. 4.7(b). Despite these differences in roughness, the morphology of the surface appears to have limited influence over the calculated value of  $\Delta\gamma_c$ . Specifically, the surface energy of a C<sub>3</sub>F<sub>6</sub>-deposited film on Fe<sub>2</sub>O<sub>3</sub> nanoparticles was calculated as  $31.9 \pm 0.6 \text{ dyn/cm}$ , compared to  $35.9 \pm 0.5 \text{ dyn/cm}$  for the same type of FC film on a Si substrate.

The surface energies of deposited FC films have also been related to observed scatter coefficients for CF and CF<sub>2</sub>, as shown in Fig. 4.6(b). Here, the indirect

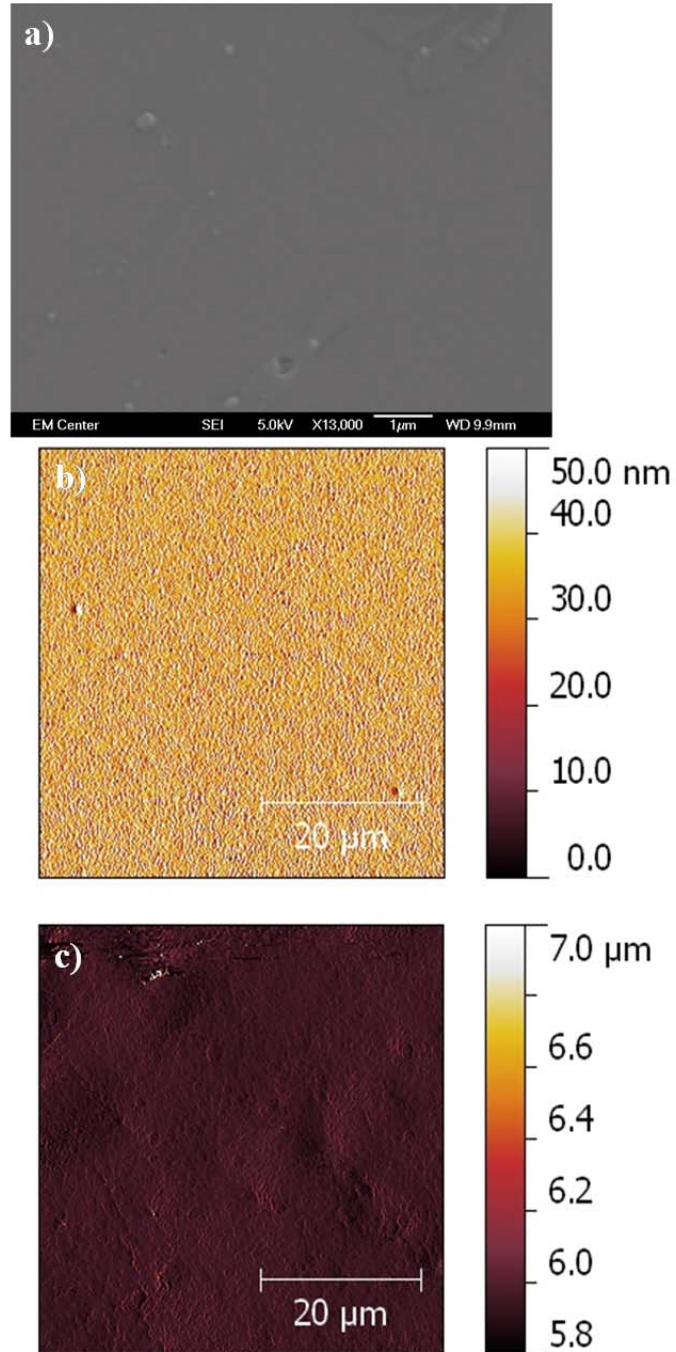


**Fig. 4.7.** a) SEM micrograph of FC film on Si deposited from  $C_2F_6$  in the IRIS experiment. The image is shown at 13000x magnification and is representative of FC films deposited from other precursors. b) AFM micrograph for  $C_3F_6$ -deposited film on Si with rms surface roughness = 11.4 nm. c) AFM micrograph for  $C_3F_6$ -deposited film on  $Fe_2O_3$  nanoparticles, with rms surface roughness = 989 nm.

relationship between  $S$  and  $\Delta\gamma_c$  suggests that there exists a net balance between the processes that drive these two measures. On one hand, a low  $\Delta\gamma_c$  and high scatter coefficient could indicate a loss of surface  $-\text{CF}_n-$  via those processes that induce large surface scatter, as discussed above. Alternatively, a dearth of scatter-inducing processes where  $S$  is low may render the film relatively unaffected, resulting in a larger  $\Delta\gamma_c$  due to a larger surface concentration of  $-\text{CF}_n-$ . The dichotomous nature of this relationship, whether  $\Delta\gamma_c$  increases because  $S$  decreases, or vice versa, is a point of ongoing consideration in our laboratory. Ultimately, the ability to tailor surface properties of deposited films via choice of plasma precursor promises to impact a wide range of applications. Some examples include the reduction of membrane fouling by membrane modification to low surface energy<sup>33</sup> or modification to high surface energy materials for use in biologically compatible implants.<sup>34</sup>

#### 4.4. Summary

Appropriate precursor selection is a critical element for further advancement of applications employing plasma-deposited fluorocarbon films. As demonstrated here, efficacy of film deposition is strongly dependent on the  $\text{C}_x\text{F}_y$  source, stemming largely from gas-phase phenomena that drive the formation of depositing units. Specifically, recombination reactions that generate oligomeric deposition precursors are significantly limited in  $\text{C}_x\text{F}_y$  with  $y/x > 3$ . The behavior of species at the depositing interface appears to dictate the resulting surface characteristics of deposited FC films, especially the surface energy. Moreover, the  $y/x$  ratio of the precursor directly affects the amount of fluorine incorporation in a deposited film, and film fluorine content, in turn, influences the arrangement of

$\text{-CF}_n\text{-}$  moieties at the surface. The combination of gas-phase diagnostics such as TR-OES, gas-surface interface data obtained via our IRIS technique, and surface analyses including XPS and contact angle measurements provide significant insight into the molecular-level mechanisms at the core of film deposition in fluorocarbon plasmas. The ability to appropriately select the appropriate plasma precursor, in addition to other plasma parameters, makes it possible to tailor the surface properties of a deposited film, thereby creating specific high performance materials for a range of applications.

#### 4.5. Supplemental Information

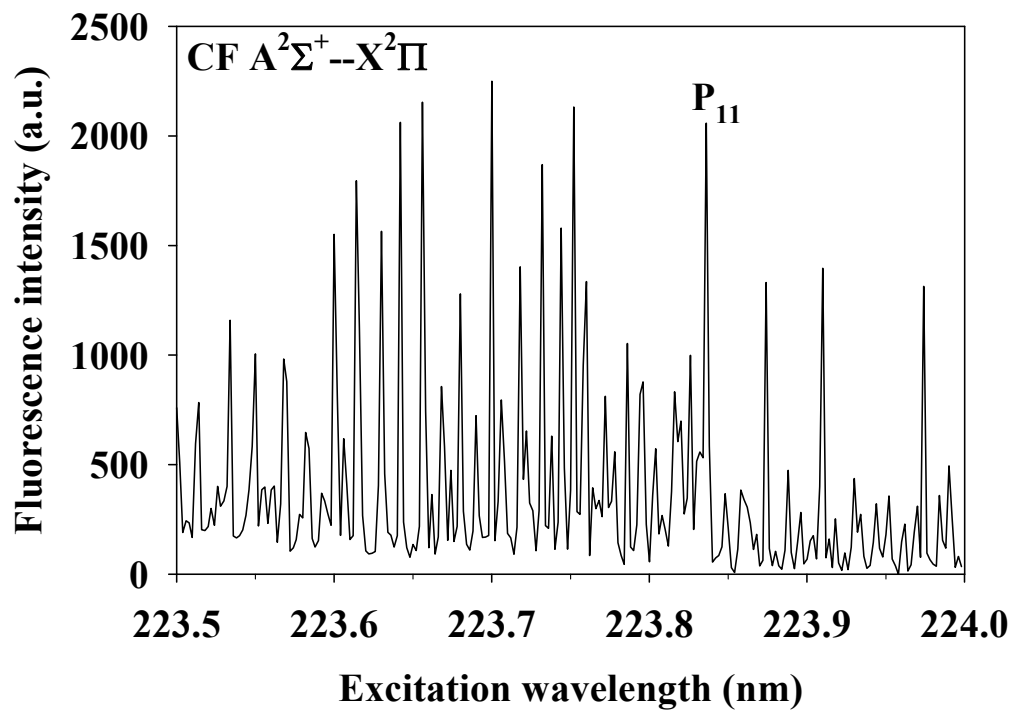


**Figure 4.8.** LIF excitation spectrum for CF in a C<sub>3</sub>F<sub>6</sub> plasma with  $P = 150$  W. The P<sub>11</sub> bandhead for the A<sup>2</sup>Σ<sup>+</sup>(1)←X<sup>2</sup>Π(0) transition is labeled and represents the on-resonance wavelength used for CF IRIS experiments.

#### 4.6. References

1. Ludvik, M.; Daniel, P., Plasma deposition of optical films and coatings: A review. *J. Vac. Sci. Technol. A* **2000**, 18, (6), 2619-2645.
2. Jin, Y.; Ajmera, P. K.; Lee, G. S.; Singh, V., Ultralow-k silicon containing fluorocarbon films prepared by plasma-enhanced chemical vapor deposition. *J. Electron. Mater.* **2005**, 34, (9), 1193-1205.
3. Feng, L.; Li, S.; Li, Y.; Li, H.; Zhang, L.; Zhai, J.; Song, Y.; Liu, B.; Jiang, L.; Zhu, D., Super-Hydrophobic Surfaces: From Natural to Artificial. *Adv. Mater.* **2002**, 14, (24), 1857-1860.
4. Haïdopoulos, M.; Turgeon, S.; Laroche, G.; Mantovani, D., Chemical and Morphological Characterization of Ultra-Thin Fluorocarbon Plasma-Polymer Deposition on 316 Stainless Steel Substrates: A First Step Toward the Improvement of the Long-Term Safety of Coated-Stents. *Plasma Process. Polym.* **2005**, 2, (5), 424-440.
5. Nelea, V.; Holvoet, S.; Turgeon, S.; Mantovani, D., Deposition of fluorocarbon thin films on outer and inner surfaces of stainless steel mini-tubes by pulsed plasma polymerization for stents. *J. Phys. D: Appl. Phys.* **2009**, 42, (22), 225208.
6. Lewis, F.; Cloutier, M.; Chevallier, P.; Turgeon, S.; Pireaux, J.-J.; Tatoulian, M.; Mantovani, D., Influence of the 316 L Stainless Steel Interface on the Stability and Barrier Properties of Plasma Fluorocarbon Films. *ACS Appl. Mater. Interfaces* **2011**, 3, (7), 2323-2331.
7. Lewis, F.; Horny, P.; Hale, P.; Turgeon, S.; Tatoulian, M.; Mantovani, D., Study of the adhesion of thin plasma fluorocarbon coatings resisting plastic deformation for stent applications. *J. Phys. D: Appl. Phys.* **2008**, 41, (4), 045310.
8. Shuwu, W.; Gupta, A. S.; Sagnella, S.; Barendt, P. M.; Kottke-Marchant, K.; Marchant, R. E., Biomimetic Fluorocarbon Surfactant Polymers Reduce Platelet Adhesion on PTFE/ePTFE Surfaces. *J. Biomat. Sci.-Polym. E.* **2009**, 20, (5/6), 619-635.
9. Smith, B. K.; Sniegowski, J. J.; LaVigne, G.; Brown, C., Thin Teflon-like films for eliminating adhesion in released polysilicon microstructures. *Sensor Actuat. A: Phys.* **1998**, 70, (1-2), 159-163.
10. Wiedemair, J.; Balu, B.; Moon, J.-S.; Hess, D. W.; Mizaikoff, B.; Kranz, C., Plasma-Deposited Fluorocarbon Films: Insulation Material for Microelectrodes and Combined Atomic Force Microscopy/Scanning Electrochemical Microscopy Probes. *Anal. Chem.* **2008**, 80, (13), 5260-5265.
11. d'Agostino, R., *Plasma Deposition, Treatment, and Etching of Polymers*. Academic Press, Inc.: San Diego, 1990.
12. Biederman, H., *Plasma Polymer Films*. Imperial College Press: London, 2004.
13. Haverlag, M.; Stoffels, E.; Stoffels, W. W.; Kroesen, G. M. W.; Hoog, F. J. d., Measurements of radical densities in radio-frequency fluorocarbon plasmas using infrared absorption spectroscopy. *J. Vac. Sci. Technol. A* **1994**, 12, (6), 3102-3108.
14. Cicala, G.; Milella, A.; Palumbo, F.; Rossini, P.; Favia, P.; d'Agostino, R., Nanostructure and Composition Control of Fluorocarbon Films from Modulated Tetrafluoroethylene Plasmas. *Macromolecules* **2002**, 35, (24), 8920-8922.

15. Martin, I. T.; Malkov, G. S.; Butoi, C. I.; Fisher, E. R., Comparison of pulsed and downstream deposition of fluorocarbon materials from C<sub>3</sub>F<sub>8</sub> and c-C<sub>4</sub>F<sub>8</sub> plasmas. *J. Vac. Sci. Technol. A* **2004**, 22, (2), 227-235.
16. Liu, D.; Fisher, E. R., Surface interactions of C<sub>3</sub> radicals during the deposition of fluorocarbon and hydrocarbon films. *J. Vac. Sci. Technol. A* **2007**, 25, (6), 1519-1523.
17. Cuddy, M. F.; Fisher, E. R., Investigation of the roles of gas-phase CF<sub>2</sub> molecules and F atoms during fluorocarbon plasma processing of Si and ZrO<sub>2</sub> substrates. *J. Appl. Phys.* **2010**, 108, (3), 033303.
18. Owens, D. K.; Wendt, R. C., Estimation of the surface free energy of polymers. *J. Appl. Polym. Sci.* **1969**, 13, (8), 1741-1747.
19. Johnson, K. L.; Kendall, K.; Roberts, A. D., Surface Energy and the Contact of Elastic Solids. *P. Roy. Soc. A-Math. Phys.* **1971**, 324, (1558), 301-313.
20. Fox, H. W.; Zisman, W. A., The spreading of liquids on low energy surfaces. I. polytetrafluoroethylene. *J. Colloid Sci.* **1950**, 5, (6), 514-531.
21. Luginbuhl, R.; Garrison, M. D.; Overney, R. M.; Weiss, L.; Schieferdecker, H.; Hild, S.; Ratner, B. D., *Fluorinated Surfaces, Coatings, and Films*. American Chemical Society: Washington, D.C., 2001.
22. Zhang, D.; Kushner, M. J., Mechanisms for CF<sub>2</sub> radical generation and loss on surfaces in fluorocarbon plasmas. *J. Vac. Sci. Technol. A* **2000**, 18, (6), 2661-2668.
23. Plumb, I. C.; Ryan, K. R., A model of the chemical processes occurring in CF<sub>4</sub>/O<sub>2</sub> discharges used in plasma etching. *Plasma Chem. Plasma Process.* **1986**, 6, (3), 205-230.
24. Gabriel, O.; Stepanov, S.; Meichsner, J., Transient and stable species kinetics in pulsed cc-rf CF<sub>4</sub>/H<sub>2</sub> plasmas and their relation to surface processes. *J. Phys. D: Appl. Phys.* **2007**, 40, (23), 7383.
25. Booth, J. P.; Cunge, G.; Chabert, P.; Sadeghi, N., CF<sub>x</sub> radical production and loss in a CF<sub>4</sub> reactive ion etching plasma: Fluorine rich conditions. *J. Appl. Phys.* **1999**, 85, (6), 3097-3107.
26. Leezenberg, P. B.; Reiley, T. C.; Tyndall, G. W., Plasma induced copolymerization of hexafluoropropylene and octafluoropropane. *J. Vac. Sci. Technol. A* **1999**, 17, (1), 275-281.
27. Martin, I. T.; Zhou, J.; Fisher, E. R., Correlating ion energies and CF<sub>2</sub> surface production during fluorocarbon plasma processing of silicon. *J. Appl. Phys.* **2006**, 100, (1), 013301.
28. Zisman, W. A., Relation of the Equilibrium Contact Angle to Liquid and Solid Constitution. In *Contact Angle, Wettability, and Adhesion*, American Chemical Society: Washington, DC, 1964; Vol. 43, pp 1-51.
29. Hoernschemeyer, D., The Relationship of Contact Angles to the Composition and Morphology of the Surface. *J. Phys. Chem.* **1966**, 70, (8), 2628-2633.
30. Zhuang, Y. X.; Menon, A., Wettability and thermal stability of fluorocarbon films deposited by deep reactive ion etching. *J. Vac. Sci. Technol. A* **2005**, 23, (3), 434-439.
31. Scholberg, H. M.; Guenther, R. A.; Coon, R. I., Surface Chemistry of Fluorocarbons and their Derivatives. *J. Phys. Chem.* **1953**, 57, (9), 923-925.

32. Shearer, J. C.; Fisher, E. R., Enhancing Surface Functionality of Supported Fe<sub>2</sub>O<sub>3</sub> Nanoparticles using Pulsed Plasma Deposition of Allyl Alcohol. *Nanosci. Nanotechnol. Lett.* **2012**, 4, 358-363.
33. Hamza, A.; Pham, V. A.; Matsuura, T.; Santerre, J. P., Development of membranes with low surface energy to reduce the fouling in ultrafiltration applications. *J. Membrane Sci.* **1997**, 131, (1-2), 217-227.
34. Baier, R. E., The role of surface energy in thrombogenesis. *Bull. NY Acad. Med.* **1972**, 48, (2), 257-272.
35. Vazquez, G.; Alvarez, E.; Navaza, J. M., Surface Tension of Alcohol Water + Water from 20 to 50 .degree.C. *J. Chem. Eng. Data* **1995**, 40, (3), 611-614.

## CHAPTER 5

### ENERGY PARTITIONING IN DIATOMIC RADICALS AND ITS INFLUENCE ON SURFACE SCATTER COEFFICIENTS FOR NO, SiF, AND CF IN INDUC- TIVELY COUPLED PLASMAS

This chapter concerns energy partitioning for molecules formed from several plasma systems, from a manuscript prepared for the *Journal of Physical Chemistry* by Michael F. Cuddy and Ellen R. Fisher. Specifically, it addresses NO in nitric oxide plasmas, SiF in tetrafluorosilane plasmas, and CF in tetrafluoromethane and hexafluoroethane plasmas. The data reported for  $\Theta_V(\text{CF})$  and  $\Theta_V(\text{SiF})$ ,  $\Theta_R(\text{CF})$ , and surface scattering coefficients,  $S$ , for NO and CF were collected and analyzed by Michael F. Cuddy. These data have been combined with previously reported data for  $S(\text{SiF})$ ,  $\Theta_T(\text{SiF})$  and  $\Theta_R(\text{SiF})$ , in order to broaden the scope of the chapter. Dr. C. I. Butoi, Ms. M. M. Morgan, Dr. K. L. Williams, and Dr. J. Zhang have contributed to this work. The following seeks to connect and generalize surface interaction phenomena discussed in previous chapters with the distribution and magnitude of internal energies of vibration and rotation for radical diatoms. Supplementary information for characteristic  $\text{CF}_2$  temperatures is provided in Appendix B.

## 5.1. Introduction

An understanding of how energy is dispersed into rotational, vibrational, and translational modes of a particular gas-phase molecule by means of plasma-stimulated decomposition of a precursor lends critical insight into molecule formation mechanisms, decomposition pathways, and overall plasma chemistry. Knowledge of internal energies, including vibrational ( $\Theta_V$ ) and rotational ( $\Theta_R$ ) temperatures, is applicable to estimates of neutral gas temperatures and plasma modeling.<sup>1</sup> Moreover, information gleaned from internal temperatures can elucidate the processes that dictate the overall character of the plasma, as the values are dependent upon such attributes as species densities, electron temperatures, formation reactions, and gas-phase and surface collisions of plasma species, among others.<sup>2</sup>

Non-thermal inductively coupled plasmas (ICPs) generally comprise molecules that follow a classical relationship wherein  $\Theta_V$  is nominally greater than  $\Theta_R$  and translational ( $\Theta_T$ ) temperature, yet each temperature remains significantly less than the characteristic electron temperature ( $T_e$ ) of the plasma.<sup>3,4</sup> Notably,  $\Theta_R$  values have long been employed as a measure of the neutral gas temperature of the plasma,<sup>5-8</sup> with the assumption that rotational and collective translational temperatures of the gas equilibrate within the plasma.<sup>9</sup> Although this estimate may be appropriate for analyses of the internal temperatures of actinometers, the Fisher group has previously demonstrated that significant differences exist between  $\Theta_R$  and  $\Theta_T$  for species such as the silyldidyne (SiH) radical in silane plasmas.<sup>10-12</sup> Furthermore, different radicals in the same plasma system often exhibit distinct internal temperatures, as has been shown for SiF and SiF<sub>2</sub> molecules in tetrafluorosilane systems.<sup>13</sup> In addition, the same type of plasma species may be formed via different mechanisms, including direct gas-phase decomposition of a monomer gas or

recombination reactions in the plasma reactor. Thus, it is useful to explicitly examine the effect of formation pathway on internal temperatures and surface reactivity of plasma species.

Of burgeoning interest is the correlation between internal energies and species behavior at surfaces. Our unique imaging of radicals interacting with surfaces (IRIS) technique affords us the capability of monitoring *in situ* both the internal energies of selected plasma species and the propensity of such molecules to react at the surface of a specific substrate. In particular, the surface scattering coefficient,  $S$ , for a given molecule can be calculated, that provides a measure of the likelihood of scattering to occur. Given that the full range of plasma species is incident on the substrate during these measurements, efforts have also sought to separate the effects arising from different types of species. For example, highly energetic plasma species, such as ions, can play an important role in determining  $S$  values for molecules such as  $\text{CF}_2$  in fluorocarbon (FC) plasmas,<sup>14</sup>  $\text{SF}_2$  in  $\text{SiF}_4$  systems,<sup>15,16</sup> and  $\text{SiCl}_2$  in  $\text{SiCl}_4$  plasmas.<sup>17</sup> In addition, the Fisher group has previously illustrated the relationship between  $S$  and  $\Theta_R$  for systems including the  $\text{SiF}$  molecule.<sup>16</sup> Nonetheless, we have not as yet offered a complete investigation into the interplay of the internal energies,  $\Theta_R$  and  $\Theta_V$ , and translational energies,  $\Theta_T$ , of molecules and their impact on observed  $S$  values. Thus, this Chapter aims to understand the effect of energy dissipation among various degrees of freedom in a particular molecule and whether different types of energy impact how the molecule behaves when interacting with a surface. Ultimately, the goal would be to predict surface behavior of a molecule given the distribution of internal energies or the reverse.

Several spectroscopic techniques have been used to measure internal temperatures of plasma species, including broadband absorption spectroscopy (BAS),<sup>18</sup> Doppler broadening analysis of spectral lines,<sup>19</sup> optical emission spectroscopy (OES),<sup>20</sup> and laser-induced fluorescence (LIF) spectroscopy.<sup>21</sup> Of these, the latter two are exploited for their simplicity of use and the complementary information that can be obtained through excited and ground state species spectral analyses. Here is offered an approach toward understanding the energetic and surface interactions of plasma species that behave similarly with respect to the relationships between internal temperatures and surface reactivity using OES and LIF. Specifically, this Chapter examines NO radicals produced from 100% nitric oxide plasmas, CF from CF<sub>4</sub>, C<sub>2</sub>F<sub>6</sub>, C<sub>3</sub>F<sub>8</sub>, and C<sub>3</sub>F<sub>6</sub> plasmas, and SiF from tetrafluorosilane ICPs. Each radical has the same ground- and first-excited state symmetry, and each demonstrates a comparable relationship between  $\Theta_v$  and  $S$ . These radicals have been extensively studied in the literature<sup>1,18,20,22-25</sup> and in our laboratories,<sup>12,13,15,16,26</sup> yet a concise illustration of the effect of internal temperatures on surface scattering coefficients has been conspicuously absent. Thus, our current line of inquiry represents a comprehensive investigation of the internal energies of diatomic molecules exhibiting a strong relationship between surface scattering coefficients measured during plasma processing events and vibrational energy.

## 5.2. Results

Vibrational temperature data were acquired from OES data as described previously<sup>26,27</sup> and modeled using LIFbase or pGopher. A section of a typical experimental OES spectrum for an NO plasma is shown in Figure 5.1 along with simulated data assuming

$\Theta_v = 1405$  K. The simulation shown represents the maximized peak correlation between the experimental data and the simulated fit.<sup>26</sup> Peaks that appear in the experimental data but not the simulated spectrum arise from the NO  $C^2\Pi-X^2\Pi$  and  $D^2\Sigma^+-X^2\Pi$  transitions, that are fit separately using the same temperature as for the  $A^2\Sigma^+-X^2\Pi$  transition. Note that these values may not be representative of the actual  $\Theta_v$  for the C and D excited states as their branches extend well beyond the spectral region in Figure 5.1. The quantum efficiency of the detector varies by only  $\sim 5\%$  over the simulated wavelength range, and as such, variations were not accounted for in the simulation. Similar procedures were used to determine  $\Theta_v$  for excited states of all three molecules, with the resulting values listed in Tables 5.1-5.3.

$\Theta_v$  values were also calculated for NO in its ground electronic state, Table 5.3, from LIF excitation spectra. These vibrational temperatures tend to increase with  $P$  in the same manner as  $\Theta_v(^2\Pi)$ , although the absolute temperatures are generally significantly lower, Fig. 5.2. The correlation coefficient of the two data sets depicted in Figure 5.2 is 0.89, indicating a strong relationship between ground and excited electronic state vibrational temperatures.

As noted in the Introduction, there is significant interest in the fundamental effects, if any, of internal energy on surface interactions of plasma radicals during plasma surface modification. Thus, IRIS experiments have been performed for all three radicals studied here, with some of the scatter coefficients having been reported previously.<sup>15,28</sup> LIF images and IRIS cross-sections are shown in Figure 5.3 for NO radicals in a 100%

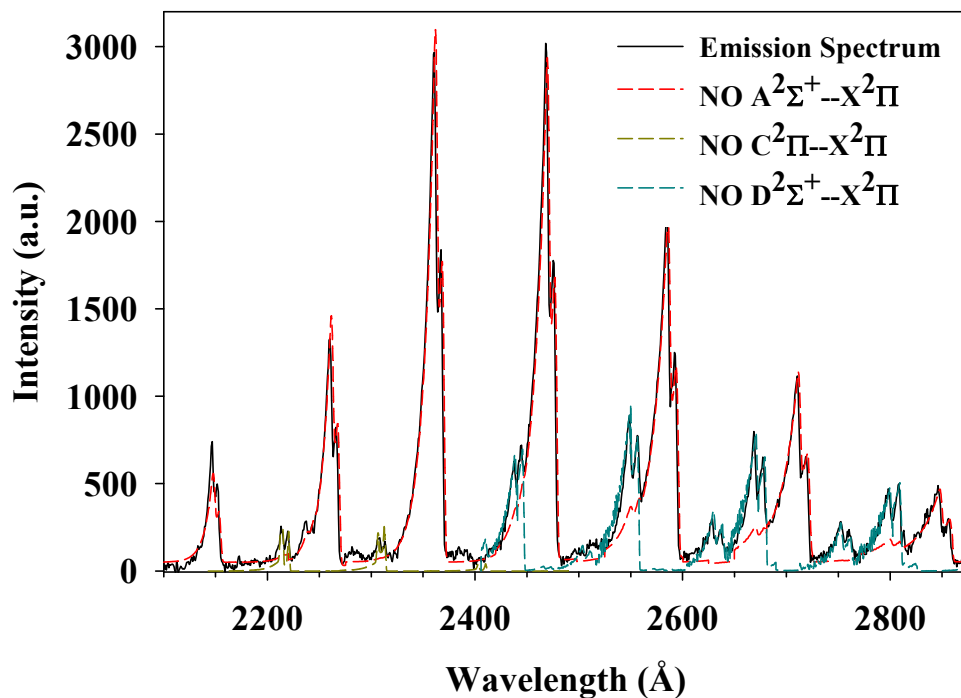


**Figure 5.1.** Raw OES data (solid line) corresponding to the  $A^2\Sigma^+ \rightarrow X^2\Pi$  emission for NO in a 100% NO plasma ( $P = 25$  W). The red dashed line represents a simulated fit to the data, with  $\Theta_V = 1405$  K. Notable overlap from NO  $C^2\Pi \rightarrow X^2\Pi$  and  $D^2\Sigma^+ \rightarrow X^2\Pi$  transitions is also included in the simulation (simulated at 1405 K).

**Table 5.1.** Scatter coefficients and  $\Theta_T$ ,  $\Theta_V$ , and  $\Theta_R$  for SiF in SiF<sub>4</sub> plasmas.<sup>†</sup>

<b><i>P</i> (W)</b>	<b><i>S</i> (SiF)</b>	<b><math>\Theta_T</math> (K)</b>	<b><math>\Theta_V</math> (K)</b>	<b><math>\Theta_R</math> (K)</b>
20	0.21(0.14)			
40	0.43(0.14)			
80	0.79(0.13)	571(180)	1813(63)	
100		598(85)	1842(18)	~450
130		802(88)	1962(13)	
170	1.20(0.13)	831(120)	1947(10)	
200		869(54)	2073(25)	

<sup>†</sup>Values for  $\Theta_V$ (SiF) are reported here for the first time.  $S$ (SiF),  $\Theta_T$ (SiF), and  $\Theta_R$ (SiF) values were previously reported in references 13, 15, and 16.

**Table 5.2.** Scatter coefficients and  $\Theta_V$  and  $\Theta_R$  for NO in 100% NO plasmas ( $p = 100$  mTorr).<sup>†</sup>

$P$ (W)	$S$ (NO), Si	$S$ (NO), Pt	$\Theta_V$ (K), $X^2\Pi$	$\Theta_V$ (K), $A^2\Sigma^+$	$\Theta_R$ (K)
50	0.27(.04)	0.21(0.08)	412(40)	1455(23)	337(29)
100	0.66(.06)	0.67(0.07)	510(60)	1533(25)	330(26)
150	1.10(0.05)	1.05(0.08)	477(65)	1674(33)	317(17)
200	1.57(0.07)	1.75(0.12)	528(37)	1740(42)	

<sup>†</sup> $S$ (NO) and  $\Theta_V(X^2\Pi)$  values are published here for the first time. All other data were previously reported in reference 26.

**Table 5.3.** Scatter coefficients and  $\Theta_V$  and  $\Theta_R$  for CF in several fluorocarbon plasmas.<sup>†</sup>

Source	<i>P</i> (W)	<i>S</i> (CF)	$\Theta_V$ (K)	$\Theta_R$ (K)
CF <sub>4</sub>	50	0.90(0.10)	3259(40)	313(14)
	100	1.52(0.09)	3373(51)	309(14)
	150	1.34(0.09)	3304(31)	317(7)
C <sub>2</sub> F <sub>6</sub>	50	0.98(0.09)	2935(23)	298(2)
	100	1.04(0.06)	2948(17)	298(2)
	150	1.17(0.10)	3029(16)	317(10)
C <sub>3</sub> F <sub>8</sub>	50	0.90(0.10)	2950(38)	~300
	100	1.02(0.06)	2940(23)	
	150	1.18(0.04)	3183(29)	
C <sub>3</sub> F <sub>6</sub>	50	0.74(0.06)	2842(19)	~300
	100	0.75(0.09)	2700(8)	
	150	0.64(0.09)	2732(10)	

<sup>†</sup>*S*(CF) data were previously reported in reference 28. All other data are shown here for the first time.

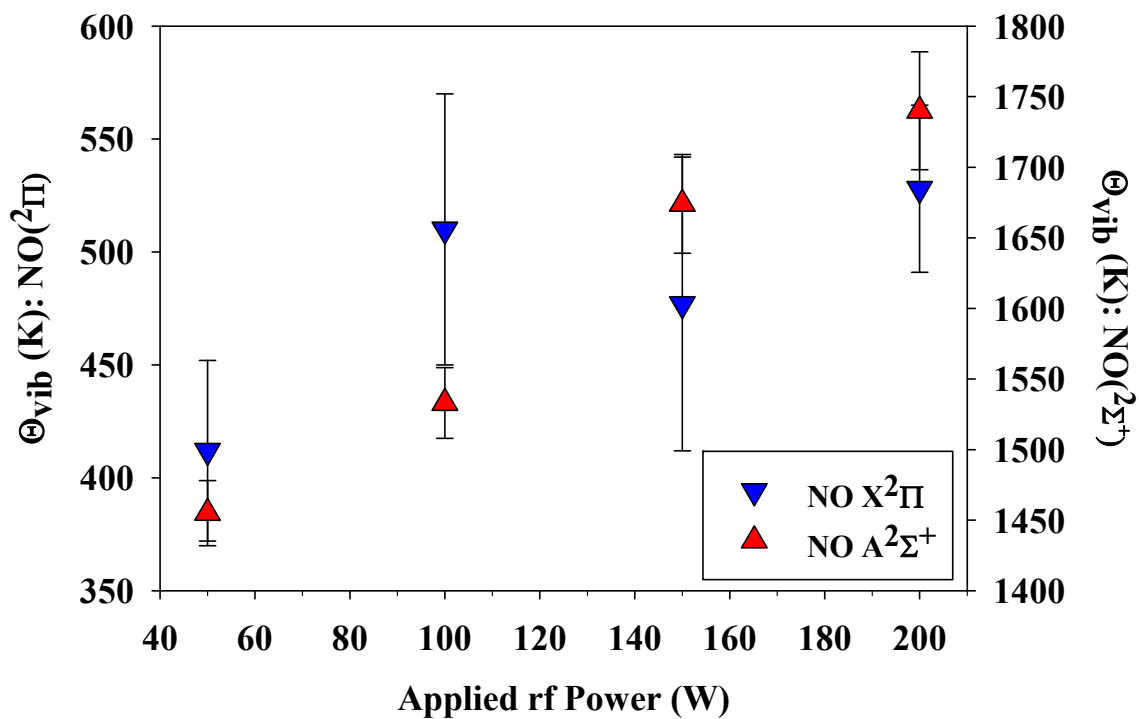


**Figure 5.2.** Comparison of ground state (left ordinate axis) and excited state (right ordinate axis) NO vibrational temperatures for 100% NO plasmas as a function of  $P$ . The correlation coefficient of the two data sets is 0.89.

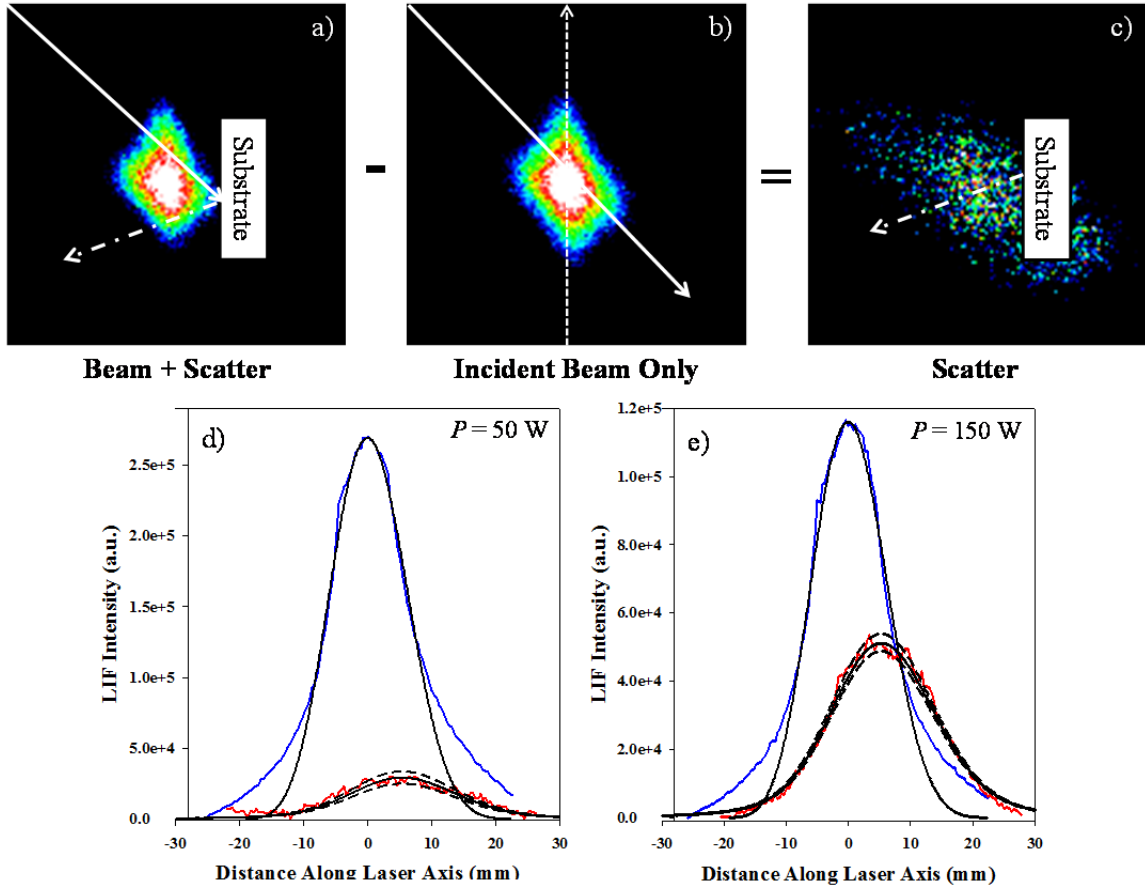


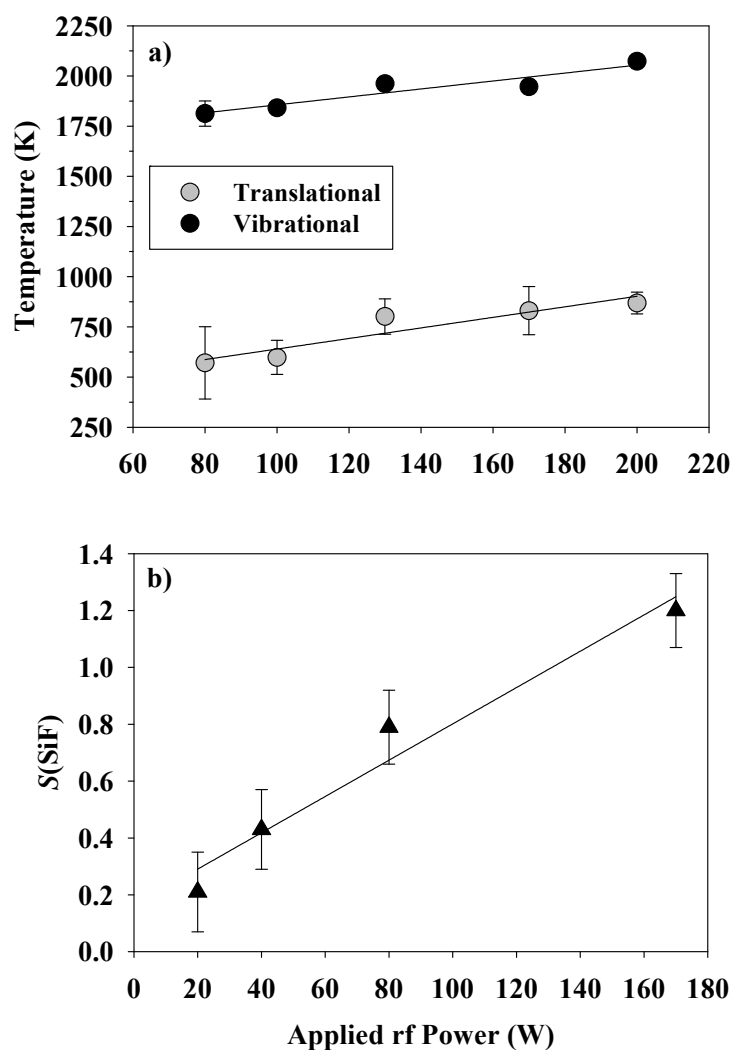
**Figure 5.3.** a-c) IRIS images for NO species in a 100% NO plasma with  $P = 50$  W. The solid white arrow indicates propagation of the plasma molecular beam, whereas the dashed arrow represents NO molecules scattering specularly from the Si substrate. Image a) corresponds to fluorescence signal collected from both NO in the plasma beam and NO scattered from the substrate (i.e. Si wafer) rotated into the path of the molecular beam. Image b) represents NO signal arising only from the plasma molecular beam (i.e. no substrate), where laser propagation is denoted by the thin dotted arrow. Image subtraction yields c) that contains only signal for scattered NO molecules. Cross-sections for NO LIF signals in the plasma molecular beam and NO scattered from a Si substrate are shown for d)  $P = 50$  W and e)  $P = 150$  W. The simulated fits to the data correspond to  $S(\text{NO}) = 0.27$  and  $S(\text{NO}) = 1.10$ , respectively.

NO plasma molecular beam. An image containing only fluorescence from NO in the molecular beam, Fig. 5.3(b), is subtracted from an image showing LIF for NO in the beam and scattered from a substrate, Fig. 5.3(a), to produce a spot corresponding to NO scatter alone, Fig. 5.3(c). Cross-sections along the laser propagation axis are compared to simulated data to extract  $S$  values, where  $S(\text{NO}) = 0.27$  and  $1.10$  for  $P = 50$  and  $150$  W, Fig. 5.3(d) and 5.3(e), respectively. Similar data were collected and calculations performed to measure both  $S(\text{CF})$  and  $S(\text{SiF})$ .

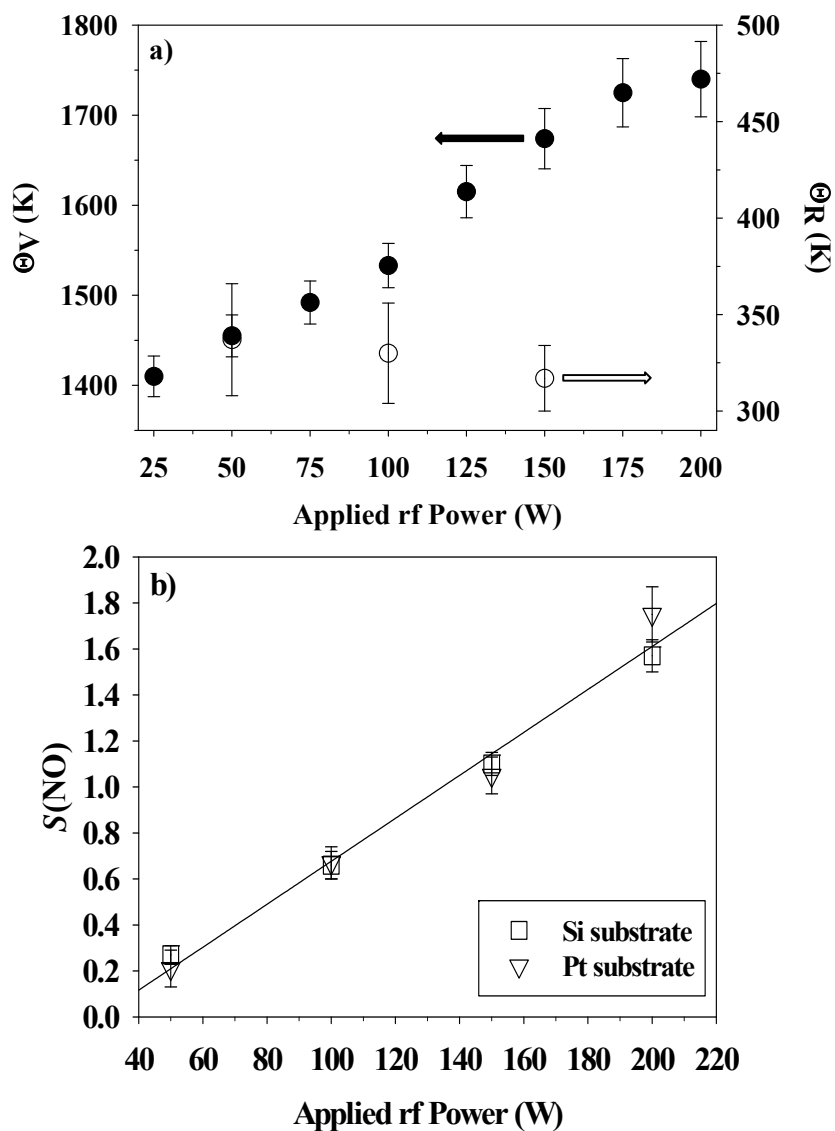
A comparison of SiF characteristic temperatures,  $\Theta_{\text{T}}$  and  $\Theta_{\text{V}}$ , is provided in Fig. 5.4(a), where the temperature values are plotted as a function of  $P$ . Vibrational temperatures are consistently about three times greater than the translational temperatures at all  $P$ , illustrated by nearly parallel linear fits to each data set where the slope  $m = 2.6 \pm 0.6$  and  $2.0 \pm 0.4$  for  $\Theta_{\text{T}}$  and  $\Theta_{\text{V}}$  respectively. Scatter coefficients for SiF are provided in Fig. 5.4(b). Note that both the characteristic temperatures and  $S$  values for SiF species increase with increasing  $P$ .

Figure 5.5(a) illustrates the dependence of  $\Theta_{\text{R}}(\text{NO})$  and  $\Theta_{\text{V}}(\text{NO})$  on  $P$ . Rotational temperatures (right ordinate axis) are essentially unchanging over the  $P$  range 50-150 W (see also Table 5.2), whereas vibrational temperatures increase to an apparent plateau at  $P > 150$  W. Because  $\Theta_{\text{V}}(^2\Pi)$  is strongly correlated with  $\Theta_{\text{V}}(^2\Sigma^+)$  for NO, Fig. 5.2, the trends depicted in Fig. 5.5(a) for excited state vibrational temperatures should be representative of ground state species behavior, as well.  $S(\text{NO})$  values increase essentially linearly with increased  $P$ , Fig. 5.5(b).

The relationship between scatter coefficients and vibrational temperatures for CF



**Figure 5.4.** a)  $\Theta_T$  and  $\Theta_V$  plotted as a function of  $P$  for SiF species in a SiF<sub>4</sub> plasma. b) Scatter coefficients for SiF interacting with Si substrates plotted as a function of  $P$ . The linear regression fit to this data yields a slope  $m = 0.0064 \pm 0.0009$  with  $R^2 = 0.96$ .



**Figure 5.5.** a)  $\Theta_V$  and  $\Theta_R$  plotted as a function of  $P$  for NO species in a 100% NO plasma. b) Scatter coefficients for NO interacting with Si and Pt substrates plotted as a function of  $P$ . The linear regression fit to this data yields a slope  $m = 0.0087 \pm 0.0003$  with  $R^2 = 0.99$ .

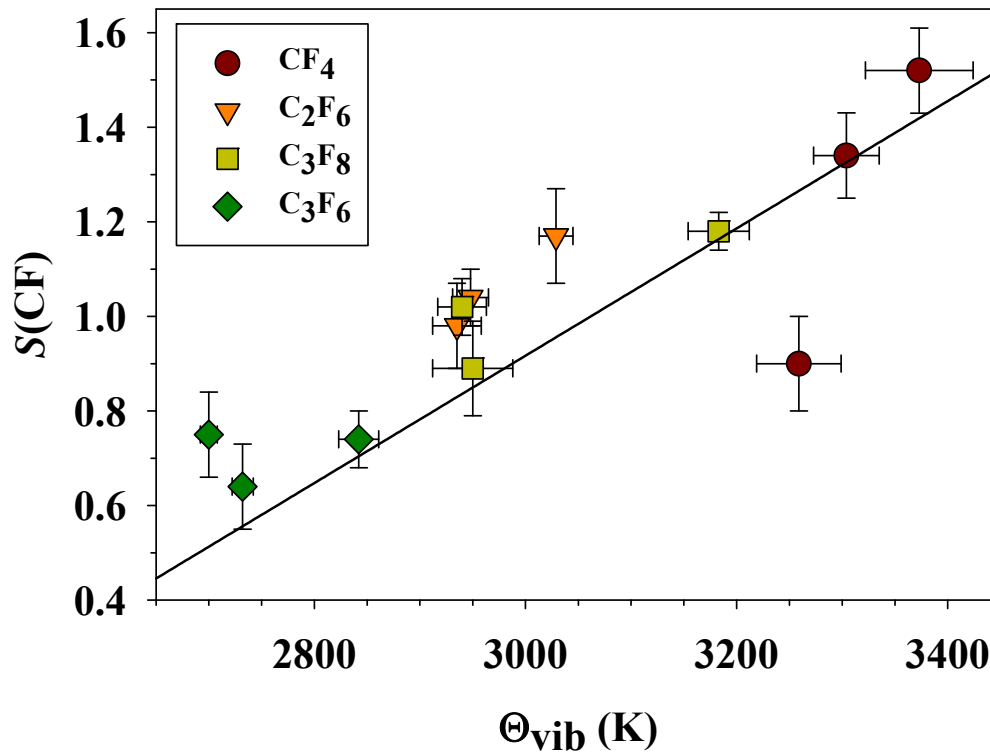


**Figure 5.6.**  $S(\text{CF})$  plotted as a function of  $\Theta_{\text{v}}$  for CF species in  $\text{CF}_4$ ,  $\text{C}_2\text{F}_6$ ,  $\text{C}_3\text{F}_8$ , and  $\text{C}_3\text{F}_6$  plasmas. The linear regression fit to this data yields a slope  $m = 0.0013 \pm 0.0002$  with  $R^2 > 0.8$ .

are shown directly in Fig. 5.6, where  $S(\text{CF})$  is plotted as a function of  $\Theta_{\text{V}}(^2\Delta \text{CF})$  for radicals formed in four different FC plasmas. Each data point represents a discrete set of plasma conditions. A linear fit is provided for the collective data, indicating that  $\text{CF}(^2\Pi)$  scatter is directly related to the vibrational temperature of excited state species.

### 5.3. Discussion

As observed in the Introduction, the compilation of data on energy partitioning and surface interactions for plasma species is important to a molecular-level understanding of plasma chemistry. The goal with this work was to compare energy partitioning and surface scattering coefficients for three diatomic molecules, SiF, NO, and CF in ICPs. Here, new data are reported for  $\Theta_{\text{V}}(\text{SiF})$ ,  $\Theta_{\text{V}}(\text{NO}, ^2\Pi)$ ,  $\Theta_{\text{V}}(\text{CF})$ ,  $\Theta_{\text{R}}(\text{CF})$ , and surface scattering coefficients,  $S$ , for NO and CF. These new data have been combined with data previously reported for  $S(\text{SiF})$ ,  $\Theta_{\text{T}}(\text{SiF})$  and  $\Theta_{\text{R}}(\text{SiF})$ ,<sup>13,15,16</sup> along with  $\Theta_{\text{V}}(^2\Sigma^+)$  and  $\Theta_{\text{R}}$  values for NO.<sup>26</sup> All of these data are provided in Tables 5.1-5.3.

As the IRIS experiment measures scatter coefficients for ground state radicals, this work has attempted to compare the vibrational temperatures for different electronic states of NO, Fig. 5.2, by employing both LIF and OES spectroscopic techniques as an avenue to determine  $\Theta_{\text{V}}$ . Although the NO  $\Theta_{\text{V}}(^2\Pi)$  values are consistently less than  $\Theta_{\text{V}}(^2\Sigma^+)$ , the two NO electronic states follow essentially the same trend with respect to  $P$ . Thus, we use the trends in the excited electronic state of NO as representations of the ground state species behavior. This renders comparison of OES and LIF data feasible. Results for similar experiments examining CF in  $\text{C}_3\text{F}_6$  systems complement these data, demonstrating that a similar  $P$  dependence is followed both by ground CF radicals and

electronically excited  $^2\Delta$  CF. Specifically,  $\Theta_V(^2\Pi)$  for CF radicals in  $C_3F_6$  plasmas ranged from 5030-5206 K over the  $P$  range 50-150 W. Inevitable overlap in the CF excitation spectrum with  $CF_2$  signal contributes to these high  $\Theta_V(^2\Pi)$  values; nonetheless, the data adhere to the same trends observed for  $\Theta_V(^2\Delta)$ , with a correlation coefficient of 0.93.

Focusing first on the energy partitioning between  $\Theta_T$ ,  $\Theta_V$ , and  $\Theta_R$  for each gas-phase molecule, Tables 5.1-5.3, some interesting trends emerge. Notably,  $\Theta_V$  for all three molecules is significantly higher than  $\Theta_R$  or  $\Theta_T$ , regardless of the experimental parameters. In general,  $\Theta_R$  for each molecule is independent of  $P$ , and is approximately room temperature for both  $NO^{26}$  and CF, indicating that the plasma temperatures of these two systems are not appreciably greater than the ambient temperature. Rotational relaxation is a relatively fast process, typically requiring  $<10$  collisions to reach equilibrium;<sup>29</sup> it is estimated that a given diatomic molecule in our plasma reactor experiences  $>100$  collisions per second. The  $\Theta_R(SiF)$  values were slightly higher, at around 450 K, yet were still independent of  $P$ ,<sup>13</sup> indicating the plasma gas temperature is significantly higher for  $SiF_4$  systems than in fluorocarbon or NO plasmas.

Translational temperatures for plasma species in our laboratory are determined from velocity measurements obtained from incrementally increasing the gate delay on the IRIS ICCD camera as described previously.<sup>10,13</sup> These measurements necessarily require a sufficiently long radiative lifetime ( $\tau_r$ ) to allow accurate determination of  $\Theta_T$ . Of the three molecules studied here, SiF ( $\tau_r = \sim 230$  ns)<sup>30</sup> is the only one for which  $\Theta_T$  can be determined accurately. Translational and vibrational temperatures for SiF molecules as a function of applied rf power ( $P$ ) are shown in Figure 5.4(a). Best-fit regression lines for each set of data are essentially parallel to each other, indicating each characteristic tem-

perature has a similar dependence on  $P$ . Although these related rates of temperature rise with increasing  $P$  are notable, another clear observation is that the translational temperatures are in all cases less than half the measured  $\Theta_V(\text{SiF})$  values. This likely indicates that the vibrational-translational (V-T) energy transfer mechanism is the predominant pathway for vibrational relaxation of  $\text{SiF}^*$ . Specifically, the translational energies of  $\text{SiF}$  may be increased through collisions with  $\text{SiF}^*$  that transfer vibrational energy from the electronically excited molecule to the ground state radical. Alternatively, interactions of  $\text{SiF}^*$  with other gaseous species (M) may lead to loss of vibrational energy to M and electronic quenching of  $\text{SiF}^*$  as in reaction (5.1). A similar relaxation pathway is expected to



exist for the diatomic oscillators NO and CF, although non-adiabatic energy transfer processes are speculated to participate in relaxation of NO through NO-NO collisions.<sup>31,32</sup>

The relationship between applied rf power and  $\Theta_V$  can be explored further for each of the three radicals.  $\Theta_V(\text{SiF})$  increases from 1813 K to 2073 K as  $P$  is increased from 80-200 W, Table 5.1. Both ground and electronically excited  $\Theta_V(\text{NO})$  increase with increasing  $P$ , following a near linear trend, especially over the range  $P = 25$ -175 W, with  $\Theta_V$  rising from  $\sim 1400$  K to  $\sim 1750$  K for the  $^2\Sigma^+$  state of NO, Fig. 5.5(a). In the FC plasma systems,  $\Theta_V(\text{CF})$  also generally increases with  $P$ , Table 5.3, although the increase is not as pronounced as for NO plasmas. Thus, partitioning of energy in SiF, NO, and CF appears to favor vibrational channels, as  $\Theta_V$  values are much greater than  $\Theta_T$  or  $\Theta_R$  and they tend to increase with increased  $P$ .

One additional piece of data that helps characterize energy partitioning among vibrational modes in plasmas is the role of electrons. Electron temperatures,  $T_e$ , were es-

estimated for selected plasma systems from analyses of OES spectral lines (see Appendix A). This calculation necessarily involves the assumptions that (1) all ionization and excitation events proceed via electron impact and (2) that there exists a Maxwellian distribution of electron energies. Assumption (1) is valid for dilute Ar in a low pressure plasma, however, assumption (2) is jeopardized due to the Druyvestyn distribution of electron energies common in plasma systems. Nonetheless, for sufficiently low electron temperatures, the deviation of Druyvestyn distributions from Maxwell distributions is small and there is little discrepancy in the measured  $T_e$ . Indeed, comparison to the literature suggests that the values measured for the fluorocarbon plasmas discussed herein are comparable to those measured using an *in situ* Langmuir probe in similar systems.<sup>33</sup>

The mean  $T_e$  values and standard deviations are listed in Table 5.4 for CF<sub>4</sub>, C<sub>2</sub>F<sub>6</sub>, NO, and SiF<sub>4</sub> plasmas at  $P = 50$ -175 W. The values in Table 5.4 indicate that  $T_e$  does not differ appreciably among the four plasma systems, nor does the electron temperature appear to depend strongly on  $P$  over the range studied here. These observations suggest that  $T_e$  does not have a strong influence on  $\Theta_V$ . One reason for this is that  $\Theta_V$  values measured from OES data depend upon excited vibrational state densities,  $n_v$ , and the vibrational excitation rate constant  $k_v$ , via equation (5.2),<sup>34</sup>

$$n_v = n_e n_g k_v \quad (5.2)$$

where  $n_e$  denotes the electron density in the plasma and  $n_g$  the ground vibrational state density. The rate constant  $k_v$  is, in turn, highly dependent upon  $T_e$ .<sup>35</sup> Because  $T_e$  does not change appreciably among systems or with changing  $P$  ( $\Delta T_e < \sim 10\%$  for  $P = 50$ -150 W),

**Table 5.4.**  $T_e$  (in eV) calculated from Ar emission lines for selected plasma systems. Values in parentheses represent standard error calculated from the mean of three trials.

Applied rf Power (W)	CF <sub>4</sub> plasma $T_e$	C <sub>2</sub> F <sub>6</sub> plasma $T_e$	NO plasma $T_e$	SiF <sub>4</sub> plasma $T_e$
50	1.82(0.02)	1.92(0.02)	1.90(0.05)	
75	1.86(0.02)	1.82(0.02)	1.91(0.05)	1.91(0.02)
100	1.85(0.02)	1.87(0.02)	1.88(0.04)	1.82(0.02)
125	1.92(0.03)	1.92(0.02)	1.89(0.04)	1.93(0.02)
150	2.03(0.03)	1.96(0.02)	1.87(0.04)	1.89(0.02)

the increases in  $\Theta_V$  for a given molecule with increasing  $P$  are predominantly a consequence of increased electron density and not electron temperature. This notion is bolstered by the results of Kim *et al.*, who demonstrated that although  $n_e$  correlates directly with  $P$  in  $\text{CF}_4$  inductively coupled plasmas,  $T_e$  remains independent of rf power.<sup>36</sup> Furthermore, Ono and Teii showed that  $\text{N}_2$  vibrational temperatures increase with increasing  $n_e$  in  $\text{CO}_2/\text{N}_2/\text{He}$  discharges.<sup>37</sup> It can thus be inferred that increases in  $\Theta_V$  are proportional to increases in  $n_e$  in each case discussed here, thereby providing a metric for monitoring  $n_e$  *ex situ*, independent of a Langmuir probe.

The second aspect of this work measures surface scattering coefficients during plasma processing using the IRIS technique. This technique is used to probe steady-state processes occurring at the plasma-surface interface. As such, it measures the interface behavior of species interacting with a substrate or film deposited on a substrate. The plasmas chosen for this study each have different effects on surfaces. Specifically,  $\text{SiF}_4$  plasmas tend to fluorinate surfaces (especially Si), whereas nitric oxide plasmas induce oxidation in Si surfaces; fluorocarbon plasmas are the only system of the three to deposit robust films. The net effect of plasma processing on surfaces has been verified through high-resolution XPS analyses.<sup>15,26,28,38,39</sup>

$\text{SiF}$  scatter coefficients measured in  $\text{SiF}_4/\text{Si}$  systems vary directly with increased  $P$ , with a linear fit of slope  $0.0064 \pm 0.0009$ , Fig. 5.4(b), and these changes in  $S(\text{SiF})$  are commensurate with similar trends in both  $\Theta_T(\text{SiF})$  and  $\Theta_V(\text{SiF})$  values, Fig. 5.4(a). It should be noted, however, that other plasma species, such as ions, can contribute to increasing  $S$  values. The Fisher group has demonstrated in other ICP systems that energetic ions contribute significantly to surface production of radicals. For example, surface pro-

duction of both SiF<sub>2</sub> in SiF<sub>4</sub> and CF<sub>2</sub> in FC systems is enhanced by high ion densities in these plasmas.<sup>14,15,39</sup> The effect of ion contributions to the observed scatter coefficient was examined for SiF in SiF<sub>4</sub> plasmas at  $P = 175$  W by employing a grounded mesh.<sup>15,16</sup> In an essentially ion-free environment, the  $S(\text{SiF})$  value decreased only slightly. This small change upon removal of ions relative to the strong correlation between  $\Theta_{\text{v}}(\text{SiF})$  and  $S(\text{SiF})$  indicates that ions do not play as significant a role in the surface production of SiF as does the vibrational temperature. Ion contributions to scatter of SiF may be limited because of the tendency for the moiety to remain “buried” in the fluorinated silicon substrate. Oehrlein and coworkers showed through reactive ion etching experiments that SiF species dominate the deepest regions of a fluorosilane film, whereas the topmost layers of the film are SiF<sub>3</sub>-rich.<sup>40</sup> Thus, if reactive ion penetration depth is smaller than the thickness of a given steady-state fluorosilane film at a substrate, SiF<sub>x</sub> species ( $x = 2, 3$ ) are more likely than SiF to desorb. Ultimately, then, the increasing scatter values observed here may have a strong dependence on the increasing translational energies of ground state SiF and/or the vibrational energy of electronically excited SiF\*. This relationship is addressed below.

$S$  values are reported here for NO radicals for the first time, Table 5.2. These values are largely independent of substrate type (Si vs. Pt) and increase with increasing  $P$ . Scatter values greater than unity indicate surface production of a molecule, and as such, a trend toward NO surface production with increasing  $P$ , Fig. 5.5(b), is observed. Indeed, the linear regression model to all of the data in Fig. 5.5(b) yields a slope of  $0.0087 \pm 0.0003$  with  $R^2 = 0.98$ . Interestingly, both  $\Theta_{\text{v}}(\text{NO})$  and  $S(\text{NO})$  values increase linearly with  $P$  in the range of 50-150 W, Fig. 5.5(a) and 5.5(b). At  $P \geq 150$  W, scatter coeffi-

cients greater than unity coincide with vibrational temperatures for NO in the plasma exceeding 1700 K, Table 5.2. The increasing scatter coefficients ostensibly result from surface interactions of vibrationally hot molecules by preliminary inspection of Fig. 5.5. Removal of ions from the NO system via incorporation of a grounded mesh in the path of the molecular beam yielded  $S(\text{NO})$  values that were generally 10-20% lower than the values shown in Fig. 5.5(b), especially at  $P > 150$  W. Likewise there is a strong dependence of  $S(\text{NO})$  on plasma pressure as pressure significantly alters the mean ion energy.<sup>38</sup> Although these changes are significant, they are not substantial enough to account for all of the observed NO scatter, however, and as such, vibrationally hot excited state species are expected to contribute significantly to  $S$  values.

Interestingly, scatter coefficients for CF radicals interacting with Si substrates have similar source gas and  $P$  dependences as  $\Theta_{\text{V}}(\text{CF})$ , Table 5.3. Specifically,  $S(\text{CF})$  values decrease concomitantly with decreasing F/C ratio for the precursor gas. The relationship between choice of feed gas and the CF scatter coefficient has been previously reported<sup>28</sup> and discussed here (Chapter 4); note that these scatter measurements are heavily influenced by ion bombardment of the surface.<sup>14,41</sup> Nonetheless, vibrational temperatures for excited state CF radicals appear to correlate strongly with observed  $S(\text{CF})$  values as well. The most profound example of the apparent relationship between vibrational temperature on scatter coefficients for the three radicals studied here is provided in Fig. 5.6, where  $S(\text{CF})$  values are plotted as a function of  $\Theta_{\text{V}}(\text{CF})$  for a range of FC precursors. As the vibrational temperature of excited state ( $^2\Delta$ ) CF radicals increases, the observed scatter coefficient of the ground state species ( $^2\Pi$ ) concomitantly grows, Fig. 5.6. Because  $S(\text{CF})$  values essentially measure a change in  $\text{CF}(^2\Pi)$  density between scattered

species and the gas-phase of the plasma molecular beam, this relationship implies that vibrationally hot CF in excited electronic states contribute significantly to the observed scatter of ground state species. This phenomenon can be rationalized in several ways. For example, the  $^2\Delta$  CF radicals in the molecular beam (undetectable in the LIF scheme) may quench at the surface of the substrate and desorb as a ground state CF, yielding a high scatter value. Energy from this process may be dissipated into the surrounding FC film or passivation layer being deposited on the substrate. It is possible that enough excess energy may cause dislodging of additional  $\text{CF}_{(s)}$  units by effectively heating the surface film, further enhancing the  $S(\text{CF})$  value. Small increases in temperature also increase the diffusivity of F atoms through FC polymers,<sup>42</sup> rendering a significant portion of the exposed FC surface CF-rich. Thus,  $\text{CF}_{(s)}$  experiences the full brunt of plasma species and as such is readily removed, resulting in high observed scatter coefficients. In this way, highly vibrationally excited CF may act indirectly as an etchant to ablate FC material. Indeed, Tsai and coworkers<sup>43</sup> speculated on this phenomenon to explain resonant energy transfer of vibrationally hot molecules with growing surface Si-H bonds during silane depositions. This rationalization of the relationship between  $\Theta_v(\text{CF})$  and  $S(\text{CF})$  may be extended to the other radicals as well.

In general, scatter coefficients for the radicals investigated here track with changes in their vibrational temperatures. There is observed essentially no dependence of  $S(\text{X})$  ( $\text{X} = \text{NO}$ ,  $\text{CF}$ , or  $\text{SiF}$ ) on  $\Theta_R$ , leading us to infer that scatter coefficients are at least partially reliant upon the internal vibrational energy associated with the radical. In IRIS experiments, for a molecule formed in the plasma source to scatter from the substrate, it must have energy sufficient to overcome the potential barrier for desorption. For exam-

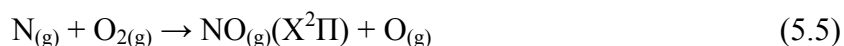
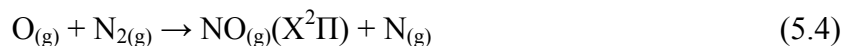
ple, the activation energy for desorption of NO from a Pt(111) surface has been calculated as  $\sim 20$  kcal/mol.<sup>44</sup> The data presented here suggest that energy in vibrational modes preferentially provides a radical with the means to desorb over molecules with energy contributions from translational and rotational modes. For each molecule, it is observed that the greater the vibrational energy associated with the molecule, the higher the propensity for scatter from a surface. This might suggest that vibrationally excited molecules interact with the substrate and rebound with some energy loss, as in Reaction (5.3)



where X denotes NO, CF, or SiF. Reaction (5.3) also implies that contributions from quenching of higher excited states not probed in the IRIS experiment could affect increases in scatter coefficients. Kim et al. showed that increases in  $n_e$  (and, as such, increased  $\Theta_V$  as discussed above) result in greater number densities of excited electronic populations.<sup>45</sup> Thus, molecule X in a given IRIS experiment, existing in an excited electronic state with correspondingly high  $\Theta_V$  in the plasma molecular beam, could quench upon contact with the substrate and subsequently desorb in a ground electronic state. This particular scenario would result in molecule X being LIF-transparent in the molecular beam of the plasma, but producing LIF signal as a scattered molecule, resulting in an apparently higher  $S(X)$  value, as discussed in the case of CF radicals above. The observation that  $S(\text{NO})$  is independent of substrate type suggests that Reaction (5.3) may also be independent of substrate material. Notably, preliminary results for CF interactions with  $\text{ZrO}_2$  substrate are similar to the  $S(\text{CF})$  values reported here for interactions with Si substrates. Ultimately, then, the relationship between internal temperatures and scatter coefficients for these molecules could provide the capability to predict surface reactivity

of plasma species. It should be noted, however, that although the contribution of vibrationally hot molecules to surface reactivity is significant, it certainly does not represent a complete embodiment of surface reactions. Other processes, including ion bombardment and/or neutralization, vibrational relaxation, particle flux, recombination reactions, and photodetachment all occur simultaneously at surfaces in these systems. Nonetheless, a clear relationship emerges linking vibrational energies to surface scatter coefficients for three distinct systems. Thus, even if internal energy contributions to surface reactivity are not exclusively causative, they are most certainly correlated to plasma-surface interactions.

One additional observation can be made regarding the vibrational temperatures of NO. As demonstrated previously, plasmas generating NO through recombination reactions, such as in N<sub>2</sub>/O<sub>2</sub> plasmas, yield essentially the same values of  $\Theta_v(\text{NO})$  as do 100% NO plasmas.<sup>26</sup> This indicates that production of NO from such formation mechanisms as the Zeldovich chain,<sup>46</sup> reactions (5.4) and (5.5), that generates ground state NO, does



not preferentially transfer vibrational energy to the NO molecule. Vibrationally hot N<sub>2</sub> is requisite for propagation of the Zeldovich chain in non-thermal plasmas. Correspondingly, a lack of vibrationally excited N<sub>2</sub> (normally observed in 100% N<sub>2</sub> plasmas) is observed in the afterglow of N<sub>2</sub>/O<sub>2</sub> systems, suggesting that molecules with significantly high  $\Theta_v(\text{N}_2)$  are consumed in the reactions forming NO.<sup>26</sup> Thus, NO vibrational temperatures appear to be independent of the source of the NO molecule. The difference in route of formation of NO likewise does not significantly impact propensity for surface interac-

tions at  $p = 100$  mTorr. The scatter coefficients for NO produced from a 100% NO plasma and for NO produced from a 90/10 N<sub>2</sub>/O<sub>2</sub> plasma (both with  $P = 100$  W and  $p = 100$  mTorr) agree within experimental error,  $0.55 \pm 0.10$  and  $0.52 \pm 0.10$ , respectively.

A remaining question focuses on the generality of the relationship between  $\Theta_v$  and  $S$  observed here for CF, SiF, and NO. Previously, it has been speculated that the spin multiplicity ( $2S + 1$  for angular spin momentum  $S$ ) of a molecule influences its surface interactions, citing data that imply that molecules with singlet electronic configurations tend to have the greatest propensity for surface scatter (i.e. are least reactive).<sup>27,47</sup> Scatter coefficients for singlet molecules, including C<sub>3</sub>, CHF, and CF<sub>2</sub>, tend to be high under all plasma conditions. The three molecules studied here all have a doublet multiplicity, and their scatter coefficients also tend to be relatively high and change with changing  $P$ . Conversely, not all doublet species adhere to this overall trend in surface reactivity. For example, CH molecules exhibit low scatter coefficients (i.e. are primarily reactive at surfaces), regardless of plasma and substrate conditions and gas-phase formation mechanism. Note that the transition monitored for the CH molecule is  $A^2\Delta - X^2\Pi$ , whereas the transition used to calculate scatter coefficients in our LIF-based IRIS experiments is  $A^2\Sigma^+ - X^2\Pi$  for NO, CF, and SiF. This difference in symmetry in the electronic configuration of the excited state molecule may contribute to the differences in observed scatter coefficients. Future work will further explore this with additional plasma species, including main group hydrides OH, NH, CH and SiH, along with species of differing electronic ground states.

#### 5.4. Summary

The relationship between vibrational temperature and surface scatter coefficients for three diatomic radical species in inductively coupled plasmas was explored. Electronically excited SiF radicals in tetrafluorosilane plasmas attain high vibrational temperatures that are significantly higher than both translational and rotational temperatures for ground state SiF. Similarly, excited state NO and CF radicals in nitric oxide and fluorocarbon based systems, respectively, have large  $\Theta_v$  values. Changes in  $\Theta_v$  with  $P$  for these excited state species are mirrored in the trends observed for ground state molecules. The preferential partitioning of energy into vibrational modes correlates with an increased propensity for scatter when a molecule interacts with a substrate. Thus, these data suggest that radical surface scatter coefficients are at least partially reliant upon the vibrational energy of the radical. It is proposed here that electronically excited, vibrationally hot radicals are significant contributors to observed  $S$  values. Ultimately, the intimate relationship between internal energies of gas-phase constituents, electronic configuration, and the overall reactivity of plasma species must be considered when developing new plasma applications as well as comprehensive models of plasma chemistry.

## 5.5. References

1. Cruden, B. A.; Rao, M.; Sharma, S. P.; Meyyappan, M., Neutral gas temperature estimates in an inductively coupled CF<sub>4</sub> plasma by fitting diatomic emission spectra. *J. Appl. Phys.* **2002**, 91, (11), 8955-8964.
2. Nagai, M.; Hori, M., Temperature and density of CF radicals in 60 MHz CCP FC Gas Plasma. *Jpn. J. Appl. Phys.* **2007**, 46, (3A), 1176-1180.
3. Britun, N.; Gaillard, M.; Ricard, A.; Kim, Y. M.; Kim, K. S.; Han, J. G., Determination of the vibrational, rotational, and electron temperatures in N<sub>2</sub> and N<sub>2</sub>/Ar rf discharge. *J. Phys. D: Appl. Phys.* **2007**, 40, 1022.
4. Fridman, A., *Plasma Chemistry*. Cambridge University Press: New York, 2008.
5. Golubovskii, Y. B.; Telezhko, V. M., Measurement of gas temperature from the unresolved rotational structure of the first positive band system of nitrogen. *J. Appl. Spectrosc.* **1983**, 39, (3), 999-1003.
6. Porter, R. A.; Harshbarger, W. R., Gas Rotational Temperature in an RF Plasma. *J. Electrochem. Soc.* **1979**, 126, (3), 460-464.
7. Davis, G. P.; Gottscho, R. A., Measurement of spatially resolved gas-phase plasma temperatures by optical emission and laser-induced fluorescence spectroscopy. *J. Appl. Phys.* **1983**, 54, (6), 3080-3086.
8. Schabel, M. J.; Donnelly, V. M.; Kornblit, A.; Tai, W. W., Determination of electron temperature, atomic fluorine concentration, and gas temperature in inductively coupled fluorocarbon/rare gas plasmas using optical emission spectroscopy. *J. Vac. Sci. Technol. A* **2002**, 20, (2), 555-563.
9. Shimada, M.; Tynan, G. R.; Cattolica, R., Rotational and translational temperature equilibrium in an inductively coupled plasma. *J. Vac. Sci. Technol. A* **2006**, 24, (5), 1878-1883.
10. McCurdy, P. R.; Venturo, V. A.; Fisher, E. R., Velocity distributions of NH<sub>2</sub> radicals in an NH<sub>3</sub> plasma molecular beam. *Chem. Phys. Lett.* **1997**, 274, 120.
11. Bogart, K. H. A.; Cushing, J. P.; Fisher, E. R., Effects of Plasma Processing Parameters on the Surface Reactivity of OH(X<sup>2</sup>Π) in Tetraethoxysilane/O<sub>2</sub> Plasmas during Deposition of SiO<sub>2</sub>. *J. Phys. Chem. B* **1997**, 101, 10016.
12. Kessels, W. M. M.; McCurdy, P. R.; Williams, K. L.; Barker, G. R.; Venturo, V. A.; Fisher, E. R., Surface Reactivity and Plasma Energetics of SiH Radicals during Plasma Deposition of Silicon-Based Materials. *J. Phys. Chem. B* **2002**, 106, 2680.
13. Zhang, J.; Williams, K. L.; Fisher, E. R., Velocity Distributions of SiF and SiF<sub>2</sub> in an SiF<sub>4</sub> Plasma Molecular Beam. *J. Phys. Chem. A* **2003**, 107, (5), 593-597.
14. Martin, I. T.; Fisher, E. R., Ion effects on CF<sub>2</sub> surface interactions during C<sub>3</sub>F<sub>8</sub> and C<sub>4</sub>F<sub>8</sub> plasma processing of Si. *J. Vac. Sci. Technol. A* **2004**, 22, (5), 2168-2176.
15. Williams, K. L.; Butoi, C. I.; Fisher, E. R., Mechanisms for deposition and etching in fluorosilane plasma processing of silicon. *J. Vac. Sci. Technol. A* **2003**, 21, (5), 1688-1701.
16. Williams, K. L.; Fisher, E. R., Substrate temperature effects on surface reactivity of SiF<sub>x</sub> (x = 1, 2) radicals in fluorosilane plasmas. *J. Vac. Sci. Technol. A* **2003**, 21, (4), 1024-1032.

17. Liu, D.; Martin, I. T.; Zhou, J.; Fisher, E. R., Surface Interactions During Film Deposition: A Sticky Situation? *Pure Appl. Chem.* **2006**, 78, 1187-1202.
18. Luque, J.; Hudson, E. A.; Booth, J. P., CF  $A^2\Sigma^+ \rightarrow X^2\Pi$  and  $B^2\Delta \rightarrow X^2\Pi$  study by broadband absorption spectroscopy in a plasma etch reactor: Determination of transition probabilities, CF  $X^2\Pi$  concentrations, and gas temperatures. *J. Chem. Phys.* **2003**, 118, (2), 622-632.
19. Hollmann, E. M.; Pigarov, A. Y.; Taylor, K., Measurement and modeling of  $H_2$  vibrational and rotational temperatures in weakly ionized hydrogen discharges. *J. Nucl. Mater.* **2005**, 337, 451-455.
20. Staack, D.; Farouk, B.; Gutsol, A. F.; Fridman, A., Spectroscopic studies and rotational and vibrational temperature measurements of atmospheric pressure normal glow plasma discharges in air. *Plasma Sources Sci. Technol.* **2006**, 15, (4), 818.
21. Lalo, C.; Deson, J.; Cerveau, C.; Ben-Aim, R. I., Air Microwave-induced plasma: detection of NO in post-discharge using an ArF laser. *PCPP* **1993**, 13, (2), 351.
22. Studer, D.; Boubert, P.; Vervisch, P., Demonstration of NO production in air plasma-metallic surface interaction by broadband laser-induced fluorescence. *J. Phys. D: Appl. Phys.* **2010**, 43, (31), 315202.
23. Booth, J.-P.; Hancock, G.; Toogood, M. J.; McKendrick, K. G., Quantitative Laser-Induced Fluorescence Spectroscopy of the CF  $A^2\Sigma^+ \rightarrow X^2\Pi$  Transition: Electronic Transition Dipole Moment Function and Predissociation. *J. Phys. Chem.* **1996**, 100, (1), 47-53.
24. Hebner, G. A., Spatially resolved CF,  $CF_2$ , SiF and  $SiF_2$  densities in fluorocarbon containing inductively driven discharges. *Appl. Surf. Sci.* **2002**, 192, (1-4), 161-175.
25. Ohta, T.; Hara, K.; Ishida, T.; Hori, M.; Goto, T.; Ito, M.; Kawakami, S.; Ishii, N., Measurement of Si, SiF, and  $SiF_2$  radicals and  $SiF_4$  molecule using very high frequency capacitively coupled plasma employing  $SiF_4$ . *J. Appl. Phys.* **2003**, 94, (3), 1428-1435.
26. Morgan, M. M.; Cuddy, M. F.; Fisher, E. R., Gas-Phase Chemistry in Inductively Coupled Plasmas for NO Removal from Mixed Gas Systems. *J. Phys. Chem. A* **2010**, 114, (4), 1722-1733.
27. Liu, D.; Cuddy, M. F.; Fisher, E. R., Comparison of CH,  $C_3$ , CHF, and  $CF_2$  Surface Reactivities during Plasma-Enhanced Chemical Vapor Deposition of Fluorocarbon Films. *ACS Appl. Mater. Interfaces* **2009**, 1, (4), 934-943.
28. Cuddy, M. F.; Fisher, E. R., Contributions of CF and  $CF_2$  Species to Fluorocarbon Film Composition and Properties for  $C_xF_y$  Plasma-Enhanced Chemical Vapor Deposition. *ACS Appl. Mater. Interfaces* **2012**, 4, (3), 1733-1741.
29. Parker, J. G., Rotational and Vibrational Relaxation in Diatomic Gases. *Phys. Fluids* **1959**, 2, (4), 449-462.
30. Davis, S. J.; Hadley, S. G., Measurement of the radiative lifetime of the  $A^2\Sigma(v'=0)$  state of SiF. *Phys. Rev. A* **1976**, 14, (3), 1146-1150.
31. Adamovich, I. V.; Macheret, S. O.; Rich, J. W.; Treanor, C. E., Vibrational relaxation and dissociation behind shock waves part 1: kinetic rate models. *AIAA J.* **1995**, 33, (6), 1064.
32. Dagdigian, P. J., State-Resolved Collision-Induced Electronic Transitions. *Annu. Rev. Phys. Chem.* **1997**, 48, (1), 95-123.

33. Sugai, H.; Ghanashev, I.; Hosokawa, M.; Mizuno, K.; Nakamura, K.; Toyoda, H.; Yamauchi, K., Electron energy distribution functions and the influence on fluorocarbon plasma chemistry. *Plasma Sources Sci. Technol.* **2001**, 10, (2), 378.
34. Huang, X.-J.; Xin, Y.; Yang, L.; Yuan, Q.-H.; Ning, Z.-Y., Spectroscopic study on rotational and vibrational temperature of N<sub>2</sub> and N<sub>2</sub><sup>+</sup> in dual-frequency capacitively coupled plasma. *Phys. Plasmas* **2008**, 15, (11), 113504-6.
35. Rehman, N. U.; Khan, F. U.; Khattak, N. A. D.; Zakaullah, M., Effect of neon mixing on vibrational temperature of molecular nitrogen plasma generated at 13.56 MHz. *Phys. Lett. A* **2008**, 372, (9), 1462-1468.
36. Kim, J.-H.; Shin, Y.-H.; Chung, K.-H.; Yoo, Y.-S., Relation between the CF<sub>2</sub> radical and plasma density measured using LIF and cutoff probe in a CF<sub>4</sub> inductively coupled plasma. *Appl. Phys. Lett.* **2004**, 85, (11), 1922-1924.
37. Ono, S.; Teii, S., Vibrational temperature in a weakly ionised CO<sub>2</sub>-N<sub>2</sub>-He discharge. *J. Phys. D: Appl. Phys.* **1985**, 18, (3), 441.
38. Blechle, J. M.; Cuddy, M. F.; Fisher, E. R., The role of ions in the gas-surface interactions of nitrogen oxide plasma systems. *J. Phys. Chem. A* **2012**, manuscript in preparation (invited article).
39. Cuddy, M. F.; Fisher, E. R., Investigation of the roles of gas phase CF<sub>2</sub> and F during FC processing of Si and ZrO<sub>2</sub>. *J. Appl. Phys.* **2010**, 108, 033303.
40. Oehrlein, G. S., Effects of ion bombardment in plasma etching on the fluorinated silicon surface layer: Real-time and postplasma surface studies. *J. Vac. Sci. Technol. A* **1993**, 11, (1), 34-46.
41. Cuddy, M. F.; Blechle, J. M.; Fisher, E. R., Ion contributions to gas-surface interactions in inductively-coupled fluorocarbon plasmas. *Int. J. Mass Spectrom.* **2012**, Submitted.
42. Standaert, T. E. F. M.; Schaepkens, M.; Rueger, N. R.; Sebel, P. G. M.; Oehrlein, G. S.; Cook, J. M., High density fluorocarbon etching of silicon in an inductively coupled plasma: Mechanism of etching through a thick steady state fluorocarbon layer. *J. Vac. Sci. Technol. A* **1998**, 16, (1), 239-249.
43. Tsai, C. C.; Knights, J. C.; Chang, G.; Wacker, B., Film formation mechanisms in the plasma deposition of hydrogenated amorphous silicon. *J. Appl. Phys.* **1986**, 59, (8), 2998-3001.
44. Bartram, M. E.; Koel, B. E.; Carter, E. A., Electronic effects of surface oxygen on the bonding of NO to Pt(111). *Surf. Sci.* **1989**, 219, (3), 467-489.
45. Kim, J. H.; Choi, Y. H.; Hwang, Y. S., Electron density and temperature measurement method by using emission spectroscopy in atmospheric pressure nonequilibrium nitrogen plasmas. *Phys. Plasmas* **2006**, 13, (9), 093501.
46. Zeldovich, Y. B., The oxidation of nitrogen in combustion and explosions. *Acta Physicochim. U.S.S.R.* **1947**, 21, 577.
47. Stillahn, J. M.; Fisher, E. R., Gas Phase Energetics of CN Radicals in Radio Frequency Discharges: Influence on Surface Reaction Probability During Deposition of Carbon Nitride Films. *J. Phys. Chem. A* **2010**, 114, (16), 5287-5294.

## CHAPTER 6

### ION CONTRIBUTIONS TO GAS-SURFACE INTERACTIONS IN INDUCTIVE- LY-COUPLED FLUOROCARBON PLASMAS

This chapter recounts the contents of a full paper submitted by Michael F. Cuddy, Joshua M. Blechle, and Ellen R. Fisher to the *International Journal of Mass Spectrometry* for a special issue honoring Peter B. Armentrout. Herein is discussed the role of plasma-generated ions for plasma processing of substrates to develop a more profound understanding of the phenomena that occur at plasma-surface interfaces. Specifically, ion-limited IRIS experiments are examined, and the results are correlated with observed trends in the total mean ion energies for nascent plasma species. Speculations on the role of low-energy ions in the plasma systems are also presented for their expected contributions to FC film propagation.

## 6.1. Introduction

Plasma ions are significant driving forces for plasma chemistry, often controlling both surface and gas-phase reactions. Indeed, ion-surface interactions are a central aspect of many plasma-based modification techniques as ions can assume dual roles as contributors to film growth for plasma deposition of films or as etchants for removal of material. To this end, the mechanisms of ion-surface interactions in plasma systems are of significant interest and have been studied extensively in both experiment and simulation.<sup>1-3</sup> Energetic ions may be employed to create active sites (broken chemical bonds) at a surface through ion bombardment, thereby promoting “ion-induced” film growth.<sup>4</sup> Concurrently, these ions may also remove material from a surface via chemical and/or physical sputtering.<sup>5</sup> The propensity for ions to experience highly exothermic gas-phase recombination reactions is also significant; neutral radicals formed by such processes can produce aggregates through a cascade of additional gas-phase reactions.<sup>6</sup> As such, it is imperative to consider the contributions of ions to plasma processing of materials for any materials application.

In the late 1980s, Armentrout and coworkers began studying gas-phase ion-molecule reactions related to Si-based plasma processing.<sup>7-15</sup> Over a period of ~15 years, they investigated the kinetic energy dependence of a number of fundamental ion-molecule reactions relevant to plasma chemistry using guided ion beam mass spectrometry (GIBMS).<sup>7</sup> The primary goals of this work were to provide energy-dependent cross sectional data for ion-molecule reactions occurring in a range of plasma systems along with accurate thermochemical data for both ionic and neutral plasma species. Interestingly, one of the notable findings from this work was a distinct coupling between transla-

tional and electronic energy during ion-molecule reactions involving rare gas ions and molecules such as  $\text{SiH}_4$  and  $\text{CF}_4$ .<sup>9, 11, 16</sup> Thus, this pioneering GIBMS on ion-molecule reactions of interest to the semiconductor industry revealed not only fundamental thermochemical and kinetic data, it also afforded significant insight into the underlying chemical mechanisms in a range of plasma systems.

One specific category of plasma systems that continues to realize significant interest from the plasma community is fluorocarbon (FC) plasmas. In particular, FC systems are widely employed in both deposition and etching regimes for applications ranging from fabrication of microelectronic devices to the development of novel materials with specific surface properties.<sup>17-24</sup> Plasma-enhanced chemical vapor deposition (PECVD) of FC films is a complex process, often involving the interaction of a multitude of gas-phase neutrals, radicals, excited species, and ions at a surface.<sup>25-27</sup> Ions are integral to FC plasma processes, including selective etching in the case of high-energy ions,<sup>28, 29</sup> and film deposition in the case of low-energy ions.<sup>30, 31</sup> FC plasma-related GIBMS work in the Armentrout group focused on the reactions of rare gas ions  $\text{O}^+$  and  $\text{O}_2^+$  with  $\text{CF}_4$  and  $\text{C}_2\text{F}_6$ .<sup>16, 32, 33</sup> This work elucidated the kinetic energy-dependent rate constants for dissociative reactions of  $\text{C}_x\text{F}_y$  species and rare gas ions so vital for accurate modeling of plasma systems. In the  $\text{O}_2^+$  and  $\text{O}^+$  systems, they found that the reactions of  $\text{O}^+$  with  $\text{C}_x\text{F}_y$  precursors led to reactive etchants such as F atoms. In all of these systems,  $\text{CF}_3^+$  was a dominant product ion, with  $\text{C}_2\text{F}_5^+$  also a strong constituent in the  $\text{C}_2\text{F}_6$  systems. Su and coworkers conducted similar studies for  $\text{CF}_3^+$  reactions with hexafluoropropylene oxide (HFPO) using selected ion flow tube (SIFT) mass spectrometry and determined that the only product of this reaction is  $\text{C}_3\text{F}_7^+$ .<sup>34</sup> Notably, in both the GIBMS

and SIFT studies, data were collected under single collision conditions, whereas in plasmas, multiple gas-phase and gas-wall collisions can occur, potentially significantly altering both the energetics and composition of the plasma.

Our laboratory has previously demonstrated that ions have a significant influence over the behavior of  $\text{CF}_2$  species at the plasma-surface interface.<sup>35, 36</sup> Specifically, mean ion energies for  $\text{CF}_2^+$  correlate linearly with scatter coefficients observed for  $\text{CF}_2$  in FC systems. Despite this body of work, a comprehensive analysis of ions in FC plasmas and their behaviors at the gas-surface interface does not exist. Thus, the aim here is to explicate the mechanisms by which ions influence  $\text{CF}_x$  scatter from surfaces during plasma processing and the contributions of gas-phase FC species to film deposition by PECVD.

Characterization of the types of ions present in a FC plasma and the energies of those ions is important both for plasma modeling and for understanding the key reactions that ultimately lead to surface modification. For instance, in other polymerizing plasma systems, such as allylamine, the interactions of gas-phase ions and molecules lead to the formation of oligomeric species.<sup>37</sup> Indeed, oligomeric gas-phase fluorocarbon species are thought to be chief contributors to polymerization and film initiation.<sup>38</sup> Models developed by Zhang and Kushner demonstrated the profound effect of increasing ion energies on  $\text{CF}_2$  loss mechanisms at surfaces. They showed that the net loss of  $\text{CF}_{2(s)}$  increased dramatically over  $\text{CF}_{2(g)}$  sticking when the plasma sheath voltage potential exceeded 78 V.<sup>39</sup>  $\text{CF}_x$  ( $x = 1-3$ ) species are of particular interest in these systems because of their dichotomous and dynamic roles as etch products or deposition precursors.<sup>40</sup>

In this Chapter, mass spectrometric measurements were employed via a high-energy mass spectrometer to not only identify nascent gas-phase ions and oligomers di-

rectly from the plasma source, but also to analyze the energies of those species. The energy analysis capability of our instrument allows for measurement of ion energy distributions (IEDs) over a broad energy range (1000 eV) with the ionizer off to sample only ions produced by the plasma itself. The mean ion energy,  $\langle E_i \rangle$ , can be calculated from an IED via equation (6.1), where  $E$  represents the ion energy in eV for a particular nascent ion in the plasma.<sup>41</sup> The instrument can also be operated in

$$\langle E_i \rangle = \frac{\int f(E) E dE}{\int f(E) dE} \quad (6.1)$$

residual gas analysis (RGA) mode with its ionization source on to observe all the gas-phase plasma species present, including oligomers formed through recombination reactions. The fundamental understanding of the behavior of gas-phase ions, coupled with the knowledge concerning the constituents of the plasma bulk, allow us to develop plasma processing mechanisms based upon complementary gas-surface interface data.

Previous chapters in this dissertation as well as additional studies from the Fisher group have examined the surface reactivity of  $CF_x$  species using our imaging of radicals interacting with surfaces (IRIS) technique.<sup>35, 36, 40, 42-45</sup> Generally, a significant decrease in the observed surface scatter coefficient of  $CF_2$ ,  $S(CF_2)$ , is commensurate with the removal of ions from the system, either through implementation of a grounded mesh or via application of a substrate bias. We have not, however, expressly developed a complete body of work regarding the effect of ions on CF and  $CF_2$  surface reactivity over a broad range of plasma parameters, such as applied rf power ( $P$ ) and choice of plasma precursor. The effect of ions on the observed scatter coefficient for  $CF_x$  radicals can be gauged by determining  $\Delta S(CF_x)$ , defined as the difference between the ion-rich case and the ion-limited case, equation (6.2).

$$\Delta S(\text{CF}_x) = S(\text{CF}_x)_{\text{ions}} - S(\text{CF}_x)_{\text{ion-limited}} \quad (6.2)$$

In the present studies, the ion-limited case was achieved by biasing the substrate exposed to the plasma molecular beam with a +200 V direct current to repel positively charged species.<sup>46</sup> Mitigating ion flux to the surface allows for examination of the processes that occur exclusive of ion influence. Thus,  $\Delta S(\text{CF}_x)$  values provide an avenue for inferring the role of ions as they dictate  $\text{CF}_x$  behavior at the gas-surface interface. Ultimately, the correlation between plasma properties and the phenomena occurring at the plasma-surface interface can be used to more fully understand the effect of ion contributions in FC systems.

## 6.2. Results

Mass spectra collected with the MS ionizer off provide information about the nascent ions present in the plasma systems. Fig. 6.1 provides such spectra for  $\text{CF}_4$ ,  $\text{C}_2\text{F}_6$ ,  $\text{C}_3\text{F}_8$ ,  $\text{C}_3\text{F}_6$ , and HFPO. Generally, the ions observed are of the general formula  $\text{C}_x\text{F}_y^+$ , are dissociation products of the precursor gas, and are indicative of a loss of C and/or F through plasma initiation processes. In some cases the ions that are observed must be produced through gas-phase recombination reactions, such as  $\text{C}_3\text{F}_3^+$ ,  $\text{C}_2\text{F}_5^+$ , and  $\text{C}_3\text{F}_7^+$  in the  $\text{CF}_4$  spectrum, Fig. 6.1(a) (inset). As should be anticipated, oxygen-containing ions are also observed in the mass spectrum of HFPO, Fig. 6.1(e).

Ion energy distributions can be obtained by selectively scanning the energies of a particular mass-to-charge ratio. IEDs for  $\text{CF}_3^+$  ions ( $m/z = 69$ ) in each of the plasma systems studied are shown in Fig. 6.2. Here, the stark differences in ion energy distributions

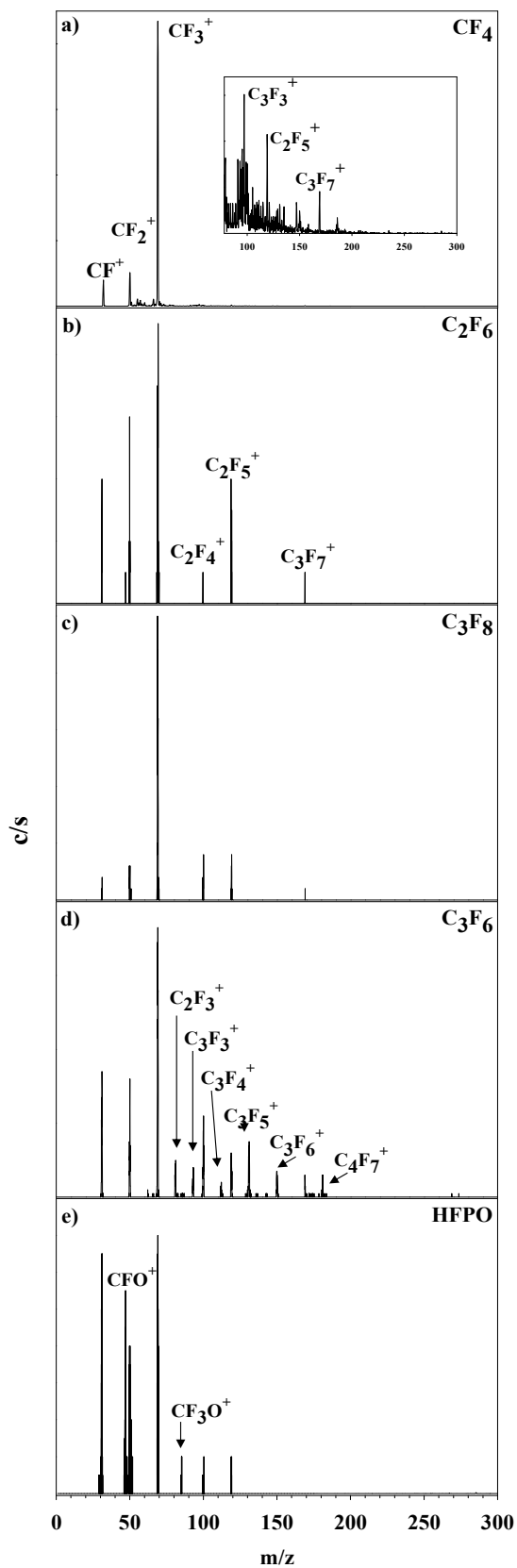


**Figure 6.1.** Representative mass spectra of nascent ions formed in a) CF<sub>4</sub>, b) C<sub>2</sub>F<sub>6</sub>, c) C<sub>3</sub>F<sub>8</sub>, d) C<sub>3</sub>F<sub>6</sub>, and e) HFPO plasmas. Each spectrum corresponds to  $P = 200$  W and  $p = 50$  mTorr. Major peaks are labeled accordingly for the first spectrum in which the ion at a particular  $m/z$  ratio appears. The inset in a) is an expanded view of the 75-300  $m/z$  range for CF<sub>4</sub>.

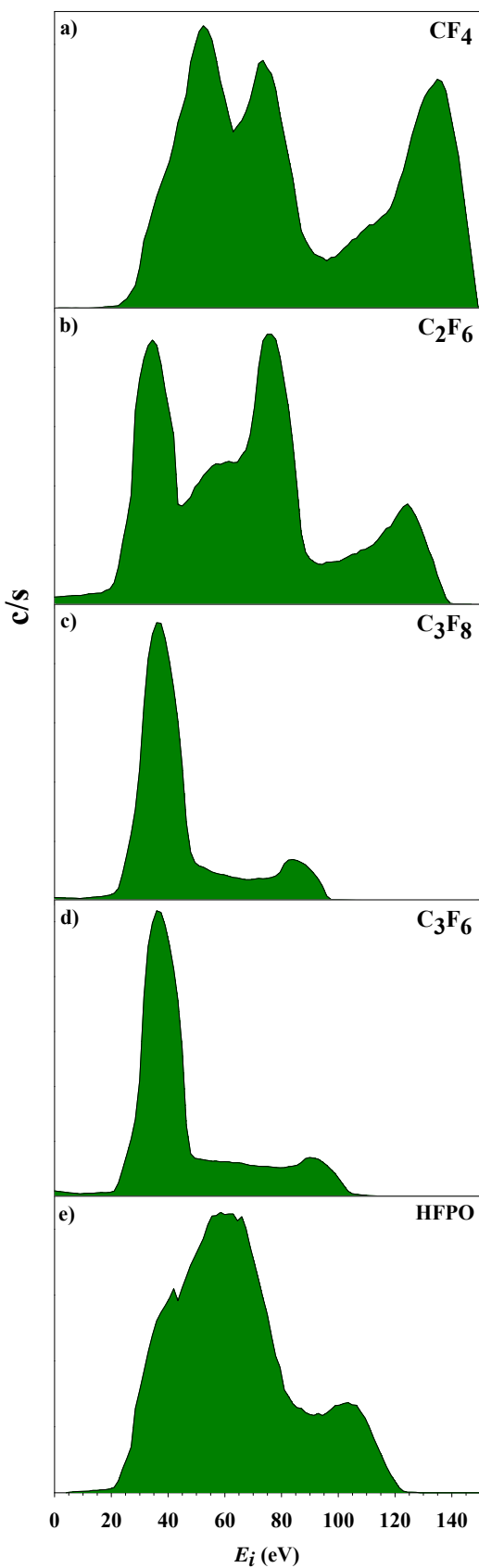


**Figure 6.2.** Ion energy distributions of nascent  $\text{CF}_3^+$  ions formed in a)  $\text{CF}_4$ , b)  $\text{C}_2\text{F}_6$ , c)  $\text{C}_3\text{F}_8$ , d)  $\text{C}_3\text{F}_6$ , and e) HFPO plasmas all operating at  $P = 150$  W and  $p = 50$  mTorr.

among the different plasma sources are readily evident.  $\text{CF}_4$  and  $\text{C}_2\text{F}_6$  plasmas tend to give rise to ions with broad, multimodal distributions of energies, Fig. 6.2(a-b), whereas  $\text{C}_3\text{F}_8$  and  $\text{C}_3\text{F}_6$  sources produce ions with narrower energy distributions and apparent lower average energy ( $\sim 40$  eV), Fig. 6.2(c-d). In contrast, HFPO plasmas, Fig. 6.2(e), tend to fall somewhere in between these two extremes, producing ions that have a slightly broader energy distribution than the  $\text{C}_3\text{F}_8$  and  $\text{C}_3\text{F}_6$  precursors, but with a slightly lower average energy than those obtained from  $\text{CF}_4$  plasmas.

Ion energy information has been obtained for each of the ions observed in each of the precursor systems listed above. This is illustrated in Fig. 6.3, where IEDs are plotted for the six major ions [identified in Fig. 6.1(b)] observed in a  $\text{C}_2\text{F}_6$  plasma with  $P = 200$  W. The more abundant ions in the plasma based upon the mass spectra,  $\text{CF}^+$ ,  $\text{CF}_2^+$ , and  $\text{CF}_3^+$ , Fig. 6.3(a-c), yield slightly broader energy distributions with less distinction between individual peaks than do those ions that are less abundant,  $\text{C}_2\text{F}_4^+$ ,  $\text{C}_2\text{F}_5^+$ , and  $\text{C}_3\text{F}_7^+$ , Fig. 6.3(d-f). Nonetheless, the average ion energy for each of these ions tends to be essentially the same at a given set of plasma conditions, Fig. 6.3(g). In this figure,  $\langle E_i \rangle$  is plotted as a function of  $P$ , and demonstrates that each nascent ion effectively thermalizes to the same average energy. As such, a simpler designation for the average ion energy for a given plasma system is  $\langle E_i \rangle_{\text{total}}$ , defined as the average  $\langle E_i \rangle$  of  $n$  total observed ions in a particular plasma.

Values of  $\langle E_i \rangle_{\text{total}}$  are plotted in Fig. 6.4 as a function of  $P$  for  $\text{CF}_4$ ,  $\text{C}_2\text{F}_6$ ,  $\text{C}_3\text{F}_8$ ,  $\text{C}_3\text{F}_6$ , and HFPO plasma sources. Generally, ion energies tend to increase with increasing  $P$  for each of the plasma sources depicted. The most significant change in  $\langle E_i \rangle_{\text{total}}$  occurs

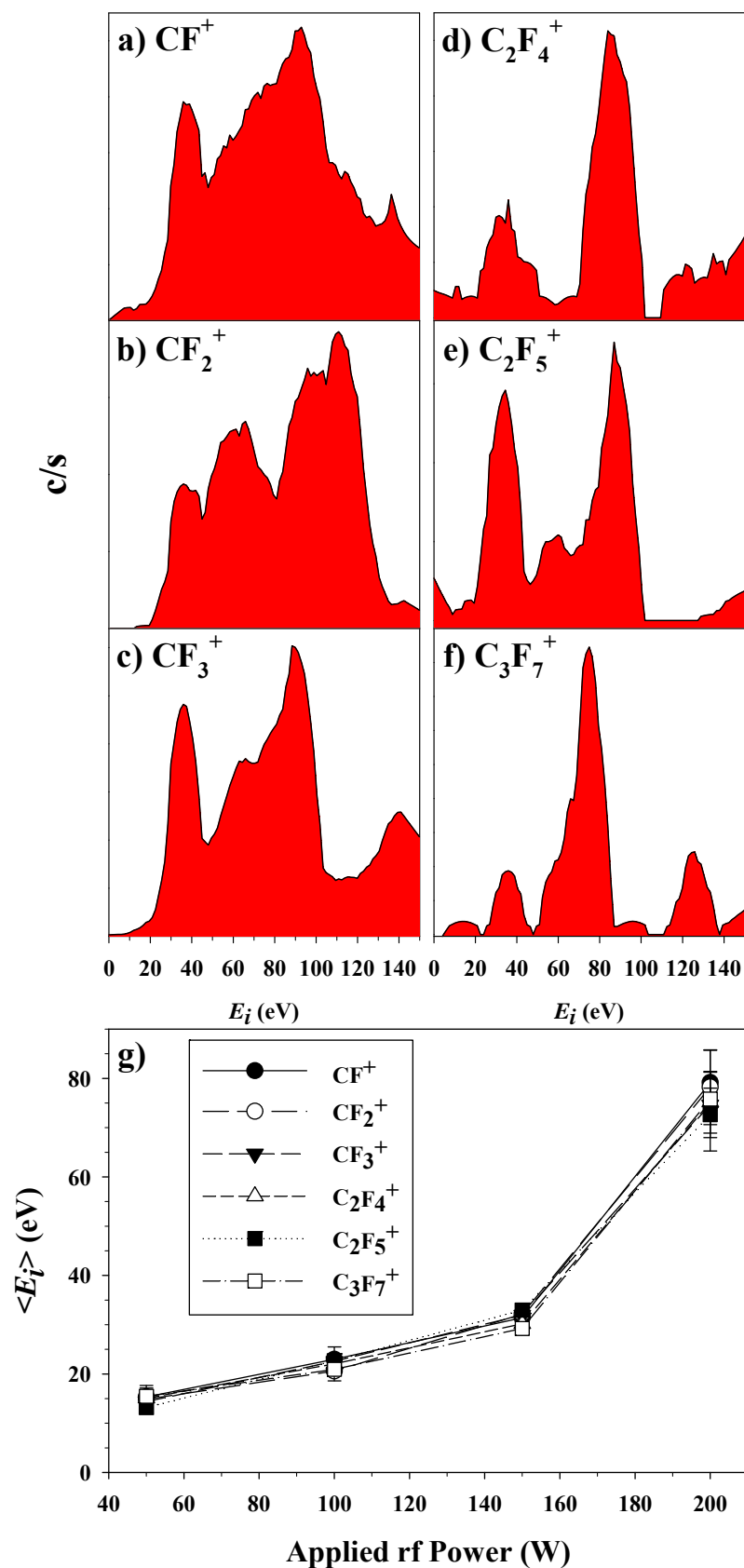


**Figure 6.3.** a)-f) Ion energy distributions for each of the nascent ions observed in a  $C_2F_6$  plasma operating at  $P = 200$  W and  $p = 50$  mTorr. g) Mean ion energies calculated from distributions such as those depicted in a)-f), plotted as a function of  $P$  for a  $C_2F_6$  plasma.

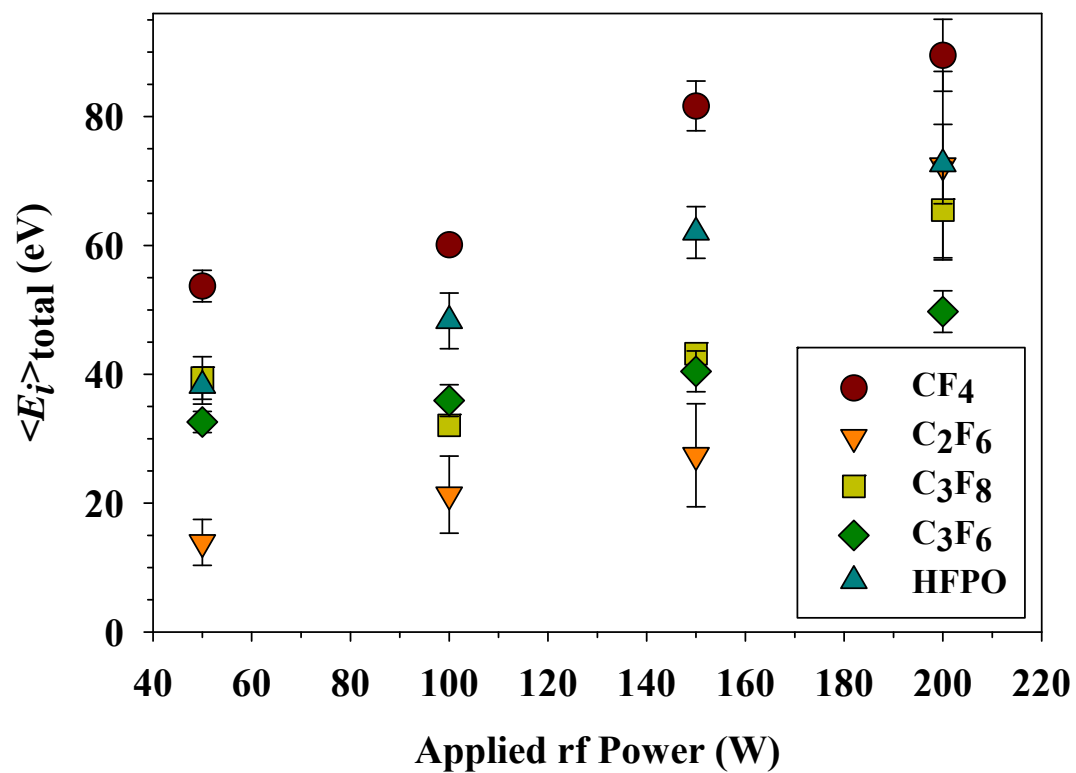


**Figure 6.4.** Total mean ion energies plotted as a function of  $P$  for nascent ions produced from  $\text{CF}_4$ ,  $\text{C}_2\text{F}_6$ ,  $\text{C}_3\text{F}_8$ ,  $\text{C}_3\text{F}_6$ , and HFPO feed gases.

for the  $C_2F_6$  plasma between 150 and 200 W. At  $P = 150$  W,  $\langle E_i \rangle_{\text{total}}$  for the  $C_2F_6$  system is approximately 27 eV, whereas at  $P = 200$  W the value increases to  $\sim 72$  eV and overlaps with the data point for the HFPO plasma at the same conditions. Another notable feature of this figure is that ion energies appear to be dependent upon the choice of precursor used in the plasma.  $CF_4$  systems in particular tend to give rise to the most energetic ions at a given  $P$ . Changes in  $\langle E_i \rangle_{\text{total}}$  are least pronounced over the range of 50-200 W for  $C_3F_6$  and  $C_3F_8$  systems.

IRIS data were collected to provide complementary data to the  $\langle E_i \rangle_{\text{total}}$  values discussed above. Representative LIF images from IRIS experiments for HFPO are shown in Fig. 6.5. Here, “beam + scatter” images for the  $CF_2$  radical are shown for both an unbiased Si substrate, Fig. 6.5(a), and a substrate with +200 V dc bias, Fig. 6.5(b). The  $CF_2$  “beam only” image, Fig. 6.5(c), is subtracted from each of the “beam + scatter” images to obtain images representative only of scatter, Fig. 6.5(d-e). Cross-sections taken along the laser propagation axis are shown for the “beam only” and “scatter” cases in Fig. 6.5(f-g), and are fit with simulated data to calculate scatter coefficients. In the case of no substrate biasing,  $S(CF_2) = 1.03$ , whereas  $S(CF_2) = 0.30$  for the biased Si. Accordingly,  $\Delta S(CF_2) = 0.73$ . Table 6.1 provides  $\Delta S(CF_x)$  values for  $CF_4$ ,  $C_2F_6$ ,  $C_3F_8$ ,  $C_3F_6$ , and HFPO systems as a function of  $P$ .

RGA mode mass spectrometric analyses of FC plasma systems were used to investigate the behavior of oligomeric species thought to be related to film growth mechanisms during PECVD of FC films. Recombination products in the gas phase of a  $CF_4$  plasma were identified and monitored as a function of  $P$ , Fig. 6.6(a). The relative

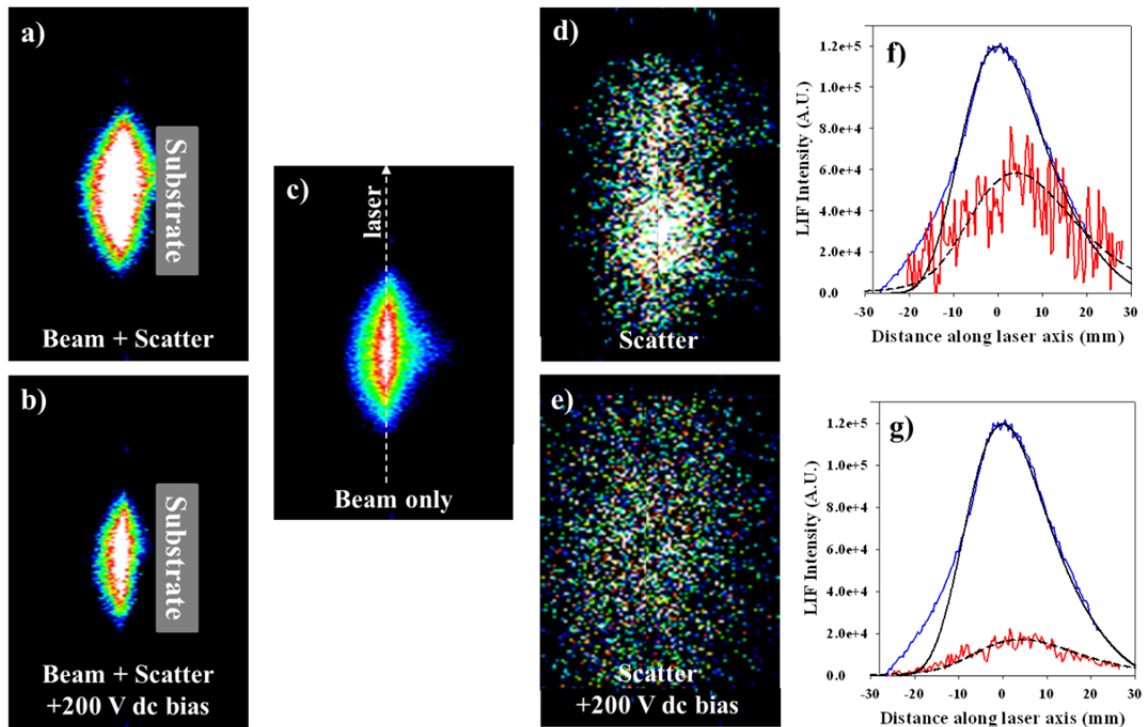


**Figure 6.5.** LIF images corresponding to  $\text{CF}_2$  species generated in a HFPO plasma with  $P = 200$  W and  $p = 50$  mTorr. a)  $\text{CF}_2$  radicals incident upon and scattered from an unbiased Si substrate, b)  $\text{CF}_2$  incident upon and scattered from a +200 V dc biased Si substrate, c)  $\text{CF}_2$  radicals in the incident beam only. Image subtraction of a) and c) yields a  $\text{CF}_2$  scatter image, d); image subtraction of b) and c) yields a  $\text{CF}_2$  scatter image for the case of the biased substrate, e). IRIS cross-sections taken along the laser propagation axis of the beam and scatter images along with fits to the data yield  $S(\text{CF}_2) = 1.03$  in the case of no substrate biasing, f), and  $S(\text{CF}_2) = 0.30$  in the case of +200 V biased Si, g). Thus,  $\Delta S(\text{CF}_2) = 0.73$  at these experimental conditions.

**Table 6.1.**  $\Delta S(\text{CF}_x)$  for different plasma feed gases.

<i>P</i> (W) Source	$\Delta S(\text{CF})$				$\Delta S(\text{CF}_2)$			
	50	100	150	200	50	100	150	200
CF <sub>4</sub>	0.30(0.13)	0.15(0.06)	0.28(0.10)	0.61(0.07)	0.26(0.07)	0.28(0.10)	0.57(0.10)	0.77(0.06)
C <sub>2</sub> F <sub>6</sub>	0.05(0.01)	0.03(0.01)	0.23(0.05)	0.84(0.05)	0.22(0.02)	0.15(0.04)	0.75(0.05)	1.08(0.05)
C <sub>3</sub> F <sub>8</sub>	0.34(0.06)	0.45(0.04)	0.85(0.02)	0.89(0.05)	0.46(0.04)	0.67(0.03)	0.64(0.03)	0.71(0.03)
C <sub>3</sub> F <sub>6</sub>	0.28(0.05)	0.31(0.06)	0.28(0.05)	0.34(0.05)	0.47(0.01)	0.49(0.02)	0.39(0.06)	0.60(0.02)
HFPO	0.22(0.06)	0.47(0.06)	0.29(0.02)	0.48(0.04)	0.13(0.03)	0.45(0.05)	0.54(0.07)	0.73(0.05)

intensity of each species was determined by comparison to the most abundant observed species,  $\text{CF}_3^+$ .  $\text{C}_2\text{F}_5^+$ ,  $\text{C}_3\text{F}_7^+$ ,  $\text{C}_2\text{F}_4^+$ ,  $\text{C}_3\text{F}_5^+$ ,  $\text{C}_3\text{F}_3^+$ , and  $\text{C}_6\text{F}_6^+$  species were identified in this RGA analysis. Notably, the maximum relative concentration of many of these species occurs at  $P = 150$  W in the  $\text{CF}_4$  plasma. These same oligomers were observed and monitored in plasmas produced from  $\text{C}_2\text{F}_6$ ,  $\text{C}_3\text{F}_8$ , and  $\text{C}_3\text{F}_6$  precursors, Fig. 6.6(b-d), despite the potential for the production of some of the oligomers to proceed through direct gas-phase decomposition of the precursor rather than through recombination reactions. Generally, oligomeric species peak in relative intensities at  $P = 150$  W, similar to the  $\text{CF}_4$  system. Moreover, the relative percentages of a given oligomeric unit increase with decreasing F/C ratios of the precursor. For example,  $\text{C}_2\text{F}_5^+$  fragments that are 1% abundant with respect to  $\text{CF}_3^+$  in a  $\text{CF}_4$  plasma with  $P = 50$  W, are roughly 10% abundant with respect to  $\text{CF}_3^+$  in a  $\text{C}_3\text{F}_6$  plasma operating under the same conditions.

Deposition rates of FC plasmas reflect the efficacy of film deposition and are intricately tied to the amount of gas-phase  $\text{C}_m\text{F}_n$  available for film initiation and propagation. Deposition rates for  $\text{CF}_4$ ,  $\text{C}_2\text{F}_6$ ,  $\text{C}_3\text{F}_8$ , and  $\text{C}_3\text{F}_6$  plasmas are provided in Fig. 6.7 as a function of  $P$ . In many cases, deposition rates increase with increasing  $P$ , maximizing at 150 W. The exception to this trend occurs with the  $\text{C}_2\text{F}_6$  feed, Fig. 6.7(b), where film deposition rates decrease as a function of  $P$ . Notably, as the precursor changes from  $\text{CF}_4$  to  $\text{C}_3\text{F}_6$ , Fig. 6.7(a-d), the values of the deposition rates increase at a given  $P$ , indicating that precursors with a lower F/C ratio yield more efficacious FC film deposition.

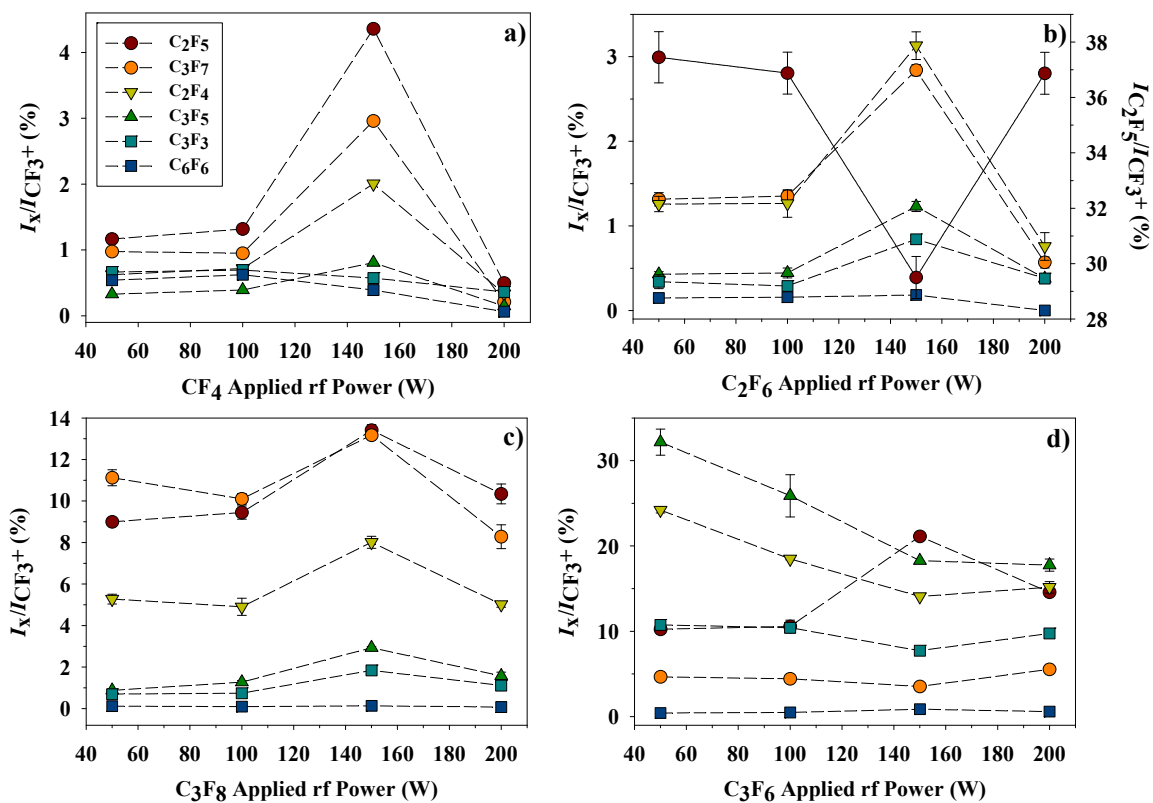


**Figure 6.6.** Relative intensities for oligomers observed in RGA mode analyses of a) CF<sub>4</sub>, b) C<sub>2</sub>F<sub>6</sub>, c) C<sub>3</sub>F<sub>8</sub>, and d) C<sub>3</sub>F<sub>6</sub> plotted as a function of  $P$ . Connecting lines are included as a guide for the eye and do not represent fits to the data.

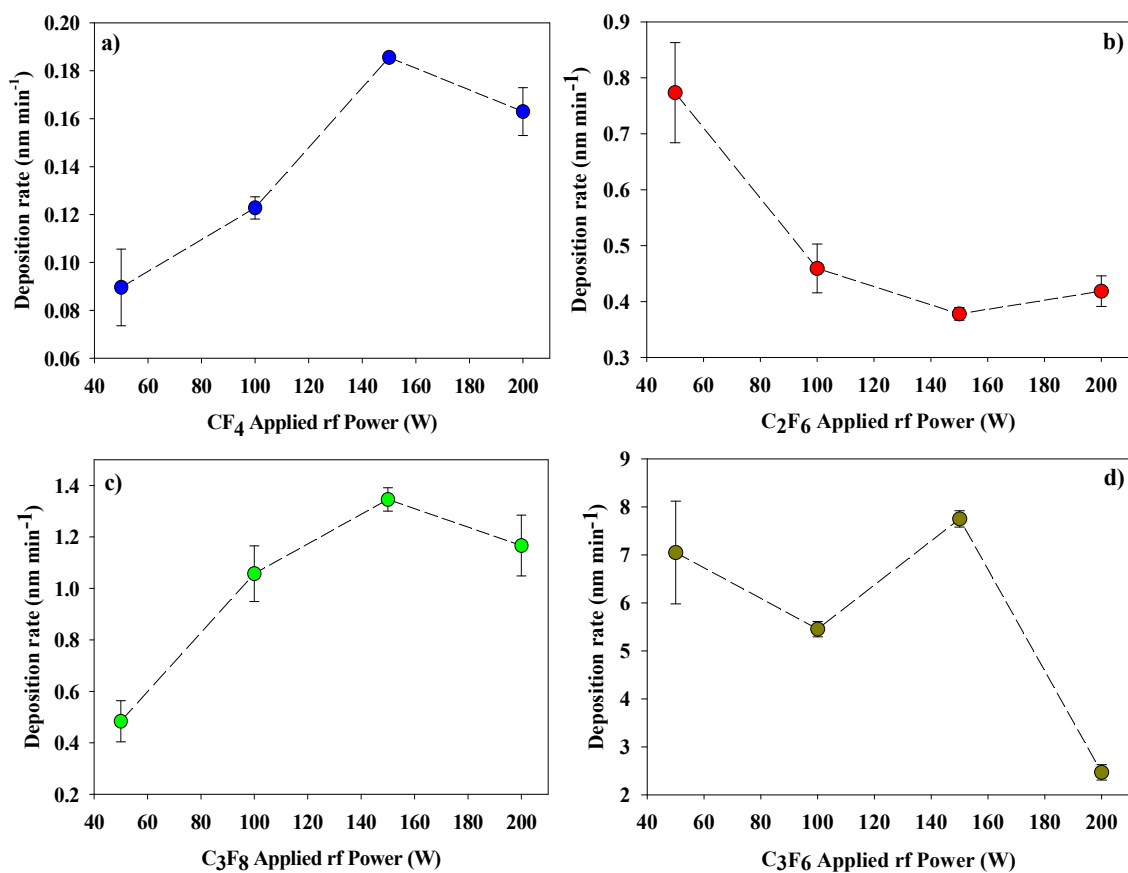


**Figure 6.7.** Deposition rates of FC films plotted as a function of  $P$  for a) CF<sub>4</sub>, b) C<sub>2</sub>F<sub>6</sub>, c) C<sub>3</sub>F<sub>8</sub>, and d) C<sub>3</sub>F<sub>6</sub> plasma sources. Connecting lines are included as a guide for the eye and do not represent fits to the data.

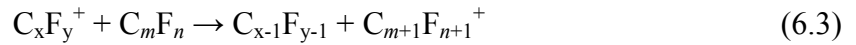
### 6.3. Discussion

The role of ions in plasma modification of materials is intricately related to both deposition and etching processes. We seek here to develop a more robust understanding of ion behavior in inductively-coupled fluorocarbon plasmas by examining ion contributions to gas-surface interactions. Mass spectrometry has been utilized to identify FC plasma species and to determine the average energies of ions produced in the plasma gas phase. Film deposition from different plasma systems can be related to the profusion of oligomeric species present in the plasma, whereas the surface reactivities of  $CF_x$  species are intimately related to the mean energies of ions.

$CF_3^+$  ions appear to dominate the mass spectra for the FC precursors studied here, Fig. 6.1. This species is a direct decomposition product of each of the feed gases. Indeed,  $CF_3^+$  has been shown to dominate the mass spectra of FC species as large as  $C_7F_{14}$  in electron impact ionization studies.<sup>47</sup> Furthermore, GIBMS experiments in the Armentrout laboratory have demonstrated complementary results. Specifically, in GIBMS experiments involving the reaction of energetic  $Ar^+$  with  $CF_4$ ,  $CF_3^+$  products predominate at all kinetic energies.<sup>16</sup> Interestingly, the onset of  $CF_2^+$  and  $CF^+$  only occurs at kinetic energies coinciding with the  $C^2T_2$  and  $D^2A_1$  electronic states of  $CF_4^+$ , respectively, implying that these products are most efficiently formed via a transition state of the tetrafluoromethane ion induced by collisions with  $Ar^+$ .<sup>16</sup> More recently, similar experiments for  $Ar^+ + C_3F_8$  have shown that  $CF_3^+$  can also be produced from other product ions, such as  $C_3F_7^+$  and possibly  $C_2F_5^+$ .<sup>48</sup> As the molecules undergo a large number of collisions prior to exiting the plasma source in our MS, our mass spectra undoubtedly reflect significant contributions from ion-molecule decomposition products. These types of data directly

connect the multi-collision conditions found in our plasmas with the single-molecule collision conditions found in the GIBMS and demonstrates the importance of both types of data.

The appearance of nascent ions with  $m/z$  ratios larger than the mass of the precursor feed in the spectra of various FC systems, notably for  $\text{CF}_4$ , Fig. 6.1a (inset), confirms that ions are formed through gas-phase recombination processes. Ions of relatively low energy may react in the gas phase, as in reaction (6.3), to form oligomeric ions or neutrals. Gas-phase



oligomerization tends to increase in both efficiency and profusion with a decrease in the precursor F/C ratio. Indeed, Stoffels and coworkers have reported plasma polymer species containing up to ten carbons.<sup>49</sup> This is also corroborated by the work of Shamamian, et al. who observed similar phenomena in isopropyl alcohol plasmas, in particular the protonation and ionization of the precursor molecule.<sup>50</sup> These species can participate in surface interactions and act directly as initiators or propagators of film growth, and can also activate surface sites on existing films. This latter process represents the well-established activated growth model (AGM), originally proposed by d'Agostino and coworkers, wherein charged particle bombardment provides an avenue for continued film growth at a passivated site.<sup>27</sup> Although surface bombardment with relatively low energy species may lead to film propagation, high energy ion bombardment is responsible for removal of material at surfaces. Hence, it is the energy distribution that controls which process dominates in a given FC system.

The IEDs for  $\text{CF}_3^+$  ions shown in Fig. 6.2 are markedly dependent upon the chosen feed gas. Notably, the multimodal distribution observed in  $\text{CF}_4$  and  $\text{C}_2\text{F}_6$  plasmas, Fig. 6.2(a,b), is essentially absent in the  $\text{C}_3\text{F}_8$ ,  $\text{C}_3\text{F}_6$ , and HFPO systems, Fig. 6.2(c-e). Indeed, IEDs for  $\text{CF}_4$  and  $\text{C}_2\text{F}_6$  sources are comparable to those reported for  $\text{CF}_3^+$  species in capacitively-coupled  $\text{CF}_4/\text{Ar}$  plasmas by Li and coworkers.<sup>51</sup> Moreover, the narrower distributions arising from  $\text{C}_3\text{F}_8$ ,  $\text{C}_3\text{F}_6$ , and HFPO are similar to those reported by Edelberg et al.<sup>41</sup> The peaks in these distributions arise due to sheath effects in the plasma, specifically, the transit time of ions across the sheath ( $\tau_{\text{ions}}$ ) and the collisional processes leading to formation of ions *within* the boundaries of the sheath. The difference in IEDs between different plasma precursors thus implies that the choice of precursor influences the sheath potential at a given set of conditions. The acceleration of positively charged ions across the sheath and the resulting IEDs thus can be considered a function of precursor choice.

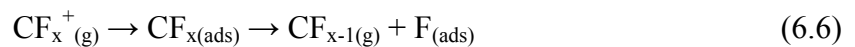
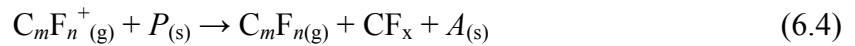
It is of interest to gauge whether IEDs are comparable for *all* nascent ions that exist in a particular plasma system at a given set of conditions. This is depicted for the ions present in a  $\text{C}_2\text{F}_6$  plasma operating with  $P = 200$  W and  $p = 50$  mTorr in Fig. 6.3(a-f). Here, the IEDs for all observed ions are relatively similar, especially those for  $\text{CF}^+$ ,  $\text{CF}_2^+$ , and  $\text{CF}_3^+$ , which are the most abundant nascent ions. The average ion energy for each of the IEDs can be calculated according to (6.1), with the results plotted as a function of  $P$  in Fig. 6.3(g). There are two important aspects of this plot. First,  $\langle E_i \rangle$  values tend to increase with increasing  $P$ . A broadening of the IED occurs with increased  $P$ , and higher energy features become more pronounced. This phenomenon can be rationalized in terms of sheath effects; sheath thickness ( $d_{\text{SH}}$ ) tends to decrease with increasing plasma

power even though the ion density of the plasma increases.  $\tau_{\text{ions}}$  decreases concomitantly with the decrease in  $d_{\text{SH}}$ , and as a result, fewer ion-ion or ion-molecule collisions resulting in energy loss occur within the sheath, and a broader distribution of ion energies result. Simulations of  $\text{Ar}^+$  in glow discharge systems as a function of sheath length have yielded complementary conclusions, where the IED is broadest at the smallest  $d_{\text{SH}}$ .<sup>52</sup> The second key aspect of Fig. 6.3(g) is the apparent equilibration of mean ion energies at a given set of plasma conditions for a range of masses ( $\text{CF}^+$ - $\text{C}_3\text{F}_7^+$ ). This result is not completely unexpected given previous reports from our laboratory<sup>35</sup> and the literature.<sup>53</sup> Kushner has modeled the IEDs for generalized capacitively-coupled plasmas and has shown that a wide range of masses attain very similar IEDs when operating with a given rf frequency.<sup>53</sup> Thus, the distribution of ion energies is relatively independent of changes in mass, but is dependent upon the chosen rf frequency.

Total average ion energies, Fig. 6.4, generally increase with increasing  $P$  for all precursors examined here, as discussed above for  $\text{C}_2\text{F}_6$ . Absolute  $\langle E_i \rangle_{\text{total}}$  values at a given set of plasma conditions appear to be strongly dependent upon the source gas. The disparity between the systems with the highest  $\langle E_i \rangle_{\text{total}}$  ( $\text{CF}_4$ ) and the lowest  $\langle E_i \rangle_{\text{total}}$  ( $\text{C}_2\text{F}_6$   $P < 200$  W,  $\text{C}_3\text{F}_6$   $P = 200$  W) is consistently around 40 eV. The differences in  $\langle E_i \rangle_{\text{total}}$  among the different plasma systems result from different plasma potentials,  $V_p$ . As such, energy analysis of positive ions has been used as an indirect method to gauge  $V_p$ .<sup>54</sup> Thus, exposure of a substrate to different plasma sources, regardless of applied rf plasma power, may result in drastically different ion effects, and ultimately different overall plasma processes. Moreover, modulation of ion energies impinging on a surface may proceed as a function of substrate surface potential,  $V_s$ ; this effect can be exacerbated

via application of an external dc bias. Thus, close examination of plasma-surface interface reactions occurring during processing of a substrate as a function of ion bombardment is imperative.

Plasma-surface interface reactions involving unsaturated species such as radicals can be strongly affected by ion bombardment.<sup>55</sup> Figure 6.5 demonstrates the influence of substrate biasing on the observed scatter coefficient for CF<sub>2</sub> radicals in the HFPO plasma. The application of +200 V dc bias results in a significant decrease in  $S(\text{CF}_2)$ , with  $\Delta S(\text{CF}_2) = 0.30$ . This decrease is a direct result of repulsion of the vast majority of the incident ions, as the IEDs in Fig. 6.4 indicate our ions are ~50 eV in average energy and the highest energy ions possess  $E_i < 120$  eV, Fig. 6.2(e). Potential ramifications of these ion-restricted IRIS measurements include: (1) limited ablation of a FC passivation layer,  $P(s)$ , to produce CF<sub>x(g)</sub> radicals and expose an active surface site,  $A(s)$  [reaction (6.4)], and (2) limited neutralization and dissociative neutralization reactions at the surface [reactions (6.5) and (6.6), respectively] because of the extremely low



concentration of impinging ions expected to penetrate the surface potential at the plasma-substrate interface. Note that reaction (6.4) can occur in systems that deposit thick FC films, in addition to those that only passivate the surface with a very thin FC layer. These processes result in an overall decrease in observed scatter coefficient for CF<sub>x</sub> species as compared to when there is no manipulation of the charged species in the molecular beam. Thus, it is anticipated that all  $\Delta S(\text{CF}_x) > 0$ , which is indeed the case, Table 6.1. These

positive values indicate that ions contribute significantly to  $CF_x$  surface production through reactions such as those depicted in reactions (6.4)-(6.6). The relationship between ion energies and  $\Delta S(CF_x)$  values is illustrated in Fig. 6.8, which demonstrates that increases in ion energy generally give rise to increased  $\Delta S(CF_x)$ . Interestingly, similar phenomena are observed [i.e. an overall decrease in  $S(CF_x)$ ] by using a grounded mesh placed in the path of the molecular beam to limit ion flux to the surface. This implies that ion-surface interactions, and not  $V_s$  effects, are major contributors to the surface-mediated production of  $CF_x$ . The energies associated with the ions in these plasma systems, however, are unlikely to etch an underlying substrate such as Si. Abrams and Graves demonstrated through molecular dynamics simulations of  $CF_x^+$  bombardment of Si that slow net etching is only achieved by the  $CF_2^+$  ion at energies approaching 200 eV.<sup>56</sup> Moreover, they showed that  $CF_3^+$  ions have a propensity to undergo reactions such as in (6.6) to form  $CF_{2(g)}$ .<sup>57</sup> Thus, the phenomena investigated here are representative of ion effects of FC gas-phase species on FC surfaces as opposed to the underlying substrate.

In addition to ion-assisted ablation processes wherein material is removed from the FC film, ions can also indirectly contribute to film deposition. For example, surface activation by ion bombardment in  $C_4F_8$  plasmas has been shown to facilitate FC film growth.<sup>58</sup> Gas-phase oligomerization reactions, such as that depicted in reaction (6.3), can generate precursor species requisite for FC film initiation and propagation. The profusion of oligomeric species in the plasma gas phase was correlated with the propensity for FC film deposition, Figs. 6.6 and 6.7. Figure 6.6 contains  $I(X)/I(CF_3^+)$  ratios for oligomeric gas-phase plasma species (X) acquired with the MS ionizing source on. In this

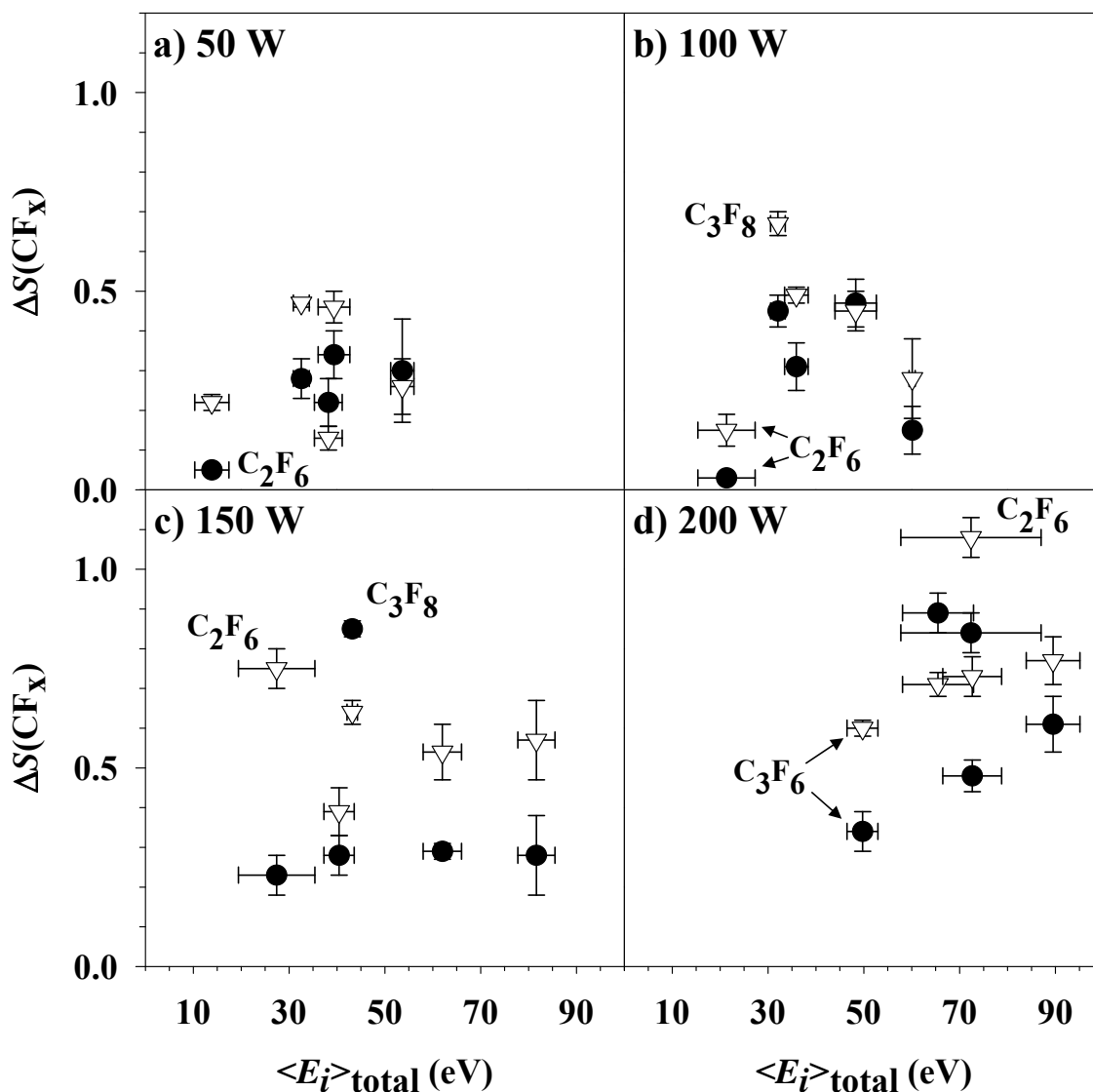


**Figure 6.8.**  $\Delta S(\text{CF})$  (circles) and  $\Delta S(\text{CF}_2)$  (triangles) values plotted as a function of  $\langle E_i \rangle_{\text{total}}$  for  $\text{CF}_4$ ,  $\text{C}_2\text{F}_6$ ,  $\text{C}_3\text{F}_8$ ,  $\text{C}_3\text{F}_6$ , and HFPO precursors with  $P = 50, 100, 150,$  and  $200$  W, a)-d), respectively. Outlying data points in each plot are labeled accordingly with the corresponding precursor gas.

configuration, the resulting data do not expressly distinguish neutral and ionic oligomers. Maximum relative concentrations of species are generally achieved at  $P = 150$  W, suggesting that the power dissipated to the plasma is a strong indicator of gas-phase recombination proclivity. Specifically, the decomposition products (neutrals, ions, etc.) of a given precursor gas increase with  $P$ . These species may recombine as in reaction (6.3) or related reactions to produce the species depicted in Fig. 6.6. However, above a certain  $P$ , in this case 150 W, these recombination reactions become inefficient as a result of either complete fragmentation of the precursor gas or inhibition of oligomer formation via immediate destruction of the recombination product.

There are several exceptions to the trend of maximum gas-phase concentrations at  $P = 150$  W. For example, it is evident that the relative proportion of  $C_2F_5^+$  in the  $C_2F_6$  system, Fig. 6.6(b), reaches a minimum at 150 W. Because  $C_2F_5$  is a direct decomposition product of the plasma feed gas in this system, it is reasonable to assume that this species actively participates in subsequent oligomerization reactions such as depicted in reaction (6.3). As such, it is largely consumed at  $P = 150$  W for production of larger gas-phase species. Nonetheless, the relative amount of  $C_2F_5^+$  in this plasma dominates all others by nearly an order of magnitude; thus this species is expected to have the greatest influence over the observed deposition rates for the  $C_2F_6$  plasma as a function of  $P$ . For  $C_3F_6$  plasmas, Fig. 6.6(d), a similar, although less dramatic, effect is observed for  $C_2F_4^+$  and  $C_3F_5^+$  as a function of  $P$ . These decomposition products are produced via the loss of  $CF_2$  or a F atom, respectively.

A second significant feature of Fig. 6.6 is that the relative counts for many of the observed oligomers increase significantly with decreasing F/C ratio of the chosen precursor.

sor. This is ostensibly a result of an increasing quantity of potential  $C_xF_y$  breakdown products that in turn yield an increasing amount of gas-phase oligomers, in the larger precursor plasmas. Overall, the anticipated effect on FC film deposition should hence be twofold: (1) the deposition rates for FC films should display a vertex at  $P = 150$  W and (2) the efficiency of the deposition (i.e. absolute value of the deposition rate) should increase with decreasing F/C content of the plasma precursors. Indeed, the film deposition rates, Fig. 6.7, mirror the trends observed in Fig. 6.6 for each of the chosen precursors. The deposition rate decreases with increasing  $P$  only for the  $C_2F_6$  plasma, Fig. 6.7(b), implying that the  $C_2F_5$  species does indeed contribute most significantly to film growth from this system.

The deposition rates for all of the FC plasmas should also be considered in terms of the corresponding  $\langle E_i \rangle_{\text{total}}$  and  $\Delta S(CF_x)$  values. The values of mean ion energies for  $CF_4$ ,  $C_2F_6$ ,  $C_3F_8$ , and  $C_3F_6$  plasmas, Fig. 6.4, do not appear to have a direct influence over FC deposition rates at a given  $P$ . Rather, a steady-state balance between film deposition and ion-assisted ablation likely develops very rapidly upon substrate exposure to the plasma. The net result of this balance gives rise to the observed scatter coefficients,  $S(CF_x)$ . It should be noted that the FC films deposited from these systems are generally amorphous, as confirmed by high-resolution x-ray photoelectron spectroscopy analyses, Chapter 4,<sup>45</sup> and thus contain a broad range of  $C-F_{x(s)}$  moieties. Results from the IRIS experiments where  $S > 1$  thus imply removal of such  $C-F_x$  units from films deposited from gas-phase  $C_mF_n$  ( $m > 1$ ) oligomers. As discussed above, energetic ions are largely responsible for ablation of FC-deposited materials. Ultimately, the effect of  $\langle E_i \rangle_{\text{total}}$  on  $\Delta S(CF_x)$  can be evaluated by examination of Fig. 6.8. A distinct “pocket” of  $\Delta S(CF_x)$

values emerges at  $P = 50$  W, Fig. 6.8(a), where small changes in  $S$  are commensurate with relatively low mean ion energies. This pocket shifts up and to the right and broadens as  $P$  increases, Fig. 6.8(b-d), reflecting the propensity for higher energy ions to give rise to a larger  $\Delta S(\text{CF}_x)$  value. Outliers in these plots suggest competing processes that dictate  $\Delta S(\text{CF}_x)$ , but do not necessarily involve ion-surface interactions.

#### 6.4. Summary

The work discussed here has sought to correlate ion behavior with plasma-surface interface phenomena. In particular, this chapter has focused on the intimate relationship between ion energies for nascent plasma species and surface reactivities of  $\text{CF}_x$  species observed in IRIS experiments. Energetic ions clearly influence the plasma-surface interface behavior of these radicals; limiting ion flux to the surface significantly decreases observed  $S(\text{CF}_x)$  values. Interestingly, the effect of ions during plasma processing relies upon the choice of FC plasma precursor, and so too does the efficacy of FC film deposition. As the precursor F/C ratio decreases, total mean ion energies decrease concomitantly, and film deposition rates increase substantially. Preliminary data regarding the effect of precursor pressure indicates that ion energies decrease significantly with increasing  $p$ . Changes in  $p$  also have profound effects on the deposition efficiency of FC plasmas; for  $\text{CF}_4$  systems, increasing  $p$  results in a significant decrease in deposition rates of FC films, whereas the opposite trend is observed for  $\text{C}_3\text{F}_6$  feeds. Though these latter studies necessitate further inquiry with regards to parameter space investigations in FC systems, it is nonetheless apparent that the results presented here complement the understanding gleaned from power studies. Experimental results help to validate models of complex

systems and advance a more comprehensive view of the fundamental aspects of plasma-surface interactions. Ultimately, these insights may pave an avenue for improved plasma processes in a wide range of applications.

## 6.5. Supplemental Information

The studies presented in the previous sections of this chapter focused largely on the effect of changing  $P$  to explicate ion behavior. However, it is also of particular interest to examine plasma systems as a function of changing feed gas pressure,  $p$ . Increases in  $p$  generally result in a decrease in concentration of fluorine atoms and an increase in electron density in FC plasmas.<sup>59</sup> The higher density of species ultimately results in a decrease in electron temperature,  $T_e$ , that, in turn, leads to a decrease in  $V_p$ .<sup>60</sup> Consequently, ions do not experience as sharp a gradient between  $V_p$  and the sheath potential,  $\Phi$  (Fig. 1.1), and thus ion energies tend to decrease. Concurrent with the increase in species densities, the mean free paths of plasma species decrease, resulting in an increased propensity for loss of energy via collisional effects with increasing  $p$ . This results in a narrowing or thermalization of ion energies. The net effect of these phenomena is depicted in Fig. 6.9, where  $\text{CF}_3^+$  IEDs are shown for  $\text{CF}_4$  plasmas as a function of changing feed gas pressure. Increasing  $p$  from 50 to 200 mTorr results in a shift from a broad, multimodal IED, Fig. 6.9(a), to a narrow, single peak of relatively low energy, Fig. 6.9(c). Each of these IEDs were collected with  $P = 200$  W. Similar effects with respect to  $p$  have been observed for Ar discharges, where decreases in  $\text{Ar}^+$  mean ion energies of up to 50% over a range of 50 mTorr were reported.<sup>61</sup>

Increasing  $p(\text{CF}_4)$  results in a decrease in  $\langle E_i \rangle$  for each of the nascent ions  $\text{CF}^+$ ,  $\text{CF}_2^+$ , and  $\text{CF}_3^+$ , Fig. 6.10 (left ordinate axis), where  $\langle E_i \rangle_{\text{total}}$  decreases by  $\sim 50\%$  over the range  $p = 50\text{-}200$  mTorr. This decrease in ion energy directly impacts the amount of

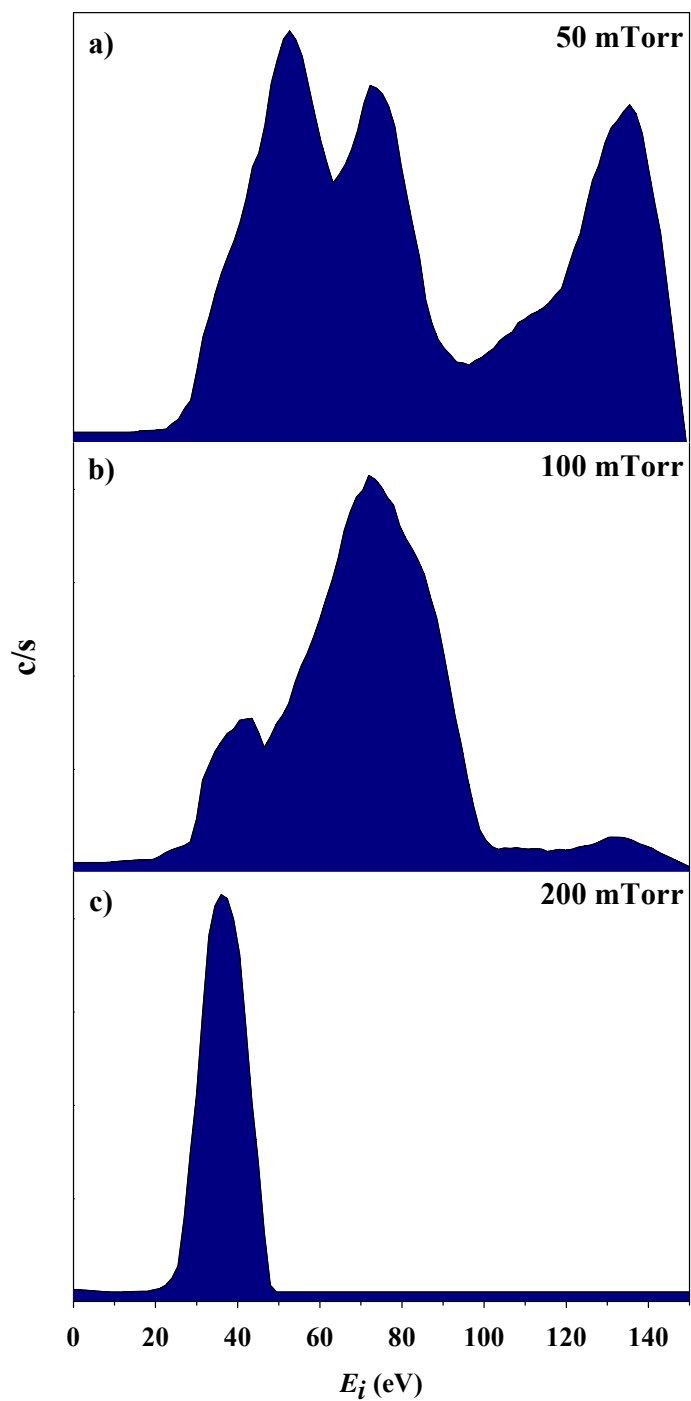


**Figure 6.9.** Ion energy distributions for the  $\text{CF}_3^+$  ion ( $m/z = 69$ ) in a  $\text{CF}_4$  plasma operating at  $P = 200$  W at feed gas pressures of a) 50, b) 100, and c) 200 mTorr.

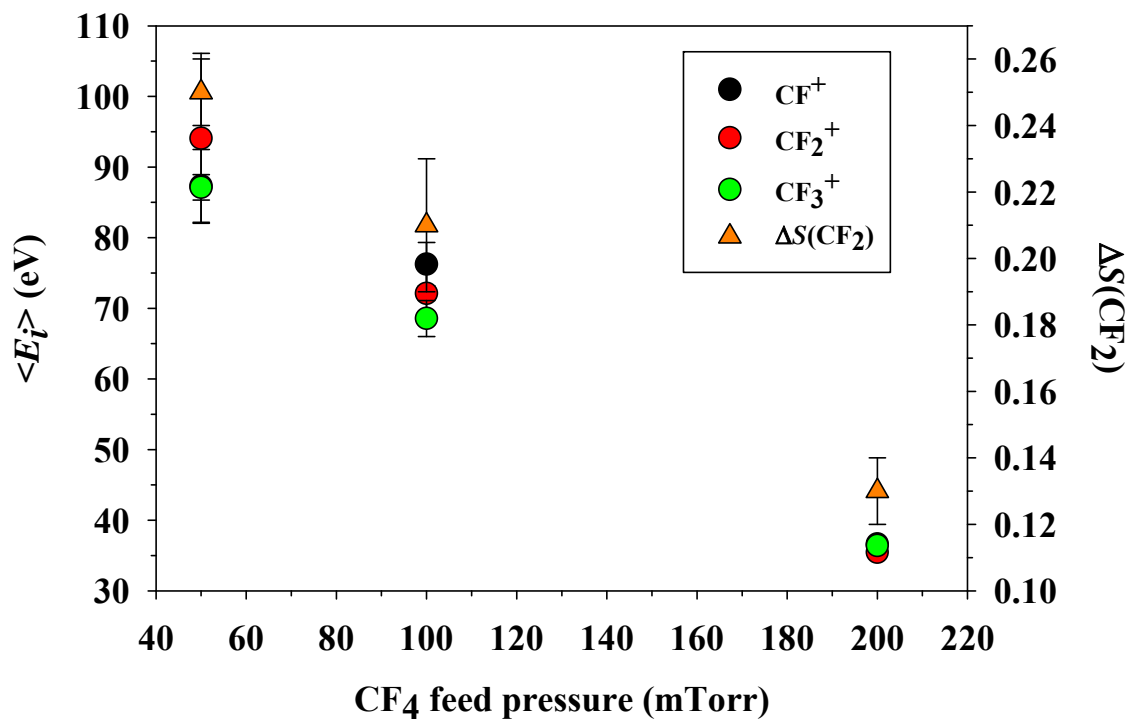


**Figure 6.10.**  $\langle E_i \rangle$  values (left y-axis) plotted as a function of  $\text{CF}_4$  plasma feed pressure for  $\text{CF}^+$ ,  $\text{CF}_2^+$ , and  $\text{CF}_3^+$  nascent ions. Also plotted are corresponding  $\Delta S(\text{CF}_2)$  values (right y-axis). All data were collected for  $P = 200$  W.

scatter observed for  $\text{CF}_2$ , Fig. 6.10 (right ordinate). Indeed,  $\Delta S(\text{CF}_2)$  decreases by  $\sim 50\%$  as well over the same pressure range. This correlation further validates the notion that ions play a substantial role in dictating  $S(\text{CF}_2)$ . These contributions could include surface neutralization processes such as outlined in reactions (6.5)-(6.6) or ablation of FC films, such as in (6.4). It should be noted that any ablation processes [i.e. reaction (6.4)] rely upon the efficacious deposition of FC films or passivation layers.

Ostensibly, increasing  $p$  ought to yield higher concentrations of polymerizing species, due to the decrease in electron energy that, in turn, inhibits complete dissociation of the plasma precursor. However, a *decrease* is observed in all oligomeric species in a  $\text{CF}_4$  plasma with increasing  $p$ , Fig. 6.11(a). These data, similar to those reported above, were collected in RGA mode, meaning that the MS ionization filament was turned on; thus the results do not distinguish between nascent plasma ions and those species ionized at the detector. The trend of decreasing oligomeric species concentrations with  $p$  is not a result of changes in  $\text{CF}_3^+$  concentration, as the  $\text{CF}_3^+$  signal does not change appreciably over the pressure range. Thus, the propensity for forming polymerizing gas-phase film precursors is inhibited in  $\text{CF}_4$  as  $p$  increases. This manifests in a significant decrease in film deposition rate, Fig. 6.11(b). The decline in oligomeric species concentrations is starkly contrasted by the trends observed for other FC systems, in particular  $\text{C}_3\text{F}_6$ , Fig. 6.11(c). Increasing  $p$  for this plasma feed results in an overall increase in polymerizing gas-phase species, and therefore, an increase in film deposition rates, Fig. 6.11(d).

The reason for the decrease in polymerizing species with  $p$  in the case of the  $\text{CF}_4$  plasma is an issue that warrants further examination; nonetheless, we present here some

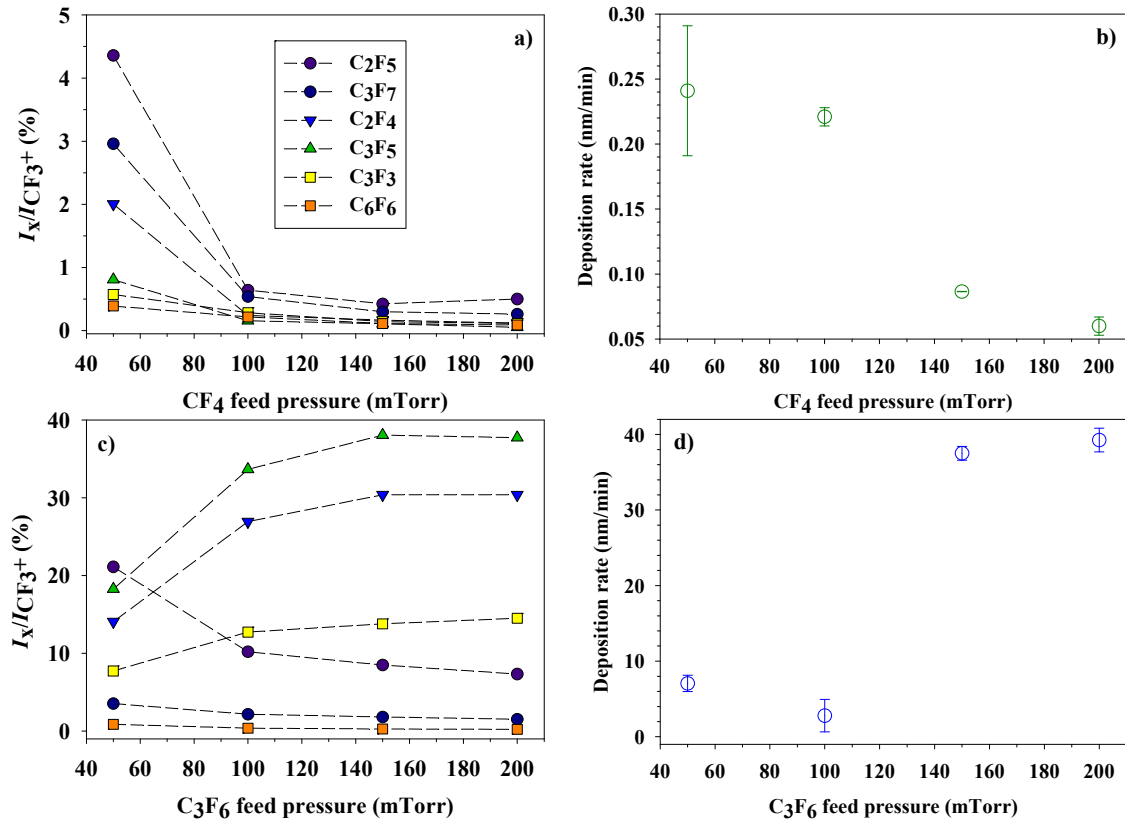


**Figure 6.11.** Relative gas-phase oligomer concentrations with respect to the  $CF_3^+$  signal are plotted as a function of pressure in a) for a  $CF_4$  plasma with  $P = 150$  W. Corresponding deposition rates on Si substrates are provided in b). Complementary data are shown for  $C_3F_6$  plasmas in c) and d).

current speculations on the nature of this system.  $\text{CF}_4$  plasmas in particular comprise a significant concentration of ions with respect to neutral species.<sup>62</sup> Increasing  $p$  results in an overall decrease in  $\text{C}_m\text{F}_n^+$  concentration due to the effects aforementioned. Assuming that a significant contribution to the profusion of oligomeric neutral species in the  $\text{CF}_4$  system is given by reactions such as that outlined in (6.3), increasing  $p$  thereby limits the production of  $\text{C}_{m+1}\text{F}_{n+1}$  oligomers by rendering  $\text{C}_m\text{F}_n^+$  the limiting reagent in the reaction. Indeed, a significant decrease in the amount of nascent  $\text{C}_m\text{F}_n^+$  ions is observed with increased  $p$  for the  $\text{CF}_4$  system, indicating that the gas-phase behavior of  $\text{C}_m\text{F}_n^+$  species are ultimately of significant import to film deposition in this system.

An additional point for consideration entails understanding the effect of ion bombardment on the characteristics of a deposited FC film. As noted above, ions can contribute to FC film formation by exposing active sites on a surface where film initiation may occur. Limiting ion flux to the surface should thus render film deposition less efficacious. Preliminary results indicate that for FC films deposited on Si wafers experiencing +200 V dc biasing, the deposition rate is approximately an order of magnitude lower than for deposition on a wafer with no applied bias. The chemical composition of the films is also an important feature to consider. FC films deposited from HFPO are expected to contain  $\text{CF}_2$ -rich moieties,<sup>63</sup> which has indeed been observed in this study, Fig. 6.12(a). However, as depicted in Fig. 6.12(b), a film deposited on biased Si is markedly different. This film is much more crosslinked ( $\sim 85\%$ ) than the film deposited on a non-biased wafer ( $\sim 53\%$ ), and has a film F/C ratio nearly an order of magnitude less (0.36 and 1.72, respectively). Such striking differences may be attributed to a dearth of active sites produced via ion bombardment in the case of substrate biasing, but may also suggest that

ions themselves are incorporated into FC films and contribute to film growth in this fashion. Ling and coworkers<sup>64</sup> have examined similar phenomena in  $C_4F_8$  plasmas and confirm that this latter effect is the determining factor for robust FC film deposition.

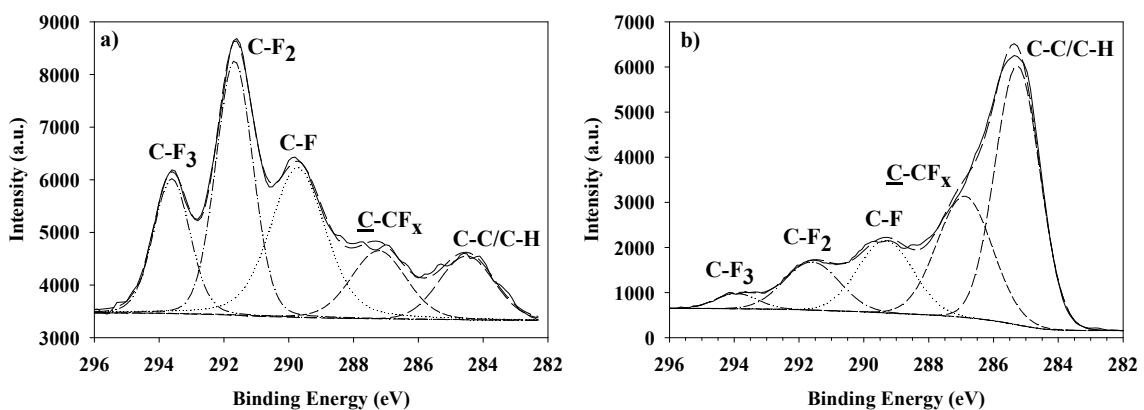


**Figure 6.12.** High-resolution C<sub>1s</sub> XPS spectra for FC films deposited from  $P = 100$  W,  $p = 50$  mTorr HFPO plasmas on Si substrates. For a), no bias was applied to the substrate during modification. In b), a continuous +200 V dc bias was applied directly to the substrate throughout the duration of plasma exposure.

## 6.6. References

1. Rossnagel, S. M.; Cuomo, J. J.; Westwood, W. D., Handbook of Plasma Processing Technology - Fundamentals, Etching, Deposition, and Surface Interactions. In William Andrew Publishing/Noyes: 1990.
2. Graves, D. B.; Brault, P., Molecular dynamics for low temperature plasma-surface interaction studies. *J. Phys. D: Appl. Phys.* **2009**, *42*, (19), 194011.
3. Oehrlein, G. S.; Phaneuf, R. J.; Graves, D. B., Plasma-polymer interactions: A review of progress in understanding polymer resist mask durability during plasma etching for nanoscale fabrication. *J. Vac. Sci. Technol. B* **2011**, *29*, (1).
4. von Keudell, A.; Jacob, W., Elementary processes in plasma-surface interaction: H-atom and ion-induced chemisorption of methyl on hydrocarbon film surfaces. *Prog. Surf. Sci.* **2004**, *76*, (1-2), 21-54.
5. Abe, H.; Yoneda, M.; Fujiwara, N., Developments of plasma etching technology for fabricating semiconductor devices. *Jpn. J. Appl. Phys.* **2008**, *47*, 1435-1455.
6. Fridman, A., *Plasma Chemistry*. Cambridge University Press: New York, 2008.
7. Armentrout, P. B., Kinetic Energy Dependence of Ion-Molecule Reactions Related to Plasma Chemistry. In *Advances In Atomic, Molecular, and Optical Physics*, Bederson, B.; Walther, H., Eds. Academic Press: 2000; Vol. 43, pp 187-229.
8. Boo, B. H.; Armentrout, P. B., Reaction of Silicon Ion (2p) with Silane (SiH<sub>4</sub>, SiD<sub>4</sub>) - Heats of Formation of SiH, SiH<sub>2</sub>, SiH<sub>3</sub>, SiH<sup>+</sup>, SiH<sub>2</sub><sup>+</sup>, SiH<sub>3</sub><sup>+</sup>, and Si<sub>2</sub><sup>+</sup>, Si<sub>2</sub>H<sup>+</sup>, Si<sub>2</sub>H<sub>2</sub><sup>+</sup>, Si<sub>2</sub>H<sub>3</sub><sup>+</sup> - Remarkable Isotope Exchange-Reaction Involving 4 Hydrogen Shifts. *J. Am. Chem. Soc.* **1987**, *109*, (12), 3549-3559.
9. Fisher, E. R.; Armentrout, P. B., Kinetic-Energy Dependence of Dissociative Charge-Transfer Reactions of He<sup>+</sup>, Ne<sup>+</sup>, Ar<sup>+</sup>, Kr<sup>+</sup>, and Xe<sup>+</sup> with Silane. *J. Chem. Phys.* **1990**, *93*, (7), 4858-4867.
10. Fisher, E. R.; Armentrout, P. B., Reactions of O<sub>2</sub><sup>+</sup>, Ar<sup>+</sup>, Ne<sup>+</sup>, and He<sup>+</sup> with SiCl<sub>4</sub> - Thermochemistry of SiCl<sub>x</sub><sup>+</sup> (X = 1-3). *J. Phys. Chem.* **1991**, *95*, (12), 4765-4772.
11. Fisher, E. R.; Armentrout, P. B., Translational and Internal Energy Effects in Reactions of O<sup>+</sup> and O<sub>2</sub><sup>+</sup> with SiF<sub>4</sub>. *Chem. Phys. Lett.* **1991**, *179*, (5-6), 435-441.
12. Kickel, B. L.; Fisher, E. R.; Armentrout, P. B., Dissociative Charge-Transfer Reactions of N<sup>+</sup>(<sup>3</sup>P), N<sub>2</sub><sup>+</sup>(<sup>2</sup>Σ<sub>g</sub><sup>+</sup>), Ar<sup>+</sup>(<sup>2</sup>P<sub>3/2,1/2), and Kr<sup>+</sup>(<sup>2</sup>P<sub>3/2) with SiF<sub>4</sub> - Thermochemistry of SiF<sub>4</sub><sup>+</sup> and SiF<sub>3</sub><sup>+</sup>. *J. Phys. Chem.* **1993**, *97*, (39), 10198-10203.</sub></sub>
13. Kickel, B. L.; Fisher, E. R.; Armentrout, P. B., Guided Ion-Beam Studies of the Reaction of Si<sup>+</sup> (<sup>2</sup>P) with Methylsilane - Reaction-Mechanisms and Thermochemistry of Organosilicon Species. *J. Phys. Chem.* **1992**, *96*, (6), 2603-2609.
14. Weber, M. E.; Armentrout, P. B., Energetics and Dynamics in the Reaction of Si<sup>+</sup> with SiF<sub>4</sub> - Thermochemistry of SiF<sub>x</sub> and SiF<sub>x</sub><sup>+</sup> (X=1,2,3). *J. Chem. Phys.* **1988**, *88*, (11), 6898-6910.
15. Weber, M. E.; Armentrout, P. B., Reactions of Ar<sup>+</sup>, Ne<sup>+</sup>, and He<sup>+</sup> with SiF<sub>4</sub> from Thermal-Energy to 50 eV CM. *J. Chem. Phys.* **1989**, *90*, (4), 2213-2224.
16. Fisher, E. R.; Weber, M. E.; Armentrout, P. B., Dissociative charge transfer reactions of Ar<sup>+</sup>, Ne<sup>+</sup>, and He<sup>+</sup> with CF<sub>4</sub> from thermal to 50 eV. *J. Chem. Phys.* **1990**, *92*, (4), 2296-2302.

17. Jin, Y.; Ajmera, P. K.; Lee, G. S.; Singh, V., Ultralow-k silicon containing fluorocarbon films prepared by plasma-enhanced chemical vapor deposition. *J. Electron. Mater.* **2005**, 34, (9), 1193-1205.
18. Itoh, A.; Inokuchi, A.; Yasuda, S.; Teramoto, A.; Goto, T.; Hirayama, M.; Ohmi, T., Low Dielectric Constant Nonporous Fluorocarbon Films for Interlayer Dielectrics. *Jpn. J. Appl. Phys.* **2008**, 47, (4), 2515-2520.
19. Schaepkens, M.; Standaert, T.; Rueger, N. R.; Sebel, P. G. M.; Oehrlein, G. S.; Cook, J. M., Study of the SiO<sub>2</sub>-to-Si<sub>3</sub>N<sub>4</sub> etch selectivity mechanism in inductively coupled fluorocarbon plasmas and a comparison with the SiO<sub>2</sub>-to-Si mechanism. *J. Vac. Sci. Technol. A* **1999**, 17, (1), 26-37.
20. Rueger, N. R.; Beulens, J. J.; Schaepkens, M.; Doemling, M. F.; Mirza, J. M.; Standaert, T.; Oehrlein, G. S., Role of steady state fluorocarbon films in the etching of silicon dioxide using CHF<sub>3</sub> in an inductively coupled plasma reactor. *J. Vac. Sci. Technol. A* **1997**, 15, (4), 1881-1889.
21. Li, X.; Hua, X. F.; Ling, L.; Oehrlein, G. S.; Barela, M.; Anderson, H. M., Fluorocarbon-based plasma etching of SiO<sub>2</sub>: Comparison of C<sub>4</sub>F<sub>6</sub>/Ar and C<sub>4</sub>F<sub>8</sub>/Ar discharges. *J. Vac. Sci. Technol. A* **2002**, 20, (6), 2052-2061.
22. Martinu, L.; Poitras, D., Plasma deposition of optical films and coatings: A review. *J. Vac. Sci. Technol. A* **2000**, 18, (6), 2619-2645.
23. Choy, K. L., Chemical vapour deposition of coatings. *Prog. Mater. Sci.* **2003**, 48, (2), 57-170.
24. Griesser, H. J.; Gengenbach, T. R.; Dai, L. M.; Li, S.; Chatelier, R. C., Plasma surface modifications for structural and biomedical adhesion applications. In *First International Congress on Adhesion Science and Technology - Invited Papers*, Brill Academy Publishing: Leiden, Netherlands, 1998; pp 307-328.
25. Sant, S. P.; Nelson, C. T.; Overzet, L. J.; Goeckner, M. J., Relationship between gas-phase chemistries and surface processes in fluorocarbon etch plasmas: A process rate model. *J. Vac. Sci. Technol. A* **2009**, 27, (4), 631-642.
26. Favia, P.; Creatore, M.; Palumbo, F.; Colaprico, V.; d'Agostino, R., Process control for plasma processing of polymers. *Surf. Coat. Technol.* **2001**, 142-144, (0), 1-6.
27. d'Agostino, R.; Capezzuto, P.; Bruno, G.; Cramarossa, F., Mechanism of etching, polymerization and deposition in rf discharges. *Pure & Appl. Chem.* **1985**, 57, (9), 1287-1298.
28. Silapunt, R.; Wendt, A. E.; Kirmse, K.; Losey, L. P., Ion bombardment energy control for selective fluorocarbon plasma etching of organosilicate glass. *J. Vac. Sci. Technol. B* **2004**, 22, (2), 826-831.
29. Wang, S. B.; Wendt, A. E., Ion bombardment energy and SiO<sub>2</sub>/Si fluorocarbon plasma etch selectivity. *J. Vac. Sci. Technol. A* **2001**, 19, (5), 2425-2432.
30. Oehrlein, G. S.; Zhang, Y.; Vender, D.; Haverlag, M., Fluorocarbon high-density plasmas. I. Fluorocarbon film deposition and etching using CF<sub>4</sub> and CHF<sub>3</sub>. *J. Vac. Sci. Technol. A* **1994**, 12, (2), 323-332.
31. Cunge, G.; Booth, J. P., CF<sub>2</sub> production and loss mechanisms in fluorocarbon discharges: Fluorine-poor conditions and polymerization. *J. Appl. Phys.* **1999**, 85, (8), 3952-3959.

32. Fisher, E. R.; Armentrout, P. B., The appearance energy of  $\text{CF}_3^+$  from  $\text{CF}_4$ : ion/molecule reactions related to the thermochemistry of  $\text{CF}_3^+$ . *Int. J. Mass. Spectrom.* **1990**, 101, (1), R1-R6.
33. Fisher, E. R.; Armentrout, P. B., Kinetic energy dependence of the reactions of atomic oxygen(1+) and dioxygenyl ion with tetrafluoromethane and hexafluoroethane. *J. Phys. Chem.* **1991**, 95, (16), 6118-6124.
34. Su, T.; Hammond, G. B.; Morris, R. A.; Viggiano, A. A.; Paulson, J. F.; Liebman, J. F.; Su, A. C. L., Gaseous ion-molecule reactions of  $\text{F}^-$ ,  $\text{CF}_3^-$ ,  $\text{C}_2\text{F}_5^-$ ,  $\text{CF}_3^+$  and  $\text{C}_2\text{F}_5^+$  with hexafluoropropene oxide. *J. Fluorine Chem.* **1995**, 74, (1), 149-157.
35. Martin, I. T.; Zhou, J.; Fisher, E. R., Correlating ion energies and  $\text{CF}_2$  surface production during fluorocarbon plasma processing of silicon. *J. Appl. Phys.* **2006**, 100, (1), 013301-10.
36. Cuddy, M. F.; Fisher, E. R., Investigation of the roles of gas-phase  $\text{CF}_2$  molecules and F atoms during fluorocarbon plasma processing of Si and  $\text{ZrO}_2$  substrates. *J. Appl. Phys.* **2010**, 108, (3), 033303-9.
37. Beck, A. J.; Candan, S.; Short, R. D.; Goodyear, A.; Braithwaite, N. S. J., The Role of Ions in the Plasma Polymerization of Allylamine. *J. Phys. Chem. B* **2001**, 105, (24), 5730-5736.
38. Booth, J.-P., Optical and electrical diagnostics of fluorocarbon plasma etching processes. *Plasma Sources Sci. Technol.* **1999**, 8, (2), 249.
39. Zhang, D.; Kushner, M. J., Mechanisms for  $\text{CF}_2$  radical generation and loss on surfaces in fluorocarbon plasmas. *J. Vac. Sci. Technol. A* **2000**, 18, (6), 2661-2668.
40. Martin, I. T.; Fisher, E. R., Ion effects on  $\text{CF}_2$  surface interactions during  $\text{C}_3\text{F}_8$  and  $\text{C}_4\text{F}_8$  plasma processing of Si. *J. Vac. Sci. Technol. A* **2004**, 22, (5), 2168-2176.
41. Edelberg, E. A.; Perry, A.; Benjamin, N.; Aydil, E. S., Energy distribution of ions bombarding biased electrodes in high density plasma reactors. *J. Vac. Sci. Technol. A* **1999**, 17, (2), 506-516.
42. Capps, N. E.; Mackie, N. M.; Fisher, E. R., Surface interactions of  $\text{CF}_2$  radicals during deposition of amorphous fluorocarbon films from  $\text{CHF}_3$  plasmas. *J. Appl. Phys.* **1998**, 84, (9), 4736-4743.
43. Butoi, C. I.; Mackie, N. M.; Williams, K. L.; Capps, N. E.; Fisher, E. R., Ion and substrate effects on surface reactions of  $\text{CF}_2$  using  $\text{C}_2\text{F}_6$ ,  $\text{C}_2\text{F}_6/\text{H}_2$ , and hexafluoropropylene oxide plasmas. *J. Vac. Sci. Technol. A* **2000**, 18, (6), 2685-2698.
44. Liu, D. P.; Cuddy, M. F.; Fisher, E. R., Comparison of CH,  $\text{C}_3$ , CHF, and  $\text{CF}_2$  Surface Reactivities during Plasma-Enhanced Chemical Vapor Deposition of Fluorocarbon Films. *ACS Appl. Mater. Interfaces* **2009**, 1, (4), 934-943.
45. Cuddy, M. F.; Fisher, E. R., Contributions of CF and  $\text{CF}_2$  Species to Fluorocarbon Film Composition and Properties for  $\text{C}_x\text{F}_y$  Plasma-Enhanced Chemical Vapor Deposition. *ACS Appl. Mater. Interfaces* **2012**, 4, (3), 1733-1741.
46. Liu, D.; Martin, I. T.; Fisher, E. R., Radical-surface interactions during film deposition: A sticky situation? *Pure Appl. Chem.* **2006**, 78, (6), 1187-1202.
47. Jiao, C. Q.; Jr, C. A. D.; Garscadden, A.; Adams, S. F., Gas-phase ion chemistries in perfluoromethylcyclohexane. *Plasma Sources Sci. Technol.* **2009**, 18, (2), 025007.

48. Williams, K. L.; Martin, I. T.; Fisher, E. R., On the importance of ions and ion-molecule reactions to plasma-surface interface reactions. *J. Am. Soc. Mass Spectrom.* **2002**, 13, (5), 518-529.
49. Stoffels, W. W.; Stoffels, E.; Tachibana, K., Polymerization of fluorocarbons in reactive ion etching plasmas. *J. Vac. Sci. Technol. A* **1998**, 16, (1), 87-95.
50. Shamamian, V. A.; Hinshelwood, D. D.; Guerin, D. C.; Denes, F. S.; Manolache, S., Mass Spectrometric Characterization of Pulsed Inductively Coupled Plasmas for Deposition of Thin Polyethylene Glycol-like Polymer Films. *J. Photopolym. Sci. Technol.* **2001**, 14, 91-100.
51. Li, Z.-C.; Chang, D.-L.; Li, X.-S.; Bi, Z.-H.; Lu, W.-Q.; Xu, Y.; Zhu, A.-M.; Wang, Y.-N., Experimental investigation of ion energy distributions in a dual frequency capacitively coupled Ar/CF<sub>4</sub> plasma. *Phys. Plasmas* **2010**, 17, (3), 033501-8.
52. Barnes, M. S.; Forster, J. C.; Keller, J. H., Ion kinetics in low-pressure, electropositive, RF glow discharge sheaths. *IEEE Trans. Plasma Sci.* **1991**, 19, (2), 240-244.
53. Kushner, M. J., Distribution of ion energies incident on electrodes in capacitively coupled rf discharges. *J. Appl. Phys.* **1985**, 58, (11), 4024-4031.
54. Coburn, J. W.; Kay, E., Positive-ion bombardment of substrates in rf diode glow discharge sputtering. *J. Appl. Phys.* **1972**, 43, (12), 4965-4971.
55. Chang, J. P.; Coburn, J. W., Plasma-surface interactions. *J. Vac. Sci. Technol. A* **2003**, 21, (5), S145-S151.
56. Abrams, C. F.; Graves, D. B., Atomistic simulation of fluorocarbon deposition on Si by continuous bombardment with energetic CF<sup>+</sup> and CF<sub>2</sub><sup>+</sup>. *J. Vac. Sci. Technol. A* **2001**, 19, (1), 175-181.
57. Abrams, C. F.; Graves, D. B., Atomistic simulation of silicon bombardment by energetic CF<sub>3</sub><sup>+</sup>: product distributions and energies. *Thin Solid Films* **2000**, 374, (2), 150-156.
58. Teii, K.; Hori, M.; Goto, T.; Ishii, N., Precursors of fluorocarbon film growth studied by mass spectrometry. *J. Appl. Phys.* **2000**, 87, (10), 7185-7190.
59. d'Agostino, R.; Cramarossa, F.; Fracassi, F.; Illuzzi, F., *Plasma Polymerization of Fluorocarbons*. Academic Press, Inc. : San Diego, CA, 1990.
60. Woodworth, J. R.; Riley, M. E.; Miller, P. A.; Nichols, C. A.; Hamilton, T. W., Ion distribution functions in inductively coupled radio frequency discharges in argon-chlorine mixtures. *J. Vac. Sci. Technol. A* **1997**, 15, (6), 3015-3023.
61. Nichols, C. A.; Woodworth, J. R.; Hamilton, T. W., Ion energy distribution functions in inductively coupled radio-frequency discharges---Mixtures of Cl<sub>2</sub>/BCl<sub>3</sub>/Ar. *J. Vac. Sci. Technol. A* **1998**, 16, (6), 3389-3395.
62. Singh, H.; Coburn, J. W.; Graves, D. B., Measurements of neutral and ion composition, neutral temperature, and electron energy distribution function in a CF<sub>4</sub> inductively coupled plasma. *J. Vac. Sci. Technol. A* **2001**, 19, (3), 718-729.
63. Limb, S. J.; Edell, D. J.; Gleason, E. F.; Gleason, K. K., Pulsed plasma-enhanced chemical vapor deposition from hexafluoropropylene oxide: Film composition study. *J. Appl. Polym. Sci.* **1998**, 67, (8), 1489-1502.
64. Ling, L.; Hua, X.; Zheng, L.; Oehrlein, G. S.; Hudson, E. A.; Jiang, P., Studies of fluorocarbon film deposition and its correlation with etched trench sidewall angle

by employing a gap structure using  $C_4F_8/Ar$  and  $CF_4/H_2$  based capacitively coupled plasmas. *J. Vac. Sci. Technol. B* **2008**, 26, (1), 11-22.

## CHAPTER 7

### EFFECT OF MIXED FLUOROCARBON PRECURSOR PLASMAS ON CARBON- AND FLUORINE-CONTAINING SPECIES

This chapter contains gas-phase diagnostic data for mixed precursor systems including FC/H<sub>2</sub>, FC/O<sub>2</sub> and FC/FC plasmas. Some of the work presented here was published as a full paper in the journal *ACS Applied Materials and Interfaces* by Dongping Liu, Michael F. Cuddy, and Ellen R. Fisher. The published work relates the effect of FC/FC mixtures on the gas-phase behavior of CH, C<sub>3</sub>, CHF, and CF<sub>2</sub>. Preliminary data are presented for FC/H<sub>2</sub> and FC/O<sub>2</sub> feeds, focusing especially on the kinetic behavior of CF<sub>2</sub><sup>\*</sup> species in mixed precursor plasmas and the net effect of substrate processing in these systems.

## 7.1. Introduction

The development of fluorocarbon (FC) systems for industrially relevant applications is a burgeoning area of research that has extensive ties to the microelectronics industry. In particular, the development of alternative low dielectric materials for interlayers in ultralarge-scale integrated circuits (ULSIs) has become an area of intense interest.<sup>1</sup> FC films with low dielectric constants have been successfully deposited using various FC or FC-containing gases such as  $\text{CF}_4$ ,<sup>2</sup>  $\text{C}_2\text{F}_6$ ,<sup>2,3</sup>  $\text{C}_3\text{F}_8$ ,<sup>4</sup>  $\text{C}_4\text{F}_8$ ,<sup>4,5</sup>  $\text{C}_3\text{F}_6\text{O}$ ,<sup>6-8</sup>  $\text{CH}_2\text{F}_2$ ,<sup>9</sup>  $\text{C}_2\text{H}_2\text{F}_4$ ,<sup>9,10</sup> and  $\text{CHF}_3$ .<sup>11</sup> In addition to deposition of FC films, FC plasmas are also of interest for selective etching of hard masks such as  $\text{Si}_3\text{N}_4$  over new photoresists used in 193 nm ArF photolithography processes.<sup>12</sup> In these systems, mixtures of two FC gases (e.g.  $\text{CHF}_3/\text{CF}_4$ ) and/or mixtures of fluorocarbon gases and  $\text{H}_2$  (e.g.  $\text{CH}_2\text{F}_2/\text{H}_2$ ) are used to enhance desirable processes, such as etch selectivity or minimization of unwanted FC deposits. Alternatively,  $\text{O}_2$  addition to the FC feed may be used to promote etch selectivity. Indeed, Harshbarger, *et al.* demonstrated that the addition of  $\text{O}_2$  to a  $\text{CF}_4$  plasma as much as doubled the etch rate of a Si substrate over the FC plasma alone.<sup>13</sup>

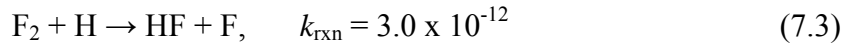
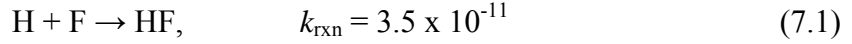
Plasma parameters such as  $P$ ,  $p$ , and feed gas type and ratio strongly influence the film chemistry of FC deposits.<sup>12, 14, 15</sup> Not surprisingly, neutral plasma species are thought to play essential roles in achieving the desired material properties and etch rates.<sup>16</sup> To optimize the performance of FC processing, a basic understanding of fundamental processes in FC plasmas is of great importance. Thus considerable effort has focused on investigating the role of  $\text{CF}_x$  ( $x = 1-3$ ) molecules in both deposition and etching FC plasmas, and the roles of other gas-phase species such as fluorine, and atomic and molecular hydrogen and oxygen. Ultimately, gas-phase diagnostics can be used in con-

junction with radical-surface reactivity data to render a more complete illustration of the complex plasma system and yield improved applications. Mixed feed gas systems are particularly interesting because recombination reactions play a much more crucial role than in a single-feed plasma. Here we focus on optical emission analyses for a range of mixed precursor plasma systems.

Initially, we address CH, C<sub>3</sub>, CHF, and CF<sub>2</sub> molecules in CH<sub>2</sub>F<sub>2</sub>/C<sub>3</sub>F<sub>8</sub> plasmas, and relate gas-phase densities and trends with changing plasma parameters of these species with surface reactivity. We have previously used our imaging of radicals interacting with surfaces (IRIS) technique that employs LIF for detection of plasma species, to measure CF<sub>2</sub> surface reactivity using depositing FC plasmas.<sup>4, 8, 11, 17, 18</sup> Results indicate CF<sub>2</sub> may contribute to the FC film growth only when adsorbing at radical sites created at the film surface. More importantly, results from a range of FC precursors demonstrate that energetic ion bombardment of the deposited FC film results in surface production of CF<sub>2</sub> under a range of conditions. Investigation of CF<sub>x</sub> radicals is not, however, sufficient to understand the overall reaction kinetics in FC plasmas and FC film deposition processes. Several other radicals likely participate in gas-phase and surface reactions during film deposition, especially in systems that involve multiple gases as precursors. Moreover, the presence of hydrogen in the source gas can have mitigating effects on the efficacy of film deposition through significant gas-phase reactions.

The effect of hydrogen in the feed can be more thoroughly investigated by examining FC/H<sub>2</sub> plasmas. Previous results from our group have demonstrated an overall increase in efficacy of film deposition from C<sub>2</sub>F<sub>6</sub> systems with H<sub>2</sub> additives with a decrease in observed scatter coefficients for CF<sub>2</sub>.<sup>2</sup> These results are thought to be associated with

fluorine scavenging events initiated by atomic and molecular hydrogen, as in reactions (7.1)-(7.3). In these schemes, the reaction rate constant  $k_{\text{rxn}}$  is given in  $\text{cm}^3 \text{mlc}^{-1} \text{s}^{-1}$ .<sup>19, 20</sup>



The abstraction of F from the gas-phase of the plasma is tantamount with efforts to limit fluorine-stimulated etch processes. Indeed, we have previously shown that H<sub>2</sub> additions of up to 50% to FC plasmas significantly enhance the efficacy of C:F,H film deposition.<sup>2</sup> In this chapter, we have assessed the effect of H<sub>2</sub> addition to C<sub>2</sub>F<sub>6</sub> systems directly, by monitoring fluctuations in relative concentrations of plasma species, including CF<sub>2</sub><sup>\*</sup>, CF<sup>\*</sup>, H<sup>\*</sup>, and F<sup>\*</sup>, using time-resolved OES (TR-OES). The ultimate effect of surface modification was gauged through XPS analyses of deposited C:F,H films.

In scenarios in which enhancement of FC deposition is undesirable or even detrimental, additives such as O<sub>2</sub> can be used to deplete FC passivation layers and sequester film-propagating units in the gas phase. Oxygen additions are expected to promote a wealth of fluorine with respect to CF<sub>x</sub> fragments; this effect is exacerbated when the FC constituent of the feed contains a high F/C ratio.<sup>21</sup> Notably, O<sub>2</sub> is an effective plasma feed gas choice for removal of materials and as such is often used as a cleaning agent.<sup>22</sup> Thus, FC/O<sub>2</sub> gas mixtures, such as C<sub>4</sub>F<sub>8</sub>/O<sub>2</sub>, are also used to etch semiconductor and interlayer materials.<sup>23</sup> We have extended our OES and TR-OES techniques to the C<sub>2</sub>F<sub>6</sub>/O<sub>2</sub> plasma system to monitor the relative concentrations of CF<sub>2</sub><sup>\*</sup>, CO<sup>\*</sup>, F<sup>\*</sup>, and O<sup>\*</sup> as a function of changing plasma parameters and to determine production kinetics for CF<sub>2</sub><sup>\*</sup> species, respectively. Overall, this work seeks to garner a more complete understanding of

complex mixed-precursor plasma systems and provide an avenue for future investigations.

## 7.2. Results and Discussion

One key to understanding the FC deposition processes is determining formation mechanisms for potential deposition precursors. Here, we determined the relative amounts of CH, C<sub>3</sub>, CF<sub>2</sub>, and CHF radicals as a function of deposition parameters, most notably gas ratios, using optical emission spectroscopy. In mixtures consisting primarily of C<sub>3</sub>F<sub>8</sub> feed gas, Fig. 7.1(a), a prominent CF<sub>2</sub> band exists at 250-350 nm. As the C<sub>3</sub>F<sub>8</sub> concentration in the feed is decreased, Fig. 7.1(b), the CF<sub>2</sub> band effectively disappears, indicating significant changes in excited species production within the plasma. Actinometric OES data provide a quantitative illustration of molecule production as the feed gas ratio is varied, Figs. 7.1(c) and 7.1(d). In its simplest form, the ratio of the emission intensity from the excited state species of interest ( $I_x$ ) to that of an actinometer ( $I_{act}$ ) is taken as the relative number density for the ground state species of interest.<sup>10</sup> Here, we used signals at the following wavelengths for the respective molecules, 251.89 nm (CF<sub>2</sub>), 405.08 nm (C<sub>3</sub>), 431.34 nm (CH), 578.5 nm (CHF).<sup>10, 16, 24, 25</sup> Formation of two species, C<sub>3</sub><sup>\*</sup> and CH<sup>\*</sup>, is not dependent upon %CH<sub>2</sub>F<sub>2</sub> in the feed, Fig. 7.1(c), suggesting these species do not arise preferentially from either precursor gas. Although CHF<sup>\*</sup> has a slight dependence on the feed gas ratio, Fig. 7.1(c), increasing slightly at higher CH<sub>2</sub>F<sub>2</sub> concentrations, the overall intensity is much smaller than that of either C<sub>3</sub><sup>\*</sup> or CH<sup>\*</sup>. Figure 7.1(d) shows the actinometric OES data for CF<sub>2</sub> in the FC plasmas, demonstrating a gas

ratio dependence nearly identical to that observed in LIF data, suggesting that C<sub>3</sub>F<sub>8</sub> is the precursor responsible for CF<sub>2</sub> production.

The dependence of CHF\* emission on %CH<sub>2</sub>F<sub>2</sub> in the plasma feed, Fig. 7.1(c), suggests a formation mechanism for this species that follows direct decomposition of the CH<sub>2</sub>F<sub>2</sub> component, rather than secondary gas-phase recombination reactions, such as that shown in reaction (7.4).



*R* (surface reactivity) values are related to *S* by the relationship  $R = 1 - S$ , and thus represent a clearer method to distinguish the propensity for a molecule to *react* at a surface rather than scatter. The surface reactivity of the CHF molecule is low (i.e.  $R < 0$ ) in the mixed precursor systems, which is in contrast to the moderately high reactivity ( $R \sim 0.2$ ) of the CF<sub>2</sub> molecule in the same system (40% CH<sub>2</sub>F<sub>2</sub>, 60% C<sub>3</sub>F<sub>8</sub>). Moreover, the scatter coefficients for CF<sub>2</sub> increase (i.e. reactivity decreases) as the gas feed approaches 100% C<sub>3</sub>F<sub>8</sub>. These results, coupled with similar previously reported data for C<sub>2</sub>F<sub>6</sub>/H<sub>2</sub> plasmas,<sup>26</sup> suggest that C:F,H-type films are generally more conducive to surface-mediated production of hydrogen-containing radicals than CF<sub>x</sub> species.

In these same systems, one species that can be readily produced through gas-phase recombination reactions is C<sub>3</sub> that may be formed through a series of three-body interactions as depicted in (7.5) and (7.6).



The actinometric analyses of C<sub>3</sub>\* species, Fig. 7.1(c), indicate that for small additions of

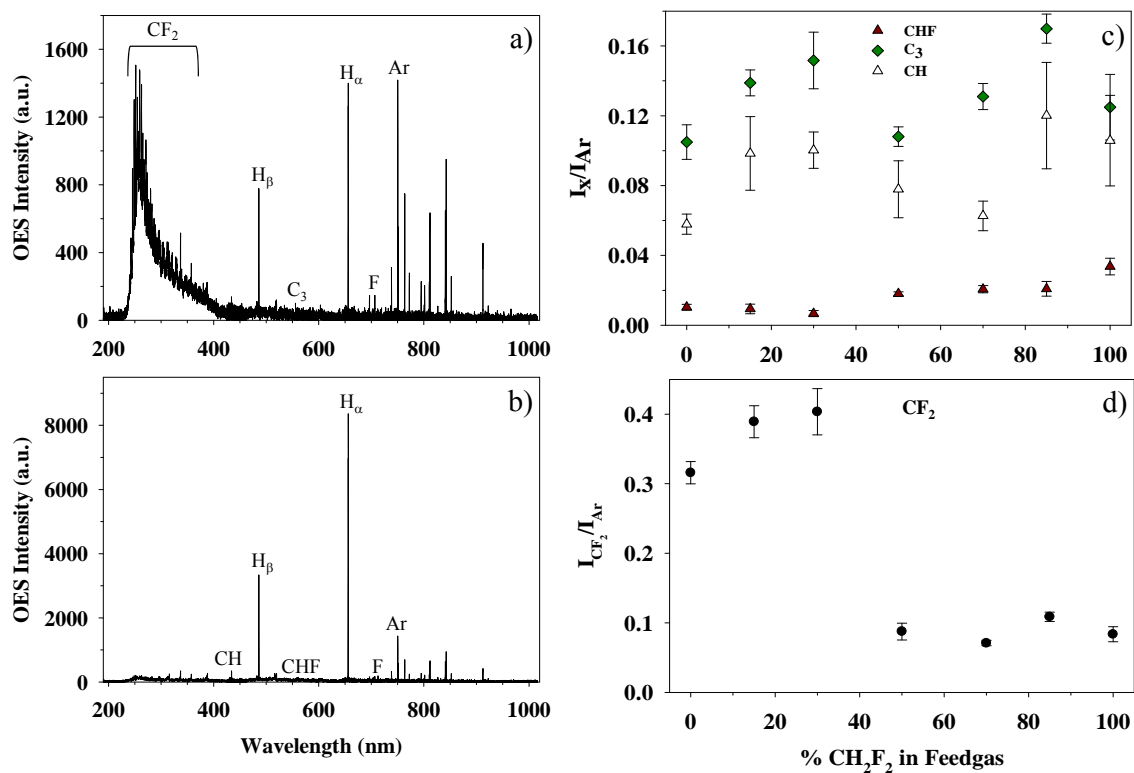


**Figure 7.1.** OES spectra of mixtures of fluorocarbon plasmas ( $P = 100$  W, total pressure of 100 mTorr) with mixtures of (a) 30/70  $\text{CH}_2\text{F}_2/\text{C}_3\text{F}_8$  and (b) 85/15  $\text{CH}_2\text{F}_2/\text{C}_3\text{F}_8$ . Actinometric OES data as a function of the  $\text{CH}_2\text{F}_2$  fraction in the feed gas are shown for (c) CH, CHF,  $\text{C}_3$  and (d)  $\text{CF}_2$ . Error bars represent one standard deviation from the mean of three trials.

$\text{CH}_2\text{F}_2$  to the  $\text{CH}_2\text{F}_2/\text{C}_3\text{F}_8$  plasma,  $\text{C}_3^*$  production is enhanced. In a 50/50 mixture, the concentration reverts to a local minimum and rises again upon introduction of additional  $\text{C}_3\text{F}_8$ . Interestingly, this trend is not observed for ground state  $\text{C}_3$  molecules, suggesting a discrepancy factor regarding the generation of excited species preferential to ground state species in mixed systems. A similar occurrence was observed for a simplified mixed precursor system, Fig. 7.2, that shows  $\text{CF}_2^*$  relative concentrations as a function of feed composition in  $\text{CF}_4/\text{C}_2\text{F}_6$  mixed plasmas at  $P = 150$  W. Here, an obvious minimum exists at approximately 80%  $\text{CF}_4/20\%$   $\text{C}_2\text{F}_6$ . The quenching rates of  $\text{CF}_2^*$  by  $\text{CF}_4$  and  $\text{C}_2\text{F}_6$  are essentially negligible,<sup>27,28</sup> meaning that the presence of these minima are the signatures of more intricate gas-phase phenomena. We speculate that imbalances in electron energy distributions and electron and gas temperatures are partially responsible for the observed trends unique to these gas mixtures. In particular, we have preliminary data showing that  $T_e(\text{total})$  for  $\text{CF}_4/\text{C}_2\text{F}_6$  mixtures is not necessarily a linear combination of  $T_e(\text{CF}_4)$  and  $T_e(\text{C}_2\text{F}_6)$ . Ultimately, this could result in incidences of diminished excitation efficiencies in the plasma, wherein processes such as that depicted in reaction (1.3) are inhibited. Nonetheless, this issue remains a candidate for continued investigation in the Fisher laboratory.

A final note on Fig. 7.1 regards the precipitous drop-off in relative  $\text{CF}_2^*$  concentrations as the  $\text{CH}_2\text{F}_2$  composition is increased. It appears that although small additions of  $\text{CH}_2\text{F}_2$  (< 40 %) promote species production, the generation of  $\text{CF}_2^*$  is not facilitated facilely by  $\text{CH}_2\text{F}_2$  itself. Even in 50/50 mixtures of  $\text{CH}_2\text{F}_2/\text{C}_3\text{F}_8$ , the relative excited state density of  $\text{CF}_2$  is at least four times lower than the concentration in a 40/60 precursor

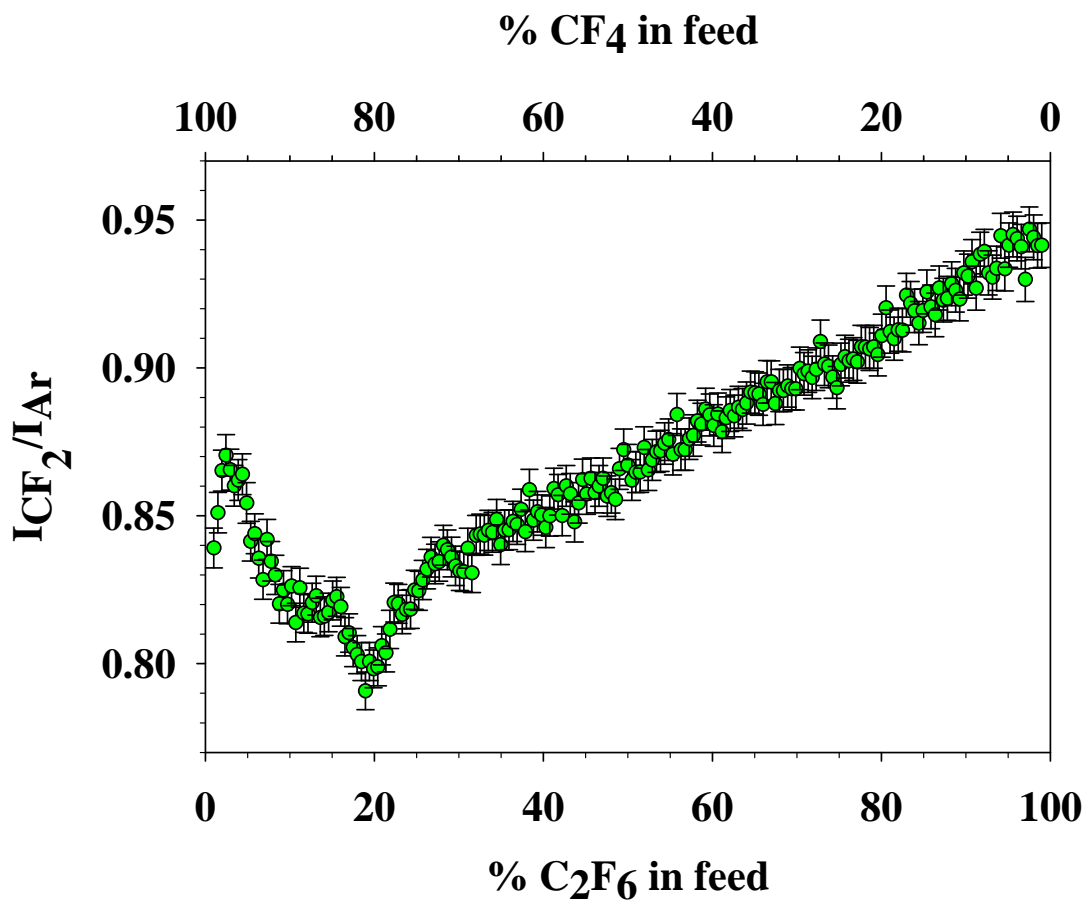


**Figure 7.2.** Actinometric analysis of  $CF_2$  emission in a  $CF_4/C_2F_6$  plasma ( $P = 150$  W,  $p = 100$  mTorr) as a function of feed gas content, with a minimum in relative  $CF_2$  concentration at 80%  $CF_4$ .

mixture. We believe that this drastic discrepancy may be due to increased hydrogen concentration in the gas-phase. Thus, we have examined the effect of hydrogen on  $\text{CF}_2^*$  more thoroughly by investigating the simpler  $\text{C}_2\text{F}_6/\text{H}_2$  system.

Figure 7.3(a) depicts time-dependent relative species concentrations for  $\text{CF}_2^*$ ,  $\text{H}_\alpha^*$ ,  $\text{CF}^*$ , and  $\text{F}^*$  in a 50/50  $\text{C}_2\text{F}_6/\text{H}_2$  plasma with  $P = 150$  W collected via actinometric TR-OES. Although small fluctuations exist as a function of time from plasma ignition for  $\text{H}_\alpha^*$ ,  $\text{CF}^*$ , and  $\text{F}^*$ , the most noteworthy observation is the exponential decay of  $\text{CF}_2^*$  signal after  $t \sim 0.5$  s. The decay persists for approximately 1 s before a steady state is reached, after which essentially no further fluctuations in relative  $\text{CF}_2^*$  concentrations are observed in a continuous plasma. This decay was fit with an exponential function of the form  $e^{-kt}$  to determine the rate constant for initial  $\text{CF}_2^*$  decay,  $k_{\text{decay}}$ . Such results in a small monomer FC plasma are not unprecedented. Indeed, Hikosaka and co-workers<sup>29</sup> reported on similar decay profiles for  $\text{CF}_3$  species in  $\text{CF}_4/\text{H}_2$  plasmas, and attributed rapid  $\text{CF}_3$  loss to reactions at C:F,H surfaces to produce  $\text{CHF}_{3(\text{ads})}$ . In our systems, the effect of reactions of  $\text{CF}_2^*$  with FC-passivated surfaces is insufficient to account for the observed loss depicted in Fig. 7.3(a), as passivating FC layers do not form rapidly enough to make this mechanism feasible. Moreover,  $k_{\text{decay}}$  values are independent for dilutions of FC/ $\text{H}_2$  plasma feeds with  $\text{H}_2 > 50\%$ , indicating some limiting step that suggests that the loss of  $\text{CF}_2^*$  is purely a gas-phase phenomenon. Interestingly,  $P$  appears to play an important role in determining  $k_{\text{decay}}$  for  $\text{CF}_2^*$ , Fig. 7.3(b). For a 50/50  $\text{C}_2\text{F}_6/\text{H}_2$  plasma, decay rate constants for  $\text{CF}_2^*$  follow a direct relationship with respect to  $P$ . This mirrors the trend of linearly increasing atomic  $\text{H}^*$  concentrations observed in actinometric OES analyses as a

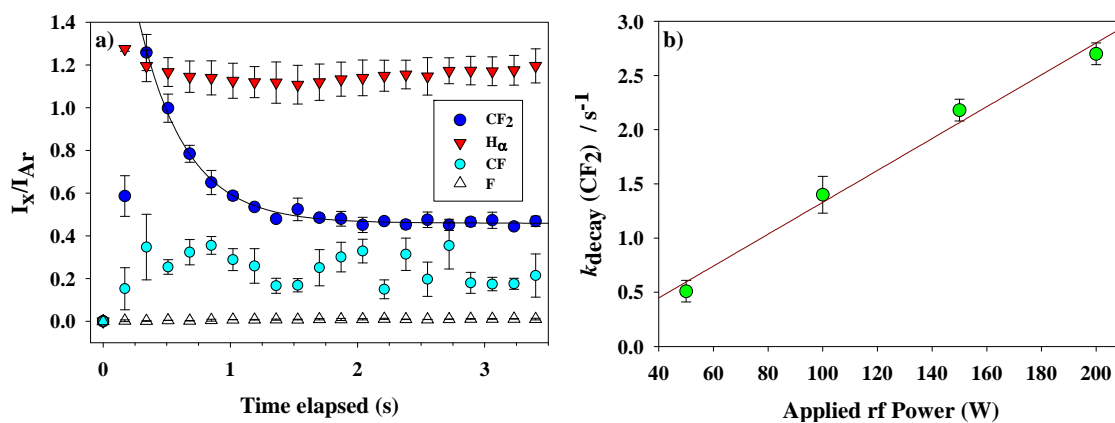


**Figure 7.3.** a) Time-resolved actinometric OES trends for  $CF_2$ ,  $H\alpha$ ,  $CF$ , and  $F$  emission in a 1:1  $C_2F_6/H_2$  plasma at  $P = 150$  W and  $p = 100$  mTorr. An exponential decay function is fit to the  $CF_2$  data from which a  $k_{decay}$  value of  $2.70$   $s^{-1}$  is calculated. b)  $k_{decay}$  values for  $CF_2$  in 1:1  $C_2F_6:H_2$  plasmas as a function of applied rf power. The best fit linear trendline ( $R^2 = 0.99$ ) yields a slope of  $0.015$   $s^{-1} W^{-1}$ .

function of  $P$ . As established above, atomic hydrogen is an effective scavenger of fluorine. Based upon rough calculations, relative  $F^*$  concentrations ought to come to steady-state within 1 s of plasma ignition. Indeed, there is essentially no discernible change in  $F^*$  at  $t > 0$  s, Fig. 7.3(a), despite a small concomitant decrease in  $H^*$  that endures for  $\sim 1$  s. Thus, we propose a loss mechanism for  $CF_2^*$  that incorporates gas-phase interaction with  $H^*$ , reaction (7.7). This reaction has been reported in the literature for ground electronic state species produced from  $CF_4/H_2$  plasmas, with an experimentally determined rate constant of  $1.7 \times 10^{-13} \text{ cm}^3 \text{ molecule}^{-1} \text{ s}^{-1}$ .<sup>30</sup> Interestingly, this phenomenon associated with  $CF_2^*$



in  $C_2F_6/H_2$  plasmas is only observed for  $H_2$  dilutions  $\geq 50\%$  of the total pressure. This strongly supports the notion that a profusion of hydrogen is responsible for the loss of  $CF_2^*$  shortly after plasma ignition. Consequently, we infer that excess  $H^*$ , which does not participate in fluorine abstraction in the gas phase, contributes to  $CF_2$  loss via the pathway outlined in (7.7).

The ramifications of the complex role that hydrogen plays in the FC system, whether H is incorporated via  $H_2$  or through  $CH_xF_y$  precursors, include an intensified propensity for film deposition. For instance, the deposition rate of a typical  $C_2F_6$  plasma with  $P = 150$  W is  $3.8 \pm 0.1 \text{ \AA min}^{-1}$ . Upon 50%  $H_2$  addition to the  $C_2F_6$  plasma, the deposition rate increases to  $62.0 \pm 2.0 \text{ \AA min}^{-1}$ . This trend, along with an overall decrease in observed  $CF_2$  scatter coefficients in FC/ $H_2$  plasmas, is a point of ongoing investigation in our laboratory and has been addressed previously.<sup>2, 3, 11, 26</sup>

The contribution of hydrogen to deposited FC films is depicted in Figs. 7.4(a) and 7.4(b). These high-resolution  $C_{1s}$  XPS spectra display the stark differences in C:F and

C:F,H films, respectively. In particular, the relative contribution of the C-C/C-H binding environment at 285 eV increases dramatically for a substrate processed in a 50/50 C<sub>2</sub>F<sub>6</sub>/H<sub>2</sub> plasma, Fig. 7.4(b), as compared to a similar substrate processed using a 100% C<sub>2</sub>F<sub>6</sub> plasma, Fig. 7.4(a). Moreover, the deposited film becomes significantly more cross-linked and less ordered (80% cross-linking; F/C ratio ~0.60) for the 50/50 C<sub>2</sub>F<sub>6</sub>/H<sub>2</sub> plasma than the 100% C<sub>2</sub>F<sub>6</sub> plasma (55% cross-linking; F/C ratio ~1.2). Additionally, IRIS surface scatter coefficients for CF and CF<sub>2</sub> decrease by up to a factor of two.

Interestingly, an effect that is nearly opposite to that of H<sub>2</sub> additions can be achieved by incorporating O<sub>2</sub> in the plasma feed. Fig. 7.4(c) depicts a typical high-resolution C<sub>1s</sub> XPS spectrum for a wafer processed in a 50/50 C<sub>2</sub>F<sub>6</sub>/O<sub>2</sub> plasma with  $P = 150$  W. Here, essentially all of the critical C-F<sub>x</sub> binding environments are lost. The deposition rate of this plasma system is a mere  $1.4 \pm 0.2 \text{ \AA min}^{-1}$ , a factor of three less than that for a 100% C<sub>2</sub>F<sub>6</sub> plasma operating under similar conditions. Indeed, O<sub>2</sub>, rather than gas-phase FC species, appears to interact most prominently with the surface of the Si wafer. As evidenced by the Si<sub>2p</sub> high-resolution spectrum depicted in Fig. 7.4(d), the characteristic SiO<sub>2</sub> binding environment, Si(-O)<sub>4</sub>, dominates the

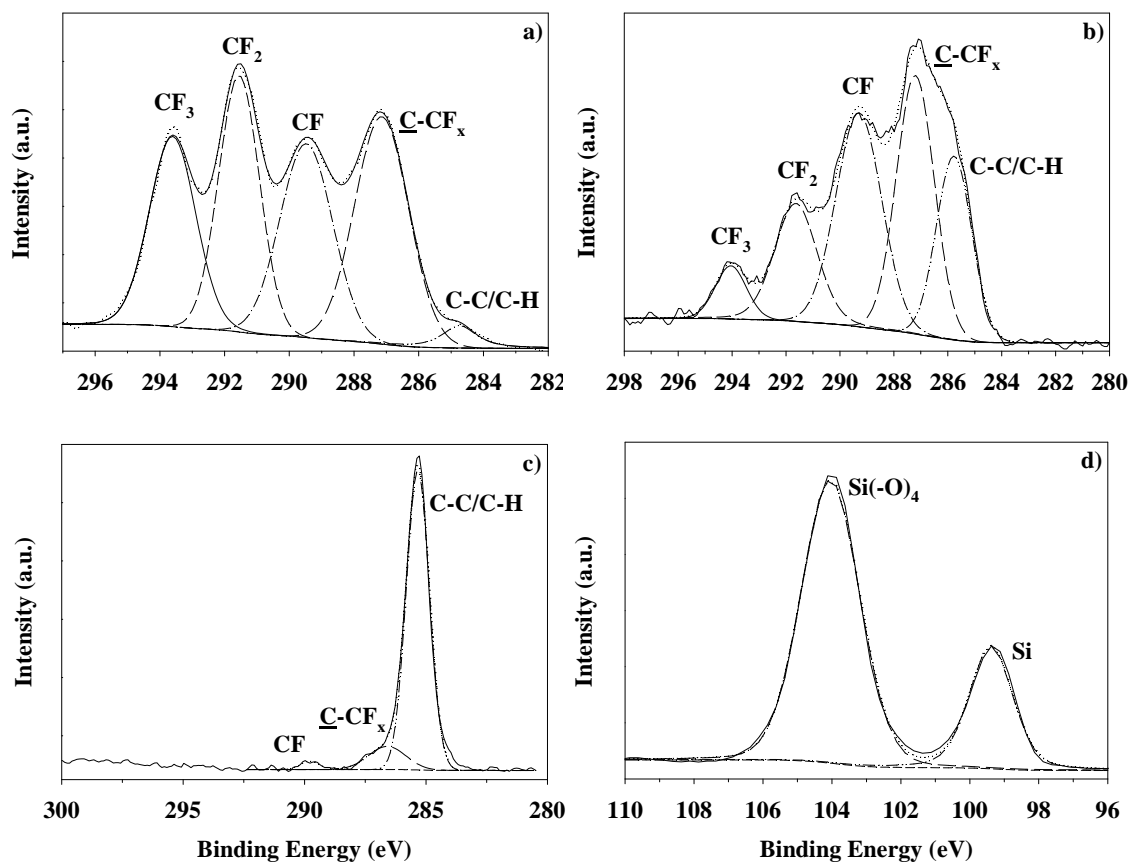
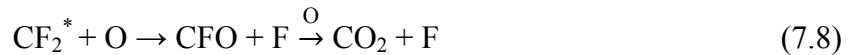


**Figure 7.4.** a) Representative high-resolution  $C_{1s}$  XPS spectrum of a Si wafer processed in a  $C_2F_6$  plasma at  $p = 100$  mTorr. High-resolution  $C_{1s}$  spectra are also provided for Si wafers processed in b) 1:1  $C_2F_6:H_2$  plasma and c) 1:1  $C_2F_6:O_2$  plasma. d) A high-resolution  $Si_{2p}$  spectrum is also provided for the same wafer processed in the 1:1  $C_2F_6:O_2$  system.

substrate composition. This is a significant increase of SiO<sub>2</sub> over an unprocessed wafer,<sup>31</sup> and indicates that excess oxygen is freely available to be incorporated into the Si wafer. It is likely that both atomic and molecular oxygen abate most FC passivating layers,<sup>32</sup> exposing sufficient Si area to promote extensive substrate oxidation. In the plasma gas-phase, O<sub>2</sub> effectively sequesters film-initiating and propagating species, including C<sub>x</sub>F<sub>y</sub> radicals. We have employed OES here to examine the behavior of gas-phase species in C<sub>2</sub>F<sub>6</sub>/O<sub>2</sub> systems. In a 50/50 C<sub>2</sub>F<sub>6</sub>/O<sub>2</sub> plasma, the relative concentration of O\* is more than an order of magnitude greater than CF<sub>2</sub>\*, Fig. 7.5(a). Note that the excitation cross sections for O (8.6 x 10<sup>-18</sup> cm<sup>2</sup>)<sup>33</sup> and CF<sub>2</sub> (2.6 x 10<sup>-17</sup> cm<sup>2</sup>)<sup>34</sup> are similar, so it is appropriate to compare their relative concentrations from actinometry. Indeed, oxygen likely reacts with gas-phase CF<sub>2</sub> in particular to form volatile products and atomic F [relative F\* concentrations are also significantly greater than CF<sub>2</sub>\* concentrations, Fig. 7.5(a)].<sup>35, 36</sup> Dominant CF<sub>2</sub> loss pathways are outlined in reactions (7.8)-(7.9).<sup>37</sup>



The effect of O<sub>2</sub> additions to the FC feed is noticed even at very small dilutions, Fig. 7.5(b). Here, the on-time *production* rate constant of CF<sub>2</sub>,  $k_{\text{CF}_2}$ , from TR-OES analyses are plotted as a function of  $P$  for various dilutions of C<sub>2</sub>F<sub>6</sub> with O<sub>2</sub>. A marked drop in  $k_{\text{CF}_2}$  occurs at  $P = 150$  W with an addition of only 10% O<sub>2</sub>, a decrease of nearly 65%. Upon addition of more O<sub>2</sub> to the plasma feed, the  $k_{\text{CF}_2}$  values decrease, and are essentially constant within error for O<sub>2</sub> feed concentrations  $\geq 25\%$ . Thus, oxygen is a potent

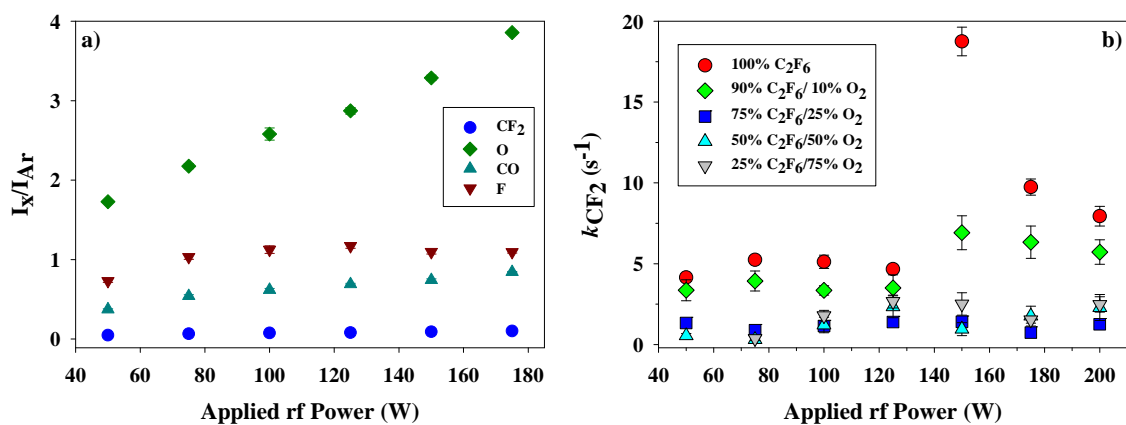


**Figure 7.5.** a) Actinometric OES data for CF<sub>2</sub>, O, CO, and F emission as a function of  $P$  in a 1:1 C<sub>2</sub>F<sub>6</sub>:O<sub>2</sub> plasma with  $p = 100$  mTorr. b) CF<sub>2</sub> production rate constants (obtained from TR-OES) plotted as a function of  $P$  in plasmas comprising various mixtures of C<sub>2</sub>F<sub>6</sub>/O<sub>2</sub>.

inhibitor of FC film growth and as such is often employed in applications wherein deposition of undesirable FC byproducts is severely detrimental, such as in microfabrication of semiconductor devices.

### 7.3. Summary

We have performed gas-phase diagnostics for FC/FC, FC/H<sub>2</sub>, and FC/O<sub>2</sub> mixed precursor plasmas specifically addressing the roles of excited species such as CH<sup>\*</sup>, C<sub>3</sub><sup>\*</sup>, CHF<sup>\*</sup>, F<sup>\*</sup>, H<sup>\*</sup>, and O<sup>\*</sup>. Significant attention was paid to CF<sub>2</sub><sup>\*</sup>, for which we determined relative gas-phase concentrations and production and/or decay kinetics from actinometric and time-resolved OES. These data demonstrate that both the ground and excited states of CF<sub>2</sub> and CHF have a strong dependence on the feed gas composition whereas CH<sup>\*</sup> and C<sub>3</sub><sup>\*</sup> do not. The addition of hydrogen to a FC plasma induces a decay in relative amounts of CF<sub>2</sub><sup>\*</sup> shortly after plasma ignition. Additionally, H<sub>2</sub> additives to C<sub>2</sub>F<sub>6</sub> systems lead to increased efficacy of C:F,H film deposition, yielding films that comprise significantly increased cross-linking and lower fluorine content than those deposited from 100% C<sub>2</sub>F<sub>6</sub> plasmas. This is attributed to fluorine scavenging by hydrogen in the plasma gas phase that ultimately results in a higher concentration of film propagating units than film etching units. In contrast, O<sub>2</sub> additions to C<sub>2</sub>F<sub>6</sub> feeds generate a dearth of CF<sub>2</sub><sup>\*</sup> with respect to atomic fluorine, and deposition rates are concomitantly lowered dramatically with respect to a 100% C<sub>2</sub>F<sub>6</sub> plasma. In this case, we believe that oxygen in the gas phase sequesters CF<sub>2</sub> and other film-initiating species to inhibit expeditious formation of FC passivation layers at surfaces. There exists a considerable opportunity for further advancement of our knowledge of these systems. This includes investigations of gas-surface interface phe-

nomena and concise correlation of gas-phase behavior and the net effects of substrate processing with a particular precursor mixture.

#### 7.4. References

1. Rothman, L. B., Properties of Thin Polyimide Films. *J. Electrochem. Soc.* **1980**, 127, (10), 2216-2220.
2. Mackie, N. M.; Dalleska, N. F.; Castner, D. G.; Fisher, E. R., Comparison of Pulsed and Continuous-Wave Deposition of Thin Films from Saturated Fluorocarbon/H<sub>2</sub> Inductively Coupled rf Plasmas. *Chem. Mater.* **1997**, 9, (1), 349-362.
3. Butoi, C. I.; Mackie, N. M.; Williams, K. L.; Capps, N. E.; Fisher, E. R., Ion and substrate effects on surface reactions of CF<sub>2</sub> using C<sub>2</sub>F<sub>6</sub>, C<sub>2</sub>F<sub>6</sub>/H<sub>2</sub>, and hexafluoropropylene oxide plasmas. *J. Vac. Sci. Technol. A* **2000**, 18, (6), 2685-2698.
4. Martin, I. T.; Fisher, E. R., Ion effects on CF<sub>2</sub> surface interactions during C<sub>3</sub>F<sub>8</sub> and C<sub>4</sub>F<sub>8</sub> plasma processing of Si. *J. Vac. Sci. Technol. A* **2004**, 22, (5), 2168-2176.
5. Takahashi, K.; Tachibana, K., Molecular composition of films and solid particles polymerized in fluorocarbon plasmas. *J. Appl. Phys.* **2001**, 89, (2), 893-899.
6. Labelle, C. B.; Limb, S. J.; Gleason, K. K., Electron spin resonance of pulsed plasma-enhanced chemical vapor deposited fluorocarbon films. *J. Appl. Phys.* **1997**, 82, (4), 1784-1787.
7. Butoi, C. I.; Mackie, N. M.; Barnd, J. L.; Fisher, E. R.; Gamble, L. J.; Castner, D. G., Control of Surface Film Composition and Orientation with Downstream PECVD of Hexafluoropropylene Oxide. *Chem. Mater.* **1999**, 11, (4), 862-864.
8. Butoi, C. I.; Mackie, N. M.; Gamble, L. J.; Castner, D. G.; Barnd, J.; Miller, A. M.; Fisher, E. R., Deposition of Highly Ordered CF<sub>2</sub>-Rich Films Using Continuous Wave and Pulsed Hexafluoropropylene Oxide Plasmas. *Chem. Mater.* **2000**, 12, (7), 2014-2024.
9. Labelle, C. B.; Gleason, K. K., Surface morphology of PECVD fluorocarbon thin films from hexafluoropropylene oxide, 1,1,2,2-tetrafluoroethane, and difluoromethane. *J. Appl. Polymer Sci.* **1999**, 74, (10), 2439-2447.
10. Labelle, C. B.; Gleason, K. K., Pulsed plasma deposition from 1,1,2,2-tetrafluoroethane by electron cyclotron resonance and conventional plasma enhanced chemical vapor deposition. *J. Appl. Polymer Sci.* **2001**, 80, (11), 2084-2092.
11. Capps, N. E.; Mackie, N. M.; Fisher, E. R., Surface interactions of CF<sub>2</sub> radicals during deposition of amorphous fluorocarbon films from CHF<sub>3</sub> plasmas. *J. Appl. Phys.* **1998**, 84, (9), 4736-4743.
12. Park, C. K.; Kim, H. T.; Lee, C. H.; Lee, N. E.; Mok, H., Effects of CH<sub>2</sub>F<sub>2</sub> and H<sub>2</sub> flow rates on process window for infinite etch selectivity of silicon nitride to ArF PR in dual-frequency CH<sub>2</sub>F<sub>2</sub>/H<sub>2</sub>/Ar capacitively coupled plasmas. *Microelectron. Eng.* **2008**, 85, (2), 375-387.
13. Harshbarger, W. R.; Porter, R. A.; Miller, T. A.; Norton, P., Study of Optical Emission from an Rf Plasma During Semiconductor Etching. *Appl. Spectrosc.* **1977**, 31, (3), 201-207.
14. d'Agostino, R.; Cramarossa, F.; Fracassi, F., *Plasma Deposition, Treatment, and Etching of Fluorocarbons*. Academic Press: San Diego, CA, 1990.

15. Haupt, M.; Barz, J.; Oehr, C., Creation and Recombination of Free Radicals in Fluorocarbon Plasma Polymers: An Electron Spin Resonance Study. *Plasma Process. Polym.* **2008**, 5, (1), 33-43.
16. Milella, A.; Palumbo, F.; Favia, P.; Cicala, G.; d'Agostino, R., Continuous and Modulated Deposition of Fluorocarbon Films from  $c\text{-C}_4\text{F}_8$  Plasmas. *Plasma Process. Polym.* **2004**, 1, (2), 164-170.
17. Liu, D.; Martin, I. T.; Fisher, E. R.,  $\text{CF}_2$  surface reactivity during hot filament and plasma-enhanced chemical vapor deposition of fluorocarbon films. *Chem. Phys. Lett.* **2006**, 430, 113-116.
18. Liu, D.; Martin, I. T.; Zhou, J.; Fisher, E. R., Radical Surface Interactions During Film Deposition: A Sticky Situation? *Pure Appl. Chem.* **2006**, 78, (6), 1187-1202.
19. Sekiguchi, H.; Honda, T.; Kanzawa, A., Thermal plasma decomposition of chlorofluorocarbons. *Plasma Chem. Plasma Process.* **1993**, 13, (3), 463-478.
20. Appelman E, H.; Clyne M. A, A., Elementary Reaction Kinetics of Fluorine Atoms, FO, and NF Free Radicals. In *Fluorine-Containing Free Radicals*, American Chemical Society: 1978; Vol. 66, pp 3-25.
21. Fanelli, F., Optical Emission Spectroscopy of Argon-Fluorocarbon-Oxygen Fed Atmospheric Pressure Dielectric Barrier Discharges. *Plasma Process. Polym.* **2009**, 6, (9), 547-554.
22. O'Kane, D. F.; Mittal, K. L., Plasma cleaning of metal surfaces. *J. Vac. Sci. Technol.* **1974**, 11, (3), 567-569.
23. Hughes, I. R. a. G., Investigation of varying  $\text{C}_4\text{F}_8/\text{O}_2$  gas ratios on the plasma etching of carbon doped ultra-low-  $k$  dielectric layers. *Semiconductor Sci. Technol.* **2007**, 22, (6), 636.
24. Ashfold, M. N. R.; Castano, F.; Hancock, G.; Ketley, G. W., *Chem. Phys. Lett.* **1980**, 73, 421.
25. Teii, K.; Hori, M.; Goto, T., *J. Appl. Phys.* **2000**, 87, 7185-7190.
26. Mackie, N. M.; Ventura, V. A.; Fisher, E. R., Surface Reactivity of  $\text{CF}_2$  Radicals Measured Using Laser-Induced Fluorescence and  $\text{C}_2\text{F}_6$  Plasma Molecular Beams. *J. Phys. Chem. B* **1997**, 101, (46), 9425-9428.
27. Hargis, J. P. J.; Kushner, M. J., Detection of  $\text{CF}_2$  radicals in a plasma etching reactor by laser-induced fluorescence spectroscopy. *Appl. Phys. Lett.* **1982**, 40, (9), 779-781.
28. Hack, W.; Langel, W., Photophysics of  $\text{CF}_2(\text{A } ^1\text{B}_1(0,6,0))$  excited by a KrF laser at 248 nm I: Quenching of  $\text{CF}_2(\text{A})$  by its common precursors. *J. Photochem.* **1983**, 21, (2), 105-110.
29. Hikosaka, Y.; Toyoda, H.; Sugai, H., Drastic change in  $\text{CF}_2$  and  $\text{CF}_3$  kinetics induced by hydrogen addition into  $\text{CF}_4$  etching plasma. *Jpn. J. Appl. Phys.* **1993**, 32, L690-L693.
30. Ryan, K.; Plumb, I., Gas-phase reactions of  $\text{CF}_3$  and  $\text{CF}_2$  with hydrogen atoms: Their significance in plasma processing. *Plasma Chem. Plasma Process.* **1984**, 4, (3), 141-146.
31. Trevino, K. J.; Shearer, J. C.; Tompkins, B. D.; Fisher, E. R., Comparing Isoelectric Point and Surface Composition of Plasma Modified Native and Deposited

- SiO<sub>2</sub> Films Using Contact Angle Titrations and X-ray Photoelectron Spectroscopy. *Plasma Process. Polym.* **2011**, 8, (10), 951-964.
32. Vitale, S. A.; Sawin, H. H., Abatement of C<sub>2</sub>F<sub>6</sub> in rf and microwave plasma reactors. *J. Vac. Sci. Technol. A* **2000**, 18, (5), 2217-2223.
  33. Doering, J. P.; Yang, J., Atomic oxygen <sup>3</sup>P - <sup>3</sup>S<sub>0</sub> (1304Å) transition revisited: Cross section near threshold. *J. Geophys. Res.* **2001**, 106, (A1), 203-209.
  34. Rozum, I.; Limao-Vieira, P.; Eden, S.; Tennyson, J.; Mason, N. J., Electron Interaction Cross Sections for CF<sub>3</sub>I, C<sub>2</sub>F<sub>4</sub>, and CF<sub>x</sub> (x = 1--3) Radicals. *J. Phys. Chem. Ref. Data* **2006**, 35, (1), 267-284.
  35. Huie, R. E.; Long, N. J. T.; Thrush, B. A., Laser induced fluorescence of CFCl and CCl<sub>2</sub> in the gas phase. *Chem. Phys. Lett.* **1977**, 51, (2), 197-200.
  36. Sugimoto, I.; Miyake, S., Optical-emission studies on the interaction between halogenated carbon species and noble gas during fluoropolymer sputtering. *J. Appl. Phys.* **1989**, 65, (12), 4639-4645.
  37. Booth, J. P.; Hancock, G.; Perry, N. D., Laser induced fluorescence detection of CF and CF<sub>2</sub> radicals in a CF<sub>4</sub>/O<sub>2</sub> plasma. *Appl. Phys. Lett.* **1987**, 50, (6), 318-319.

## **CHAPTER 8**

### **RESEARCH SUMMARY AND PERSPECTIVES**

The results and general considerations addressed in this dissertation are summarized here. Particular emphasis in this chapter focuses on the utility of this work in a broader setting and those aspects that warrant further inquiry.

## 8.1. Research Summary

Fluorocarbon plasma processing is a widely employed technique with far-reaching applications, especially within the semiconductor industry. Moore's Law stipulates that the number of transistors that can be placed on a computer chip doubles roughly every two years.<sup>1</sup> Such rapid advances in technology necessitate adequate fundamental knowledge of the tools used to design and process these products. The research presented in this dissertation may offer contributions to improved plasma processing efficiency. Specific attention has focused on the gas-phase contributions to surface modification by FC plasmas.

One global theme of this dissertation has concentrated on deciphering the role of gas-phase species present in FC plasma systems. The approach to this problem utilized spectroscopic techniques, including LIF, OES, and MS, to identify ground state, electronically excited, and charged species, respectively. These analyses were extended to investigate the inherent properties of the identified species. In particular, internal temperatures of vibration and rotation were calculated for diatomic radicals including CF, NO, and SiF. Vibrational temperature values appear to rely upon complex plasma processes, such as the V-T energy exchange mechanism, whereas rotational temperatures provide a suitable gauge of overall plasma temperature. Ion energy distributions for a range of nascent plasma ions were also determined. Generally, ions increase in energy with changing plasma parameters such as  $P$ . Mean energy values tend to be greater for CF<sub>4</sub>-generated ions than for other FC plasma systems. The effect of additives to FC plasmas was also examined, and preliminary data espouse the notion that hydrogen abstracts F atoms in the gas-phase and oxygen affects the profusion of CF<sub>x</sub> species.

A second chief aspect of this work was dedicated to understanding the net effect of surface modification by FC plasmas. High-resolution XPS spectra and other surface-sensitive techniques were employed to this end. Commonly, the films deposited from FC plasmas are robust and amorphous and demonstrate a relatively high degree of crosslinking. The deposition rates of FC systems increase significantly with a decrease in F/C ratio of the precursor gas. Concomitantly, the surface energies of deposited films increase substantially. These general trends suggest that a high degree of control over surface properties is possible by careful manipulation of plasma parameters.

The ultimate aim of this work sought to interconnect the gas-phase behaviors of plasma species with the net effect of surface modification by examining the plasma-substrate interface through IRIS experiments. Scatter coefficients for CF and CF<sub>2</sub> radicals typically exceed unity, indicating that surface-mediated production of these species is a primary process occurring in the FC plasma system. Ion bombardment of FC films is considered one avenue toward surface production of these CF<sub>x</sub> species. Additionally, CF(<sup>2</sup>Δ) species are speculated to quench at surfaces and readily desorb as ground electronic radicals. The totality of this work offers additional insight into the fundamental plasma processes so critical for fabrication of semiconductor and microelectronics devices. Moreover, facets of these studies may be employed in other areas, including advanced material design for hydrophobic biocompatible components. Despite the extensive coverage of various aspects of FC plasma chemistry presented in this work, future investigations of the FC plasma system should continue to yield important and valuable information about the nature of plasma-surface interactions.

## 8.2. Future Directions

The work discussed in the bulk of this dissertation could be used to advance technological frontiers in materials processing, but there yet remain a substantial number of studies that could expand the understanding of these plasma systems even further. For example, comprehensive pressure-dependent studies should be carried out. Although some work presented here focused on the effect of changing  $p$ , the vast majority of data were provided for  $p = 50$  mTorr. Changes in the feed gas pressure are expected to significantly influence the characteristics of the FC plasma (see section 6.5), and possibly  $\text{CF}_x$  surface interactions. In particular, careful modulation of FC feed pressure has been shown to be a crucial parameter for determining substrate etch selectivity and/or film deposition efficacy.<sup>2</sup> Gas-phase diagnostics of FC plasmas as a function of  $p$  and complementary surface analyses and IRIS data should round out our understanding of these systems and provide for a thorough compilation of inductively-coupled FC plasma phenomena.

The dynamics of FC film initiation and propagation is another area for which a dearth of information exists. One method to probe film formation at the plasma-surface interface *in situ* is through use of sum frequency generation vibrational spectroscopy (SFGVS).<sup>3</sup> SFGVS has been employed to study PTFE films,<sup>4</sup> protein adsorption to FC films,<sup>5</sup> and investigate plasma-wall interactions.<sup>5</sup> The selectivity associated with this technique (SFG is generated at regions of asymmetry) makes this approach ideal for examining the interfacial properties of a FC film on a substrate such as Si. We have designed an experimental apparatus for performing *in situ* SFGVS experiments on plasma-modified surfaces (Fig. 8.1). Plasma feed gases enter a traditional glass barrel reactor in

region ①, and the generated plasma beam participates in surface modification in a vacuum chamber, region ②. The substrate can be repositioned through a gate valve using a z-translator to region ③ where spectroscopic analysis ensues. Implementation of this system is expected to commence imminently. Results gleaned from SFGVS studies should further elucidate the phenomena occurring at the gas-surface interface and shed new light upon film formation dynamics. Although we have examined in detail the effect of vibrationally excited radicals and ions in a wide range of plasma systems (Chapter 5), a similar fundamental understanding of ground state species is lacking. Instrumental limitations preclude data collection for relevant absorption experiments. A relatively straightforward equipment upgrade to the optical emission spectrometer (i.e. incorporation of a D<sub>2</sub> or Xe lamp) would afford the capability to probe ground state species behavior. Comparable broadband absorption spectroscopy (BAS) experiments have already found utility to not only determine vibrational temperatures of ground state molecules, but also to determine absolute concentrations of CF (X <sup>2</sup>Π) plasma species.<sup>6</sup> These crucial measurements will fill in gaps in our understanding of the plasma system, and complement the wealth of data already amassed for excited state plasma species.

A second upgrade to the emission spectrometer, to increase temporal resolution, would allow for experiments that expound the kinetic behavior of plasma species besides CF<sub>2</sub>. At present, the maximum resolution achievable is approximately 0.15 sec/scan. This limits the ability to monitor processes that occur on the millisecond time-scale, such as CF<sub>x</sub> radical formation from a FC precursor, Fig. 8.2. Although rate constant data were presented in this dissertation for CF<sub>2</sub>, those experiments were

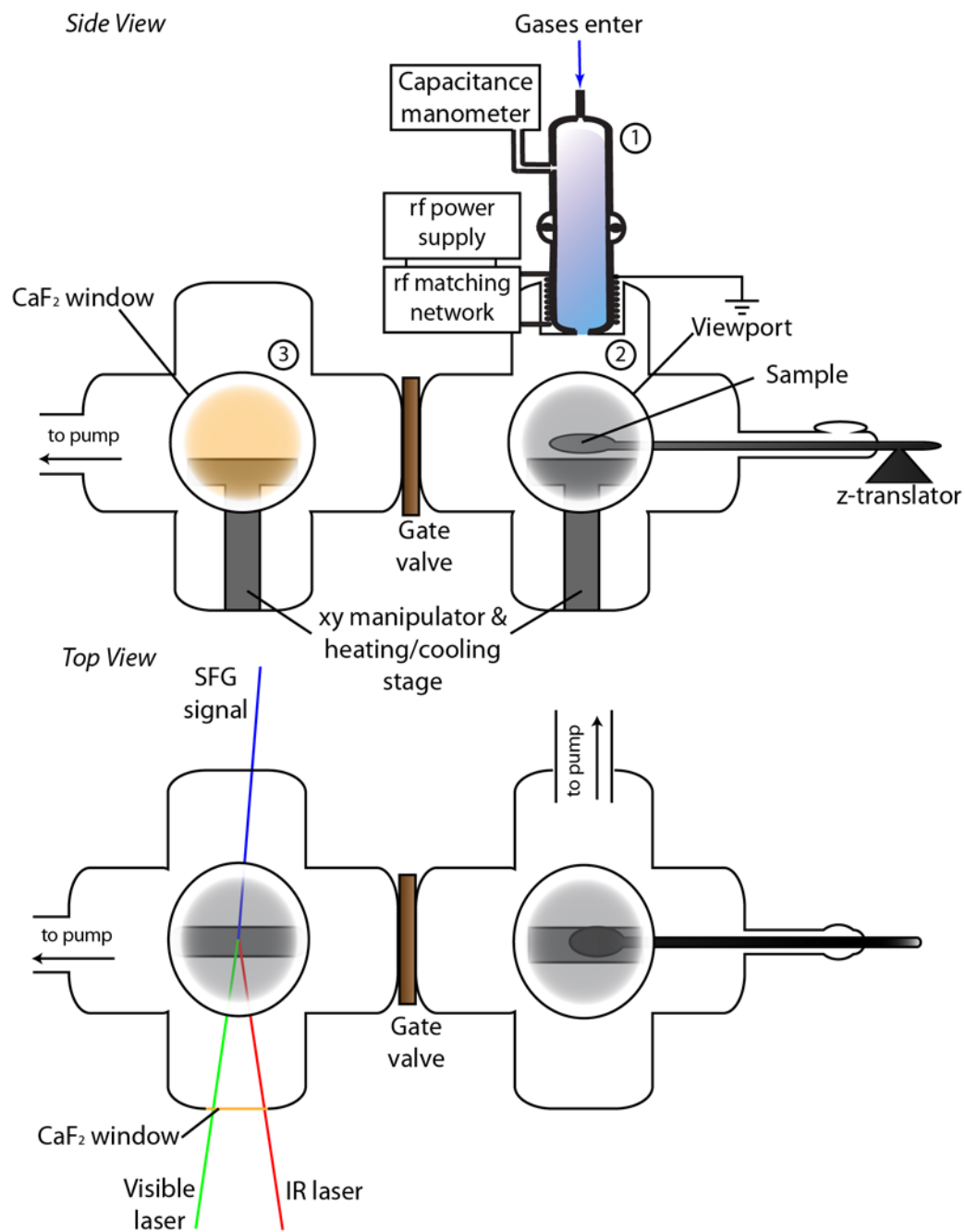


**Figure 8.1.** Side-view and top-down schematics of the chamber design for *in situ* SFGVS analyses of plasma-modified materials.

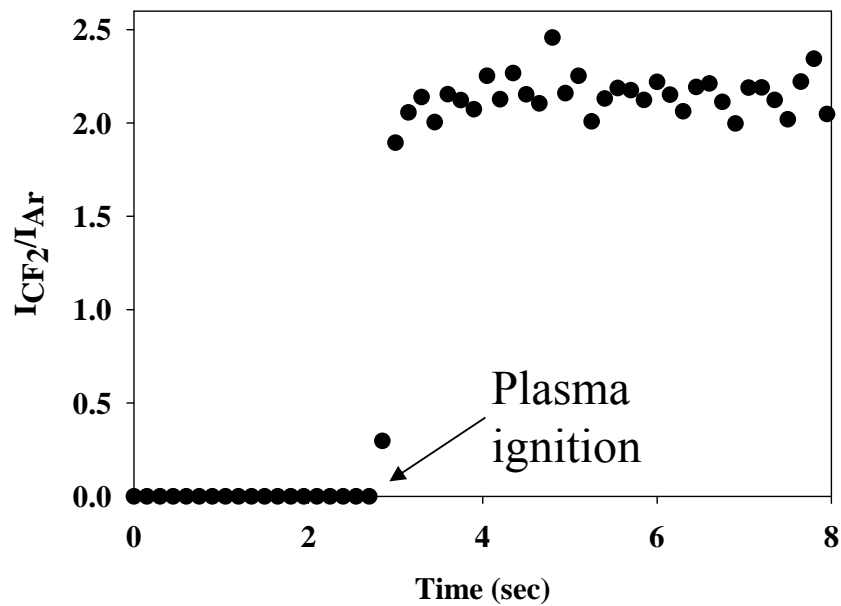


**Figure 8.2.** Time-dependent emission signal for  $\text{CF}_2^*$  in a  $\text{C}_2\text{F}_6$  plasma with  $P = 50$  W. The maximum temporal resolution of the spectrometer is insufficient to resolve the features associated with the  $\text{CF}_2^*$  species very shortly after plasma ignition.

performed using a loaned spectrometer. Using an upgraded instrument, kinetic measurements can be made for a wide range of plasma systems, and investigations of various formation mechanisms may commence for other plasma sources (i.e. gas-phase plasma formation of OH via direct decomposition of H<sub>2</sub>O vs. recombination process in NH<sub>3</sub>/O<sub>2</sub>).

These future directions should serve to further build on the central knowledge of plasma characteristics and provide additional insights into the phenomena associated with the plasma-surface interface. Moreover, they should offer enhanced insight into the parameter space affecting plasma processing. Ultimately, by controlling the parameters associated with our plasma systems, we can create tailored films with specific compositions and surface energies. These custom properties so crucial for advancement of plasma technology have far-reaching implications in both fundamental research and industrial applications. The perpetual and continued expansion of frontiers of science and exploration depend upon the pursuit of such fundamental processes. This dissertation has sought to offer some modicum of contribution to such progress.

### 8.3. References

1. Bondyopadhyay, P. K., Moore's law governs the silicon revolution. *Proc. IEEE* **1998**, 86, (1), 78-81.
2. Oehrlein, G. S.; Zhang, Y.; Vender, D.; Haverlag, M., Fluorocarbon high-density plasmas. I. Fluorocarbon film deposition and etching using  $\text{CF}_4$  and  $\text{CHF}_3$ . *J. Vac. Sci. Technol. A* **1994**, 12, (2), 323-332.
3. Lambert, A. G.; Davies, P. B.; Neivandt, D. J., Implementing the Theory of Sum Frequency Generation Vibrational Spectroscopy: A Tutorial Review. *Appl. Spectrosc. Rev.* **2005**, 40, (2), 103-145.
4. Ji, N.; Ostroverkhov, V.; Lagugne-Labarthe, F.; Shen, Y.-R., Surface Vibrational Spectroscopy on Shear-Aligned Poly(tetrafluoroethylene) Films. *J. Am. Chem. Soc.* **2003**, 125, (47), 14218-14219.
5. Weidner, T.; Samuel, N. T.; McCrea, K.; Gamble, L. J.; Ward, R. S.; Castner, D. G., Assembly and structure of  $\alpha$ -helical peptide films on hydrophobic fluorocarbon surfaces. *Biointerphases* **2010**, 5, (1), 9-16.
6. Luque, J.; Hudson, E. A.; Booth, J.-P.,  $\text{CF A } ^2\Sigma^+ \rightarrow \text{X } ^2\Pi$  and  $\text{B } ^2\Delta \rightarrow \text{X } ^2\Pi$  study by broadband absorption spectroscopy in a plasma etch reactor: Determination of transition probabilities,  $\text{CF X } ^2\Pi$  concentrations, and gas temperatures. *J. Chem. Phys.* **2003**, 118, (2), 622-632.

## Appendix A. Calculations of Characteristic Plasma Temperatures

As noted in the Introduction to this dissertation, the inherent nature of the plasma system gives rise to a number of characteristic gas temperatures and influences the rotational, vibrational, and translational energy of molecules. Attempts to calculate representative gas temperatures such as the electron temperature *in situ* have long relied upon the introduction of one or more electrodes to the plasma (e.g. a Langmuir probe). One disadvantage of using the Langmuir probe is that the probe itself may lose a significant fraction of its current to the plasma and, in so doing, perturb those values it seeks to measure.<sup>1</sup> Accurate measurements of internal temperatures for molecules rely upon rigorous calculations best approached via computational methods. Herein are discussed simulations developed in conjunction with experimental optical emission data to determine plasma electron temperatures and molecular vibrational temperatures *ex situ*.

### A.1. Electron Temperatures

Plasma mean electron temperatures ( $T_e$ ) were determined *ex situ* via analyses of Ar emission lines in OE spectra. The routine was condensed in an Excel macro to enable calculation of  $T_e$  after querying the user through a series of input boxes. Input data were iteratively compared for four Ar transitions, as summarized in Table A.1, such that the intensity for Transition 1 was compared to each of the three others in turn. This yielded three  $T_e$  values for statistical comparison. For each calculation, the **linest()** function in Excel was used in a 5x2 array to determine the ordinate intercept,  $T_e$ , of the following

**Table A.1.** Emission parameters for Ar used in  $T_e$  determination.<sup>2,3</sup>

<b>Transition</b>	<b><math>\nu \times 10^{13}</math> (<math>s^{-1}</math>)</b>	<b>A (<math>s^{-1}</math>)</b>	<b>Excitation Energy (eV)</b>
(1) 3d—4p	4.86	2.00E7	21.127
(2) 4p—6s	4.68	1.16E6	14.839
(3) 4p—6s	4.70	4.21E5	14.848
(4) 4p—4d	4.44	1.93E6	14.743

equation:

$$\frac{(E_n - E_1)}{kT_e} = \ln \left[ \frac{I_1 \nu_n A_n (E_n + 2kT_e)}{I_n \nu_1 A_1 (E_1 + 2kT_e)} \right] \quad (\text{A.1})$$

where  $E_n$  represents the excitation energy of arbitrarily defined transition  $n$ ,  $I_n$  is the emission intensity obtained from the OE spectrum,  $\nu_n$  is the frequency of the transition, and  $A_n$  is the transition probability. As might be expected,  $T_e$  values depend not only upon plasma parameters, but also on the physical location being probed along the reactor. We have employed the preceding technique to determine  $T_e$  as a function of distance along the reactor for  $\text{C}_2\text{F}_6$  plasmas, Fig. A.1, using radially resolved OES data.

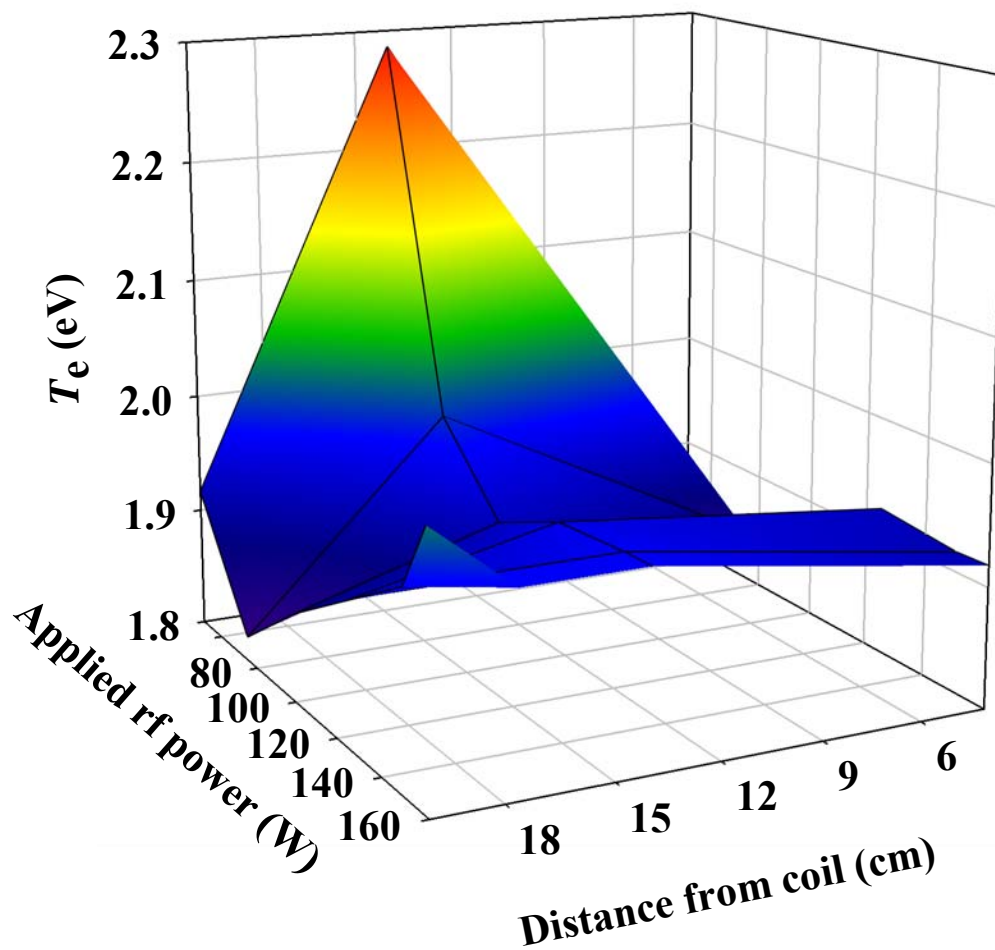


**Figure A.1.** Electron temperatures in  $C_2F_6$  plasmas plotted as a function of both applied rf power and distance measured from the start of the reactor coil region.

## A.2. Vibrational Temperatures

CF and NO vibrational temperatures can be calculated using the software package LIFbase,<sup>4</sup> which includes preset simulation parameters for a range of diatomic molecules. Vibrational temperatures of polyatomic ( $N > 2$ , where  $N$  is the number of atoms) oscillators cannot be evaluated using this program. Instead, we have employed the simulation tool pGopher,<sup>5</sup> a multipurpose spectrum fitting routine. This software generates diagonalized Hamiltonian matrices consisting of all states of the same total angular momentum and rovibronic symmetry. Thus, it requires user input of molecular symmetry, vibrational modes, and the origin for a transition of interest. For example, the parameters necessary to simulate the  $A \rightarrow X$  transition for calculation of  $\text{CF}_2^*$  ( $C_{2v}$  point group) vibrational temperatures from OES spectra are summarized in Table A.2.  $\text{CF}_2$  has  $3N-6$  or three degrees of freedom, including the symmetric stretching (sym. str.), bending, and asymmetric stretching (asym. str.) vibrational modes. The  $A$  electronic state lies  $37216 \text{ cm}^{-1}$  above the ground  $X$  state.<sup>6</sup> Peak height matching was accomplished by varying the Einstein  $A$  coefficient according to equation (A.2) which assumes spontaneous emission for an arbitrary  $A \rightarrow B$  transition. Peaks were matched using 80% Gaussian/20% Lorentzian line-shapes.

$$A = \frac{8\pi^2\nu^3}{3\epsilon_0c^3h} |\langle A | \hat{\mu} | B \rangle|^2 \quad (\text{A.2})$$

Vibrational temperatures were determined by evaluating the simulation temperature at the maximized overlap of simulated and experimental spectra. An example of the simulated fit to experimental data is provided in Fig. A.2 for  $\text{CF}_2^*$  in a  $\text{CF}_4$  plasma.

**Table A.2.** pGopher parameters used for determination of CF<sub>2</sub> vibrational temperature. Energy values obtained from reference 4.

<b>Electronic State</b>	<b>Vibrational modes (symmetry)</b>	<b>Energy (cm<sup>-1</sup>)</b>
$X^1A_1$	sym. str. (a <sub>1</sub> )	1225.1
	bend (a <sub>1</sub> )	666.3
	asym. str. (b <sub>2</sub> )	1114.4
$A^1B_1$	sym. str. (a <sub>1</sub> )	1012.1
	bend (a <sub>1</sub> )	496.7
	asym. str. (b <sub>2</sub> )	1180.2

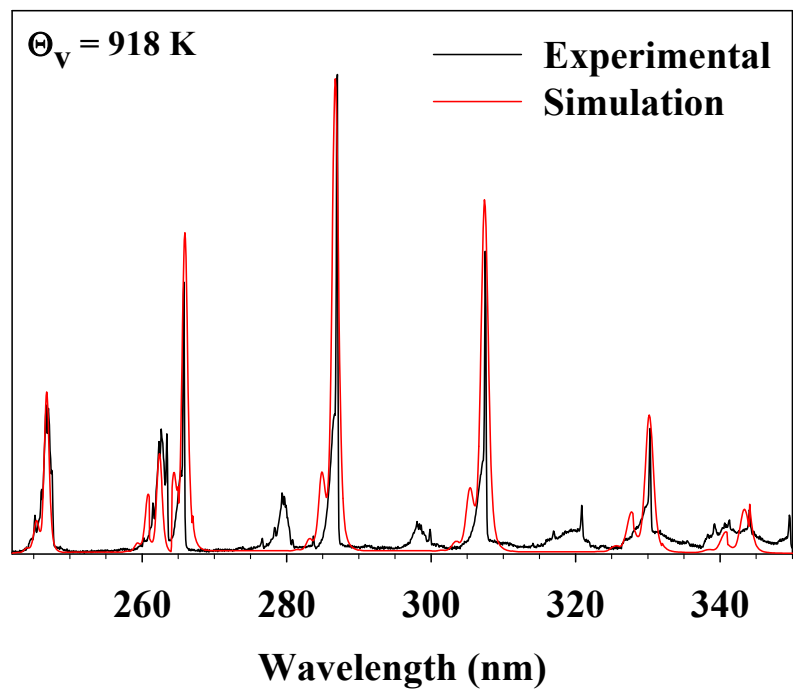


**Figure A.2.** Enlarged region of the emission spectrum for a CF<sub>4</sub> plasma ( $P = 100 \text{ W}$ ) depicting the  $A^1B_1 \rightarrow X^1A_1$  for CF<sub>2</sub>. Overlap from CF  $A^2\Sigma^+ \rightarrow X^2\Pi$  and CF<sub>2</sub>  $a^3B_1 \rightarrow X^1A_1$  is also observed. The red line is a spectral simulation performed in pGopher, which, when matched to the experimental data, yields  $\Theta_v(\text{CF}_2) = 918 \text{ K}$ .

### A.3. References

1. Mawardi, O. K., Use of Langmuir Probes for Low-Density Plasma Diagnostics. *Amer. J. Phys.* **1966**, 34, (2), 112-120.
2. Norlen, G., Wavelengths and Energy Levels of Ar I and Ar II based on New Interferometric Measurements in the Region 3400-9800 Å. *Physica Scripta* **1973**, 8, (6), 249.
3. Boogaard, A.; Kovalgin, A. Y.; Aarnink, A. A. I.; Wolters, R. A. M.; Holleman, J.; Brunets, I.; Schmitz, J. In *Measurement of electron temperatures of Argon Plasmas in a High-Density Inductively-Coupled Remote Plasma System by Langmuir Probe and Optical Emission Spectroscopy*, Proceedings of the 9th annual workshop on semiconductor advances for future electronics and sensors, Veldhoven, Netherlands, 2006; Veldhoven, Netherlands, 2006; pp 412-418.
4. Luque, J.; Crosley, D. R. *LIFBASE: Database and Spectral Simulation Program*, 1.5; SRI International Report MP 99-009: 1999.
5. Western, C. M. *PGOPHER, a Program for Simulating Rotational Structure*, University of Bristol, <http://pgopher.chm.bris.ac.uk>.
6. Linstrom, P. J.; Mallard, W. G., Eds., *NIST Chemistry WebBook, NIST Standard Reference Database Number 69*. National Institute of Standards and Technology: Gaithersburg, MD 20899.

## Appendix B. Preliminary Results for Characteristic CF<sub>2</sub> Temperatures

### B.1. Vibrational Temperatures

Although the discussions in Chapter 5 focused on characteristic temperatures for diatomic molecules, significant attention was also given to the CF<sub>2</sub> radical in FC plasmas. Vibrational temperatures for CF<sub>2</sub><sup>\*</sup> were calculated from emission spectra using the simulation tool pGopher<sup>1</sup> (see Appendix A). A representative simulated spectrum is provided in Fig. A.2.  $\Theta_V(\text{CF}_2)$  are plotted in Fig. B.1 as a function of  $P$  for CF<sub>4</sub> and C<sub>2</sub>F<sub>6</sub> plasma sources. Generally, the values increase with increasing  $P$ , and  $\Theta_V(\text{CF}_2)$  values are larger for C<sub>2</sub>F<sub>6</sub> systems than for CF<sub>4</sub>. We have calculated  $T_e$  values for both plasma systems; values for C<sub>2</sub>F<sub>6</sub> plasmas are generally slightly larger than  $T_e$  for CF<sub>4</sub> systems (see Chapter 5), suggesting the vibrational energy associated with CF<sub>2</sub><sup>\*</sup> originates from excess vibrational excitation during electron impact formation processes. Reactions such as that shown in (1.15) have relatively low threshold energy, 4.5 eV. However, there must be a significant portion of electrons with energies exceeding this threshold present in the plasma; the disparities in  $\Theta_V(\text{CF}_2)$  offer indirect evidence thereof.

The absolute values for CF<sub>2</sub> vibrational temperatures can provide additional insight into the formation mechanism of the radical. For example, Cruden and coworkers<sup>2</sup> used CF<sub>2</sub> vibrational temperatures to calculate the CF<sub>2</sub> total number density from the vibrational partition function. They showed that increases in filament temperature associated with CF<sub>2</sub> production from HFPO during pyrolytic chemical vapor

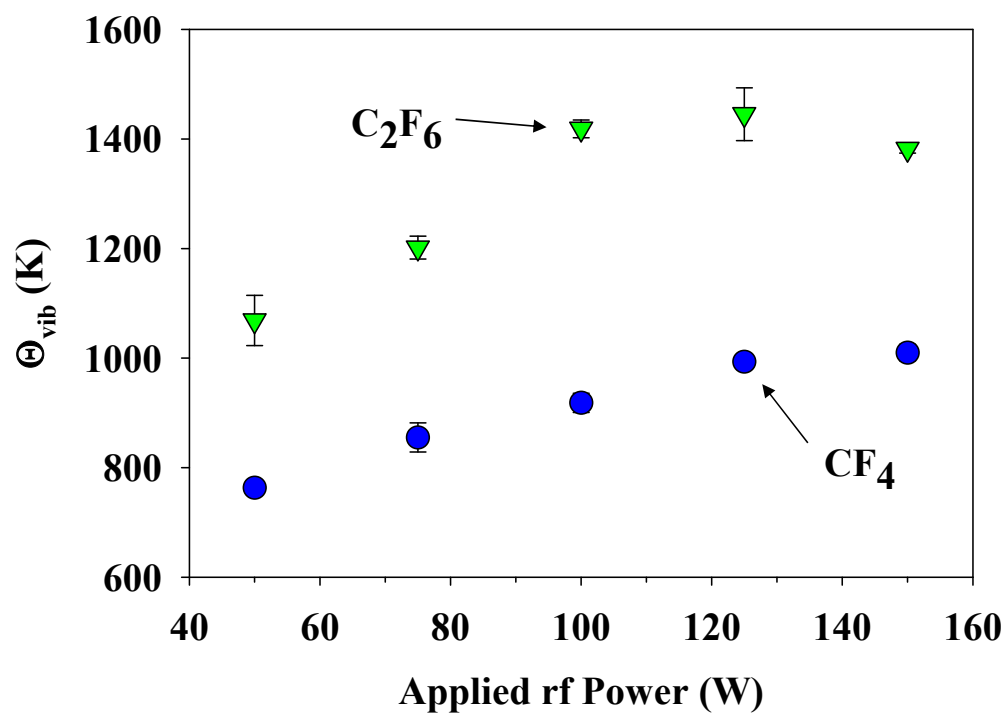


**Figure B.1.** Vibrational temperatures of the  $\text{CF}_2$  molecule plotted as a function of plasma power for  $\text{CF}_4$  and  $\text{C}_2\text{F}_6$  systems.

deposition resulted in increases in vibrational temperature. This complements the results shown here in that increases in energy supplied to the plasma system dictate  $\Theta_V(\text{CF}_2)$ . In the work of Cruden *et al.*, vibrational temperatures were calculated based on the ratio of  $\text{CF}_2$  densities in both its ground and excited states, equation (B.1).

$$\Theta_V = -\frac{h\nu_2}{k_b} \ln\left(\frac{n_{(v_1', v_2', v_3')}}{n_{(v_1'', v_2'', v_3'')}}\right) \quad (\text{B.1})$$

For their work, Cruden *et al.* examined the  $n_{(0,1,0)} \rightarrow n_{(0,0,0)}$  densities for  $\text{CF}_2$ . Equation (B.1) could easily be reconfigured to determine proportions of  $\text{CF}_2$  total densities for species in our plasma systems given  $\Theta_V(\text{CF}_2)$ .

A second important insight regarding  $\Theta_V(\text{CF}_2)$  values stems from the work of Rubio *et al.*<sup>3</sup> Their work implicates vibrational temperatures as being indicative of formation mechanisms for direct decomposition of  $\text{C}_3\text{F}_6$  through infrared multiphoton dissociation. Specifically,  $\text{CF}_2$  produced directly from the precursor gas exhibited vibrational temperatures of  $\sim 2500$  K. The  $\Theta_V(\text{CF}_2)$  values shown in Fig. B.1 are significantly lower, suggesting that not all  $\text{CF}_2$  species are produced from direct decomposition of the plasma precursor (a theme expounded upon throughout this dissertation). It is thought that the ejection of a species such as  $\text{CF}_2$  from a FC film as a result of some energetic process (e.g. ion bombardment) dissipates a significant amount of excess energy into surrounding film moieties rather than solely into the desorbing molecule. Hence, lower than anticipated  $\Theta_V(\text{CF}_2)$  are observed. Certainly, this is a point of ongoing consideration in the Fisher laboratory.

## B.2. Translational Temperatures

Translational temperatures,  $\Theta_T$ , were estimated for  $\text{CF}_2$  species through LIF techniques.<sup>4</sup> Briefly, the experiment incorporates spatially and temporally resolved LIF data with a straight-forward data fitting routine to determine the line-of-sight kinetic energy of the radical. Nominally, this approach is best suited to radicals with long fluorescent lifetimes,  $\tau$ . Efforts to mitigate the fluorescent lifetime limitation for  $\text{CF}_2$  ( $\tau = 61$  ns, Table 2.2) included increasing the ICCD resolution by eliminating pixel binning and increasing laser power to ensure saturation of the transition. An optimal geometry was employed, whereby the laser was reconfigured from its traditional configuration (Fig. 2.1) to intersect the plasma molecular beam at a  $90^\circ$  angle, such that the laser, molecular beam, and ICCD are mutually orthogonal. Figure B.2(a-e) depicts the raw data associated with determination of  $\Theta_T$ . In these images, the laser propagation axis spans from bottom to top across the center of the image. Gate delay times for the ICCD camera were stepped appropriately to monitor  $\text{CF}_2$  “movement” along the plasma axis (abscissa). Cross-sections along the x-axis of the images were averaged for an 80 pixel swath and plotted as a function of distance along the plasma axis, Fig. B.2(f). These cross-sections were fit with Gaussian functions to determine the  $x_0$  position of the apex. Such “spot positions” were plotted as a function of corresponding delay times, Fig. B.2(g), and fit with a linear regression to determine the slope, or velocity ( $v$ ), of the molecule. Translational temperatures are then calculated according to equation (B.2), where  $m$  is the mass of the radical.

$$\Theta_T = \frac{\pi m v^2}{8 k_b} \quad (\text{B.2})$$

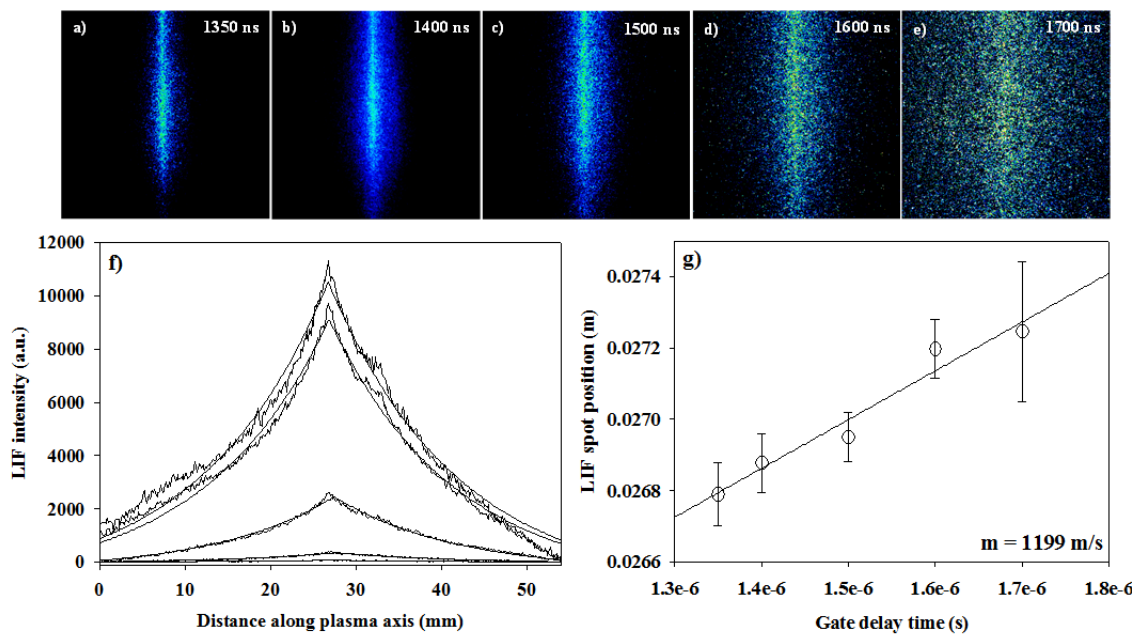


**Figure B.2.** a)-e)  $\text{CF}_2$  LIF spots at varying ICCD gate delay times. Laser light propagates from bottom to top in each image, through the center of the frame. The line-of-sight direction of the plasma molecular beam propagates from left to right. f) Cross-sections taken along the plasma axis as a function of delay times, fit with 3-parameter Gaussian functions. g) LIF spot position (x-position of Gaussian maxima) plotted as a function of delay time. The fit is a linear regression to the data yielding a slope,  $m = 1199 \text{ m/s}$ , with  $R^2 = 0.96$ .

Preliminary  $\Theta_T(\text{CF}_2)$  values are shown for  $\text{C}_2\text{F}_6$  and  $\text{C}_3\text{F}_6$  systems in Table B.1. Although the *total* translational temperature of the collective plasma vapor in the systems discussed here is typically near room temperature ( $\sim 300$  K, see Chapter 5), the temperature values observed for  $\text{CF}_2$  radicals are much higher. The reason for this discrepancy is that the total gas temperature is a measure of the average translational energy of all gas-phase species. Within the plasma, a broad distribution of translational energies may exist for individual species. Generally, translational temperatures of small molecules and noble gases equilibrate with the total gas temperature,<sup>5</sup> but other species such as OH radicals do not appear to thermalize.<sup>6</sup> High translational temperatures imply that complex multicollisional and/or surface-mediated mechanisms are involved in the formation of a species. Thus, the high  $\Theta_T(\text{CF}_2)$  might be attributed to the scattering proclivity of the molecule. Interestingly, observed surface scatter coefficients for  $\text{CF}_2$  are typically higher for  $\text{C}_2\text{F}_6$ -based plasmas than for  $\text{C}_3\text{F}_6$  systems, mirroring the preliminary results for  $\Theta_T(\text{CF}_2)$  in the same two systems. It should also be noted that the  $\Theta_T(\text{CF}_2)$  measurements discussed here relate only line-of-sight energies along the laser axis and ignore the angular distribution of energies. Hence, the values listed in Table B.1 are likely upper limits of the true  $\Theta_T(\text{CF}_2)$ .

**Table B.1.**  $\Theta_T(\text{CF}_2)$  values.

<b>Source Gas</b>	<b><math>P</math> (W)</b>	<b><math>\Theta_T(\text{CF}_2)</math> / K</b>
	50	$3064 \pm 564$
$\text{C}_2\text{F}_6$	100	$3323 \pm 560$
	150	$3396 \pm 239$
$\text{C}_3\text{F}_6$	150	$1099 \pm 345$

### B.3. References

1. Western, C. M. *PGOPHER, a Program for Simulating Rotational Structure*, University of Bristol, <http://pgopher.chm.bris.ac.uk>.
2. Cruden, B. A.; Gleason, K. K.; Sawin, H. H., Relationship of CF<sub>2</sub> concentration to deposition rates in the pyrolytic chemical vapor deposition process. *J. Vac. Sci. Technol. B* **2002**, *20* (2), 690-695.
3. Rubio, L.; Santos, M.; Torresano, J. A., Laser induced fluorescence detection of CF, CF<sub>2</sub> and CF<sub>3</sub> in the infrared multiphoton dissociation of C<sub>3</sub>F<sub>6</sub>. *J. Photochem. Photobiol. A* **2001**, *146* (1-2), 1-8.
4. McCurdy, P. R.; Venturo, V. A.; Fisher, E. R., Velocity distributions of NH<sub>2</sub> radicals in an NH<sub>3</sub> plasma molecular beam. *Chem. Phys. Lett.* **1997**, *274* (1-3), 120-126.
5. Haverlag, M.; Stoffels, E.; Stoffels, W. W.; Kroesen, G. M. W.; de Hoog, F. J., Measurement of the gas temperature in fluorocarbon radio frequency discharges using infrared absorption spectroscopy. *J. Vac. Sci. Technol. A* **1996**, *14* (2), 380-383.
6. Bogart, K. H. A.; Cushing, J. P.; Fisher, E. R., Effects of Plasma Processing Parameters on the Surface Reactivity of OH(X<sup>2</sup>Π) in Tetraethoxysilane/O<sub>2</sub> Plasmas during Deposition of SiO<sub>2</sub>. *J. Phys. Chem. B* **1997**, *101* (48), 10016-10023.

## **APPENDIX C**

### **INDEPENDENT RESEARCH PROPOSAL**

The following relates the entirety of an independent research proposal, entitled *A Novel Approach to Determine the Fates of Munitions Constituents and Emerging Contaminants in Aquatic and Terrestrial Systems*, prepared by Michael F. Cuddy in accordance with the doctoral requirements of the Department of Chemistry at Colorado State University. It details fundamental investigations of surface interactions of explosives materials and emerging contaminants with particular emphasis on routes toward improved remediation efforts.

### **C.1. Abstract**

The United States Department of Defense (DOD) Directive 4715.11 articulates the sustainable use of military training ranges and the protection of off-range areas from munitions materials, by-products, and related constituents, including, but not limited to: nitro amines, nitro aromatics, nitrate esters, and perchlorate salts. These munitions constituents (MCs) nevertheless accumulate and aggregate in soils and groundwater near live-fire training sites and munitions production facilities. The ultimate fates and modes of transport through terrestrial and aquatic ecosystems are not well understood; thus, efforts to combat the spread of such emerging contaminants (ECs) suffer from a lack of efficient removal. Herein, we propose a method to investigate the interactions of munitions constituents and emerging contaminants with soil and groundwater on the laboratory scale. We will address this problem in two ways:

- 1) Determine the binding energies of emerging contaminants with soil components to complement a sophisticated computational model of munitions constituent/surface interactions.
- 2) Design and implement a two-dimensional spectrofluorometric approach to monitor MC and EC migration through aqueous and soil environments.

The first phase of the proposed experiments will incorporate a straight-forward thermodynamic analysis of MC/EC-substrate complexes. Thermal desorption analyses coupled with mass spectrometry will help elucidate the propensity for a particular contaminant to adhere to a model soil substrate. In the second phase of experimentation, the unique optical properties of single-walled carbon nanotubes (SWNT) will be exploited through a simple two-dimensional spectroscopic technique to determine SWNT chirality

changes upon exposure to particular contaminants. Upon completion of in-laboratory validation, the above techniques will be extended to applications using real-world samples. Ultimately, this work promises to identify the mechanisms by which the aforementioned contaminants migrate through ecosystems and may contribute to improved efforts to remediate polluted sites.

## **C.2. Background and Significance**

The fates of munitions constituents (MCs) and emerging contaminants (ECs) in soil are of significant concern in terms of their environmental repercussions. Secondary explosives introduced from munitions testing and waste disposal, such as hexahydro-1,3,5-trinitro-1,3,5-triazine (RDX), trinitrotoluene (TNT), and derivatives, including nitrotoluenes and nitrobenzenes, pose substantial threats to the environment. For example, Best et al. have demonstrated that the effects of exposure to TNT- and RDX-spiked soil samples include decreased biomass in both plant and worm populations, with toxicity attributed chiefly to TNT.<sup>1,2</sup> Moreover, both dinitrotoluene and nitrotoluene, impurities often present in residues of TNT munitions, are known carcinogens in rats.<sup>3,4</sup> The compounds TNT and RDX are considered by the EPA to be group C, or possible human carcinogens and DNT is classed as a group B, or probable human carcinogen. Triazine-based compounds, specifically atrazine, are widely used and controversial herbicides with possible carcinogenic properties.<sup>5</sup> Pyridine is toxic and relatively robust in soil<sup>6</sup> while pyrazine has been shown to be a potent inhibitor of embryo growth.<sup>7</sup>

MCs and ECs (collectively referred to as “contaminants”) are generally introduced to the environment at munitions testing sites and through waste dumping at muni-

tions production facilities. A 2005 analysis of soil contamination via high explosive detonation yielded concentrations of TNT and RDX surpassing  $2000 \text{ ng m}^{-2}$ .<sup>8</sup> In 1988, an investigation of RDX in groundwater near the Cornhusker Army Ammunition Plant in Grand Island, Nebraska, determined that the concentration of RDX was nearly ten times the federally recommended maximum contaminant level.<sup>9</sup> More recently, perchlorates, salts of which are often used as propellants and additives for explosives, have come under increased scrutiny for their detrimental health effects in conjunction with the proliferation of this EC in aquatic ecosystems.<sup>10</sup>

Efforts aimed at remediating sites contaminated by munitions residues and other emerging contaminants have included composting and the use of slurry reactors and activated sludge systems.<sup>11</sup> The effectiveness of contaminant removal depends upon the method(s) of remediation along with contaminant concentration and the identities of the

contaminants themselves. Composting, for example, may eliminate explosive materials at the cost of formation of degradation products which may in turn have negative, if less severe, environmental effects.<sup>11, 12</sup> Mechanisms of pathways toward removal are not fully understood. An efficient method for contaminant removal, then, necessarily includes elucidation of the fundamental behavior of MC and EC adsorbates in soil

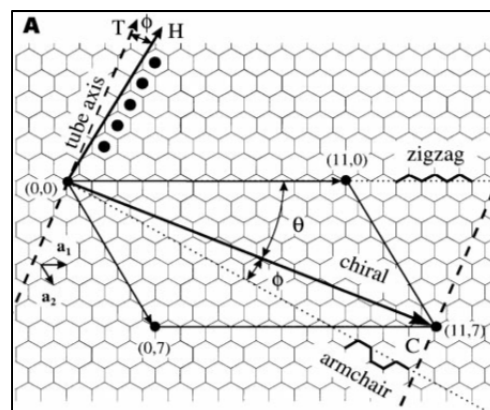


**Figure C.1.** Representation of the chirality of a carbon nanotube. The chirality is determined by “rolling” the graphene sheet depicted here from its origin at  $(0,0)$  to some point,  $(n, m)$ . Adapted from reference 10.

media and aqueous systems. *To this end, we shall examine in this proposed work model and real-world contaminated media for the express purposes of determining contaminant binding energies and analyzing modes of species desorption from surfaces.*

This proposed work includes the development of a detection system based upon the unique optical properties of carbon nanotubes (CNTs) and other nanomaterials. The

structure of single-walled carbon nanotubes (SWNTs) was discussed in the seminal article from Wilder et al.,<sup>13</sup> in which the relationship between the nanotube lattice and the chirality of the SWNT was established, Fig.

C.1. Here,  $n$  and  $m$  define the chiral vector,

$\vec{C}$ , where  $\vec{C} = n\vec{a}_1 + m\vec{a}_2$ . One important optical property of CNTs is that different chiralities exhibit significant differences in flu-

orescence emission and excitation.<sup>14</sup> Discrete signals arise from strong dipole-allowed transitions between van Hove singularities associated with a particular  $(n, m)$  orientation.

Thus, it is possible to “map” spectral signals arising from a sample of CNTs of mixed chirality to identify the chiralities present through use of two-dimensional fluorescence

spectroscopy, as in Fig. C.2. Peaks in the fluorescence spectra correspond not only to the  $(n, m)$  identifier, but also to nanotube diameter,<sup>14</sup> making this technique particularly ef-

fective for rapid identification of CNT distribution.

SWNTs have been employed as gas sensors to detect ammonia and nitrogen dioxide,<sup>15, 16</sup> and in myriad applications from biosensors to pressure sensors.<sup>17</sup> Detection typ-

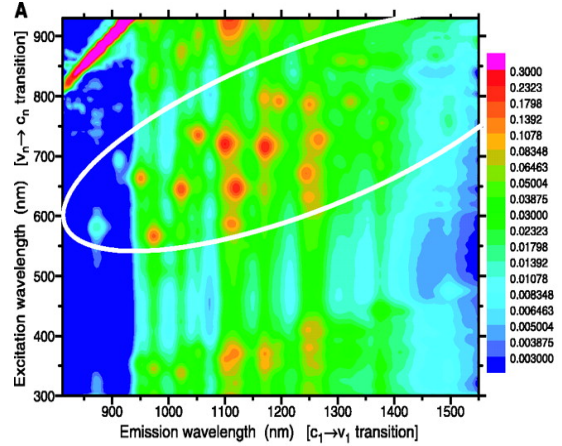


**Figure C.2.** Fluorescence intensities of SWNTs suspended in SDS/D<sub>2</sub>O as a function of both excitation and emission wavelengths. The transitions corresponding to clusters of intense fluorescence are attributed to specific and distinct chiralities. From reference 14.

ically relies upon charge transfer events in semiconducting SWNTs (defined as nanotubes with  $\text{mod}(2n + m, 3) = 1,2$ ).<sup>16</sup> Thus, the utility of the carbon nanotube as a sensor necessarily requires that a detectable species offer an electron donating or accepting capability. This is particularly relevant in the case of high explosives, many of which contain multiple electron-withdrawing nitro groups. Indeed, this feature of TNT has already been exploited for development of CNT-based sensors to determine aqueous concentrations down to 2 ppb.<sup>18-20</sup> TNT, along with other nitro-containing species, is thought to interact with semiconducting and metallic ( $\text{mod}(2n + m, 3) = 0$ ) CNTs alike primarily through  $\pi$ — $\pi$  interactions.<sup>21</sup> Certain charge transfer reactions with organic molecules have been shown to effectively bleach the fluorescence signal of low-energy SWNTs, indicating that the interactions of organic material with the SWNTs influences the spectral phenomena. *To this end, we will seek to take advantage of the interactions of MC/SWNT interactions to probe the fates of the contaminants in both model and real-world soil and aquatic systems.*

### **C.3. Research Design and Methods**

#### *C.3.1. Experimental Approaches*

##### *C.3.1.a. Analysis of Binding Strengths of ECs*

As an initial indicator of the propensity for detection and ultimate remediation of ECs from soils, the binding strength of a variety of test materials to model soil components, Table C.1, will be gauged. A simple apparatus will be designed utilizing a high-vacuum temperature-programmed desorption system interfaced with a mass spectrometer operating at base pressure  $<10^{-5}$  Torr. Model soil samples will be dosed with a solution

of a particular EC in an appropriate solvent (e.g. dichloromethane, ethanol, or water). The resulting slurry will be loaded onto the thermal desorption system to analyze for the EC of interest as a function of temperature using a linear temperature ramp. It is expected that, due to the low pressure of the system, any non-adsorbed solvent/EC constituent will immediately evaporate at ambient temperature. Hence, any particulate experiencing binding interactions with the substrate ought to desorb at some  $T$  greater than ambient conditions. Chemical identification of the species of interest will be accomplished by simultaneously collecting mass spectra during the temperature ramp. Ultimately, the desorption temperature,  $T_{\max}$ , can be determined for the EC of interest and the binding energy to the model substrate may be calculated via the Redhead analysis.<sup>22</sup> Briefly, this method assumes an Arrhenius relationship to determine binding energies,  $E^*$ , through the following expression,

$$E^* = k_b T_{\max} \left[ \ln\left(\frac{v T_{\max}}{\beta}\right) - 3.64 \right] \quad (\text{C.1})$$

where  $k_b$  is the Boltzmann constant,  $\beta$  is the heating rate, and  $v$  is a preexponential frequency factor. The value of  $v$  depends upon several features of the adsorbate compound, including the sticking coefficient,  $s$ , surface coverage,  $\sigma$ , its mass,  $m$ , and the vapor pressure extrapolated to an infinitely high temperature regime,  $p_0$ . The frequency factor is expressed in equation (C.2).

$$v = \frac{s}{\sigma \sqrt{2\pi m k_b T_{\max}}} p_0 \quad (\text{C.2})$$

**Table C.1.** Potential test materials for EC/substrate binding experiments.

<b>Compound (EC)</b>	<b>Chemical Formula</b>
Toluene	C <sub>7</sub> H <sub>8</sub>
4-nitrotoluene (4-NT)	C <sub>7</sub> H <sub>7</sub> NO <sub>2</sub>
Nitrobenzene (NB)	C <sub>6</sub> H <sub>5</sub> NO <sub>2</sub>
2,4-dinitrotoluene (2,4-DNT)	C <sub>7</sub> H <sub>6</sub> N <sub>2</sub> O <sub>4</sub>
2,6-dinitrotoluene (2,6-DNT)	C <sub>7</sub> H <sub>6</sub> N <sub>2</sub> O <sub>4</sub>
1,3-dinitrobenzene (1,3-DNB)	C <sub>6</sub> H <sub>4</sub> N <sub>2</sub> O <sub>4</sub>
2,4,6-trinitrotoluene (TNT)	C <sub>7</sub> H <sub>5</sub> N <sub>3</sub> O <sub>6</sub>
1,3,5-trinitrobenzene (TNB)	C <sub>6</sub> H <sub>3</sub> N <sub>3</sub> O <sub>6</sub>
Hexahydro-1,3,5-trinitro-1,3,5-triazine (RDX)	C <sub>3</sub> H <sub>6</sub> N <sub>6</sub> O <sub>6</sub>
Pyridine (Pyr)	C <sub>5</sub> H <sub>5</sub> N
Pyrazine (Pyz)	C <sub>4</sub> H <sub>4</sub> N <sub>2</sub>
1,3,5-triazine (Trz)	C <sub>3</sub> H <sub>3</sub> N <sub>3</sub>
<b>Model Soil Materials</b>	
Graphitic carbon	Silica gel
Sand	Alumina

We will assume here that  $s$  is unity, which is an appropriate approximation for weakly interacting molecules at surfaces.<sup>23</sup> Surface coverages can be estimated as  $\sim 10^{18}$  molecules  $\text{cm}^{-2}$  based upon the work of Zacharia, et al., who reported similar values for polyaromatic hydrocarbons as large as ovalene.<sup>23</sup> Vapor pressures can be extrapolated using the Antoine expression (equation (C.3), where A, B, and C are Antoine parameters) derived from the Clausius-Clapeyron equation. The values required to calculate  $p_0$  are available either from the NIST database<sup>24</sup> or from various sources in the literature.<sup>25-28</sup>

$$\ln(p) = A - \frac{B}{T + C} \quad (\text{C.3})$$

The results of these studies will be used to validate computational models already in development.<sup>29</sup> These DFT models will form the foundation for an extensive library of substrate/EC binding energies and could ultimately predict the binding energies with a surface or substrate of some unknown or given EC. We will also investigate how munitions constituents and emerging contaminants interact with SWNTs in a similar method. The binding energy of an aromatic molecule increases as the molecule approaches the nanotube itself, based upon first principles calculations performed by Zhao and coworkers, Fig. C.3.<sup>30</sup> Thus, we anticipate being able to calculate binding energies to SWNTs in much the same manner as we would any of the other substrates mentioned above. The results of these experiments will be used to gauge the propensity for EC/MC interaction with

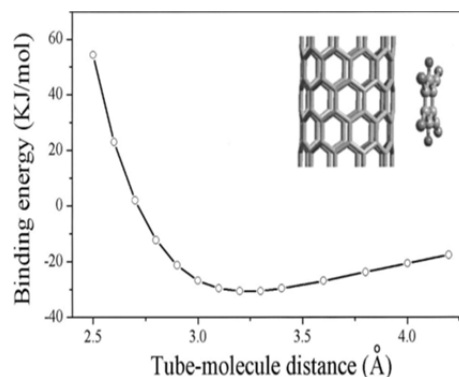


**Figure C.3.** Relationship between binding energy and tube-molecule separation for 2,3-dichloro-5,6-dicyano-1,4-benzoquinone approaching a SWNT. Reproduced from reference 30.

SWNTs and will represent a preliminary validation for subsequently employing a fluorescence monitoring technique.

*C.3.1.b. Two-dimensional Fluorescence Imaging of SWNT/EC Solutions, Complexes*

The second phase of the proposed work will seek to establish the relationship between particular ECs and the effect of these materials on the two-dimensional fluorescence spectra of SWNTs. It will comprise two avenues of investigation: 1) transport of MC/EC materials in water and 2) transport of materials in model soil systems. Initially, SWNTs in solution, solubilized in D<sub>2</sub>O and stabilized using a sodium dodecyl sulfate, SDS, surfactant,<sup>31</sup> will be exposed to varying concentrations of a particular EC. A two-dimensional spectrofluorometric technique will be applied to undosed and, subsequently, dosed SWNT solutions to evaluate changes in nanotube chirality. Ultimately, optimal concentration limits for this indirect detection of the MCs/ECs will be determined.

A relatively small concentration of SWNTs will be required for each of these experiments. Although SWNT fluorescence has been observed for single nanotubes,<sup>6, 32</sup> the concentrations we anticipate using will generally be 1-10 wt% in solution (SWNTs are commercially available in a powder form). Fluorescence spectra will be acquired as a function of both excitation and emission wavelengths using a commercially available instrument, such as the Jobin Yvon NanoLog spectrofluorometer available from Horiba. We anticipate that fluorescence through a sufficiently porous medium, such as a soil sample, can be detected. Indeed, researchers have recently begun using fluorescent carbon nanotubes to image internal organs of mice.<sup>33</sup> This instrument utilizes a liquid-

nitrogen cooled InGaAs array detector for rapid data collection corresponding to SWNT fluorescence. Conceivably, we could realize real-time analyses of EC/MC migration through a soil sample.

Fluorescence spectra of SWNTs in solid materials, including the model soil components listed in Table C.1 will also be collected. SWNTs have limited mobility in natural soil,<sup>34</sup> whereas ECs such as TNT and RDX are comparatively quite mobile,<sup>35</sup> making a SWNT-spiked soil sample ideal for monitoring the transport of ECs across a particular area in a soil matrix. To monitor the transport of ECs across a model soil sample, we will first scan an undosed sample containing SWNTs, then dose the same sample with a specific contaminant and monitor in real time the fluorescence signal arising from SWNTs at a particular stationary point along the soil sample. Changes in chirality at that physical location can then be attributed to the migration of some MC/EC to that point. A major advantage of this technique over chromatographic methods is that there is no need to rely upon a mobile phase or solvent to achieve the goals of the experiment, and as such, we can eliminate solvent effects, specifically, undesirable interactions of solvent materials with MCs/ECs. Moreover, essentially any location within the soil sample may be probed individually, which represents a significant advantage over relying upon a column. By understanding how the MC and EC materials move through soil and incorporating knowledge of the affinity of these materials for particular soil constituents, achieved through the experiments outlined in the previous section, we anticipate being able to effectively arrive at improved methods for complete remediation of detrimental contaminants in soils and water.

We also aim to examine the behavior of MCs and ECs in real-world contaminated systems. Thus, these studies will be extended to water and soil samples collected from contaminated sites, once the experiments and methodologies have been validated for model systems. Potential sites for study include the Holston River watershed near Kingsport, Tennessee, where the CDC has uncovered evidence of RDX biodegradation near the Holston Army Ammunition Plant, and the Aberdeen Proving Ground in Aberdeen, Maryland, still in use for live-fire exercises. We will introduce SWNTs to these samples and analyze using methods similar to those aforementioned. Because the composition of these materials and the identities of would-be contaminants are a relative unknown, additional characterizations will need to be performed on such samples. For instance, chromatographic techniques such as GC/MS or HPLC can be used to ascertain the identities and concentrations of contaminant species. Ultimately, we anticipate being able to map out and identify pathways for MC/EC migration and transport through real environmental media and suggest alternative methods for remediation of these materials.

### *C.3.2. Potential Limitations*

Although we anticipate performing the above experiments to the full extent of the preceding details, we have considered alternatives to several potential complicating events. The most pressing issue involves identification of a change in fluorescence signal from SWNTs exposed to MCs/ECs as compared to undosed nanotubes. It is expected that the majority of the MCs/ECs will interact in such a way that we will observe localized photobleaching of the fluorescence spectra or a change in signal intensities for particular SWNT chiralities due to the presence of nitro groups. However, not all of the ma-

materials listed in Table C.1 contain functionalities associated with typical charge-transfer reactions. To compensate for this in the case of such a material, we propose the use of functionalized carbon nanotubes. SWNTs can be modified with essentially any number of functional groups to improve the sensitivity and selectivity to a particular species. For example, Zhang and coworkers developed triphenylene-functionalized carbon nanotubes for ultra-trace detection (<50 nM) of TNT.<sup>36</sup> In addition, CNTs have also been treated with metals to improve selectivity.<sup>37</sup> A potential drawback to using such a system, however, lies in the spontaneous formation of environmentally detrimental and spectroscopically spurious metal nanoparticles which can form under conditions such as those present in natural groundwater.<sup>38</sup>

Another potential limitation in this work is the intensity of the signal observed in the fluorescence spectra. If the signal intensity is simply too low, we may not be able to discern changes in SWNT chirality. One contingency plan for rectifying this problem, beyond simply increasing the concentration of SWNTs in our samples, is the utilization of Raman spectroscopy to observe the radial breathing modes (RBM) of the nanotubes to complement our fluorescence data. Similar to the fluorescence technique described above, this Raman application can be used to map chirality changes in SWNTs through visualization of changes in RBM phonon frequencies. Anderson and coworkers have demonstrated the applicability of this technique using a combination of Raman microscopy and spectroscopy to image semiconducting-to-metal chirality changes in SWNTs.<sup>39</sup> The drawback to using this method at the outset, however, is that the Raman method is a much more expensive, cumbersome and time-intensive experiment than the fluorescence method.

#### **C.4. Summary and Outlook**

The experiments and methodologies described herein will be developed to determine the fates of hazardous munitions waste materials in the environment. Upon completion of this work, we will have calculated binding energies for a wide range of munitions constituents and emerging contaminants with soil components and used this information to refine predictive computational models. In addition, we will have developed a method to indirectly monitor transport and migration of MCs and ECs through aquatic and soil systems through use of fluorescent carbon nanotubes. Eventually, we anticipate being able to deploy analysis tools, such as a compact fluorometer, to the field in order to assess, on-site, the impact of munitions contamination. Ultimately, we will, through this work, establish improved methods for determining courses of remediation for contaminated sites and expand upon the current knowledge of MC/EC behavior in natural ecosystems through communication of this work in the open literature.

## C.5. References

1. Best, E. P. H.; Geter, K. N.; Tatem, H. E.; Lane, B. K., Effects, transfer, and fate of RDX from aged soil in plants and worms. *Chemosphere* **2006**, 62, (4), 616-625.
2. Best, E. P. H.; Tatem, H. E.; Geter, K. N.; Wells, M. L.; Lane, B. K., Effects, uptake, and fate of 2,4,6-trinitrotoluene aged in soil in plants and worms. *Environ. Toxicol. Chem.* **2008**, 27, (12), 2539-2547.
3. Dunnick, J. K.; Burka, L. T.; Mahler, J.; Sills, R., Carcinogenic potential of o-nitrotoluene and p-nitrotoluene. *Toxicology* **2003**, 183, (1-3), 221-234.
4. Bermudez, E.; Tillery, D.; Butterworth, B. E., *Environ. Mutagen.* **1979**, 1, (4), 391-398.
5. Muller, S. R.; Berg, M.; Ulrich, M. M.; Schwarzenbach, R. P., Atrazine and Its Primary Metabolites in Swiss Lakes: Input Characteristics and Long-Term Behavior in the Water Column. *Environ. Sci. Technol.* **1997**, 31, (7), 2104-2113.
6. Hartschuh, A.; Pedrosa, H. N.; Peterson, J.; Huang, L.; Anger, P.; Qian, H.; Meixner, A. J.; Steiner, M.; Novotny, L.; Krauss, T. D., Single Carbon Nanotube Optical Spectroscopy. *ChemPhysChem* **2005**, 6, (4), 577-582.
7. Melkonian, G.; Eckelhoefer, H.; Wu, M.; Wang, Y.; Tong, C.; Riveles, K.; Talbot, P., Growth and angiogenesis are inhibited in vivo in developing tissues by pyrazine and its derivatives. *Toxicol. Sci.* **2003**, 75, 227-228.
8. Hewitt, A. D.; Jenkins, T. F.; Walsh, M. E.; Walsh, M. R.; Taylor, S., RDX and TNT residues from live-fire and blow-in-place detonations. *Chemosphere* **2005**, 61, (6), 888-894.
9. Spalding, R. F.; Fulton, J. W., Groundwater munition residues and nitrate near Grand Island, Nebraska, U.S.A. *Journal of Contaminant Hydrology* **1988**, 2, (2), 139-153.
10. Parker, D. R., Perchlorate in the environment: the emerging emphasis on natural occurrence. *Environ. Chem.* **2009**, 6, (1), 10-27.
11. Snellinx, Z.; Nepovím, A.; Taghavi, S.; Vangronsveld, J.; Vanek, T.; van der Lelie, D., Biological remediation of explosives and related nitroaromatic compounds. *Environ. Sci. Pollut. Res.* **2002**, 9, (1), 48-61.
12. Thorn, K. A.; Pennington, J. C.; Kennedy, K. R.; Cox, L. G.; Hayes, C. A.; Porter, B. E., N-15 NMR study of the immobilization of 2,4- and 2,6-dinitrotoluene in aerobic compost. *Environ. Sci. Technol.* **2008**, 42, 2542-2550.
13. Wilder, J. W. G.; Venema, L. C.; Rinzler, A. G.; Smalley, R. E.; Dekker, C., Electronic structure of atomically resolved carbon nanotubes. *Nature* **1998**, 391, (6662), 59-62.
14. Bachilo, S. M.; Strano, M. S.; Kittrell, C.; Hauge, R. H.; Smalley, R. E.; Weisman, R. B., Structure-Assigned Optical Spectra of Single-Walled Carbon Nanotubes. *Science* **2002**, 298, (5602), 2361-2366.
15. Kong, J.; Franklin, N. R.; Zhou, C.; Chapline, M. G.; Peng, S.; Cho, K.; Dai, H., Nanotube Molecular Wires as Chemical Sensors. *Science* **2000**, 287, (5453), 622-625.

16. Capek, I., Dispersions, novel nanomaterial sensors and nanoconjugates based on carbon nanotubes. *Advances in Colloid and Interface Science* **2009**, 150, (2), 63-89.
17. Varghese, S. H.; Nair, R.; Nair, B. G.; Hanajiri, T.; Maekawa, T.; Yoshida, Y.; Kumar, D. S., Sensors Based On Carbon Nanotubes and Their Applications: A Review. *Current Nanoscience* 6, (4), 331-346.
18. Roberts, M. E.; LeMieux, M. C.; Bao, Z., Sorted and Aligned Single-Walled Carbon Nanotube Networks for Transistor-Based Aqueous Chemical Sensors. *ACS Nano* **2009**, 3, (10), 3287-3293.
19. Kuang, Z.; Kim, S. N.; Crookes-Goodson, W. J.; Farmer, B. L.; Naik, R. R., Biomimetic Chemosensor: Designing Peptide Recognition Elements for Surface Functionalization of Carbon Nanotube Field Effect Transistors. *ACS Nano* **2009**, 4, (1), 452-458.
20. Park, M.; Cella, L. N.; Chen, W.; Myung, N. V.; Mulchandani, A., Carbon nanotubes-based chemiresistive immunosensor for small molecules: Detection of nitroaromatic explosives. *Biosensors and Bioelectronics* **2010**, 26, (4), 1297-1301.
21. Woods, L. M.; Badescu, S. C.; Reinecke, T. L., Adsorption of simple benzene derivatives on carbon nanotubes. *Phys. Rev. B* **2007**, 75, (15), 155415.
22. Redhead, P. A., Thermal desorption of gases. *Vacuum* **1962**, 12, (4), 203-211.
23. Zacharia, R.; Ulbricht, H.; Hertel, T., Interlayer cohesive energy of graphite from thermal desorption of polyaromatic hydrocarbons. *Phys. Rev. B* **2004**, 69, (15), 155406.
24. Linstrom, P. J.; Mallard, W. G., Eds NIST Chemistry WebBook Standard Reference Database Number 69, June 2005, National Institute of Standards and Technology, Gaithersburg, MD 20899. <http://webbook.nist.gov> (2 January 2011),
25. Dykyj, J.; Svoboda, J.; Wilhoit, R. C.; Frenkel, M.; Hall, K. R., *Vapor Pressure and Antoine Constants for Nitrogen Containing Organic Compounds: Pressure of Chemicals, Part C*. Springer: 2001; Vol. 20.
26. De Wit, H. G. M.; Van Miltenburg, J. C.; De Kruif, C. G., Thermodynamic properties of molecular organic crystals containing nitrogen, oxygen, and sulphur 1. Vapour pressures and enthalpies of sublimation. *J. Chem. Thermodyn.* **1983**, 15, 651-663.
27. Steele, W. V.; Chirico, R. D.; Knipmeyer, S. E.; Nguyen, A., Measurements of Vapor Pressure, Heat Capacity, and Density along the Saturation Line for  $\hat{\mu}$ -Caprolactam, Pyrazine, 1,2-Propanediol, Triethylene Glycol, Phenyl Acetylene, and Diphenyl Acetylene. *J. Chem. Eng. Data* **2002**, 47, 689-699.
28. Morris, J. B., Solubility of RDX in dense carbon dioxide at temperatures between 303 K and 353 K. *J. Chem. Eng. Data* **1998**, 43, 269-273.
29. Sviatenko, L.; Isayev, O.; Gorb, L.; Hill, F.; Leszczynski, J., Toward robust computational electrochemical predicting the environmental fate of organic pollutants. *J. Comput. Chem.* **2011**, 32, (10), 2195-2203.
30. Zhao, J.; Lu, J. P.; Han, J.; Yang, C.-K., Noncovalent functionalization of carbon nanotubes by aromatic organic molecules. *Appl. Phys. Lett.* **2003**, 82, (21), 3746-3748.

31. Weisman, R. B.; Bachilo, S. M.; Tsyboulski, D., Fluorescence spectroscopy of single-walled carbon nanotubes in aqueous suspension. *Appl. Phys. A: Mater. Sci. Process.* **2004**, 78, (8), 1111-1116.
32. Hartschuh, A.; Pedrosa, H. N.; Novotny, L.; Krauss, T. D., Simultaneous Fluorescence and Raman Scattering from Single Carbon Nanotubes. *Science* **2003**, 301, (5638), 1354-1356.
33. Welsher, K.; Sherlock, S. P.; Dai, H., Deep-tissue anatomical imaging of mice using carbon nanotube fluorophores in the second near-infrared window. *PNAS* **2011**, published online.
34. Jaisi, D. P.; Elimelech, M., Single-Walled Carbon Nanotubes Exhibit Limited Transport in Soil Columns. *Environ. Sci. Technol.* **2009**, 43, (24), 9161-9166.
35. Selim, H. M.; Xue, S. K.; Iskandar, I. K., Transport of 2, 4, 6-Trinitrotoluene and Hexahydro-1, 3, 5-Trinitro-1, 3, 5-Triazine in Soils. *Soil Science* **1995**, 160, (5), 328-339.
36. Zhang, H.-X.; Hu, J.-S.; Yan, C.-J.; Jiang, L.; Wan, L.-J., Functionalized carbon nanotubes as sensitive materials for electrochemical detection of ultra-trace 2,4,6-trinitrotoluene. *Phys. Chem. Chem. Phys.* **2006**, 8, (30), 3567-3572.
37. Zhao, Q.; Buongiorno Nardelli, M.; Lu, W.; Bernholc, J., Carbon Nanotube-Metal Cluster Composites: A New Road to Chemical Sensors? *Nano Letters* **2005**, 5, (5), 847-851.
38. Akaighe, N.; MacCuspie, R. I.; Navarro, D. A.; Aga, D. S.; Banerjee, S.; Sohn, M.; Sharma, V. K., Humic Acid-Induced Silver Nanoparticle Formation Under Environmentally Relevant Conditions. *Environ. Sci. Technol.* **2011**, 45, (9), 3895-3901.
39. Anderson, N.; Hartschuh, A.; Novotny, L., Chirality Changes in Carbon Nanotubes Studied with Near-Field Raman Spectroscopy. *Nano Lett.* **2007**, 7, (3), 577-582.

## LIST OF ABBREVIATIONS

$A_{(s)}$	activated surface site
AFM	atomic force microscopy
AOES	actinometric optical emission spectroscopy
CA	contact angle goniometry
d.s.	downstream
$\langle E_i \rangle$	mean ion energy
FC	fluorocarbon
HFPO	hexafluoropropylene oxide
ICCD	intensified charge-coupled device
ICP	inductively coupled plasma
IED	ion energy distribution
IRIS	imaging of radicals interacting with surfaces
$k$	dielectric constant; rate constant
$k_b$	Boltzmann constant
LIF	laser-induced fluorescence
MS	mass spectrometry
OES	optical emission spectroscopy
$P$	applied rf power
$p$	total system pressure
$P_{(s)}$	passivated surface site
PECVD	plasma-enhanced chemical vapor deposition
PTFE	poly(tetrafluoroethylene), Teflon <sup>®</sup>

$R$	surface reactivity coefficient
rf	radio frequency
RGA	residual gas analysis
$S$	surface scatter coefficient
sccm	standard cubic centimeters per minute
SEM	scanning electron microscopy
$T_e$	electron temperature
$T_i$	ion temperature
TR-OES	time-resolved optical emission spectroscopy
$V_p$	plasma potential
$V_s$	surface potential
VASE	variable angle spectroscopic ellipsometry
XPS	x-ray photoelectron spectroscopy
$\gamma_{lv}$	liquid-vapor surface tension
$\gamma_{sl}$	surface-liquid surface tension
$\gamma_{sv}$	surface-vapor surface tension; surface energy
$\Delta\gamma_c$	critical surface energy
$\theta$	contact angle value
$\Theta_R$	rotational temperature
$\Theta_T$	translational temperature
$\Theta_V$	vibrational temperature
$\Phi$	sheath potential